Tesis Doctoral
Doctorado en Electrónica, Tratamiento de Señal y Comunicaciones

Continuous and Discontinuous Modulation Techniques for Multiphase Drives: Analysis and Contributions

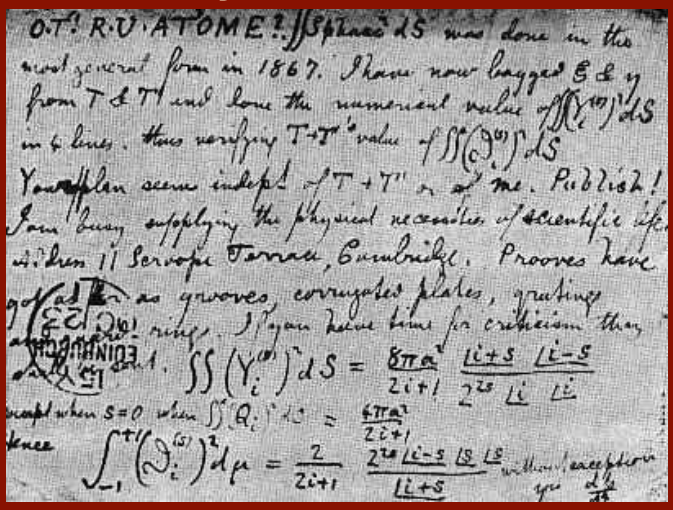

Autor: Joel Prieto Corvalán
Directores: Federico José Barrero García
Sergio Luis Toral Marín

Departamento de Ingeniería Electrónica
Escuela Técnica Superior de Ingeniería
Universidad de Sevilla

Sevilla, 2016

Tesis Doctoral
Doctorado en Electrónica, Tratamiento de Señal y Comunicaciones

Continuous and Discontinuous Modulation Techniques for Multiphase Drives: Analysis and Contributions

Autor:

Joel Prieto Corvalán

Directores:

Federico José Barrero García
Sergio Luis Toral Marín

Departamento de Ingeniería Electrónica
Escuela Técnica Superior de Ingeniería
Universidad de Sevilla

2016

Tesis Doctoral: Continuous and Discontinuous Modulation Techniques for Multiphase Drives: Analysis and Contributions

Autor: Joel Prieto Corvalán
Directores: Federico José Barrero García
Sergio Luis Toral Marín

El tribunal nombrado para juzgar la Tesis arriba indicada, compuesto por los siguientes doctores:

Presidente:

Vocales:

Secretario:

acuerdan otorgarle la calificación de:

El Secretario del Tribunal

Fecha:

Dedicado a:
Irina y Jimena
Que me llenan
de alegría cada día

–

Don Amado y Doña Mirta
Quienes siempre apostaron por
mi educación, crecimiento
personal y satisfacción
profesional

Summary

The study of multiphase machines applications is an emergent field of research mainly because of the high reliability they offer for high power applications. Nowadays, they are predominantly supplied from two-level voltage source inverters (VSIs). For the purpose of the inverter control, both carrier-based and space vector pulse width modulation (PWM) techniques have been developed, for various phase numbers, which are capable of generating required sinusoidal output voltages. Both methods are usually a general extension of modulation methods used in the three-phase case.

The relationship between continuous carrier-based and space vector PWM has been reported in the scientific literature for the multiphase case, stating analogies and differences. Discontinuous PWM techniques for multiphase inverters have also received some attention as well, but at a lesser extent than the continuous PWM techniques, always in relation to multiphase systems. In order to fill the aforementioned gap, discontinuous modulation methods are first analysed in multiphase drives.

The natural consequence of the existence of different PWM strategies is the inherently different behaviour with regard to the performance indicators that can be used to assess the quality of output waveforms. Among these performance indicators, one of the most interesting used in three phase induction machines for the evaluation of switching characteristics and the current ripple are the flux harmonic distortion factor (HDF). However, HDF has been only recently introduced in the multiphase case, and for asymmetrical six-phase induction machines that can be considered like two three phase machines in the same case. Consequently, there is quite few work in the scientific literature and within the multiphase induction machine case about the evaluation of switching characteristics and the current ripple using HDF. Therefore, the extension of HDF for the evaluation of switching characteristics and the current ripple in the multiphase case is studied and analysed like a second main goal of this Thesis.

Notice that SVM has been also extended to the multiphase case. However, most of the scientific literature only relates the general case, where linear operation

regions are only considered. A third goal of the work is the extension of the operation region of the SVM-multiphase scheme. In this field, non linear operation in the overmodulation region is also considered, guaranteeing a smooth and linear transition characteristic between linear and overmodulation regions, minimizing the unwanted voltage amplitude of low order voltage harmonic components. Then, a simple algorithm is proposed with the ability to minimize $x-y$ voltage and current components in any multiphase induction machine with any odd number of phases.

Finally, the reduction of Common Mode Voltage (CMV) is an interesting topic in the modulation techniques field because it is known to be the cause of electromagnetic interference (EMI), breakdown of windings insulation, fault activation of current detector circuits and leakage currents problems that can damage the motor bearings. The common-mode voltage issue is also studied in this Thesis, and a SVM method is proposed to minimize its content in the electromechanical system.

Major contributions of this dissertation have been published in seven journal and three conferences papers, although some related work have been also published in another four journal papers. The main contributions covered in this work are the following:

Paper 1: D. Dujic, M. Jones, E. Levi, J. Prieto, F. Barrero, "Switching Ripple Characteristics of Space Vector PWM Schemes for Five-Phase Two Level Voltage Source Inverters-Part 1: Flux Harmonic Distortion Factors," IEEE Transactions on Industrial Electronics, vol.58, no.7, pp.2789-2798, July 2011.

Paper 2: M. Jones, D. Dujic, E. Levi, J. Prieto, F. Barrero, "Switching Ripple Characteristics of Space Vector PWM Schemes for Five-Phase Two Level Voltage Source Inverters-Part 2: Current Ripple," IEEE Transactions on Industrial Electronics, vol.58, no.7, pp. 2799-2808, July 2011.

Paper 3: J. Prieto, M. Jones, F. Barrero, E. Levi, S. Toral, "Comparative Analysis of Discontinuous and Continuous PWM Techniques in VSI-Fed Five-Phase Induction Motor," IEEE Transactions on Industrial Electronics, vol.58, no.12, pp.5324-5335, Dec. 2011.

Paper 4: J. Prieto, F. Barrero, E. Levi, S. Toral, M. Jones, M. J. Durán, "Analytical Evaluation of Switching Characteristics in Five-Phase Drives with Discontinuous Space Vector Pulse Width Modulation Techniques", EPE Journal, vol.23, no.2, pp.24-33, Jun. 2013.

Paper 5: J. Prieto, E. Levi, F. Barrero, S. Toral, "Output current ripple analysis for asymmetrical six-phase drives using double zero-sequence injection PWM," Proceedings of 37th Annual Conference on IEEE Industrial Electronics Society (IECON 2011), pp.3692-3697, Nov. 2011.

Paper 6: M.J. Durán, J. Prieto, F. Barrero, J.A. Riveros, H.Guzmán, "Space-Vector PWM With Reduced Common-Mode Voltage for Five-Phase Induction Motor Drives," IEEE Transactions on Industrial Electronics, vol.60, no.10, pp.4159-4168, Oct. 2013.

Paper 7: M.J. Duran, J. Prieto, F. Barrero, "Space Vector PWM With Reduced Common-Mode Voltage for Five-Phase Induction Motor Drives Operating in Overmodulation Zone," IEEE Transactions on Power Electronics, vol.28, no.8, pp.4030-4040, Aug. 2013.

Paper 8: J. Prieto, F. Barrero, M. J. Durán, S. Toral, M.A. Perales, "SVM Procedure for n-phase VSI With Low Harmonic Distortion in the Overmodulation Region," IEEE Transactions on Industrial Electronics, vol.61, no.1, pp.92-97, Jan. 2014.

Notice that all the contributions were validated using simulation and experimental results, and different five-phase and asymmetrical six-phase induction machines available at the laboratories of the Liverpool John Moores University and the University of Seville, being the candidate one of the main contributors to the obtained publications.

Agradecimientos

Llegado este momento hay varias personas e instituciones que se merecen mi sincero agradecimiento.

En primer lugar, quiero expresar el más profundo agradecimiento a mis directores de Tesis *Dr. Federico Barrero* y *Dr. Sergio Toral* por su dirección y guía durante estos años. Con su constante apoyo y orientación fue posible la realización de este proyecto. Además, la excepcional capacidad de superación frente a los problemas inyecta dinamismo al quehacer diario de las personas que tenemos el orgullo de formar parte de su grupo de investigación. En especial a Federico, quien me enseñó que aunque durante el camino aparezcan adversidades, lo importante es mirar hacia adelante y seguir trabajando para alcanzar el objetivo.

A *Emil Levi* y su equipo de trabajo, por recibirme en dos ocasiones en Liverpool John Moores University. Ha sido un placer y también un gran desafío trabajar con personas como él, que buscan la excelencia en cada uno de sus trabajos.

Además, una mención especial a *Itaipu Binacional/Parque Tecnológico de Itaipú* y al *Consejo Nacional de Ciencia y Tecnología - CONACYT*, por la beca concedida para culminar este trabajo. También a la *Universidad Sevilla* por haberme permitido colaborar en diferentes proyectos y al *Gobierno Español*, por el soporte económico proveído a través del Plan Nacional de Investigación, Desarrollo e Innovación bajo la referencia DPI2005/04438. Sin la ayuda económica recibida por todos estos organismos, no hubiera podido realizar este trabajo.

Del mismo modo, un recuerdo especial para mis amigos en Sevilla. Con su calidez humana, la estadía fuera de mi país se ha convertido en una hermosa experiencia

de vida. A los que se han convertido en mi familia: *Federico*, *María Ángeles*, *Hugo*, *José Alberto*; a mis compañeros de Investigación: *Esteban*, *José* y *Blas*.

A *Irina*, porque su apoyo en la última etapa de este trabajo fue fundamental.

Por último, agradezco a mis padres *Mirta* y *Amado* por el constante cariño y apoyo de siempre, pero especialmente por haberme brindado un hogar cálido y enseñarme que la perseverancia y el esfuerzo son los medios que permiten lograr los objetivos.

Joel Prieto
Sevilla, 2016

Índice General

Índice de Figuras

Índice de Tablas

Capítulo 1

Introducción

1.1. Consideraciones preliminares

Los accionamientos electromecánicos en sus diferentes aplicaciones industriales de tipo motor y generador representan una parte muy importante del consumo y producción energética mundial. Tradicionalmente se han venido usando dispositivos de tipo trifásico, especialmente desde el desarrollo de los semiconductores que funcionan como interruptores de potencia y la aparición de los sistemas microprocesadores, lo que ha permitido su uso como variadores de velocidad en aplicaciones tan recientes como los Vehículos Eléctricos (VEs) o generación eólica. En los últimos años, y gracias al desarrollo y evolución de los dispositivos antes mencionados, la comunidad científica ha centrado su atención en un tipo de accionamientos electromecánicos en el que el número de fases es mayor de tres. Estos dispositivos, conocidos como máquinas eléctricas multifásicas, se desarrollan en paralelo con las máquinas trifásicas ofreciendo ventajas interesantes al generar un bajo par pulsante y bajo contenido armónico en el DC-link, obteniendo mayor fiabilidad y generando una mejor distribución de corriente entre las fases. Son, por tanto, especialmente adecuados en aplicaciones relacionadas con la propulsión eléctrica y en VEs por los siguientes motivos:

1. La fuerza magnetomotriz del entrehierro tiene un menor contenido en armónicos espaciales en el accionamiento multifásico, lo que produce menores rizado de par, ruido acústico, vibraciones y pérdidas Joule en el estátor y rótor, mejorando la eficiencia del accionamiento. Esta ventaja resulta de

interés claro en propulsión eléctrica puesto que mejoraría la eficiencia y autonomía del VE.

2. El valor de la corriente por fase disminuye (para la misma tensión y potencia nominal) de forma proporcional al número de fases del accionamiento. En un VE, donde la tensión asociada a la batería (DC-link) es baja y la potencia necesaria es de varias decenas de kW, esta característica es interesante porque el accionamiento multifásico permite el reparto natural de la corriente entre un mayor número de fases, lo que ayudaría en la elección del convertidor e interruptores de potencia.

3. La fiabilidad aumenta por la redundancia que existe al aumentar el número de fases, que permite el funcionamiento post-falta. Esta característica es de claro interés en propulsión eléctrica puesto que permitiría detectar el fallo y seguir circulando hasta su reparación.

4. El par generado puede aumentarse mediante la inyección de ciertos armónicos de corriente en la máquina, siempre que ésta sea de devanados concentrados. Este par adicional hace que las máquinas, para una misma potencia nominal, sean más compactas, lo que facilitaría su implantación en propulsión de VE donde el peso y el volumen del sistema son aspectos muy relevantes.

Sin importar la finalidad o el tipo de máquina empleados en los variadores electromecánicos, hoy en día es imprescindible incluir en ellos convertidores de potencia. La arquitectura comercial más habitual incluye un inversor de dos niveles cuya salida es controlada empleando normalmente algún algoritmo basado en modulación por anchura de pulso (PWM, por sus siglas en inglés) para generar a la salida un amplio rango de tensiones y frecuencias de las que depende la velocidad de giro del variador, a las que se suman componentes de armónicos que se tratan generalmente de minimizar. El desarrollo de esta arquitectura ha sido ampliamente estudiado y analizado tanto a nivel de investigación como industrial en el caso de los accionamientos trifásicos. Por ejemplo, en la actualidad la tecnología relacionada con los vehículos energéticamente eficientes y la propulsión eléctrica de tipo trifásico ha madurado notablemente con el desarrollo de nuevos y más eficientes sistemas de almacenamiento energético (baterías) y accionamiento (motores eléctricos). Algunos vehículos comerciales de las más importantes compañías del sector de la automoción ya incorporan estas nuevas tecnologías energéticamente eficientes,

destacándose el Renault Z.E. (motor eléctrico de 65 kW síncrono con rotor bobinado), el Peugeot iON o el Mitsubishi i-MiEV (motor eléctrico síncrono de 49 kW de imán permanente), el Nissan Leaf (motor eléctrico síncrono de 80 kW) o el Chevrolet Volt y el Opel Ampera (con motor eléctrico de 63 kW, combinado con un motor de combustión y un generador eléctrico para aumentar la autonomía), utilizando motores de alterna de tecnología más eficiente en generación de par, tamaño y peso que los motores de inducción de rotor en jaula de ardilla.

Sustentada en las ventajas de la utilización de variadores electromecánicos y aprovechando el incesante desarrollo de los convertidores de potencia y de los microprocesadores, también se han propuesto arquitecturas para accionmientos multifásicos. Sin embargo, a pesar de las interesantes características que ofrece el uso de estos accionamientos, su aplicación actual está muy restringida por la dificultad que existe en encontrar una estrategia de modulación y control versátil y extrapolable a cualquier tipo de accionamiento independientemente del número de fases implicadas, a semejanza de lo que ocurre en el caso del accionamiento trifásico convencional con la modulación denominada Space Vector (SV) o el control orientado en campo (FOC por sus siglas en inglés).

El desarrollo de esta Tesis se orienta a la extensión de las técnicas de modulación empleadas en los accionamientos de tres fases a accionamientos multifásicos de n-fases, particularizando a los casos más habituales de cinco y seis fases, su análisis y evaluación experimental en su aplicación final en variadores de velocidad. El trabajo de investigación consta de dos partes diferenciadas. La primera parte se concentra en la extensión de técnicas de modulación PWM en accionamientos multifásicos de 5 y 6 fases, así como en su análisis comparativo, centrándose principalmente en los métodos de modulación discontinuos aplicados en la zona de modulación lineal, para determinar las ventajas e inconvenientes de cada una de las estrategias determinando así los diferentes ámbitos de aplicación de las mismas. La segunda parte se basa en el desarrollo de nuevas estrategias de modulación que modifican las estrategias anteriores para contemplar situaciones especiales no analizadas hasta la fecha por la comunidad científica internacional. En concreto se han propuesto estrategias de modulación que permiten extender el rango de uso de la zona lineal a la zona de sobremodulación, así como métodos que minimizan la tensión generada en modo común (CMV en sus siglas en inglés) en el dispositivo con el fin de minimizar el daño que se puede producir en los rodamientos del accionamiento. El trabajo desarrollado incorpora un extenso

análisis teórico basado en los denominados factores de distorsión armónica de flujo (HDF en sus siglas en inglés) que permite deducir la componente armónica del flujo en el estator y lo que es más importante, extender el análisis para calcular la corriente generada en un accionamiento multifásico de cinco y seis fases, acompañado por un extenso análisis experimental de validación de la metodología propuesta. Se presentan asimismo diversos métodos de modulación que permiten su aplicación en el rango de sobremodulación o centrados en la eliminación del CMV generado en la máquina eléctrica. La Tesis se sustenta en un total de 7 publicaciones en revistas internacionales de reconocido prestigio dado su elevado factor de impacto, así como a una importante cantidad de comunicaciones o ponencias en congresos internacionales. Comentar, por último, que la aplicación de las estrategias presentadas en el desarrollo de variadores multifásicos ha dado lugar a otras publicaciones en las que interviene el doctorando y que no se detallan en este documento por no haberse considerado núcleo principal del trabajo desempeñado. Estos trabajos si se incluyen en la bibliografía, al considerar el autor su relevancia en el desarrollo del estado actual de la ciencia relacionada con los variadores electromecánicos multifásicos.

1.2. Motivación

La principal motivación que ha impulsado esta Tesis es el desarrollo de aportes en el campo de la extensión de las estrategias de modulación con aplicación en accionamientos multifásicos. El objetivo final será el desarrollo de un variador de velocidad basado en accionamientos multifásicos con aplicación en propulsión de vehículos eléctricos. El estudio de los vehículos eléctricos constituye una de las líneas de investigación con mayor crecimiento e impacto social de esta última década. A pesar de los avances conseguidos en esta línea, los vehículos eléctricos aún no superan a los convencionales, considerándose necesaria su potenciación con el apoyo a la actividad investigadora en el área en particular en los campos relacionados con el desarrollo de nuevos y más eficientes sistemas de almacenamiento energético (baterías) y tecnologías de propulsión (motores eléctricos). El VE, como cualquier nueva tecnología, deberá superar ciertas barreras para su introducción, tanto por el desconocimiento de los usuarios de las posibilidades reales y beneficios que ofrece como por la necesidad de que la oferta se desarrolle lo más ampliamente posible. Existe un claro fomento público del VE como medio de transporte futuro

para superar dichas barreras. Como ejemplo de estas actividades de promoción se puede destacar la reciente propuesta de Directiva comunitaria que obligaría a los países de la Unión Europea a disponer de un total de 8 millones de puntos de abastecimiento para coches eléctricos (a España le corresponderían 824.000 de los que 82.000 deberán ser públicos). La Unión Europea y España están lanzadas en el horizonte del 2020 con el objetivo de impulsar el uso de vehículos limpios, con la previsión por parte del gobierno español de que circulen 2,5 millones de coches eléctricos en sus carreteras.

El sistema de propulsión representa la parte más importante del vehículo eléctrico y ha focalizado el interés reciente de la comunidad científica internacional y de este trabajo, en el que se ha contemplado el uso de los accionamientos multifásicos, que poseen características que lo hacen adecuados para estas aplicaciones aunque la tecnología de las máquinas multifásicas no se encuentre actualmente en su estado de madurez. Es necesario, por tanto, consolidar el uso de los accionamientos multifásicos en ámbitos de aplicaciones de interés como la que se propone en esta Tesis.

1.3. Objetivos

El objetivo de esta Tesis es el estudio de los accionamientos multifásicos centrado en las máquinas de inducción de cinco y seis fases, su análisis y la extensión de estrategias de modulación empleadas en accionamientos convencionales de tipo trifásico. En concreto, se pueden enumerar los siguientes objetivos particulares:

1. Extender los algoritmos de modulación en zona lineal a los accionamientos multifásicos, estableciendo una relación unívoca entre las estrategias de modulación basadas en basadas en portadora y aquellas basadas en SV.
2. Establecer una metodología para el análisis comparativo de las estrategias de modulación que se pueden emplear en los convertidores de potencia multifásicos de dos niveles de entrada a las máquinas multifásicas, para la posterior identificación de las ventajas e inconvenientes que ofrecen comparativamente dichas estrategias de modulación en el caso multifásico así como su respectivo ámbito de utilización.
3. Extender los algoritmos de modulación en los accionamientos multifásicos a casos particulares no analizados hasta la fecha, como son el caso de

sobremodulación y la mitigación de la tensión en modo común generada en el accionamiento.

1.4. Organización del documento

El documento se ha organizado en tres partes, que responden a la estructura definida por la Normativa Reguladora del Régimen de Tesis Doctoral vigente de la Universidad de Sevilla, en cumplimiento con el Real Decreto 99/2011 (BOE 10 de febrero de 2011) que establece: *"Podrán presentarse para su evaluación como tesis doctoral un conjunto de trabajos publicados por el doctorando (...) Además de las publicaciones, la tesis doctoral deberá incluir necesariamente: introducción en la que se justifique la unidad temática de la tesis, objetivos a alcanzar, un resumen global de los resultados, la discusión de estos resultados y las conclusiones finales..."*

En la primera parte de este trabajo se detallan las generalidades del mismo. Se realiza una presentación del mismo, sus fundamentos y demás cuestiones preliminares (Capítulo 1).

En el Capítulo 2 se introducen los resultados obtenidos en los trabajos de investigación realizados. Primero se detallan los conceptos básicos relacionados con el análisis de las técnicas de modulación empleadas en los accionamientos multifásicos, donde se propone el empleo de los factores HDF como modo de evaluación de las estrategias de modulación de accionamientos multifásicos, analizándose su adecuación al caso de 5 y 6 fases. Posteriormente se introduce el interés en nuevas variantes para modular los convertidores de potencia conectados a los variadores multifásicos con los objetivos de actuar en las zonas de sobremodulación, de minimizar la tensión de modo común o cumpliendo ambos objetivos.

En el Capítulo 3 se presentan los artículos basados en ideas originales, desarrollados y publicados durante la realización de la investigación presentada. En los dos primeros artículos se realiza un estudio detallado del rizado de corriente estatórica para diferentes técnicas de modulación continua en zona lineal para accionamientos de 5 fases, estableciéndose la dependencia analítica con el HDF de flujo y considerando el modelo del motor. En los artículos 3 y 4 se extiende el estudio anterior en su empleo en zona lineal utilizando técnicas de modulación discontinuas. En todos los trabajos presentados se realiza un estudio teórico y de

simulación que relaciona el parámetro HDF con el rizado de corriente estatórica, correspondencia que se corrobora posteriormente con resultados obtenidos en diferentes bancadas de ensayo de accionamientos multifásicos. El amplio estudio realizado en los 4 trabajos descritos con anterioridad se extiende en el artículo 5, por último, al análisis de las técnicas de modulación utilizables en accionamientos de 6 fases. Posteriormente, en un segundo grupo de artículos (artículos 6, 7, 8) se estudia la extensión de las técnicas de modulación en el caso multifásico en situaciones especiales no analizadas con anterioridad en la literatura científica, para lidiar con problemas relacionados con sobremodulación o mitigación de la tensión de modo común generada en el neutro del motor. Así, en el artículo 6 se proponen diferentes técnicas de modulación para disminuir el CMV en zona lineal utilizando máquinas de 5 fases. Estas propuestas se extienden a zona de sobremodulación en los siguientes artículos (artículos 7 y 8), en los que se realiza un estudio matemático de optimización del CMV para sintetizar una tensión en zona de sobremodulación aun manteniendo en mínimos la tensión en modo común en el accionamiento de 5 fases (artículo 7), generalizándose el estudio a cualquier máquina multifásica de n fases (siendo n un número impar cualquiera) en el artículo 8, en el que se utiliza una estrategia de modulación basadas en SV que permite la transición suave de zona lineal a sobremodulación y viceversa, minimizando los armónicos de bajo orden y logrando la tensión fundamental de referencia deseada.

Finalmente se exponen las conclusiones alcanzadas y se presentan futuros trabajos en la línea de investigación planteada en esta Tesis (Capítulo 4).

Capítulo 2

Modulación en Convertidores Multifásicos

The present work is based on the study of multiphase modulation techniques, their comparison analysis on the basis of different figure of merits, and the proposal of new methods with the ability of facing the overmodulation zone or reducing the generated common mode voltage.

The higher number of available voltage space vectors that appear in a multiphase converter, compared with a conventional three-phase one, increases the flexibility of the implemented PWM technique in the power system. This is the case in 5-phase [1, 2] and 6-phase [3, 4] power converters, where linear region has been considered and different multiphase modulation methods have been proposed. Different multiphase PWM techniques have been recently presented, and their performances have been also analyzed using different methods based on harmonic distortion flux (HDF), current ripple (current THD) and voltage ripple (voltage THD). While HDF and current THD have been extensively studied in the three-phase case [5–10], however it has not been easily extended to the multiphase case [11, 12]. During the following sections the interest of HDF as a figure of merit for the evaluation of the quality of the multiphase power converter's output and its relation with the current THD will be firstly stated.

The extension of the conventional modulation techniques to the multiphase case is mainly reduced to the linear case. This is the main reason to extend the research and consider unusual operation areas like the overmodulation zone or

to study new topics in the modulation field with particular interest in reducing the common mode voltage and the electromagnetic interferences in the system. They constitute an important research field within the work and is analyzed in the second part of this chapter.

2.1. Current Ripple Analysis in Multiphase Drives

The development of different modulation methods and power converters introduces also the necessity of new analytical techniques to compare them, taking into account different performance aspects (generated harmonic content and quality of the obtained output voltage mainly). In [6] an analytical study of this research issue is proposed for the first time. The study is then extended to PWM converters in [13], where the switching losses, the harmonic content in the input and output side of the power converter and in the dc-link are analyzed. This later study shows the interest of combining CPWM (Continuous Pulse Width Modulation) and zero-order injection techniques as well as DPWM (Discontinuous Pulse Width Modulation) methods, to reduce the current harmonic content in the power converter and to improve the utilization of the DC-link voltage. The Harmonic Distortion Determining Factor or HDF is first introduced like figure of merits in the field in 1997, based on the proposals presented in [6, 8, 13, 14]. Conventional PWM-based three-phase power converters are extensively studied in [14], where the current rms value is analyzed using the harmonic flux concept. This harmonic flux is the time integral of the harmonic voltage vector. It represents the generated error in the power converter due to its intrinsic discrete operation (the error that appears between the reference voltage vector and the obtained modulated voltage vector using the PWM method due to the discretization process). This figure of merits measures the quality of the output waveform and it is followed by the analysis of the rms current ripple and the space vectors' theory [13, 14]. Different approaches also appears in the area, where the delta connection of the three-phase load constitutes the basis of the analysis [5, 6, 8, 15]. No matter the perspective of the applied analysis, obtained improvements (the current harmonic content reduction and the improvement in the utilization of the DC-link voltage) agree if SPWM (Sine Pulse Width Modulation) methods with zero-order voltage injection techniques are used. However, the solution is easier to understand using the state vectors' approach. This section introduces all the study made in this work (see

papers 1 to 4 in chapter 3) in relation with the theoretical and analytical evaluation of the current ripple in symmetrical 5-phase and asymmetrical 6-phase induction machines.

2.1.1. Multiphase Modulation Methods

Multiphase machines are nowadays predominantly supplied from two-level voltage source inverters (VSIs). For the purpose of the VSI control, both continuous carrier-based and space vector PWM methods have been developed, for various phase numbers, which generate sinusoidal output voltages. Relationship between continuous carrier-based and space vector PWM has also been studied [16, 17]. Discontinuous PWM techniques for multiphase inverters have received some attention as well, and such PWM schemes are available for five-phase and seven phase inverters [18–22].

Different PWM strategies lead to different behaviour with regard to the performance indicators that can be used to assess the quality of output waveforms. Recently, an effort has been put into evaluation of the switching characteristics (flux HDF and current ripple) of multiphase PWM strategies. For this purpose, complex space vector approach has been adapted to be used in multiphase systems in [23], where a comprehensive study and comparison of various continuous PWM techniques for five-phase systems have been reported. This was followed by the extension of the commonly used approach in three-phase systems, based on delta connection, to multiphase systems in [24], based on multiple polygon connections. A further study related to two specific continuous SVPWM techniques for five-phase VSIs has been reported in [25, 26]. Detailed investigation of both flux HDF and current ripple has been conducted, using again the complex space vector approach.

Discontinuous multiphase PWM techniques have been studied to a lesser extent than the corresponding continuous PWM methods. This is especially true with regard to the flux HDF and current ripple, where the only available considerations are those of [20, 27]. However, the approach used in [20] is different from the one that will be proposed in this work, which utilises the polygon approach developed in [24] for continuous PWM techniques.

The five-phase VSI is characterized with 32 space vectors (30 active plus two zero states), which have projections in two orthogonal planes according to the Clarke decomposition theory and assuming that the machine has star connected winding with isolated neutral point. Figure 2.1 illustrates space vector projections

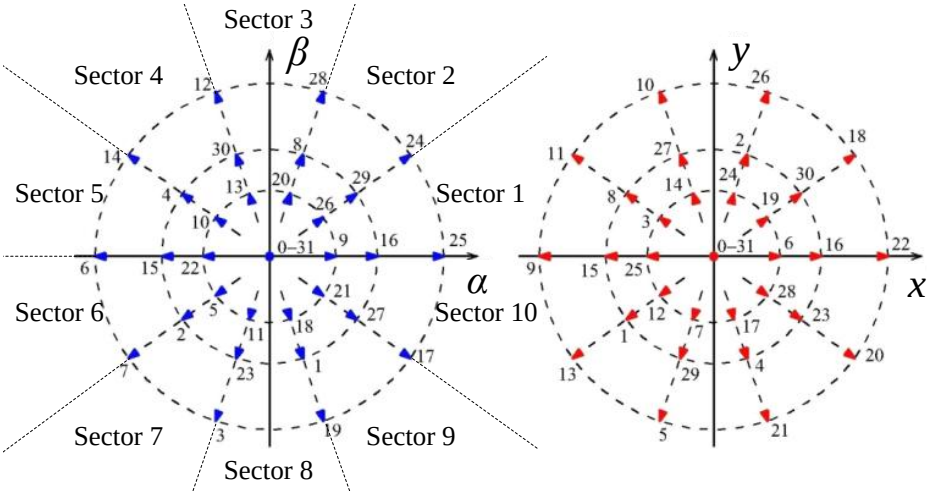

FIGURE 2.1. Voltage vectors in the $\alpha-\beta$ and $x-y$ planes for a five-phase VSI.

TABLE 2.1. Duty cycles using (2L+2M) and (4L) SVPWM methods.

(2L+2M) SVPWM	**(4L) SVPWM**
$\delta_{am} = MK_1 \sin\left(s\frac{\pi}{5} - \vartheta\right)$	$\delta_{cl} = MK_1 \sin\left(s\frac{\pi}{5} - \vartheta\right)$
$\delta_{al} = MK_2 \sin\left(s\frac{\pi}{5} - \vartheta\right)$	$\delta_{al} = MK_1 \left[\sin\left(\vartheta - (s-1)\frac{\pi}{5}\right) + (2J_1 - 1)\sin\left(s\frac{\pi}{5} - \vartheta\right)\right]$
$\delta_{bm} = MK_1 \sin\left(\vartheta - (s-1)\frac{\pi}{5}\right)$	$\delta_{bl} = MK_1 \left[\sin\left(s\frac{\pi}{5} - \vartheta\right) + (2J_1 - 1)\sin\left(\vartheta - (s-1)\frac{\pi}{5}\right)\right]$
$\delta_{bl} = MK_2 \sin\left(\vartheta - (s-1)\frac{\pi}{5}\right)$	$\delta_{dl} = MK_1 \sin\left(\vartheta - (s-1)\frac{\pi}{5}\right)$
$\delta_z = 1 - MK_2 \cos\left((2s-1)\frac{\pi}{10} - \vartheta\right)$	$\delta_z = 1 - MK_2 \cos\left((2s-1)\frac{\pi}{10} - \vartheta\right)$

in these planes. To achieve the desired reference in the first $(\alpha-\beta)$ plane while simultaneously zeroing the voltage (on average) in the second $(x-y)$ plane, it is necessary to select four active vectors. In the two available SVPWM methods [25], the active vectors are selected either as two medium and two large vectors that border the reference in the first plane, termed further on as (2L+2M) method, or as four large vectors neighbouring the reference, denoted further on as (4L) method. These two vector selections are illustrated in Figs. 2.2 and 2.3. Table 2.1 summarizes the duty cycles (relative on-times over the switching period δ) of selected active vectors, where the modulation index is defined as $M = V_1/(V_{dc}/2)$, s is an integer from 1 to 10 representing the sector where the reference is placed in the $(\alpha-\beta)$ plane, V_1 is the peak of the fundamental voltage, and the defined constants are $K_1 = \sin\pi/5$, $K_2 = \sin 2\pi/5$, $J_1 = \cos\pi/5$ and $J_2 = cos2\pi/5$.

Regardless of the vector selection scheme, both (2L+2M) and (4L) SVPWM techniques achieve the same utilisation of the dc bus voltage [25]. Also, the duty

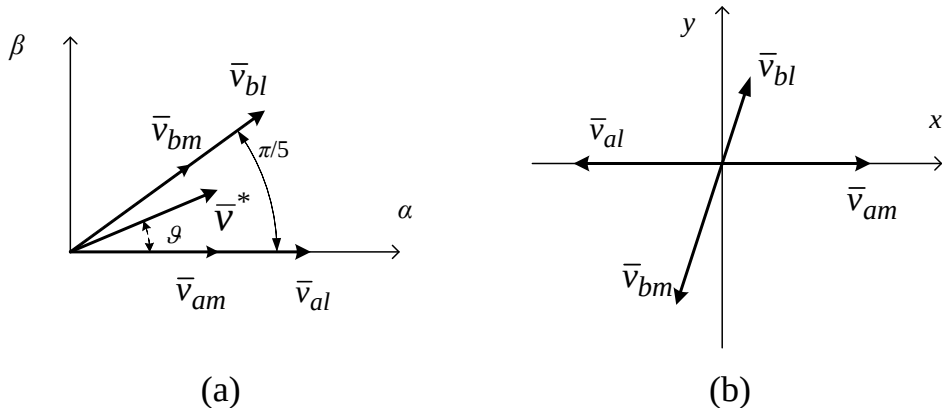

FIGURE 2.2. Selected vectors when reference is in sector 1 for (2L+2M) SVPWM: a) $\alpha-\beta$ plane b) $x-y$ plane.

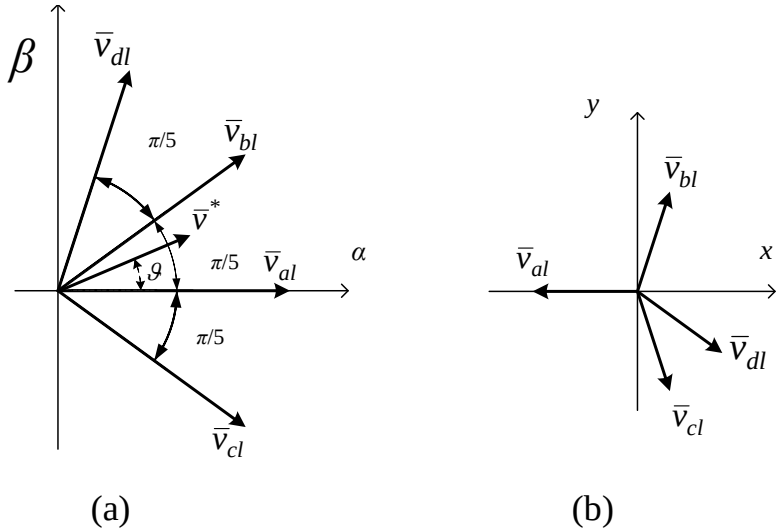

FIGURE 2.3. Selected vectors when reference is in sector 1 for (4L) SVPWM: a) $\alpha-\beta$ plane b) $x-y$ plane.

cycles of the zero vectors (δ_z) are the same and equally shared between two zero states. The most important consequence of using either (2L+2M) or (4L) vector selection schemes is the different switching pattern, which means that the number of commutations within a period is not the same: the average switching frequency of the (4L) SVPWM method is 1.4 times higher than with the (2L+2M) SVPWM method [25].

The (2L+2M) and (4L) continuous SVPWM techniques can be extended to

TABLE 2.2. Duty cycles of zero vectors applied in SVPWM techniques.

	Sector 1	Sector 2	Sector 3	Sector 4	Sector 5	Sector 6	Sector 7	Sector 8	Sector 9	Sector 10
SVPWM	$\delta_0 = \delta_{31} = \delta_z/2$									
DPWMMAX	$\delta_0 = 0$									
DPWMMIN	$\delta_{31} = 0$									
DPWM0	$\delta_{31} = 0$	$\delta_0 = 0$	$\delta_{31} = 0$	$\delta_0 = 0$	$\delta_{31} = 0$	$\delta_0 = 0$	$\delta_{31} = 0$	$\delta_0 = 0$	$\delta_{31} = 0$	$\delta_0 = 0$
DPWM1		$\delta_{31} = 0$	$\delta_0 = 0$	$\delta_{31} = 0$	$\delta_0 = 0$	$\delta_{31} = 0$	$\delta_0 = 0$	$\delta_{31} = 0$	$\delta_0 = 0$	$\delta_{31} = 0$
DPWM2	$\delta_0 = 0$	$\delta_{31} = 0$	$\delta_0 = 0$	$\delta_{31} = 0$	$\delta_0 = 0$	$\delta_{31} = 0$	$\delta_0 = 0$	$\delta_{31} = 0$	$\delta_0 = 0$	$\delta_{31} = 0$
DPWM3		$\delta_0 = 0$	$\delta_{31} = 0$	$\delta_0 = 0$	$\delta_{31} = 0$	$\delta_0 = 0$	$\delta_{31} = 0$	$\delta_0 = 0$	$\delta_{31} = 0$	$\delta_0 = 0$

discontinuous methods using only one zero voltage vector within a switching period. Although infinite number of discontinuous patterns can be developed, the six relevant cases are called DPWMMAX, DPWMMIN, DPWM0, DPWM1, DPWM2 and DPWM3. The main consequence of using a discontinuous method is that the switching state of one VSI leg is kept constant during the switching period.

Table 2.2 shows different methods of zero state partitioning which yield continuous and all the discontinuous modulation techniques discussed in this work. These partitions are valid for both (2L+2M) and (4L) schemes. Note that DPWM0, DPWM1, DPWM2 and DPWM3 can be derived from DPWMMAX and DPWMMIN depending on the sector (or half-sector). For example, DPWM0 is like DPWMMIN in sector 1, but like DPWMMAX in sector 2; DPWM1 is the same as DPWMMAX in the first half-sector 1 and the second half-sector 2, while it is like DPWMMIN in between these two half-sectors.

2.1.2. HDF considering Space Vector Approach

The evaluation of HDF using different modulation schemes and the Space Vector Approach is detailed in chapter 3 of this Thesis, as well as the relationship with the current harmonic content in the multiphase induction drive (papers 1 to 3). The basic considerations in relation with this study will be presented in what follows.

2.1.2.1. Trajectories of harmonic flux

At any arbitrary time instant there is an error between the applied voltage vector and the reference vector, because of the discrete nature of the inverter. This deviation of the output voltage will cause current ripple when it is applied to the load. The model for the analysis can be simplified into:

$$\Delta\bar{i} = \frac{\bar{v} - \bar{v}^*}{L_\sigma}\Delta t \tag{2.1}$$

where $\bar{v}$ represents the space vectors activated over the time interval Δt within a switching period, $\bar{v}^*$ is the reference voltage vector, and L_σ is the equivalent inductance for the switching harmonics. Since this equivalent inductance is not so simple to define in multi-phase systems [23, 24] as it is the case in three-phase systems, the notion of harmonic flux $\Delta\bar{\lambda}$ [9] is used, where:

$$\Delta\bar{\lambda} = L_\sigma \Delta\bar{i} = (\bar{v} - \bar{v}^*)\Delta t \tag{2.2}$$

This definition allows the analysis of the harmonic flux to be performed independently in each plane. Based on equation (2.2), and assuming zero initial value for the deviation of the harmonic flux, it is possible to generate harmonic flux trajectories (trajectories of error voltage vectors) in both planes over the switching period, for all SVPWM schemes (continuous and discontinuous). Due to the existence of a symmetrical switching pattern, it is enough to consider only one half of the switching period, obtaining deviations of the harmonic flux ($\Delta\lambda$) at the end of every sub-interval over the first half of the switching period. The normalisation factor for the harmonic flux is selected the same as in [23], [25]:

$$\Delta\lambda_N = L\Delta i_N = \frac{V_{dc}T_s}{8} \tag{2.3}$$

Expression 2.2 can now be applied to each plane, respecting the ordering of applied vectors. Since the order is different for (2L+2M) and (4L) methods[1], and different sequence orders are used in odd and even sectors, the applied active vectors are denoted as I to IV in order to be able to consider the general case. The harmonic flux trajectory value at the end of every sub-interval is given with [25]:

$$\begin{aligned}
&\Delta\bar{\lambda}(0) = 0\\
&\Delta\bar{\lambda}(t_1) = -\delta_0\bar{v}^*T_s/2\\
&\Delta\bar{\lambda}(t_2) = \Delta\bar{\lambda}(t_1) + \delta_I(\bar{v}_I - \bar{v}^*)T_s/2\\
&\Delta\bar{\lambda}(t_3) = \Delta\bar{\lambda}(t_2) + \delta_{II}(\bar{v}_{II} - \bar{v}^*)T_s/2\\
&\Delta\bar{\lambda}(t_4) = \Delta\bar{\lambda}(t_3) + \delta_{III}(\bar{v}_{III} - \bar{v}^*)T_s/2\\
&\Delta\bar{\lambda}(t_5) = \Delta\bar{\lambda}(t_4) + \delta_{IV}(\bar{v}_{IV} - \bar{v}^*)T_s/2\\
&\Delta\bar{\lambda}(t_6) = \Delta\bar{\lambda}(t_5) - \delta_{31}\bar{v}^*T_s/2
\end{aligned} \tag{2.4}$$

[1] This nomenclature refers the use of 2 large and 2 medium voltage vectors (2L+2M) within a switching period or 4 large voltage vectors (4L).

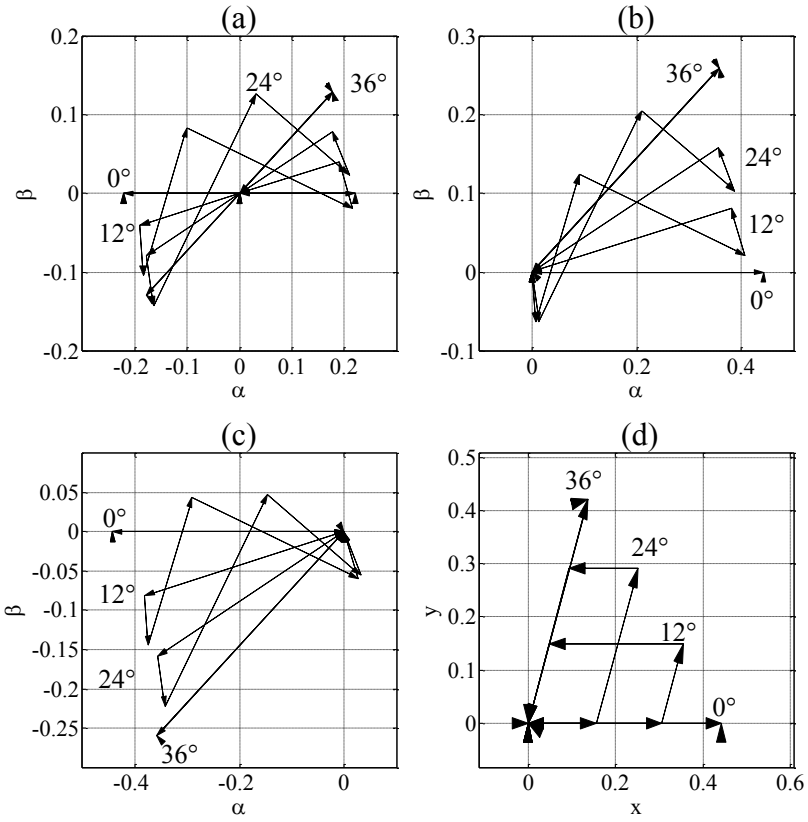

FIGURE 2.4. Harmonic flux trajectories over a sub-cycle (Ts/2) for M = 0.8. Considered methods: a) continuous (2L+2M) SVPWM, $\alpha-\beta$ plane, b) (2L+2M) DPWMMAX, $\alpha-\beta$ plane, c) (2L+2M) DPWMMIN, $\alpha-\beta$ plane, d) plane $x-y$ for all considered methods with (2L+2M).

Figures 2.4 and 2.5 show the harmonic flux trajectories over a sub-cycle for applied vectors with $M = 0.8$ and $\vartheta = 0°$, 12°, 24° and 36°. Only trajectories of continuous SVPWM, DPWMMAX ($\delta_0 = 0$) and DPWMMIN ($\delta_{31} = 0$), for both (2L+2M) and (4L) selections are plotted, in order to emphasize some important facts:

- As stated in [23], harmonic flux trajectories in the $x-y$ plane are not function of the zero space vector duty cycle (Fig. 2.4d and Fig. 2.5d). Because differences between continuous and discontinuous methods rely on the zero state partitioning, both continuous and discontinuous methods have the

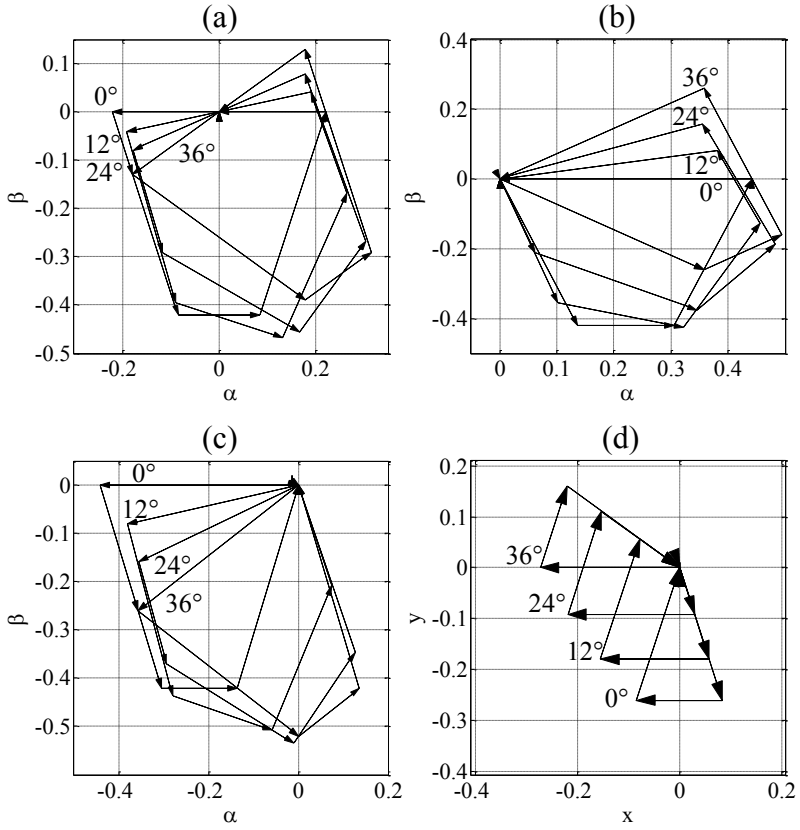

FIGURE 2.5. Harmonic flux trajectories over a sub-cycle (Ts/2) for M = 0.8. Considered methods: a) continuous (4L) SVPWM, $\alpha-\beta$ plane, b) (4L) DPWMMAX, $\alpha-\beta$ plane, c) (4L) DPWMMIN, $\alpha-\beta$ plane, d) plane $x-y$ for all considered methods with (4L).

same harmonic flux trajectory, which is however different for (2L+2M) and (4L) SVPWM techniques.

- Harmonic flux trajectories with (4L) discontinuous methods are larger in the $\alpha-\beta$ plane, compared to the trajectories of the (2L+2M) SVPWM.
- Harmonic flux trajectories with (4L) discontinuous and (4L) continuous methods are quite similar in the $\alpha-\beta$ plane.
- Harmonic flux trajectories with (2L+2M) SVPWM show smaller excursions from the origin in the $\alpha-\beta$ plane, compared with the trajectories of the (4L) SVPWM scheme.

- Harmonic flux trajectories with (4L) SVPWM depict smaller excursions from the origin in the $x-y$ plane, compared with the trajectories of the (2L+2M) SVPWM technique.
- Continuous SVPWM methods have equal zero state partition while discontinuous do not. This means that $\Delta\bar{\lambda}(t_1)$ and $\Delta\bar{\lambda}(t_5)$ in the $\alpha-\beta$ plane will be symmetrical to the origin for continuous methods, but this will not be the case for discontinuous techniques.

The second step involves an analysis of harmonic flux over the switching period, so the average squared value of the harmonic flux is taken as a figure of merit. Since the first and the second halves of the trajectory have the same rms value due to symmetry, the operation can be reduced only for $T_s/2$. So, the following integral has to be solved:

$$\Delta\lambda^2{}_{abcde-RMS} = \frac{2}{T_s}\int_0^{\frac{T_s}{2}} \Delta\lambda^2{}_{abcde}\, dt \tag{2.5}$$

The left-hand side of equation (2.5) represents all five phases, so that the total five-phase system solution is obtained. The quantity $\Delta\lambda^2{}_{abcde-RMS}$ can be related to the harmonic flux deviations in each of the two 2-D planes [23], so that equation (2.5) takes the form:

$$\begin{aligned}\Delta\lambda^2{}_{abcde-RMS} &= \Delta\lambda^2{}_{abcde\ -\ RMS\alpha\beta} + \Delta\lambda^2{}_{abcde-RMSxy} = \\ &= \frac{5}{2}\frac{2}{T_s}\left[\int_0^{\frac{T_s}{2}} [\Delta\lambda_\alpha{}^2 + \Delta\lambda_\beta{}^2]dt + \int_0^{\frac{T_s}{2}} [\Delta\lambda_x{}^2 + \Delta\lambda_y{}^2]dt\right]\end{aligned} \tag{2.6}$$

Expression 2.6 can be separated into several integrals in accordance with the existing sub-intervals and, manipulating according to the procedure detailed in [23], it is possible to obtain a general solution in each of two 2-D planes, which can be numerically evaluated. The squared harmonic flux rms characteristics of (2L+2M) and (4L) modulation techniques, analyzed in this section, are plotted in Figs. 2.6 to 2.9.

It can be seen that each modulation method has a unique and different characteristic in the $\alpha-\beta$ plane, while the characteristic in the $x-y$ plane is the same

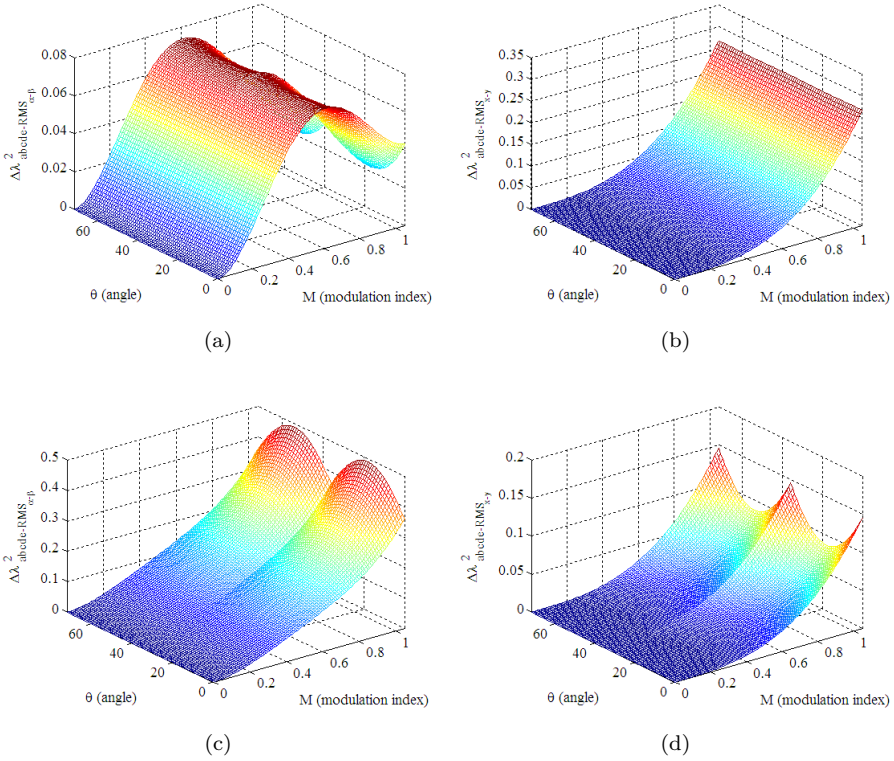

FIGURE 2.6. Squared harmonic flux of continuous SVPWM: a) (2L+2M) SVPWM, $\alpha-\beta$ plane, b) (2L+2M) SVPWM, $x-y$ plane, c) (4L) SVPWM, $\alpha-\beta$ plane, d) (4L) SVPWM, $x-y$ plane.

for all (2L+2M) and (4L) methods, respectively. Again, some conclusions can be made on the basis of Figs. 2.6 to 2.9 and related to continuous (2L+2M) and (4L) SVPWM [25]:

- $\alpha-\beta$ plane: (2L+2M) offers significantly lower values of the squared harmonic flux than (4L). Peak values appear around $M=0.6$, which are followed by lower values when the modulation index increases towards its maximum. Conversely, the characteristic obtained for (4L) increases with the modulation index.

- $x-y$ plane: squared harmonic flux rms using SVPWM (4L) shows lower values than using SVPWM (2L+2M). This is so because the selected voltage vectors for SVPWM (4L) in the $x-y$ plane are within available voltage

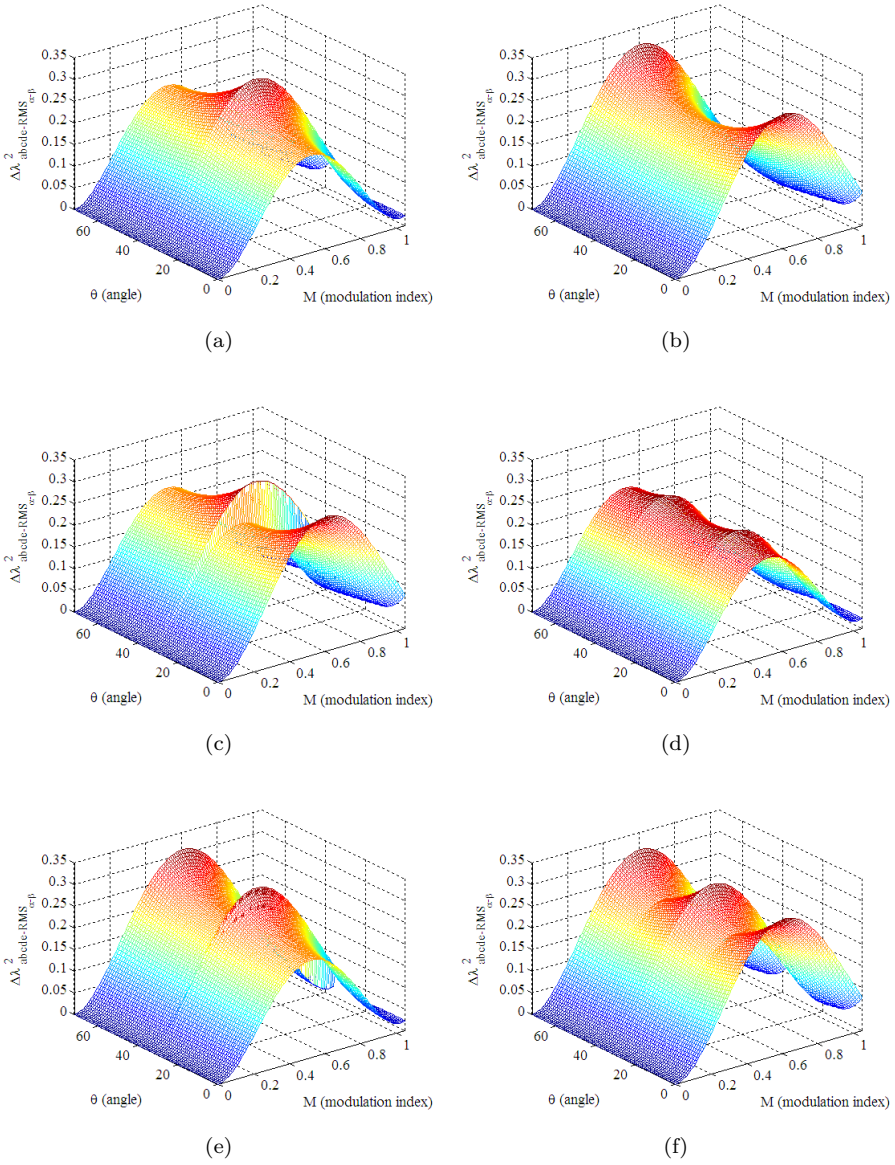

FIGURE 2.7. Squared harmonic flux in $\alpha-\beta$ plane for discontinuous (2L+2M) SVPWM: a) DPWMMAX, b) DPWMMIN, c) DPWM0, d) DPWM1, e) DPWM2, f) DPWM3.

vectors with the minimum modulus.

As noted, plots in the $x-y$ plane are the same for continuous and discontinuous schemes and only depend on the vector selection. Therefore, there is a unique

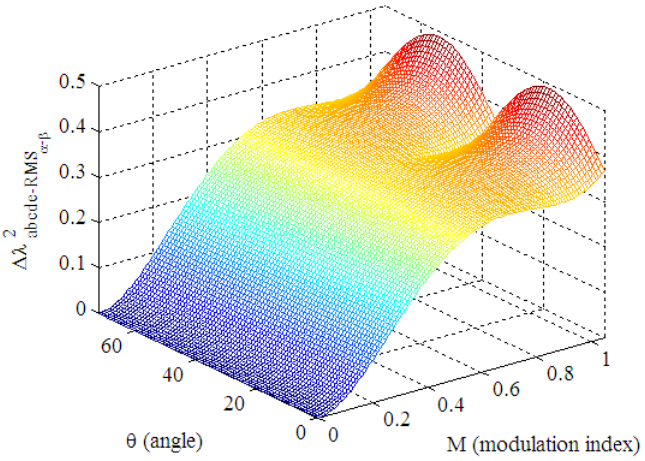

FIGURE 2.8. Squared harmonic flux in the $\alpha-\beta$ plane for discontinuous PWM techniques using (4L) vector selection.

characteristic for all (2L+2M) schemes and a different one for all (4L) methods. This is so since harmonic flux trajectories in this plane are not function of the zero state partitioning, so that the squared harmonic flux rms is also independent of this.

When discontinuous schemes are examined for (2L+2M) selection (Fig. 2.7), the following applies to the $\alpha-\beta$ plane:

- As in the case of the continuous method, the peak values appear around $M = 0.6$, and then the obtained values decreases when the modulation index increases. The squared harmonic flux rms values for the maximum modulation index are quite similar in magnitude.
- If DPWMMAX and DPWMMIN are plotted for all sectors (Figs. 2.7a and 2.7b plot only the first two sectors), the shape of the curves would be the same, but shifted 36°.
- DPWM0, DPWM1, DPWM2 and DPWM3 characteristics can be derived from DPWMMAX and DPWMMIN depending on the sector (or half-sector). For example, DPWM0 is like DPWMMIN in sector 1, but like DPWMMAX in sector 2 (see Figs. 2.10 and 2.7c), while DPWM1 is the same as DPWMMAX in the first half-sector 1 and the second half-sector 2, but similar to DPWMMIN in between these two half-sectors.

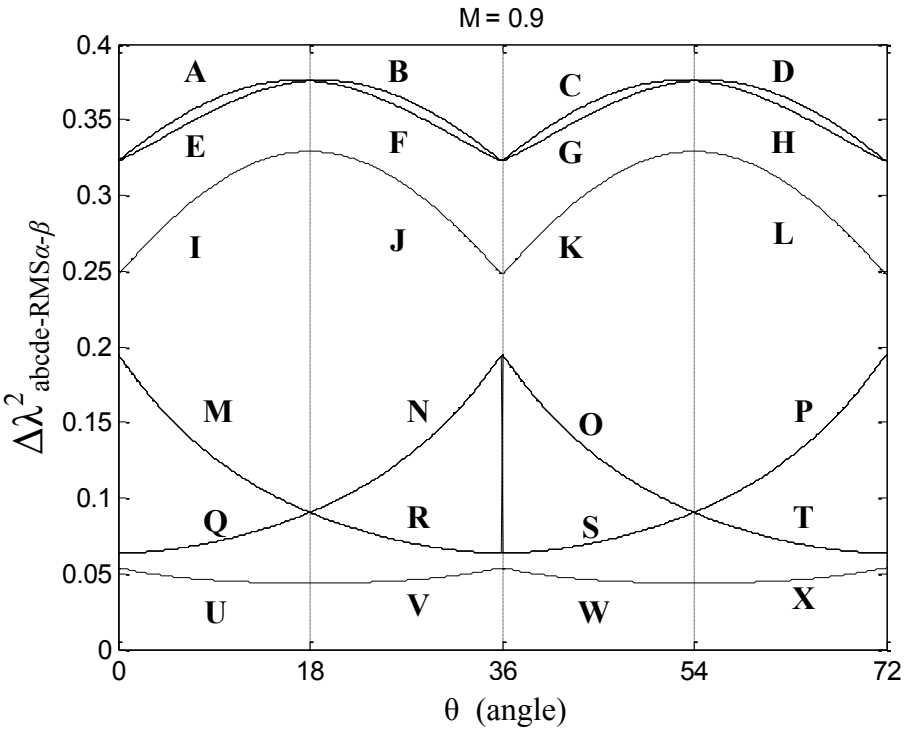

(2L+2M) SVPWM	→ U-V-W-X	(4L) SVPWM	→ I-J-K-L
(2L+2M) DPWMMAX	→ Q-N-O-T	(4L) DPWMMAX	→ A-F-G-D
(2L+2M) DPWMMIN	→ M-R-S-P	(4L) DPWMMIN	→ E-B-C-H
(2L+2M) DPWM0	→ M-R-O-T	(4L) DPWM0	→ E-B-G-D
(2L+2M) DPWM1	→ Q-R-S-T	(4L) DPWM1	→ A-B-C-D
(2L+2M) DPWM2	→ Q-N-S-P	(4L) DPWM2	→ A-F-C-H
(2L+2M) DPWM3	→ M-N-O-P	(4L) DPWM3	→ E-F-G-H

FIGURE 2.9. Squared harmonic flux in the $\alpha-\beta$ plane for all analyzed techniques when M = 0.9.

- On the basis of the analysis of Fig. 2.7, DPWMMAX, DPWMMIN, DPWM0 and DPWM2 are expected to have the same current harmonic content, while DPWM1 and DPWM3 should have better and worse current harmonic content, respectively.

With regard to discontinuous schemes based on (4L) vector selection, only one plot is shown in Fig. 2.8. This is so because all have an almost identical shape, so that no differences can be observed in this type of plot. Figure 2.9 shows a slice of Figs. 2.6-2.8 for $M = 0.9$, revealing the angular position dependencies of the

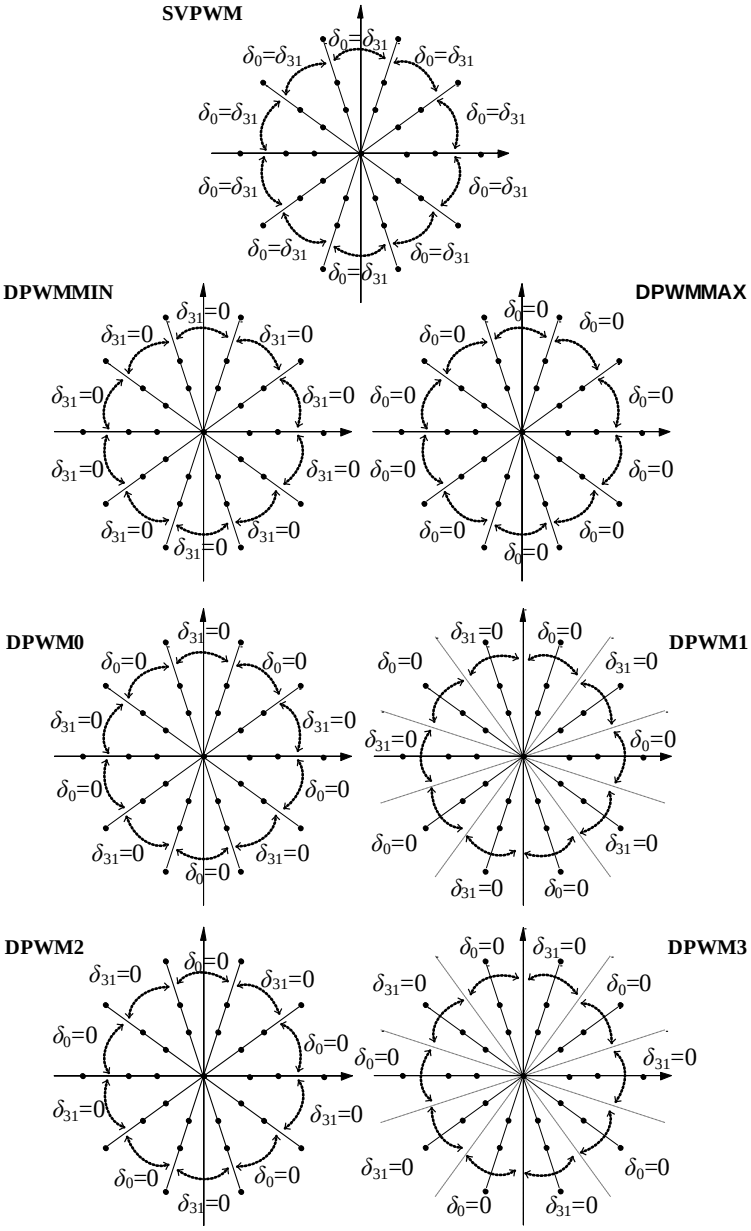

FIGURE 2.10. Zero state partitioning for the analyzed space vector PWM techniques. The following applies: for SVPWM $\delta_{31} = \delta_0 = 0.5\delta_z$; for DPWMAX $\delta_0 = 0$; and for DPWMIN $\delta_{31} = 0$, regardless of the sector.

squared harmonic flux in the $\alpha-\beta$ plane for every technique. Squared harmonic flux in the $\alpha-\beta$ plane for all (2L+2M) analyzed techniques is qualitatively the same for different modulation indices, and similar behavior is obtained when only (4L) methods are considered. However, the ratios of squared harmonic flux values for (2L+2M) and (4L) modulation schemes are not necessarily as in Fig. 2.9 for all modulation index values. Other modulation indices can offer different qualitative behavior, and the curves obtained using (4L) and (2L+2M) methods can have crossovers anywhere.

Because the zero state partition is the same for (2L+2M) and (4L) vector selections, DPWM0, DPWM1, DPWM2 and DPWM3 characteristics can be derived from DPWMMAX and DPWMMIN depending on the sector (or half-sector). Analyzing the same figure, the correspondence between various curves and zones is as follows (underlined letters identify DPWMMAX curves, while bold font represents DPWMMIN curves):

(4L) DPWMMAX → A-F-G-D
(4L) DPWMMIN → **E-B-C-H**
(4L) DPWM0 → **E-B**-G-D
(4L) DPWM1 → A-**B-C**-D

Hence, again, DPWM0, DPWM1, DPWM2 and DPWM3 characteristics can be derived from DPWMMAX and DPWMMIN. It can be expected that DPWMMAX, DPWMMIN, DPWM0 and DPWM2 will have the same current harmonic content but, in contrast to (2L+2M) schemes, the DPWM3 will now have smaller and DPWM1 higher current harmonic.

2.1.2.2. Harmonic Distortion Factor

Finally, in order to obtain flux HDFs in every plane, squared harmonic flux has to be integrated over the fundamental period. Similarly to the procedure applied in previous sections, the integration should be performed over the first two sectors:

$$\Delta\lambda^2{}_{abcde-RMSF} = \frac{5}{2\pi}\int_0^{\frac{2\pi}{5}} \Delta\lambda^2{}_{abcde-RMS}\, d\vartheta \tag{2.7}$$

Polynomial closed-form solution of equation (2.7) is not always easy to express in short and compact manner, as it was demonstrated in [23, 24]. Therefore, HDFs

TABLE 2.3. Average Switching Frequency (ASF) normalized with respect to switching frequency of countinuous (2L+2M) SVPWM.

PWM method	**ASF**	**PWM method**	**ASF**
(2L+2M) SVPWM	1	(4L) SVPWM	1.4
(2L+2M) DPWMMAX	0.8	(4L) DPWMMAX	1
(2L+2M) DPWMMIN	0.8	(4L) DPWMMIN	1
(2L+2M) DPWM0	0.8	(4L) DPWM0	1
(2L+2M) DPWM1	0.8	(4L) DPWM1	1
(2L+2M) DPWM2	0.8	(4L) DPWM2	1
(2L+2M) DPWM3	0.8	(4L) DPWM3	1

of analyzed modulation schemes are obtained by numerical integration of equation (2.7) in Matlab, and the obtained results are shown in Fig. 2.11 for (2L+2M) and (4L) modulation methods, using the same base switching frequency. Notice that the base switching frequency of 1 per unit corresponds to the switching frequency of the continuous SVPWM (2L+2M) method. The relationship between the average switching frequency and the base switching frequency for studied methods is then listed in Table 2.3 and the correlation between HDF considering the average switching frequency and the base switching frequency is:

$$\mathrm{HDF}_{\mathrm{av}} = (\mathrm{ASF})^2 \cdot \mathrm{HDF}_{\mathrm{base}} \tag{2.8}$$

Since the discontinuous (2L+2M) methods have two less switchings per carrier cycle than continuous SVPWM (2L+2M) method, the side-band harmonics of the discontinuous methods are wider and larger in magnitude. The same should be the case for continuous (4L) SVPWM and all discontinuous methods with (4L) vector selection, because the number of switchings is not the same for all legs. The following applies to HDF behavior:

- In the $\alpha-\beta$ plane, (2L+2M) SVPWM has a significantly lower flux HDF (due to the increment in the modulation index) compared to the (4L) SVPWM [3]. Continuous SVPWM in each of the two vector selection cases has lower HDF than the corresponding discontinuous methods, if the same base switching frequency is considered. In the high modulation index range, the discontinuous methods are superior to continuous SVPWM in the case of (2L+2M) vector selection for the same ASF, because of the factor $(0.8)^2$

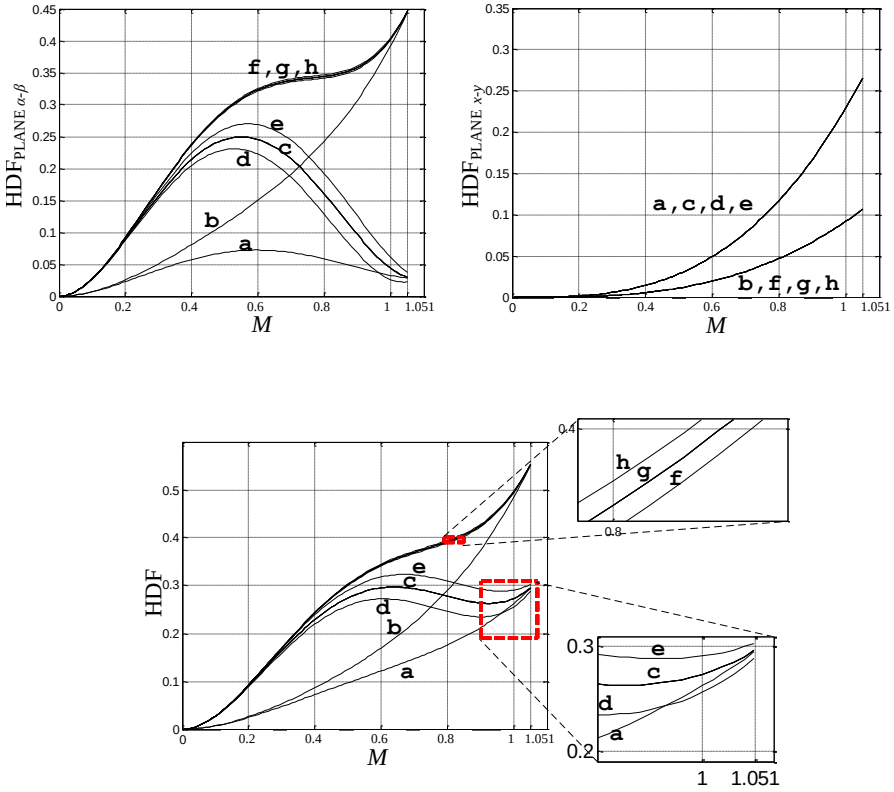

PWM TECHNIQUES

a →	(2L+2M) SVPWM	**d** →	(2L+2M) DPWM1
b →	(4L) SVPWM	**e** →	(2L+2M) DPWM3
c →	(2L+2M) DPWMMAX, (2L+2M) DPWMIN, (2L+2M) DPWM0, (2L+2M) DPWM2	**f** →	(4L) DPWM3
		h →	(4L) DPWM1
		g →	(4L) DPWMMAX, (4L) DPWMIN, (4L) DPWM0, (4L) DPWM2

FIGURE 2.11. HDF curves for the range of the achievable modulation indices, for the same base switching frequency.

in equation (2.8).

- In the $x-y$ plane, all modulation schemes with (2L+2M) and (4L) methods, respectively, have the same behavior. In this plane, (4L) selections have lower HDFs. However, the differences are much smaller between the two vector

selection schemes. It should be noted that the impact of the $x-y$ plane on the current ripple is more pronounced as the modulation index increases.

- For (2L+2M) selections, DPWM1 is better than other discontinuous techniques, and for (4L) selections, DPWM3 is better. However, in both cases the improvement is marginal and the modulator selection criteria should be based on other characteristics, such as the switching losses.
- DPWMMIN, DPWMMAX, DPWM0 and DPWM2 have the same HDF for the corresponding cases of (2L+2M) or (4L) vector selection. This agrees with the statements obtained when harmonic flux was analyzed.

2.1.3. HDF considering Polygonal Approach

The approach in the flux HDF evaluation follows the one developed in [24], where the analysis was however only applied to continuous modulation techniques. A previous work also compares the obtained flux HDF using continuous and discontinuous modulation techniques, but the proposed analysis was based on a completely different analytical approach, the complex space vector technique [27].

The polygonal approach is based on the two possible polygon connections of the five-phase system (Fig. 2.12) and utilization of the H-bridge inverter and an equivalent load (Fig. 2.13), as detailed in [24]. The phase load is represented with a resistance (R), an inductance (L) and an internal electromotive force or emf (e) connected in series. It is assumed for the analysis that switching frequency is much higher than the fundamental frequency, so that the resistance can be neglected during a switching period and the current variation can be assumed linear. The load emf can be also considered constant and equal to the reference line voltage during the switching period.

The first step in the analysis is the establishment of the switching patterns that characterise the modulation techniques. Different switching patterns are shown in Fig. 2.14 for the (2L+2M) case and in Fig. 2.15 for the (4L) case. Figures 2.14 and 2.15 represent the switching pattern of each leg (m_A, m_B, m_C, m_D and m_E), and the adjacent and the non-adjacent line voltages (m_{AB} and m_{AC}, respectively), during the first half of a switching period ($T_s/2$). The continuous PWM case is shown. Ten commutations appear in each switching period and sector in the (2L+2M) SVPWM, two per leg. Figure 2.15 shows the switching pattern in sectors 1 and 2 for the (4L) SVPWM. It requires fourteen commutations in a switching period:

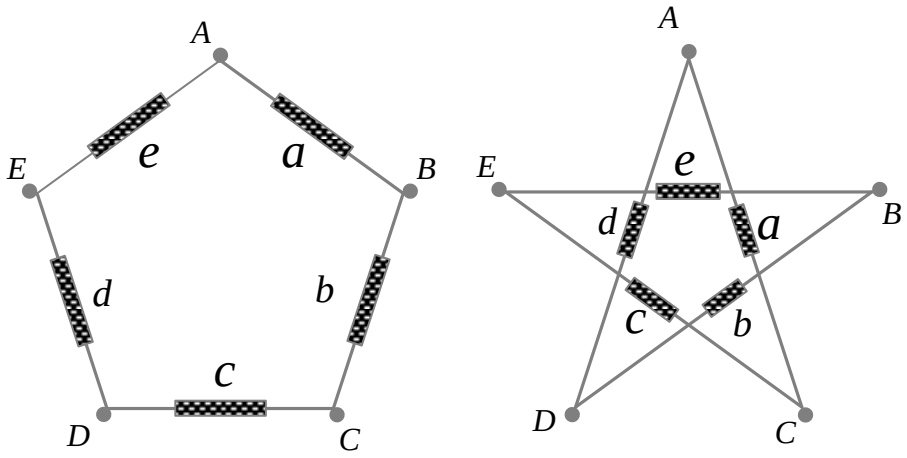

FIGURE 2.12. Five-phase machine windings showing adjacent polygon connection (left), and non-adjacent polygon connection (right).

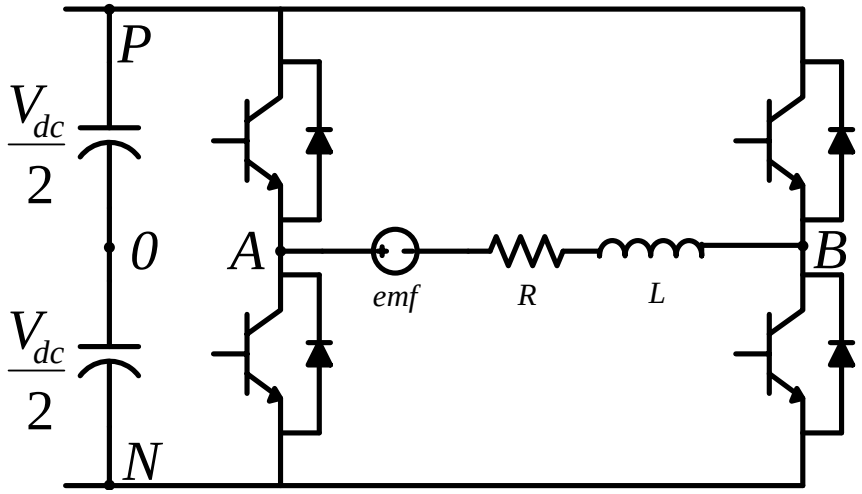

FIGURE 2.13. H-bridge inverter and the equivalent phase load representation for the analysis.

four legs are similar as in the (2L+2M) case, but one leg has six commutations. As can be seen from Fig. 2.15, the leg with an increased number of commutations changes from sector to sector.

Discontinuous (2L+2M) schemes can be derived from Fig. 2.14, using the δ_0 and δ_{31} values given in Table 2.2. When considering a discontinuous SVPWM method, the number of commutations per switching period decreases. For instance, leg A remains clamped for the (2L+2M) DPWMMAX method in sector 1 ($\delta_0 = 0$

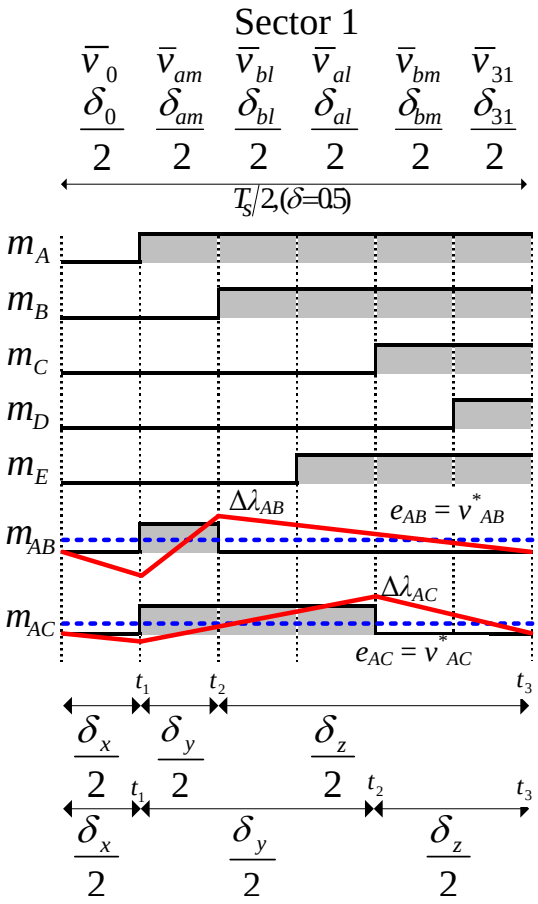

FIGURE 2.14. Switching patterns over the first half of the switching period for (2L+2M) SVPWM in sector 1.

in sector 1, according to Table 2.2), while the same happens with leg D for the (2L+2M) DPWMMIN technique in sector 1 (in this case $\delta_{31} = 0$, 2.2). Total number of commutations for (2L+2M) SVPWM methods in a switching period reduces to eight. The discontinuous (4L) SVPWM switching patterns can be also deduced considering the δ_0 and δ_{31} values given in Table 2.2 and using Fig. 2.15. For discontinuous (4L) SVPWM techniques the total number of commutations is reduced to ten.

The polygon analysis is carried out using the duty cycles shown in Table 2.1. The reasons behind this approach are that equivalent carrier-based PWM techniques for all the continuous and discontinuous (4L) SVPWM methods are not available,

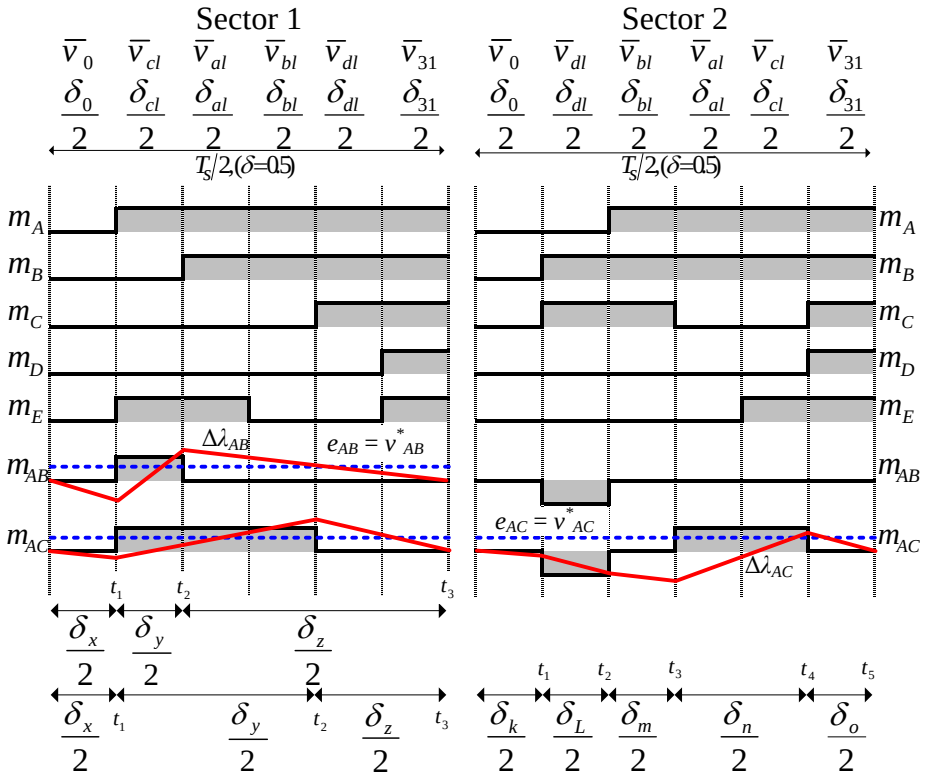

FIGURE 2.15. Switching patterns over the first half of the switching period for (4L) SVPWM in sectors 1 and 2.

and that for (4L) SVPWM there is an excessive number of integration intervals (see Table 2.2). The reference line voltages using either (2L+2M) or (4L) techniques are the same. These values are expressed as follows:

$$\begin{aligned} v^*_{AB} &= M\left(\cos(\vartheta) - \cos(\vartheta - 2\pi/5)\right) = 2K_1 M \sin(\pi/5 - \vartheta) \\ v^*_{AC} &= M\left(\cos(\vartheta) - \cos(\vartheta - 4\pi/5)\right) = 2K_2 M \sin(2\pi/5 - \vartheta) \end{aligned} \tag{2.9}$$

An error exists between the applied and the reference voltage vectors at any instant of time due to the discrete nature of the inverter. This error produces current ripple in the load, and generates the harmonic flux ($\Delta\lambda$), which can be given as:

$$\Delta\lambda = L_\sigma \Delta i = (v - v^*)\Delta t \tag{2.10}$$

where v is the instantaneous line voltage of each polygon connection, v^* is the

TABLE 2.4. Characterisation of the considered subintervals in the analytical analysis. Each sector and polygon is detailed in a switching period.

	(2L+2M)		(4L)	
Sector (range)	POLYGON 1	POLYGON 2	POLYGON 1	POLYGON 2
1 $(0,\pi/5)$	$\delta_x = \delta_0$ $\delta_y = \delta_{am}$ $\delta_z = \delta_{bl} + \delta_{al} + \delta_{bm} + \delta_{31}$	$\delta_x = \delta_0$ $\delta_y = \delta_{am} + \delta_{bl} + \delta_{al}$ $\delta_z = \delta_{bm} + \delta_{31}$	$\delta_x = \delta_0$ $\delta_y = \delta_{cl}$ $\delta_z = \delta_{al} + \delta_{bl} + \delta_{dl} + \delta_{31}$	$\delta_x = \delta_0$ $\delta_y = \delta_{cl} + \delta_{al} + \delta_{bl}$ $\delta_z = \delta_{dl} + \delta_{31}$
2 $(\pi/5,2\pi/5)$	$\delta_x = \delta_0$ $\delta_y = \delta_{bm}$ $\delta_z = \delta_{al} + \delta_{bl} + \delta_{am} + \delta_{31}$	$\delta_x = \delta_0 + \delta_{bm}$ $\delta_y = \delta_{al}$ $\delta_z = \delta_{bl} + \delta_{am} + \delta_{31}$	$\delta_x = \delta_0$ $\delta_y = \delta_{dl}$ $\delta_z = \delta_{bl} + \delta_{al} + \delta_{cl} + \delta_{31}$	$\delta_k = \delta_0$ $\delta_l = \delta_{dl}$ $\delta_m = \delta_{bl}$ $\delta_n = \delta_{al} + \delta_{cl}$ $\delta_p = \delta_{31}$
3 $(2\pi/5,3\pi/5)$	$\delta_x = \delta_0$ $\delta_y = \delta_{am} + \delta_{bl}$ $\delta_z = \delta_{al} + \delta_{bm} + \delta_{31}$	$\delta_x = \delta_0 + \delta_{am}$ $\delta_y = \delta_{bl}$ $\delta_z = \delta_{al} + \delta_{bm} + \delta_{31}$	$\delta_x = \delta_0 + \delta_{cl} + \delta_{al}$ $\delta_y = \delta_{bl} + \delta_{dl}$ $\delta_z = \delta_{31}$	$\delta_k = \delta_0$ $\delta_l = \delta_{cl}$ $\delta_m = \delta_{al}$ $\delta_n = \delta_{bl} + \delta_{dl}$ $\delta_p = \delta_{31}$
4 $(3\pi/5,4\pi/5)$	$\delta_x = \delta_0 + \delta_{bm}$ $\delta_y = \delta_{al} + \delta_{bl}$ $\delta_z = \delta_{am} + \delta_{31}$	$\delta_x = \delta_0$ $\delta_y = \delta_{bm} + \delta_{al} + \delta_{bl}$ $\delta_z = \delta_{am} + \delta_{31}$	$\delta_x = \delta_0 + \delta_{dl}$ $\delta_y = \delta_{bl} + \delta_{al}$ $\delta_z = \delta_{cl} + \delta_{31}$	$\delta_x = \delta_0$ $\delta_y = \delta_{dl} + \delta_{bl} + \delta_{al}$ $\delta_z = \delta_{cl} + \delta_{31}$
5 $(4\pi/5,\pi)$	$\delta_x = \delta_0 + \delta_{am} + \delta_{bl}$ $\delta_y = \delta_{al} + \delta_{bm}$ $\delta_z = \delta_{31}$	$\delta_x = \delta_0$ $\delta_y = \delta_{am} + \delta_{bl} + \delta_{al} + \delta_{bm}$ $\delta_z = \delta_{31}$	$\delta_x = \delta_0$ $\delta_y = \delta_{cl} + \delta_{al}$ $\delta_z = \delta_{bl} + \delta_{dl} + \delta_{31}$	$\delta_x = \delta_0$ $\delta_y = \delta_{cl} + \delta_{al} + \delta_{bl} + \delta_{dl}$ $\delta_z = \delta_{31}$
6 $(-\pi,-4\pi/5)$	$\delta_x = \delta_0 + \delta_{bm} + \delta_{al} + \delta_{bl}$ $\delta_y = \delta_{am}$ $\delta_z = \delta_{31}$	$\delta_x = \delta_0 + \delta_{bm}$ $\delta_y = \delta_{al} + \delta_{bl} + \delta_{am}$ $\delta_z = \delta_{31}$	$\delta_x = \delta_0 + \delta_{dl} + \delta_{bl} + \delta_{al}$ $\delta_y = \delta_{cl}$ $\delta_z = \delta_{31}$	$\delta_x = \delta_0 + \delta_{dl}$ $\delta_y = \delta_{bl} + \delta_{al} + \delta_{cl}$ $\delta_z = \delta_{31}$
7 $(-4\pi/5,-3\pi/5)$	$\delta_x = \delta_0 + \delta_{am} + \delta_{bl} + \delta_{al}$ $\delta_y = \delta_{bm}$ $\delta_z = \delta_{31}$	$\delta_x = \delta_0 + \delta_{am} + \delta_{bl}$ $\delta_y = \delta_{al}$ $\delta_z = \delta_{bm} + \delta_{31}$	$\delta_x = \delta_0 + \delta_{cl} + \delta_{al} + \delta_{bl}$ $\delta_y = \delta_{dl}$ $\delta_z = \delta_{31}$	$\delta_k = \delta_0$ $\delta_l = \delta_{cl} + \delta_{al}$ $\delta_m = \delta_{bl}$ $\delta_n = \delta_{dl}$ $\delta_p = \delta_{31}$
8 $(-3\pi/5,-2\pi/5)$	$\delta_x = \delta_0 + \delta_{bm} + \delta_{al}$ $\delta_y = \delta_{bl} + \delta_{am}$ $\delta_z = \delta_{31}$	$\delta_x = \delta_0 + \delta_{bm} + \delta_{al}$ $\delta_y = \delta_{bl}$ $\delta_z = \delta_{am} + \delta_{31}$	$\delta_x = \delta_0$ $\delta_y = \delta_{dl} + \delta_{bl}$ $\delta_z = \delta_{al} + \delta_{cl} + \delta_{31}$	$\delta_k = \delta_0$ $\delta_l = \delta_{dl} + \delta_{bl}$ $\delta_m = \delta_{al}$ $\delta_n = \delta_{cl}$ $\delta_p = \delta_{31}$
9 $(-2\pi/5,-\pi/5)$	$\delta_x = \delta_0 + \delta_{am}$ $\delta_y = \delta_{bl} + \delta_{al}$ $\delta_z = \delta_{bm} + \delta_{31}$	$\delta_x = \delta_0 + \delta_{am}$ $\delta_y = \delta_{bl} + \delta_{al} + \delta_{bm}$ $\delta_z = \delta_{31}$	$\delta_x = \delta_0 + \delta_{cl}$ $\delta_y = \delta_{al} + \delta_{bl}$ $\delta_z = \delta_{dl} + \delta_{31}$	$\delta_x = \delta_0 + \delta_{cl}$ $\delta_y = \delta_{al} + \delta_{bl} + \delta_{dl}$ $\delta_z = \delta_{31}$
10 $(-\pi/5,0)$	$\delta_x = \delta_0$ $\delta_y = \delta_{bm} + \delta_{al}$ $\delta_z = \delta_{bl} + \delta_{am} + \delta_{31}$	$\delta_x = \delta_0$ $\delta_y = \delta_{bm} + \delta_{al} + \delta_{bl} + \delta_{am}$ $\delta_z = \delta_{31}$	$\delta_x = \delta_0 + \delta_{dl} + \delta_{bl}$ $\delta_y = \delta_{al} + \delta_{cl}$ $\delta_z = \delta_{31}$	$\delta_x = \delta_0$ $\delta_y = \delta_{dl} + \delta_{bl} + \delta_{al} + \delta_{cl}$ $\delta_z = \delta_{31}$

reference line voltage during the switching period, and L_σ is the inductance of the equivalent load which is much more difficult to define in multiphase machines than in the three-phase case [24, 26]. Notice that the harmonic flux normalisation factor, introduced in [24] as $\lambda_N = V_{dc}T_s/8$, is also utilised here.

Next, the harmonic flux generated on the load during a switching period must be determined. Table 2.4 characterises the subintervals that appear in a switching period of the analytical analysis. These subintervals depend on the considered polygon and sector, as shown in Fig. 2.14. Notice that (2L+2M) schemes have only three different intervals (further on x, y, z). The same applies to (4L) techniques, however five subintervals appear in sectors 2, 3, 7 and 8 (from now on k, l, m, n, p) when considering the non-adjacent polygon. If v_{12} is the line voltage defined in Fig. 2.13, then $v_{12} = v_{AB}$ for the adjacent polygon (polygon 1) and $v_{12} = v_{AC}$ for the non-adjacent polygon (polygon 2). The normalized harmonic flux deviations

at the end of the x, y, z subintervals (see Table 2.4) are:

$$\begin{aligned}
&\Delta\lambda\,(0) = 0\\
&\Delta\lambda\,(t_1) = -2v_{12}\delta_x\\
&\Delta\lambda\,(t_2) = -2v_{12}\delta_x + 2\,(sign(v_{12})\cdot 2 - v_{12})\,\delta_y\\
&\Delta\lambda\,(t_3) = 0
\end{aligned} \tag{2.11}$$

However, the normalized harmonic flux deviations at the end of the k, l, m, n, p subintervals are in sectors 2, 3 given by:

$$\begin{aligned}
&\Delta\lambda\,(0) = 0\\
&\Delta\lambda\,(t_1) = -2v_{12}\delta_k\\
&\Delta\lambda\,(t_2) = -2v_{12}\delta_k + 2(-\mathrm{sign}(\mathrm{v}_{12})\cdot 2 - \mathrm{v}_{12})\delta_\mathrm{l}\\
&\Delta\lambda\,(t_3) = -2v_{12}\delta_k + 2(-\mathrm{sign}(\mathrm{v}_{12})\cdot 2 - \mathrm{v}_{12})\delta_\mathrm{l} - 2\mathrm{v}_{12}\delta_\mathrm{m}\\
&\Delta\lambda\,(t_4) = -2v_{12}\delta_k + 2(-\mathrm{sign}(\mathrm{v}_{12})\cdot 2 - \mathrm{v}_{12})\delta_\mathrm{l} - 2\mathrm{v}_{12}\delta_\mathrm{m} + 2(\mathrm{sign}(\mathrm{v}_{12})\cdot 2 - \mathrm{v}_{12})\delta_\mathrm{n}\\
&\Delta\lambda\,(t_5) = 0
\end{aligned} \tag{2.12}$$

while in sectors 7, 8 the corresponding expressions are:

$$\begin{aligned}
&\Delta\lambda\,(0) = 0\\
&\Delta\lambda\,(t_1) = -2v_{12}\delta_k\\
&\Delta\lambda\,(t_2) = -2v_{12}\delta_k + 2(\mathrm{sign}(\mathrm{v}_{12})\cdot 2 - \mathrm{v}_{12})\delta_\mathrm{l}\\
&\Delta\lambda\,(t_3) = -2v_{12}\delta_k + 2(\mathrm{sign}(\mathrm{v}_{12})\cdot 2 - \mathrm{v}_{12})\delta_\mathrm{l} - 2\mathrm{v}_{12}\delta_\mathrm{m}\\
&\Delta\lambda\,(t_4) = -2v_{12}\delta_k + 2(\mathrm{sign}(\mathrm{v}_{12})\cdot 2 - \mathrm{v}_{12})\delta_\mathrm{l} - 2\mathrm{v}_{12}\delta_\mathrm{m} + 2(-\mathrm{sign}(\mathrm{v}_{12})\cdot 2 - \mathrm{v}_{12})\delta_\mathrm{n}\\
&\Delta\lambda\,(t_5) = 0
\end{aligned} \tag{2.13}$$

As the next step, the squared value of the harmonic flux over the switching period has to be obtained. This evaluation can be conducted, due to the existing symmetry in two half-periods of the switching period, using one half of the switching period as follows:

$$\Delta\lambda^2{}_{RMS} = \frac{2}{T_s}\int_0^{T_s/2} \Delta\lambda^2\,(t)\,dt \tag{2.14}$$

Assuming a linear change of $\Delta\lambda$, the continuous integration defined in equation (2.14) can be replaced by a generic solution. This solution depends on the number of subintervals evaluated during the switching period. As a consequence, different

expressions are valid depending on the number of subintervals. The generic solution for sectors characterised by three subintervals is given with

$$\Delta\lambda^2{}_{RMS} = \frac{1}{3}\begin{bmatrix} \delta_x \Delta\lambda^2(t_1) \\ +\delta_y[\Delta\lambda^2(t_1) + \Delta\lambda(t_1)\Delta\lambda(t_2) + \Delta\lambda^2(t_2)] \\ +\delta_z \Delta\lambda^2(t_2) \end{bmatrix} \tag{2.15}$$

while the solution for sectors with five subintervals is

$$\Delta\lambda^2{}_{RMS} = \frac{1}{3}\begin{bmatrix} \delta_k \Delta\lambda^2(t_1) \\ +\delta_l[\Delta\lambda^2(t_1) + \Delta\lambda(t_1)\Delta\lambda(t_2) + \Delta\lambda^2(t_2)] \\ +\delta_m[\Delta\lambda^2(t_2) + \Delta\lambda(t_2)\Delta\lambda(t_3) + \Delta\lambda^2(t_3)] \\ +\delta_n[\Delta\lambda^2(t_3) + \Delta\lambda(t_3)\Delta\lambda(t_4) + \Delta\lambda^2(t_4)] \\ \delta_p \Delta\lambda^2(t_4) \end{bmatrix} \tag{2.16}$$

The flux HDF is then determined by integrating the squared harmonic flux over a fundamental period. Assuming positive values of emf and taking into account the symmetric properties of the line voltages, this evaluation can be reduced to the positive half-waveform of the fundamental line voltage for polygons 1 and 2, respectively, so that the following is obtained:

$$HDF_{P1} = \Delta\lambda^2{}_{RMSF} = \frac{1}{\pi}\int_{-4\pi/5}^{\pi/5} \Delta\lambda^2{}_{RMS} d\vartheta \tag{2.17}$$

$$HDF_{P2} = \Delta\lambda^2{}_{RMSF} = \frac{1}{\pi}\int_{-3\pi/5}^{2\pi/5} \Delta\lambda^2{}_{RMS} d\vartheta \tag{2.18}$$

It must be noted that equations (2.17) and (2.18) are divided into a number of integrals, depending on the angular span involved in a particular discontinuous modulation technique. While SVPWM, DPWMMAX, DPWMMIN, DPWM0 and DPWM2 techniques split the original integral into segments of $\pi/5$ radians span, DWPM1 and DPWM3 methods use $\pi/10$ radians span.

The per-phase flux HDF of the equivalent star connection is obtained by summing equations (2.17) and (2.18) and dividing by 5. The analytical expressions of flux HDF using individual polygons and complete flux HDF solution are evaluated and detailed in Tables 2.5 and 2.6. These analytical expressions, which define HDF as a function of the modulation index, are used to examine the behaviour of all the discontinuous SVPWM techniques and to compare them with the corresponding

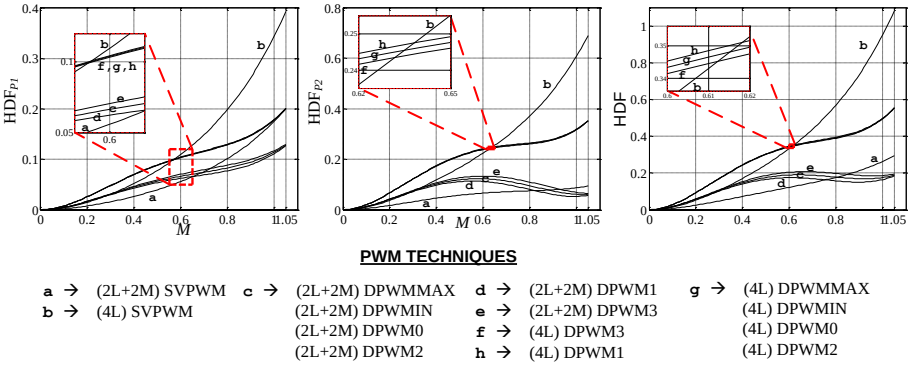

FIGURE 2.16. Flux HDF for all considered PWM techniques for the same average switching frequency.

continuous schemes. To make a fair comparison of the flux HDF, the same average switching frequency (ASF) should be used. For this purpose squared harmonic flux rms (i.e. HDF) has to be pre-multiplied by the squared average switching frequency (ASF^2). If the continuous (2L+2M) SVPWM switching frequency is considered as the base switching frequency (ASF=1), then ASF=1 for all discontinuous (4L) PWM techniques; ASF=1.4 for continuous (4L) SVPWM, and ASF=0.8 for all discontinuous (2L+2M) techniques. Hence the derived analytical expressions are multiplied by ASF^2, and plots are shown in Fig. 2.16.

An extended analysis is presented in the next chapter, where the obtained results using different continuous and discontinuous modulation techniques are studied and compared (see paper 4).

2.1.4. Current Ripple rms

Flux HDF determination does not depend on the load, and it is very helpful in real applications for the analysis of the generated current ripple and the calculation of the current THD. The final goal in the analysis is to derive the current THD from the flux HDF for any load. To obtain these relationships, a correspondence between flux HDF using the polygonal and space vector approaches must be established. This is so because different harmonics are multiplied by different factors for each set of line voltages applied to the load. This correspondence can be given as:

$$HDF_{P1} = (2K_1)^2 HDF_{\alpha\beta} + (2K_2)^2 HDF_{xy} \tag{2.19}$$

TABLE 2.5. Flux HDF for (2L+2M) PWM techniques using the polygon connection and the same base switching frequency.

SVPWM (2L+2M)	$HDF_{P1} = \frac{1}{16\pi}\left(8\pi - 35K_1 + 20K_2 - 2\pi J_1 - 10\pi J_2\right) M^4 - \frac{8}{9\pi}\left(3K_1 - K_2\right) M^3 + \frac{1}{3}\left(1 - J_2\right) M^2$ $HDF_{P2} = \frac{1}{16\pi}\left(6\pi - 15K_1 + 5K_2 + 4\pi J_1 - 2\pi J_2\right) M^4 - \frac{8}{9\pi}\left(K_1 + 3K_2\right) M^3 + \frac{1}{3}\left(1 + J_1\right) M^2$ $HDF = \frac{1}{16\pi}\left(14\pi - 50K_1 + 25K_2 + 2\pi J_1 - 12\pi J_2\right) M^4 - \frac{16}{9\pi}\left(2K_1 + K_2\right) M^3 + \frac{1}{3}\left(2 + J_1 - J_2\right) M^2$
DPWMMIN, DPWM0, DPWM2 (2L+2M)	$HDF_{P1} = \frac{1}{8\pi}\left(6\pi - 5K_1 + 10K_2 - 6\pi J_2\right) M^4 - \frac{1}{9\pi}\left(159K_1 - 53K_2\right) M^3 + \frac{4}{3}\left(1 - J_2\right) M^2$ $HDF_{P2} = \frac{1}{8\pi}\left(6\pi + 5K_1 + 15K_2 + 6\pi J_1\right) M^4 - \frac{1}{9\pi}\left(98K_1 + 69K_2\right) M^3 + \frac{4}{3}\left(1 + J_1\right) M^2$ $HDF = \frac{1}{8\pi}\left(12\pi + 25K_2 + 6\pi J_1 - 6\pi J_2\right) M^4 - \frac{1}{9\pi}\left(257K_1 + 16K_2\right) M^3 + \frac{4}{3}\left(2 + J_1 - J_2\right) M^2$
DPWM1 (2L+2M)	$HDF_{P1} = \frac{1}{4\pi}\left(3\pi + 15K_1 - 5K_2 - 3\pi J_2\right) M^4 + \frac{2}{9\pi}\left(45 - 12K_1 + 4K_2 - 45J_1 - 90J_2\right) M^3 + \frac{4}{3}\left(1 - J_2\right) M^2$ $HDF_{P2} = \frac{1}{4\pi}\left(3\pi + 10K_1 + 5K_2 + 3\pi J_1\right) M^4 + \frac{2}{9\pi}\left(-4K_1 - 12K_2 - 45J_1 - 45J_2\right) M^3 + \frac{4}{3}\left(1 + J_1\right) M^2$ $HDF = \frac{1}{4\pi}\left(6\pi + 25K_1 + 3\pi J_1 - 3\pi J_2\right) M^4 + \frac{2}{9\pi}\left(45 - 16K_1 - 8K_2 - 90J_1 - 135J_2\right) M^3 + \frac{4}{3}\left(2 + J_1 - J_2\right) M^2$
DPWM3 (2L+2M)	$HDF_{P1} = \frac{1}{4\pi}\left(3\pi - 20K_1 + 15K_2 - 3\pi J_2\right) M^4 + \frac{2}{9\pi}\left(-45 - 147K_1 + 49K_2 + 45J_1 + 90J_2\right) M^3 + \frac{4}{3}\left(1 - J_2\right) M^2$ $HDF_{P2} = \frac{1}{4\pi}\left(3\pi - 5K_1 + 10K_2 + 3\pi J_1\right) M^4 + \frac{2}{9\pi}\left(-94K_1 - 57K_2 + 45J_1 + 45J_2\right) M^3 + \frac{4}{3}\left(1 + J_1\right) M^2$ $HDF = \frac{1}{4\pi}\left(6\pi - 25K_1 + 25K_2 + 3\pi J_1 - 3\pi J_2\right) M^4 + \frac{2}{9\pi}\left(-45 - 241K_1 - 8K_2 + 90J_1 + 135J_2\right) M^3 + \frac{4}{3}\left(2 + J_1 - J_2\right) M^2$

$$HDF_{P2} = (2K_2)^2 HDF_{\alpha\beta} + (2K_1)^2 HDF_{xy} \tag{2.20}$$

$$HDF_{P1} + HDF_{P2} = 4\left(K_1^2 + K_2^2\right)\left(HDF_{\alpha\beta} + HDF_{xy}\right) \tag{2.21}$$

$$HDF_{P1} + HDF_{P2} = 5\left(HDF_{\alpha\beta} + HDF_{xy}\right) \tag{2.22}$$

The first step to obtain the current THD is to derive squared current ripple rms from the flux HDF analysis. This is a complex task because it is not easy to identify a unique inductance for each polygon. However, use of equations (2.19) to (2.22) and the space vector approach simplify this step, allowing the following expressions for the current ripple to be derived:

$$Irms_{P1}^2 = \left(\frac{V_{DC} T_s}{8}\right)^2 (2K_1)^2 \frac{HDF_{\alpha\beta}}{L_{\alpha\beta}^2} + (2K_2)^2 \frac{HDF_{xy}}{L_{xy}^2} \tag{2.23}$$

TABLE 2.6. Flux HDF for (4L) PWM techniques using the polygon connection and the same base switching frequency.

SVPWM (4L)	$HDF_{P1} = \frac{1}{16\pi}(8\pi - 35K_1 + 20K_2 - 2\pi J_1 - 10\pi J_2)M^4 + \frac{1}{9\pi}(-24K_1 + 8K_2)M^3 + \frac{1}{3}(1 - J_2)M^2$ $HDF_{P2} = \frac{1}{16\pi}(6\pi - 15K_1 + 5K_2 + 4\pi J_1 - 2\pi J_2)M^4 + \frac{1}{9\pi}(-96K_1 + 37K_2)M^3 + \frac{1}{3}(1 + J_1)M^2$ $HDF = \frac{1}{16\pi}(14\pi - 50K_1 + 25K_2 + 2\pi J_1 - 12\pi J_2)M^4 + \frac{1}{3\pi}(-40K_1 + 15K_2)M^3 + \frac{1}{3}(2 + J_1 - J_2)M^2$
DPWMMIN, DPWM0, DPWM2 (4L)	$HDF_{P1} = \frac{1}{8\pi}(6\pi - 5K_1 + 10K_2 - 6\pi J_2)M^4 + \frac{1}{9\pi}(-159K_1 + 53K_2)M^3 + \frac{4}{3}(1 - J_2)M^2$ $HDF_{P2} = \frac{1}{8\pi}(6\pi + 5K_1 + 15K_2 + 6\pi J_1)M^4 + \frac{1}{9\pi}(-186K_1 - 8K_2)M^3 + \frac{4}{3}(1 + J_1)M^2$ $HDF = \frac{1}{8\pi}(12\pi + 25K_2 + 6\pi J_1 - 6\pi J_2)M^4 - \frac{5}{3\pi}(23K_1 - 3K_2)M^3 + \frac{4}{3}(2 + J_1 - J_2)M^2$
DPWM1 (4L)	$HDF_{P1} = \frac{1}{16\pi}(12\pi + 30K_1 - 5K_2 - 12\pi J_2)M^4 - \frac{1}{9\pi}(18 + 189K_1 - 113K_2 + 24J_1 + 6J_2)M^3 + \frac{4}{3}(1 - J_2)M^2$ $HDF_{P2} = \frac{1}{16\pi}(12\pi + 25K_1 + 20K_2 + 12\pi J_1)M^4 - \frac{1}{9\pi}(42 + 156K_1 - 82K_2 + 66J_1 + 24J_2)M^3 + \frac{4}{3}(1 + J_1)M^2$ $HDF = \frac{1}{16\pi}(24\pi + 55K_1 + 15K_2 + 12\pi J_1 - 12\pi J_2)M^4 - \frac{5}{9\pi}(12 + 69K_1 - 39K_2 + 18J_1 + 6J_2)M^3 + \frac{4}{3}(2 + J_1 - J_2)M^2$
DPWM3 (4L)	$HDF_{P1} = \frac{1}{16\pi}(12\pi - 50K_1 + 45K_2 - 12\pi J_2)M^4 - \frac{1}{9\pi}(-18 + 129K_1 + 7K_2 - 24J_1 - 6J_2)M^3 + \frac{4}{3}(1 - J_2)M^2$ $HDF_{P2} = \frac{1}{16\pi}(12\pi - 5K_1 + 40K_2 + 12\pi J_1)M^4 - \frac{1}{9\pi}(-42 + 216K_1 + 98K_2 - 66J_1 - 24J_2)M^3 + \frac{4}{3}(1 + J_1)M^2$ $HDF = \frac{1}{16\pi}(24\pi - 55K_1 + 85K_2 + 12\pi J_1 - 12\pi J_2)M^4 - \frac{5}{9\pi}(-12 + 69K_1 + 21K_2 - 18J_1 - 6J_2)M^3 + \frac{4}{3}(2 + J_1 - J_2)M^2$

$$Irms_{P2}^2 = \left(\frac{V_{DC}T_s}{8}\right)^2 (2K_2)^2 \frac{HDF_{\alpha\beta}}{L_{\alpha\beta}^2} + (2K_1)^2 \frac{HDF_{xy}}{L_{xy}^2} \tag{2.24}$$

$$Irms_{polygonal}^2 = 4\left(K_1^2 + K_2^2\right)\left(\frac{V_{DC}T_s}{8}\right)^2 \left(\frac{HDF_{\alpha\beta}}{L_{\alpha\beta}^2} + \frac{HDF_{xy}}{L_{xy}^2}\right) \tag{2.25}$$

Here $L_{\alpha\beta}$ and L_{xy} are the equivalent inductances of the $\alpha-\beta$ and $x-y$ planes for switching harmonics, and $L_{\alpha\beta} \approx L_{ls} + L_{lr}$, $L_{xy} = L_{ls}$. It follows from equation (2.25) that squared current ripple rms is five times higher using the polygonal connection approach than the per-phase value of the equivalent star-connected load, obtained using the space vector approach. The per-phase value of the equivalent star connected load is thus 1/5 of the value obtained using equation (2.25). Finally,

per-phase stator current THD can be obtained from equations (2.23) and (2.24) as

$$THD_{\text{star}} = \sqrt{\frac{\left(Irms_{P1}^2 + Irms_{P2}^2\right)/5}{Irms_{fundP1}^2/(2K_1)^2}} = \sqrt{\frac{\left(Irms_{P1}^2 + Irms_{P2}^2\right)/5}{Irms_{fundP2}^2/(2K_2)^2}} \tag{2.26}$$

In order to verify analytical and theoretical results, a simulation study has been performed using Matlab/Simulink and an experimental evaluation has been also conducted with the load connected in the star topology. Obtained results are presented and detailed in paper 4 (chapter 3).

2.1.5. Current THD

Before starting the analysis, the following assumptions are made: Modulation index M is defined as $M = V_1/(V_{DC}/2)$, where V_1 is the peak value of the fundamental phase voltage and total harmonic distortion (THD) of a phase variable x (voltage or current) is defined as

$$\text{THD}_x = \sqrt{\sum_{\nu=2}^{\infty} X_\nu^2}\Big/ X_1 \tag{2.27}$$

If the inverter is operated in open-loop V/f mode, then the inverter dead-time effect leads to flow of low-order odd current harmonics, which map into the $x-y$ plane [28]. Since these harmonics are not related to the inverter switching behaviour, THD can be calculated in all cases where the dead time exists by summing the harmonics in equation (2.27) above the 10th.

THD of phase voltage or current is related to the corresponding THDs in the two planes of a five-phase system, on the basis of Clarke's decoupling transformation, through:

$$\text{THD}_x = \sqrt{\text{THD}_{x(\alpha\beta)}^2 + \text{THD}_{x(xy)}^2} \tag{2.28}$$

Being the squared harmonic ripple rms value of phase voltage or current related to the corresponding THD as follows:

$$X_{\text{RMS}}^2 = \text{THD}_x^2 X_1^2 \tag{2.29}$$

In a three-phase machine there is a single inductance, relevant for the switching

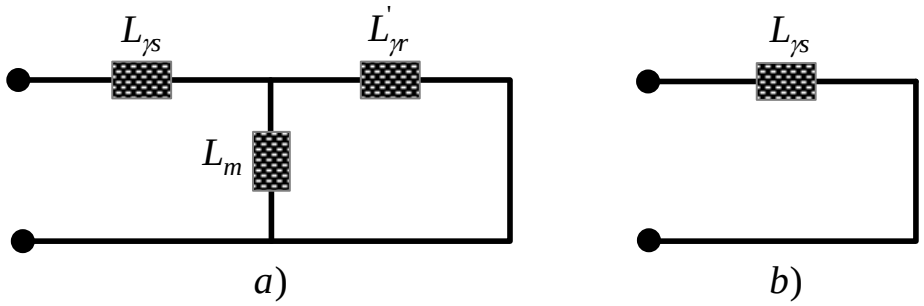

FIGURE 2.17. Equivalent circuit of a five-phase induction machine in a) $\alpha-\beta$ and b) $x-y$ plane for current THD analysis (L_m = magnetizing inductance; L_s, L'_r = stator and rotor leakage inductance, respectively) .

harmonics. However, this is not the normal case in multi-phase machines. Recalculating the flux ripple definition in terms of the current ripple and the flux normalization factor, introduced in [25] in the process of flux HDF development, leads to:

$$\Delta\bar{\lambda} = L_\sigma \Delta\bar{i} \tag{2.30}$$

$$\Delta\lambda_N = L_\sigma \Delta i_N = V_{DC} T_s/8 \tag{2.31}$$

where L_σ is the equivalent inductance for the switching harmonics. If the equivalent inductance in the two planes is the same, current ripple and total flux HDF are related in a simple manner, as already shown in [25]:

$$I^2_{\mathrm{RMS}} = \left(\frac{V_{DC} T_s}{8}\right)^2 \frac{1}{L^2_\sigma} HDF = A \cdot HDF \tag{2.32}$$

where HDF stands for the total per-phase flux HDF of a given PWM method, using a certain modulation index value. Hence current THD can be given, using equations (2.27), (2.29) and (2.32), as

$$\mathrm{THD}_i = \left(\frac{V_{DC} T_s}{8}\right) \frac{1}{L_\sigma} \frac{\sqrt{HDF}}{I_1} \tag{2.33}$$

Correlation given by equation (2.33) may suffice for some types of multi-phase permanent magnet synchronous machines (for example, the fault tolerant design with surface mounted magnets and no mutual magnetic coupling between stator

phases [29]). However, the inductances relevant for switching harmonics in the two $\alpha-\beta$ and $x-y$ planes will always be different in multi-phase induction machines. To obtain realistic values for the current squared ripple rms and for the current THD, per-phase equivalent circuits at switching frequencies of five-phase machines in the $\alpha-\beta$ and $x-y$ planes need to be considered. Since the switching frequency is assumed to be much higher than the fundamental frequency, resistances can be neglected and reduced per-phase equivalent schemes, shown in Fig. 2.17 for an induction machine, are sufficient for the analysis. The equivalent inductances for the $\alpha-\beta$ and the $x-y$ planes, respectively, can be given as:

$$L_{\alpha\beta} = L_{\gamma s} + \frac{L_{\gamma r}^{'} L_m}{L_{\gamma r}^{'} + L_m} = L_{\gamma s} + L_{\gamma r}^{'} \tag{2.34}$$

$$L_{xy} = L_{\gamma s} \tag{2.35}$$

Stator leakage inductance in the two planes may or may not be equal, this being dependent on the stator winding design [30]. As shown in [30], if stator winding is double-layer, the stator leakage inductances of the two planes are in principle different. Assuming for simplicity that the stator winding is single-layer, the stator leakage inductance in the two planes may be regarded as being the same.

The problem of frequency-related variation of the rotor leakage inductance of induction machines due to skin effect is well-known [31]. It means in essence that the rotor leakage inductance in equation (2.34) will have a particular and different value for each switching harmonic, with an ever-decreasing trend as the frequency increases. Considering that flux HDF represents simultaneously all the relevant switching harmonics, it is not possible to take into account the frequency related variation of the rotor leakage inductance and it is considered constant further on. While this does not have an impact on analytical studied (like results obtained through simulation), experimental results will obviously be affected.

Let flux per-phase HDFs of the two planes, obtained in [25] for the two considered SVPWM techniques, be identified with indices 1 and 2, respectively. For a five-phase induction machine the relationships between squared current ripple rms and per-plane flux HDFs, and current THD and per-plane flux HDFs, equations (2.32)

and (2.33), respectively, take the following form:

$$I_{RMS}^2 = \left(\frac{V_{DC}T_s}{8}\right)^2 \left(\frac{HDF_1}{\left(L_{\alpha\beta}\right)^2} + \frac{HDF_2}{\left(L_{xy}\right)^2}\right) \tag{2.36}$$

$$\mathrm{THD}_i = \left(\frac{V_{DC}T_s}{8}\right) \frac{\sqrt{HDF_1 \Big/ L_{\alpha\beta}^2 + HDF_2 \Big/ L_{xy}^2}}{I_1} \tag{2.37}$$

2.2. Common Mode Voltage

Reduction of common–mode voltage has been an issue of interest in the design of PWM techniques because CMV is known to cause electromagnetic interference (EMI), breakdown of windings insulation, fault activation of current detector circuits and leakage currents that may damage the motor bearings [32–37]. A percentage of the CMV (typically 10% [37]) appears between the motor shaft and the grounded motor frame, allowing parasitic currents to flow via the motor bearings. These leakage currents, associated to the shaft–to–frame voltage, depend on variables like the motor speed, bearing temperature, type of bearings or power level to name a few [33]. They can severely damage the bearings and reduce the drive robustness. While the displacement bearing currents are generated by the dv/dt of the inverter, the electric discharge machining (EDM) bearing currents are generated when the peak value of the CMV exceeds a certain threshold, causing the dielectric breakdown of the bearing lubricant [32–35, 35]. Aiming to avoid bearing currents, different modulation techniques for three–phase machines have been proposed both for two–level [37–39] and three–level [40, 41] VSIs. Sine–triangle PWM with interleaved carriers [39] inherently reduces the appearance of the zero vectors 000 and 111, thus reducing the rms value of the CMV but still allowing CMV peaks of $\pm V_{DC}/2$. Zero vectors can however be fully eliminated by substituting the zero vectors by active vectors in phase opposition with equal duty cycles. This approach is adopted in [38] proving that the peak values of the CMV can be reduced to $\pm V_{DC}/6$. Carrier–based version of this strategy can be found in [37] with some modifications of the basic idea of [38]. However, all these works are devoted to three–phase drives and have not been extended to the multiphase case.

The work in multiphase loads must extend the fundamental idea of [38] to the higher number of phases case, like the five-phase induction motor drive (Fig. 2.18). As in three-phase drives [37–39], the modulation techniques with reduced CMV can be used in any multiphase application where the bearings can be damaged due to the peak–to–peak CMV. Five–phase VSIs, in comparison to their three–phase counterparts, present an increased complexity because the number of voltage vectors is increased (from $2^3 = 8$ to $2^5 = 32$), the size of the voltage vectors is not unique (zero, small, medium and large vectors are present) and an additional subspace appears (x–y plane) [42]. Compared to the three-phase case, the dv/dt of

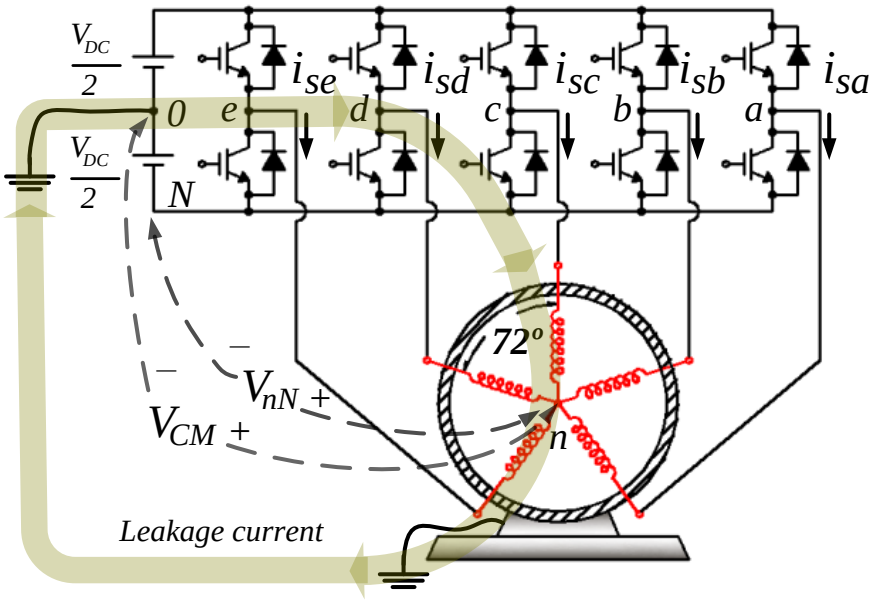

FIGURE 2.18. Two–level five–phase induction motor drive scheme showing the leakage currents flowing via the grounded motor frame.

the CMV in five-phase drives is inherently reduced because it is in general equal to V_{DC}/n, being n the number of phases of the system. Nevertheless, the peak-to-peak CMV remains as in the three-phase case equal to V_{DC}. Similarly to the approach adopted for three-phase drives [37–39], the modification of the switching pattern cannot reduce the dv/dt but can effectively reduce the peak–to–peak CMV. In the five-phase system, the CMV presents now six different levels, and elimination of zero vectors does not ensure minimum CMV peak values as it occurs in three–phase VSIs.

The CMV, from now on V_{CM}, relates the motor neutral voltage to the mid–point of the DC link and its expression in two–level three–phase drives is [41]:

$$V_{CM} = \frac{V_{DC}}{3} \cdot (S_a + S_b + S_c) - \frac{V_{DC}}{2} = V_{nN} - \frac{V_{DC}}{2} \tag{2.38}$$

where V_{DC} is the DC link voltage, V_{nN} relates the motor neutral voltage to the negative rail of the VSI (Fig. 2.18) and $S_i \in 0{,}1$ are the switching functions of each VSI leg. From equation (2.38) it follows that the maximum peak value of the CMV is $|V_{CM}| = V_{DC}/2$, the minimum voltage variation is $\pm V_{DC}/3$ and the number of

TABLE 2.7. Magnitude of CMV according to the switching states.

.	**Switching state**	$\alpha-\beta$	$x-y$	**VCM**
Large·CMV (0–5)	{00000}, {11111}	Size Z	Size Z	0.5VDC
Medium CMV (1–4)	{00001} {00010} {00100} {01000} {10000}	M	M	0.3VDC
	{11110} {11101} {11011} {10111} {01111}	M	M	
Small CMV (2–3)	{00011} {00101} {01001} {10001} {00110} {01010} {10010} {01100} {10100} {11000}	L	S	0.1VDC
	{11100} {11010} {10110} {01110} {11001} {10101} {01101} {10011} {01011} {00111}	S	L	

CMV levels is four. Most of the techniques for CMV reduction avoid the zero states $S_aS_bS_c = 000$ or 111, maintaining the voltage variation of $\pm\, V_{DC}/3$ but reducing the peak value of the CMV to $V_{DC}/6$ (66% of reduction). Consequently, the dv/dt (cause of displacement bearing currents) remains constant but the reduction of the maximum $|V_{CM}|$ helps to mitigate the main source of leakage current, namely the EDM bearing currents.

The expression of the CMV in five–phase drives can be directly extrapolated from equation (2.38) as:

$$V_{CM} = \frac{V_{DC}}{5} \cdot (S_a + S_b + S_c + S_d + S_e) - \frac{V_{DC}}{2} \tag{2.39}$$

In this case, the maximum peak value of the CMV is still $|V_{CM}| = V_{DC}/2$ but the number of CMV levels is increased to six and the minimum voltage variation is reduced to $\pm V_{DC}/5$. Therefore, in spite of dealing with a two–level VSI, the CMV presents more levels because additional switching combinations are possible due to the multiphase nature of the converter. The dv/dt is thus reduced in five–phase drives independently of which SVPWM technique is selected.

From equation (2.39), it can be deduced that the switching combinations generate six different values of the CMV: $\pm\, 0.1{\cdot}V_{DC}$, $\pm 0.3{\cdot}V_{DC}$ and $\pm 0.5{\cdot}V_{DC}$. The switching states can be grouped (Table 2.7 and Fig. 2.18) into those that generate:

- Large CMV ($\pm 0.5{\cdot}V_{DC}$): switching states with all switches ON or vice versa, referred as 0–5.

- Medium CMV ($\pm 0.3 \cdot V_{DC}$): switching states with one switch ON and four switches OFF or vice versa, referred as 1–4.
- Small CMV ($\pm 0.1 \cdot V_{DC}$): switching states with two switches ON and three switches OFF or vice versa, referred as 2–3.

As in the three–phase case, zero vectors (0–5) generate the higher CMV and must therefore be avoided if the bearing voltage needs to be diminished. However, avoiding the selection of zero vectors only reduces the CMV by 40 %, so the use of medium CMV voltage vectors should be also restrained in order to further reduce the bearing voltage.

SVPWM methods have not been extended to the multiphase case with the goal of reducing CMV. This is an important research area in this work, as it will be stated in the next section, where different methods are proposed and compared with conventional 5-phase SVPWM techniques (see papers 6 and 7).

2.3. Modulation Techniques in Non-linear Operating Zones

The voltage source converter is usually operated in the linear modulation region, but overmodulation can also be used to improve the dynamic response of the drive increasing the output voltage of the power converter. The main consequence of using overmodulation is the generation of low order voltage harmonics. Linear modulation region is reached using different SVM schemes that applies adjacent active voltage vectors to the voltage reference [43]. However, the overmodulation region requires much more attention than in the 3-phase case because effective impedances differ between fundamental and some specific harmonics components not involved within the mechanical energy conversion. These low order harmonic voltage components face very low effective impedances in the multiphase drive, increasing the Joule losses in the machine. Some trials have been made to deal with this problem in [44] where two different space vector modulation methods in the overmodulation region are developed. Another modulation technique based on a carrier based approach was studied in [45], where the switching current harmonic content was detailed. Finally, two complex and optimal mathematical solutions for the five phase case have been recently proposed in [46, 47]. The objective proposed in [46] is to minimize the voltage generated in $x-y$ plane, while [47] is additionally focused on common mode voltage.

When three-phase converters enter the overmodulation zone the zero vectors no longer need to be used and consequently the operation in the pulse dropping region inherently provides low CMV. However, this is not the case of multiphase converters because the overmodulation algorithms become more complex due to the additional voltage space vectors and subspaces [42]. The non-linear operating regions constitute the last issue analyzed in this work, where two modulation techniques are proposed to reduced the generated CMV in paper 7 and low-order harmonics in paper 8 (see chapter 3).

Capítulo 3

Aportaciones

Major contributions of this dissertation have been published in different journal and conference papers. The work contributes to reduce the gap between research and industry applications in the multiphase drives' field, where the Thesis firstly extends the analysis of continuous and discontinuous PWM and SVPWM techniques into the multiphase VSI area (Paper 1 to paper 5), and secondly presents new modulation techniques to reduce the CMV in linear and non-linear operation zones and in the overmodulation region to reduce undesired low order harmonic components (paper 6 to paper 8).

It is important to highlight that the research has been extensively validated using simulation and experimental results and different multiphase induction machines available at the labs of the Liverpool John Moores University (UK) and the University of Seville (SPAIN), being the candidate one of the main contributors of the obtained publications.

The main contributions in this research work (more publications and research papers from the author are listed in the bibliography section of this document but they are not included here because they are not directly in relation with the Thesis) are the following:

> **Paper 1:** D. Dujic, M. Jones, E. Levi, J. Prieto, F. Barrero, "Switching Ripple Characteristics of Space Vector PWM Schemes for Five-Phase Two Level Voltage Source Inverters-Part 1: Flux Harmonic Distortion Factors," IEEE Transactions on Industrial Electronics, vol.58, no.7, pp.2789-2798, July 2011.

Paper 2: M. Jones, D. Dujic, E. Levi, J. Prieto, F. Barrero, "Switching Ripple Characteristics of Space Vector PWM Schemes for Five-Phase Two Level Voltage Source Inverters-Part 2: Current Ripple," IEEE Transactions on Industrial Electronics, vol.58, no.7, pp. 2799-2808, July 2011.

Paper 3: J. Prieto, M. Jones, F. Barrero, E. Levi, S. Toral, "Comparative Analysis of Discontinuous and Continuous PWM Techniques in VSI-Fed Five-Phase Induction Motor," IEEE Transactions on Industrial Electronics, vol.58, no.12, pp.5324-5335, Dec. 2011.

Paper 4: J. Prieto, F. Barrero, E. Levi, S. Toral, M. Jones, M. J. Durán, "Analytical Evaluation of Switching Characteristics in Five-Phase Drives with Discontinuous Space Vector Pulse Width Modulation Techniques", EPE Journal, vol.23, no.2, pp.24-33, Jun. 2013.

Paper 5: J. Prieto, E. Levi, F. Barrero, S. Toral, "Output current ripple analysis for asymmetrical six-phase drives using double zero-sequence injection PWM," Proceedings of 37th Annual Conference on IEEE Industrial Electronics Society (IECON 2011), pp.3692-3697, Nov. 2011.

Paper 6: M.J. Durán, J. Prieto, F. Barrero, J.A. Riveros, H.Guzmán, "Space-Vector PWM With Reduced Common-Mode Voltage for Five-Phase Induction Motor Drives," IEEE Transactions on Industrial Electronics, vol.60, no.10, pp.4159-4168, Oct. 2013.

Paper 7: M.J. Duran, J. Prieto, F. Barrero, "Space Vector PWM With Reduced Common-Mode Voltage for Five-Phase Induction Motor Drives Operating in Overmodulation Zone," IEEE Transactions on Power Electronics, vol.28, no.8, pp.4030-4040, Aug. 2013.

Paper 8: J. Prieto, F. Barrero, M. J. Durán, S. Toral, M.A. Perales, "SVM Procedure for n-phase VSI With Low Harmonic Distortion in the Overmodulation Region," IEEE Transactions on Industrial Electronics, vol.61, no.1, pp.92-97, Jan. 2014.

3.1. Paper 1

Authors: D. Dujic, M. Jones, E. Levi, J. Prieto y F. Barrero.
Title: Switching Ripple Characteristics of Space Vector PWM Schemes for Five-Phase Two-Level Voltage Source Inverters-Part 1: Flux Harmonic Distortion Factors.
Journal: IEEE Transactions on Industrial Electronics.
Volume: 58.
Number: 7.
Pages: 2789-2798.
Date: July 2011.
Abstract: Multiphase variable-speed drives supplied from two-level voltage source inverters (VSIs) are, at present, contenders for numerous industrial applications. Various pulsewidth modulation (PWM) methods for multiphase VSIs, aimed at sinusoidal output voltage generation, have been developed using both carrier-based and space-vector approaches. An increased number of voltage space vectors, available for the synthesis of the output voltage, offer greater flexibility for the PWM scheme development, compared to the three-phase case. This paper presents comprehensive analytical analysis and comparison of switching ripple characteristics of two continuous space vector PWM (SVPWM) methods for a five-phase two-level VSI. Considered SVPWM schemes select a different set of four active space vectors per switching period in order to generate sinusoidal output voltages. This paper also presents the evaluation of the flux harmonic distortion factors of the SVPWM techniques. Correlation with corresponding current ripple and total harmonic distortion is established in Part 2 of this paper, where theoretical considerations are verified by simulations and through experimental investigation on a five-phase VSI-fed induction motor drive.

IEEE TRANSACTIONS ON INDUSTRIAL ELECTRONICS, VOL. 58, NO. 7, JULY 2011 2789

Switching Ripple Characteristics of Space Vector PWM Schemes for Five-Phase Two-Level Voltage Source Inverters—Part 1: Flux Harmonic Distortion Factors

Drazen Dujic, *Member, IEEE*, Martin Jones, *Member, IEEE*, Emil Levi, *Fellow, IEEE*, Joel Prieto, *Student Member, IEEE*, and Federico Barrero, *Senior Member, IEEE*

***Abstract*—Multiphase variable-speed drives supplied from two-level voltage source inverters (VSIs) are, at present, contenders for numerous industrial applications. Various pulsewidth modulation (PWM) methods for multiphase VSIs, aimed at sinusoidal output voltage generation, have been developed using both carrier-based and space-vector approaches. An increased number of voltage space vectors, available for the synthesis of the output voltage, offer greater flexibility for the PWM scheme development, compared to the three-phase case. This paper presents comprehensive analytical analysis and comparison of switching ripple characteristics of two continuous space vector PWM (SVPWM) methods for a five-phase two-level VSI. Considered SVPWM schemes select a different set of four active space vectors per switching period in order to generate sinusoidal output voltages. This paper also presents the evaluation of the flux harmonic distortion factors of the SVPWM techniques. Correlation with corresponding current ripple and total harmonic distortion is established in Part 2 of this paper, where theoretical considerations are verified by simulations and through experimental investigation on a five-phase VSI-fed induction motor drive.**

***Index Terms*—Flux harmonic distortion factor (HDF), multiphase drives, space vector pulsewidth modulation (SVPWM), voltage source inverters (VSIs).**

I. Introduction

MULTIPHASE variable-speed drives are utilized nowadays for various industrial applications, including those involving high power ratings and situations where fault tolerance is the major concern [1], [2]. While use of multilevel voltage source inverters (VSIs) in conjunction with multiphase machines is also possible [3], the customary solution is, at present, utilization of a multiphase two-level VSI. This has led to development of numerous pulsewidth modulation (PWM) strategies for multiphase two-level VSIs [4]–[13], which are, in principle, either of the carrier type (e.g., [6]) or space vector PWM (SVPWM) type (e.g., [4] and [5]) and can be either continuous or discontinuous, with the desired output voltage being either sinusoidal [4]–[11] or having a multifrequency output [12], [13]. Those relevant here are the continuous space vector techniques aimed at sinusoidal output voltage generation.

Application of decoupling transformation [14] in conjunction with an n-phase system (n is taken here as an odd number) leads to representation in multiple $((n-1)/2)$ 2-D mutually perpendicular planes [1], [2]. This greatly facilitates the design of the PWM, and as a consequence, application of the vector space decomposition [4] is the natural choice in the process of synthesis of multiphase SVPWM techniques [5], [7]–[9]. In principle, as long as purely sinusoidal output voltages are required, the modulator has to provide zero average values over the switching period in all 2-D planes other than the first one, where the fundamental gets mapped.

A common feature of the multiphase (n-phase) SVPWM schemes with sinusoidal output is that they utilize $(n-1)$ active space vectors in the switching period [4], [5], [7]–[10]. This fully corresponds to the situation that arises when carrier-based PWM, based on comparison of n modulating signals with the triangular carrier signal, is applied. If the active space vectors of the SVPWM are selected as those neighboring the reference, the triggered active vectors of the SVPWM and carrier-based PWM will be the same. Thus, the situation will be, in this respect, identical as in a three-phase system [15], and these properties of multiphase PWM have been demonstrated already for a five-phase VSI [5]–[7], seven-phase VSI [8] and a nine-phase VSI [9], [10].

An increase in the number of space vectors of multiphase VSIs, which equals 2^n, offers more flexibility during synthesis of the SVPWM, particularly regarding the selection of active space vectors involved in the switching pattern. This has been discussed in [16] and [17], where two different selections of active space vectors were considered for sinusoidal output voltage generation with a five-phase VSI. The first SVPWM method is the same as the one in [5] and [7], and it is based on the application of two large and two medium (2L+2M) space vectors per switching period, while the second SVPWM technique follows the idea in [4] and applies four large (4L)

Manuscript received February 4, 2010; revised May 7, 2010; accepted August 7, 2010. Date of publication August 30, 2010; date of current version June 15, 2011.

D. Dujic is with the ABB Corporate Research Centre, 5400 Baden-Dättwil, Switzerland (e-mail: drazen.dujic@ieee.org).

M. Jones and E. Levi are with the School of Engineering, Liverpool John Moores University, L3 3AF Liverpool, U.K. (e-mail: m.jones2@ljmu.ac.uk; e.levi@ljmu.ac.uk).

J. Prieto and F. Barrero are with the Electronic Engineering Department, University of Seville, 41092 Seville, Spain (e-mail: jprieto@esi.us.es; fbarrero@esi.us.es).

Color versions of one or more of the figures in this paper are available online at http://ieeexplore.ieee.org.

Digital Object Identifier 10.1109/TIE.2010.2070777

space vectors per switching period. Both active vector selection strategies lead to the same dc bus utilization in the linear modulation region. The considerations in [16] and [17] are, however, restricted to basic properties of these two SVPWM techniques and do not include any discussion of their switching characteristics. The two SVPWM techniques encompassed by the analysis in this paper are the (2L+2M) and (4L) methods for a five-phase VSI.

Different selection of active space vectors will inherently offer different behavior with regard to the performance indicators that can be used to assess the quality of output waveforms [15]. In very recent times, the attention has started to be paid not only to the development of PWM strategies for multiphase VSIs but also to the evaluation of their switching characteristics, such as flux harmonic distortion factor (HDF) and current ripple (current total harmonic distortion) as well. The principles of flux HDF and current ripple analysis are well established for three-phase systems [15], [18]–[25]. However, moving from a three-phase to a multiphase system with regard to the flux HDF (and, subsequently, current ripple) evaluation requires more than just a straightforward extension, as attempted in the first works devoted to this topic [26], [27]. As a consequence, the results in [26] and [27], related to a five-phase system, are of very limited usability since calculated flux HDFs represent only one part of the solution rather than the complete solution. This has been clearly shown in [28] and [29]. In [28], flux HDF was analytically determined for five-phase sinusoidal PWM, harmonic injection PWM, and SVPWM (2L+2M) methods. The approach in [28] is based on vector space decomposition [4] into two planes, thus allowing determination of per-plane flux HDFs. The alternative approach, based on original domain and consideration of polygon connections [29], has been developed for a general multiphase system with an odd number of phases, for sinusoidal PWM and harmonic injection PWM. Analyses and findings in [29] have fully verified the results in [28] for the particular (five-phase) case and have also shown that the total flux HDF can only be obtained by means of the polygon approach if and only if HDFs of individual polygons are all, at first, determined and their respective HDFs are finally summed. Further recent studies, related to the switching characteristics of various multiphase PWM schemes, include analyses of continuous [30] and discontinuous [31] PWM techniques, using, in essence, again multiple polygon connection approach. The PWM techniques encompassed by the studies in [28]–[31] do not include the five-phase SVPWM based on the selection of four large active vectors, which has never been considered in this context until now. Corresponding flux HDF and current ripple determination for asymmetrical six-phase drives with two neutral points has been reported in [32].

In this paper, an evaluation of the harmonic flux HDF and current ripple, produced by (2L+2M) and (4L) SVPWM techniques in conjunction with a five-phase induction motor drive, is performed. While an analytical solution for the flux HDF of the SVPWM (2L+2M) is a relatively simple equation, as demonstrated in [28], this is not the case for SVPWM (4L). Hence, the approach followed in this paper is numerical, rather than analytical (as in [28] and [29]). The analysis utilizes vector space decomposition and corresponding space vector approach (similar to [28]) and offers an insight into the mechanism of flux ripple and current ripple creation. This paper numerically evaluates flux HDF of the two SVPWM schemes. It is shown that the total flux HDF of the SVPWM (2L+2M) is significantly smaller, compared to the SVPWM (4L). Part 2 of this paper further explores correlation between the current ripple and the flux HDF and includes simulation and experimental results that fully verify the theoretical considerations in both parts.

II. SVPWM Methods for Five-Phase Inverters

A set of five-phase quantities can be decomposed using the decoupling transformation matrix (power-variant form is used and $\varphi = 2\pi/5$)

$$\underline{C}_5 = \frac{2}{5}\begin{bmatrix} 1 & \cos(\varphi) & \cos(2\varphi) & \cos(3\varphi) & \cos(4\varphi) \\ 0 & \sin(\varphi) & \sin(2\varphi) & \sin(3\varphi) & \sin(4\varphi) \\ 1 & \cos(2\varphi) & \cos(4\varphi) & \cos(\varphi) & \cos(3\varphi) \\ 0 & \sin(2\varphi) & \sin(4\varphi) & \sin(\varphi) & \sin(3\varphi) \\ 1/2 & 1/2 & 1/2 & 1/2 & 1/2 \end{bmatrix} \tag{1}$$

into a new set of variables, which belong to two mutually perpendicular planes, labeled further on as d_1–q_1 and d_2–q_2. The fifth variable, zero-sequence component, can be omitted from further consideration due to the star connection of the winding with isolated neutral point.

Since there are $2^5 = 32$ possible switching configurations for a five-phase VSI, there is a total of 32 switching states which determine 30 active space vectors and a zero space vector (two switching states). Each active space vector has, in principle, four components, governed with (1), along d_1–q_1 and d_2–q_2 axes of the two planes. Space vectors in each plane can be classified according to their magnitudes (small, medium, and large active space vectors, plus zero space vector), and each plane can be divided into ten sectors [7]. Since small vectors of the first plane map into large vectors in the second plane and vice versa, small vectors in the first plane are never utilized in the SVPWM [5], [7]–[10]. Hence, Fig. 1 shows large and medium active vectors in the first plane and their mapping into the second plane (where they appear as small and medium, respectively). Binary equivalent of the decimal number, which identifies each vector, represents the state of the upper switch in the corresponding inverter leg (“1” and “0” mean that the switch in on and off, respectively).

Since the desired output voltage is sinusoidal, the reference voltages map into a reference voltage space vector in the first $(d_1$–$q_1)$ plane. The reference in the second plane is zero, and thus, the PWM scheme must ensure that the average voltage in the d_2–q_2 plane is zero in each switching period. As already discussed, the common approach to realize reference space vector in the d_1–q_1 plane is to apply four active vectors and two zero switching states over the switching period. The considered two five-phase SVPWM schemes are reviewed next.

A. SVPWM Using (2L+2M) Active Vectors

The first SVPWM scheme is based on the selection of two large and two medium space vectors in the first plane, which

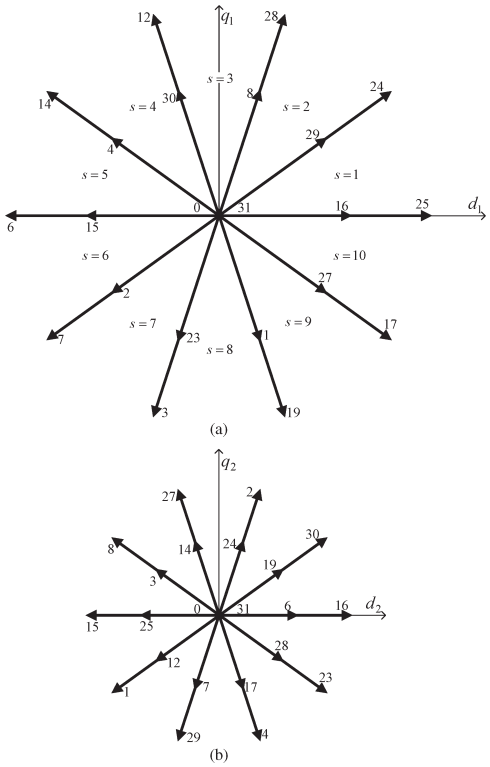

Fig. 1. Space vectors of a five-phase system in (a) d_1–q_1 plane and (b) d_2–q_2 plane (only those utilized in the (2L+2M) and (4L) SVPWMs are shown).

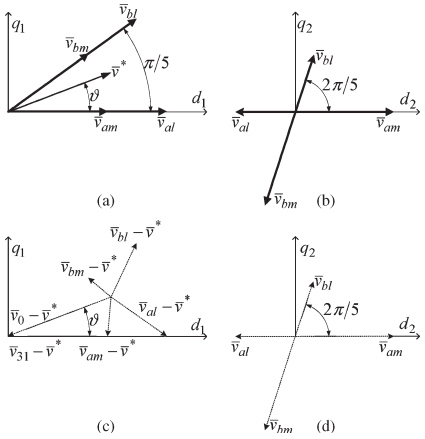

Fig. 2. Space vectors used for SVPWM (2L+2M) scheme in the [(a) and (b)] d_1–q_1 and d_2–q_2 planes and [(c) and (d)] generated error voltage vectors.

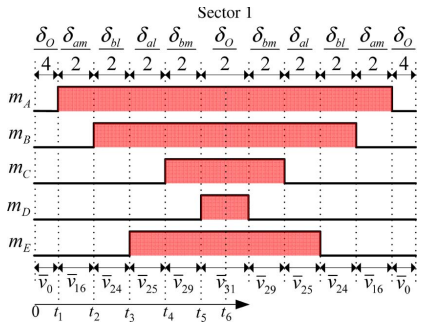

Fig. 3. SVPWM (2L+2M) method—switching pattern in the first sector.

neighbor the reference $\bar{v}^* = Me^{j\vartheta}$ (in per unit), and is available in, for example, [5] and [7]. Assuming that the reference space vector is in the first sector $(s = 1)$, as shown in Fig. 2, it is possible to determine the duty cycles for selected space vectors as

$$\delta_{am} = MK\sin\left(\frac{\pi}{5} - \vartheta\right) \qquad \delta_{bm} = MK\sin(\vartheta)$$
$$\delta_{al} = MK_2\sin\left(\frac{\pi}{5} - \vartheta\right) \qquad \delta_{bl} = MK_2\sin(\vartheta)$$
$$\delta_0 = \delta_{31} = \frac{1}{2}\delta_o = \frac{1}{2}\left[1 - MK_2\cos\left(\frac{\pi}{10} - \vartheta\right)\right] \quad (2)$$

where M is the modulation index, defined as $M = V_1/(V_{\rm dc}/2)$, and V_1 is the peak value of the phase voltage fundamental. Duty cycles (relative on-times over the switching period T_s) are defined as $\delta = T/T_s$. The following trigonometric constants are already introduced in (2) or will be utilized later:

$$K_p = \sin\left(p\frac{\pi}{5}\right) \qquad J_p = \cos\left(p\frac{\pi}{5}\right) \quad (3)$$

where $p = 1$ or 2 for a five-phase system. In the particular case when $p = 1$, the use of subscript is omitted. It can be seen from (2) that the total zero space vector duty cycle is shared equally among two zero space vector states. Some other distributions are possible as well, but this is beyond the scope of this paper. Solution given with (2) is valid only for the first sector, while solutions for other sectors can be determined in a similar manner.

Disposition of the applied space vectors in the two planes is shown in Fig. 2(a) and (b), where subscripts a and b are used to distinguish between active space vectors on the boundaries of the current (the first in Fig. 2) sector in the d_1–q_1 plane, while indices m and l stand for medium and large vectors. Fig. 2(c) and (d) show the corresponding error voltages, created when space vectors are activated, which underlines the mechanism for creation of output flux and current ripple.

Switching pattern in the first sector is shown in Fig. 3. It can be seen that each inverter leg switches at the same rate, so that the average switching frequency is equal to $1/T_s$. Use of medium and large space vectors from the d_1–q_1 plane activates medium and small space vectors in the d_2–q_2 plane, respectively. Attributes of the space vectors, used in the first sector, are summarized in Table I.

TABLE I
ATTRIBUTES OF APPLIED SPACE VECTORS (NORMALIZED WITH RESPECT TO $V_{dc}/2$)

SVPWM (2L+2M)	$\bar{v}_0$	$\bar{v}_{am}$	$\bar{v}_{bl}$	$\bar{v}_{al}$	$\bar{v}_{bm}$	$\bar{v}_{31}$
d_1-q_1	0	$\frac{4}{5}$	$\frac{8}{5}Je^{j\frac{\pi}{5}}$	$\frac{8}{5}J$	$\frac{4}{5}e^{j\frac{\pi}{5}}$	0
d_2-q_2	0	$\frac{4}{5}$	$\frac{8}{5}J_2e^{j2\frac{\pi}{5}}$	$-\frac{8}{5}J_2$	$\frac{4}{5}e^{-j3\frac{\pi}{5}}$	0
SVPWM (4L)	$\bar{v}_0$	$\bar{v}_{cl}$	$\bar{v}_{al}$	$\bar{v}_{bl}$	$\bar{v}_{dl}$	$\bar{v}_{31}$
d_1-q_1	0	$\frac{8}{5}Je^{-j\frac{\pi}{5}}$	$\frac{8}{5}J$	$\frac{8}{5}Je^{j\frac{\pi}{5}}$	$\frac{8}{5}Je^{j2\frac{\pi}{5}}$	0
d_2-q_2	0	$\frac{8}{5}J_2e^{-j2\frac{\pi}{5}}$	$-\frac{8}{5}J_2$	$\frac{8}{5}J_2e^{j2\frac{\pi}{5}}$	$\frac{8}{5}J_2e^{-j\frac{\pi}{5}}$	0
Used in (7) and (8) as:	N/A	$\bar{v}_I$	$\bar{v}_{II}$	$\bar{v}_{III}$	$\bar{v}_{IV}$	N/A

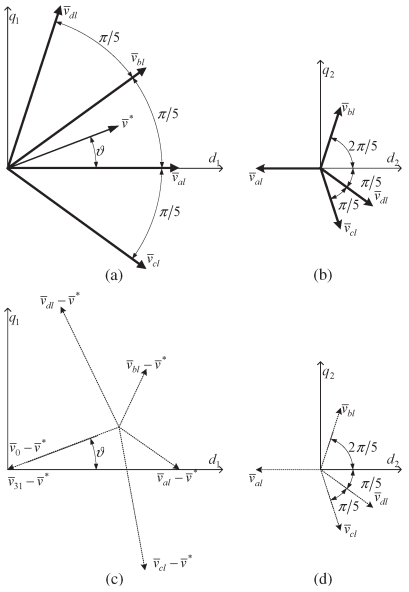

Fig. 4. Space vectors used for SVPWM (4L) scheme in the [(a) and (b)] d_1–q_1 and d_2–q_2 planes and [(c) and (d)] generated error voltage vectors.

B. SVPWM Using (4L) Active Vectors

The second SVPWM scheme applies four adjacent large active space vectors from the d_1–q_1 plane. Two outer (additional) large space vectors are identified with subscripts cl and dl in Fig. 4. Once more, for the reference space vector positioned in the first sector of the d_1–q_1 plane, one can obtain a solution for duty cycles in the form

$$\delta_{al} = MK\left[\sin(\vartheta) + (2J-1)\sin\left(\frac{\pi}{5}-\vartheta\right)\right]$$
$$\delta_{bl} = MK\left[\sin\left(\frac{\pi}{5}-\vartheta\right) + (2J-1)\sin(\vartheta)\right]$$
$$\delta_{cl} = MK\sin\left(\frac{\pi}{5}-\vartheta\right) = \delta_{am}$$

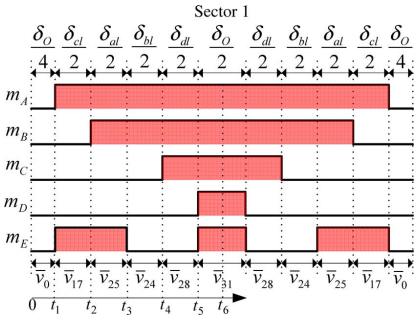

Fig. 5. SVPWM (4L) method—switching pattern in the first sector.

$$\delta_{dl} = MK\sin(\vartheta) = \delta_{bm}$$
$$\delta_0 = \delta_{31} = \frac{1}{2}\delta_o = \frac{1}{2}\left[1 - MK_2\cos\left(\frac{\pi}{10}-\vartheta\right)\right]. \quad (4)$$

It follows that the duty cycles of the c and d vectors are the same as the duty cycles of the medium vectors in SVPWM (2L+2M), (2). Duty cycle of the zero space vector is also the same. As with (2L+2M) method, the two zero space vector states are selected to have equal duty cycles.

The application of four large space vectors in the d_1–q_1 plane activates four small vectors in the d_2–q_2 plane, resulting in error voltages of lower magnitudes [Fig. 4(c) and (d)]. However, situation in the d_1–q_1 plane is actually the opposite, since smaller error voltages can be observed with the SVPWM (2L+2M) scheme. Yet, illustrations in Fig. 2 and Fig. 4 correspond to only one particular instant in time, while the reference space vector moves through the first sector and takes all possible positions. Further evaluation is therefore required, encompassing a longer time interval.

Switching pattern of the SVPWM (4L) scheme is shown in Fig. 5 for the first sector. Assuming the same reference space vector, both SVPWM schemes will produce equal per-leg duty cycles, as can be seen by comparing shaded areas in Figs. 3 and 5. However, the SVPWM (4L) scheme introduces additional commutations in one of the inverter legs in each of the sectors, as shown in Fig. 5 for the first sector. It can

be easily shown that each leg has an increased number of commutations every five sectors (or in two out of ten sectors). Since the basic switching period T_s is here regarded as being the same for the two techniques, the average switching frequency of the SVPWM (4L) is then 1.4 times higher. From the point of view of switching losses, this is certainly a drawback of an SVPWM (4L) method over the SVPWM (2L+2M) method. At the same time, implementation of such a switching pattern is not straightforward with low-cost digital signal processors and their counter-/timer-based PWM units. Thus, using these two criteria alone, one would come to the conclusion that (2L+2M) method is to be preferred to the (4L) SVPWM in real-world applications.[1]

III. Harmonic Flux Trajectories

Similar to the analysis presented in [28], it is possible to determine flux HDFs and current ripple for both considered SVPWM schemes. Application of the space vector theory allows for many intermediate results to be generated as well. Using the same assumptions as in [28]–[31], it is possible, at first, to graphically illustrate trajectories of harmonic flux, in each of two planes, over the switching period. A model for the analysis can be simplified into

$$\Delta\bar{i} = \frac{\bar{v} - \bar{v}^*}{L_\sigma}\Delta t. \tag{5}$$

Here, $\bar{v}$ represents the space vector activated over the time interval Δt within a switching period, while L_σ is the equivalent inductance for the switching harmonics. Since this equivalent inductance is not as simple to define in multiphase systems [28], [29] as is the case in three-phase systems, discussion of the current ripple is adjourned for the Part 2. The notion of "harmonic flux" ($\bar{\lambda}$) is introduced instead, where harmonic flux is the time integral of the error voltage vectors [22]–[24]. Hence, (5) takes an alternative form, which can be easily applied in both planes

$$\Delta\bar{\lambda} = L_\sigma\Delta\bar{i} = (\bar{v} - \bar{v}^*)\Delta t. \tag{6}$$

Thus, the analysis of the harmonic current is now replaced by the analysis of harmonic flux, which can be performed independently in each plane. Based on (6), it is possible to generate harmonic flux trajectories (trajectories of error voltage vectors) in both planes over the switching period, for both SVPWM schemes. Due to the existence of the symmetrical switching pattern, it is enough to consider only one-half of the switching period and obtain deviations of the harmonic flux ($\Delta\bar{\lambda}$) at the end of every subinterval over the first half of the switching period. Required time subintervals are labeled in Figs. 3 and 5 as $t_1, t_2, \ldots, t_6$, and since their number is equal in both cases (since the number of the applied vectors is the same), a generic set of equations is used to describe the harmonic flux trajectories of both SVPWM schemes.

[1]Note that the maximum modulation index for sinusoidal voltage output is the same for the (4L) and (2L+2M) SVPWMs, i.e., 1.0515 [5], [7].

Assuming zero initial value for the deviation of the harmonic flux, one can calculate normalized values of the harmonic flux (space vector $\Delta\bar{\lambda}$) in the d_1–q_1 plane directly, at the end of every subinterval, over the first half of the switching period, as

$$\begin{aligned}
\Delta\bar{\lambda}_{dq1}(0) &= 0\\
\Delta\bar{\lambda}_{dq1}(t_1) &= -2\bar{v}^*\delta_0\\
\Delta\bar{\lambda}_{dq1}(t_2) &= 2\left[\bar{v}_I\delta_I - \bar{v}^*[\delta_0+\delta_I]\right]\\
\Delta\bar{\lambda}_{dq1}(t_3) &= 2\left[\bar{v}_I\delta_I + \bar{v}_{II}\delta_{II} - \bar{v}^*[\delta_0+\delta_I+\delta_{II}]\right]\\
\Delta\bar{\lambda}_{dq1}(t_4) &= 2\left[\bar{v}_I\delta_I + \bar{v}_{II}\delta_{II} + \bar{v}_{III}\delta_{III} - \bar{v}^*[\delta_0+\delta_I+\delta_{II}+\delta_{III}]\right]\\
\Delta\bar{\lambda}_{dq1}(t_5) &= 2\bar{v}^*\delta_{31}\\
\Delta\bar{\lambda}_{dq1}(t_6) &= 0.
\end{aligned} \tag{7}$$

Similarly, for the d_2–q_2 plane, one has

$$\begin{aligned}
\Delta\bar{\lambda}_{dq2}(0) &= 0\\
\Delta\bar{\lambda}_{dq2}(t_1) &= 0\\
\Delta\bar{\lambda}_{dq2}(t_2) &= 2\bar{v}_I\delta_I\\
\Delta\bar{\lambda}_{dq2}(t_3) &= 2[\bar{v}_I\delta_I + \bar{v}_{II}\delta_{II}]\\
\Delta\bar{\lambda}_{dq2}(t_4) &= 2[\bar{v}_I\delta_I + \bar{v}_{II}\delta_{II} + \bar{v}_{III}\delta_{III}]\\
\Delta\bar{\lambda}_{dq2}(t_5) &= 0\\
\Delta\bar{\lambda}_{dq2}(t_6) &= 0.
\end{aligned} \tag{8}$$

Normalization factor, applied in (7) and (8), originates from the analysis of the current ripple of a half-bridge inverter [15] and is given by

$$\Delta\lambda_N = L_\sigma\Delta i_N = V_{\mathrm{dc}}T_s/8. \tag{9}$$

Active space vectors and their corresponding duty cycles in (7) and (8) are identified with roman numbers in subscripts. By replacing appropriate active space vectors from Table I and corresponding duty cycles [(2) for SVPWM (2L+2M) and (4) for SVPWM (4L)] into (7) and (8), trajectories of the harmonic flux, in both planes, over the first half of the switching period are obtained. These are shown in Fig. 6, where the modulation index is set to $M = 0.8$ and only four angular positions of the reference space vector are shown.

Particular trajectories, obtained for $\vartheta = 12^\circ$, have the added arrows in order to provide an additional information on the direction of the harmonic flux vector movement. The trajectories start and finish in the origin of the corresponding plane. This is a consequence of the assumption that the resistance can be neglected in the ripple analysis [28], [29] due to the high switching frequency.

It can be observed from Fig. 6 that harmonic flux trajectories of the SVPWM (2L+2M) are with smaller excursions from the origin in the d_1–q_1 plane, compared with the trajectories of the SVPWM (4L) scheme. However, it is the other way around in the d_2–q_2 plane, since trajectories of the SVPWM (4L) are the result of application of only small vectors, in contrast to the application of small and medium vectors in the case of SVPWM (2L+2M). More detailed explanations regarding the movement

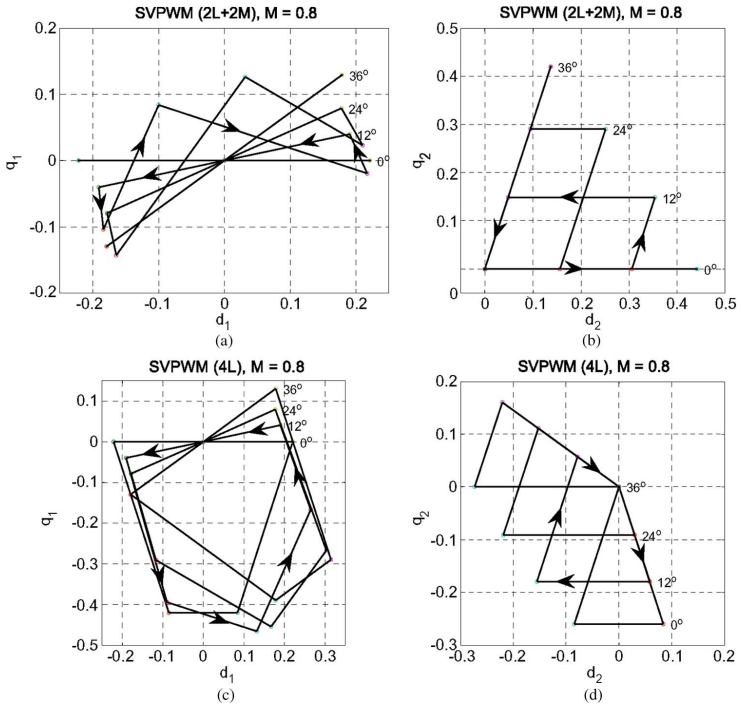

Fig. 6. Normalized harmonic flux trajectory during the first half of the switching period of the SVPWM (2L+2M) in the (a) d_1–q_1 plane and (b) d_2–q_2 plane and of the SVPWM (4L) in the (c) d_1–q_1 plane and (d) d_2–q_2 plane.

of the harmonic flux vector in each of the planes are available in [28].

IV. Squared Harmonic Flux

Obtained trajectories of the harmonic flux provide an insight into the creation of the flux ripple, and they are related to a particular instant in time defined by a reference space vector. Using as a figure of merit the value of the squared harmonic flux over the switching period, it is possible to obtain a more meaningful characteristic which describes a particular SVPWM scheme. For that purpose, the following integral has to be solved (due to the symmetry of the switching pattern, only-half of the switching period is sufficient for the analysis):

$$\Delta\lambda^2_{abcde-RMS} = \frac{2}{T_s}\int_0^{T_s/2} \Delta\lambda^2_{abcde}dt. \tag{10}$$

The left-hand side of (10) represents all five phases of the load, so that the total five-phase system solution is obtained. The quantity $\Delta\lambda^2_{abcde}$ can be related to the harmonic flux deviations in each of the two 2-D planes by means of the following correlation, governed by (1) [28]:

$$\Delta\lambda^2_{abcde} = \frac{5}{2}\left[\Delta\lambda^2_{d1} + \Delta\lambda^2_{q1} + \Delta\lambda^2_{d2} + \Delta\lambda^2_{q2}\right]. \tag{11}$$

Substituting (11) into (10), separating into several integrals in accordance with the existing subintervals (Figs. 3 and 5), and manipulating according to the procedure detailed in [28], it is possible to obtain a very general solution for (10), in each of the two 2-D planes, which can be easily evaluated numerically. These solutions are given by (12) and (13), shown at the top of the next page, for the d_1–q_1 plane and the d_2–q_2 plane, respectively, and they apply to both analyzed SVPWM schemes. For a numerical evaluation, it is enough to substitute duty cycles of the corresponding space vectors and squared values of axis components in each of the planes, as defined by (7) and (8).

Results of the numerical evaluation are shown in Fig. 7 as 3-D plots, illustrating dependence of the squared harmonic flux rms on the value of the reference space vector (described by the modulation index and angular position) over one sector (span of 36°). It can be seen that both SVPWM schemes are with unique and different characteristics in each of the two planes, which is the consequence of the different space vectors used for the implementation.

By comparing the vertical axes of the 3-D plots in the d_1–q_1 plane, it can be observed that SVPWM (2L+2M) has significantly lower values of the squared harmonic flux than SVPWM (4L), with peak values appearing around $M = 0.6$, which are followed by a decrease as the modulation index

$$\Delta\lambda^2_{abcde-RMS1} = \frac{5}{6}\left[\delta_0\left[\Delta\lambda^2_{d1}(t_1)+\Delta\lambda^2_{q1}(t_1)\right]\right.$$
$$+\delta_I\left[\Delta\lambda^2_{d1}(t_1)+\Delta\lambda_{d1}(t_1)\Delta\lambda_{d1}(t_2)+\Delta\lambda^2_{d1}(t_2)+\Delta\lambda^2_{q1}(t_1)+\Delta\lambda_{q1}(t_1)\Delta\lambda_{q1}(t_2)+\Delta\lambda^2_{q1}(t_2)\right]$$
$$+\delta_{II}\left[\Delta\lambda^2_{d1}(t_2)+\Delta\lambda_{d1}(t_2)\Delta\lambda_{d1}(t_3)+\Delta\lambda^2_{d1}(t_3)+\Delta\lambda^2_{q1}(t_2)+\Delta\lambda_{q1}(t_2)\Delta\lambda_{q1}(t_3)+\Delta\lambda^2_{q1}(t_3)\right]$$
$$+\delta_{III}\left[\Delta\lambda^2_{d1}(t_3)+\Delta\lambda_{d1}(t_3)\Delta\lambda_{d1}(t_4)+\Delta\lambda^2_{d1}(t_4)+\Delta\lambda^2_{q1}(t_3)+\Delta\lambda_{q1}(t_3)\Delta\lambda_{q1}(t_4)+\Delta\lambda^2_{q1}(t_4)\right]$$
$$+\delta_{IV}\left[\Delta\lambda^2_{d1}(t_4)+\Delta\lambda_{d1}(t_4)\Delta\lambda_{d1}(t_5)+\Delta\lambda^2_{d1}(t_5)+\Delta\lambda^2_{q1}(t_4)+\Delta\lambda_{q1}(t_4)\Delta\lambda_{q1}(t_5)+\Delta\lambda^2_{q1}(t_5)\right]$$
$$\left.+\delta_{31}\left[\Delta\lambda^2_{d1}(t_5)+\Delta\lambda^2_{q1}(t_5)\right]\right] \quad (12)$$

$$\Delta\lambda^2_{abcde-RMS2} = \frac{5}{6}\left[\delta_1\left[\Delta\lambda^2_{d2}(t_2)+\Delta\lambda^2_{q2}(t_2)\right]\right.$$
$$+\delta_{II}\left[\Delta\lambda^2_{d2}(t_2)+\Delta\lambda_{d2}(t_2)\Delta\lambda_{d2}(t_3)+\Delta\lambda^2_{d2}(t_3)+\Delta\lambda^2_{q2}(t_2)+\Delta\lambda_{q2}(t_2)\Delta\lambda_{q2}(t_3)+\Delta\lambda^2_{q2}(t_3)\right]$$
$$+\delta_{III}\left[\Delta\lambda^2_{d2}(t_3)+\Delta\lambda_{d2}(t_3)\Delta\lambda_{d2}(t_4)+\Delta\lambda^2_{d2}(t_4)+\Delta\lambda^2_{q2}(t_3)+\Delta\lambda_{q2}(t_3)\Delta\lambda_{q2}(t_4)+\Delta\lambda^2_{q2}(t_4)\right]$$
$$\left.+\delta_{IV}\left[\Delta\lambda^2_{d2}(t_4)+\Delta\lambda^2_{q2}(t_4)\right]\right] \quad (13)$$

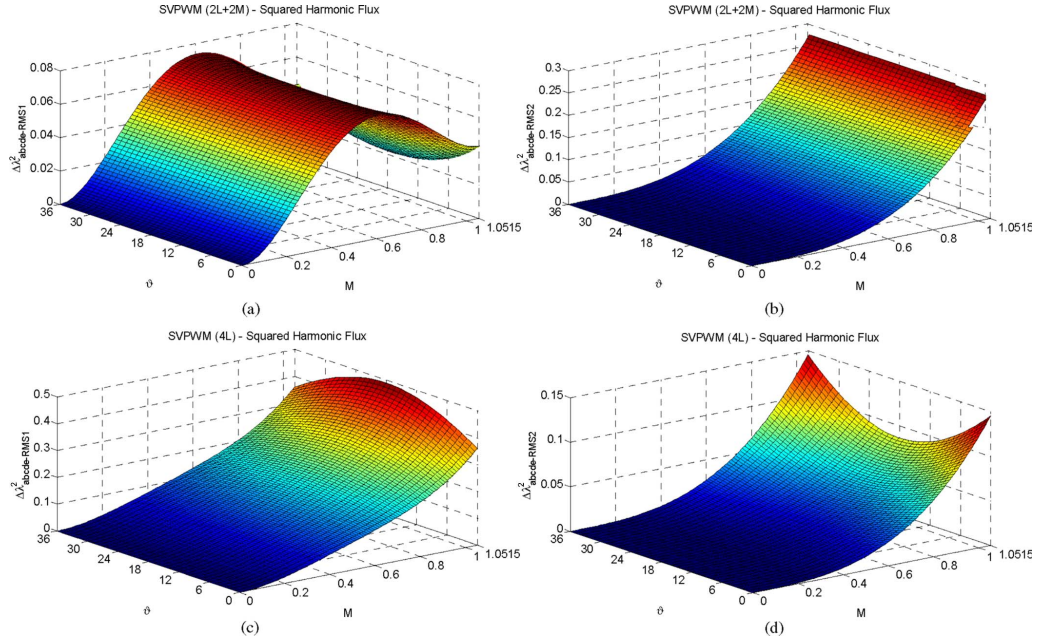

Fig. 7. Squared harmonic flux of the SVPWM (2L+2M) in the (a) d_1–q_1 plane and (b) d_2–q_2 plane and of the SVPWM (4L) in the (c) d_1–q_1 plane and (d) d_2–q_2 plane.

increases toward the maximum value. Squared harmonic flux rms of the SVPWM (4L) is with an ever increasing characteristic as a function of the modulation index. On the other hand, comparison of the 3-D plots in the d_2–q_2 plane reveals that squared harmonic flux rms of the SVPWM (4L) is actually with lower values than the one of the SVPWM (2L+2M). However, differences in values of the squared harmonic flux of two SVPWM schemes in the d_2–q_2 plane are much smaller than the differences in the d_1–q_1 plane.

V. Flux HDFs

Finally, in order to obtain flux HDFs in each of the planes, squared harmonic flux has to be integrated over the fundamental

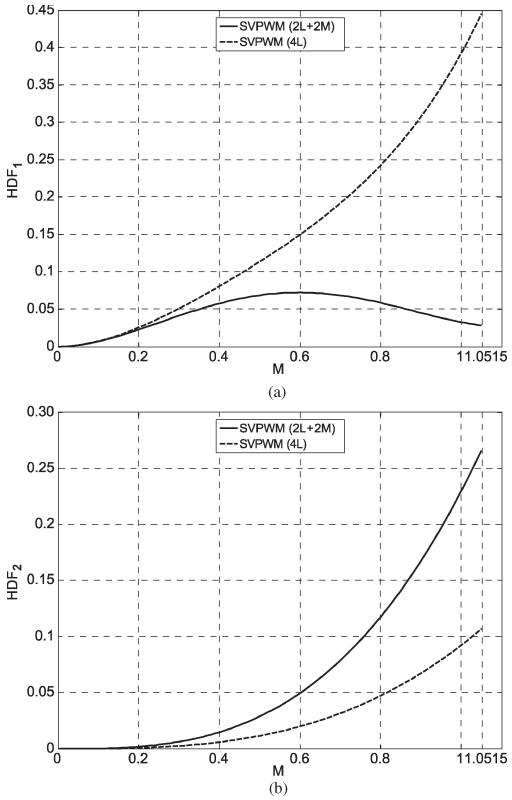

Fig. 8. HDFs of the SVPWM schemes in the (a) d_1–q_1 plane and (b) d_2–q_2 plane.

period. Due to the symmetry which exists in the system, it is enough to perform integration over the first sector only

$$HDF = \Delta\lambda^2_{abcde-RMSF} = \frac{5}{\pi}\int_0^{\pi/5} \Delta\lambda^2_{abcde-RMS} d\vartheta. \quad (14)$$

Polynomial closed-form solution of (14) is not always easy to express in short and compact form, as it is demonstrated in [28] and [29]. Therefore, in this paper, HDFs of analyzed SVPWM schemes are obtained by numerical integration of (14) in Matlab and are shown in Figs. 8 and 9 for (2L+2M) and (4L) SVPWMs, respectively.

It can be seen from Fig. 8 that, in the d_1–q_1 plane, SVPWM (2L+2M) has a significantly lower flux HDF (as the modulation index increases) compared to the SVPWM (4L). However, in the d_2–q_2 plane, the situation is reversed, but with much smaller differences between the two SVPWM schemes. This is in agreement with the results and comments given in relation to 3-D plots of the squared harmonic flux, since in essence, HDF represents the average value of the squared harmonic flux. It also supports the intuitive reasoning that the application of only

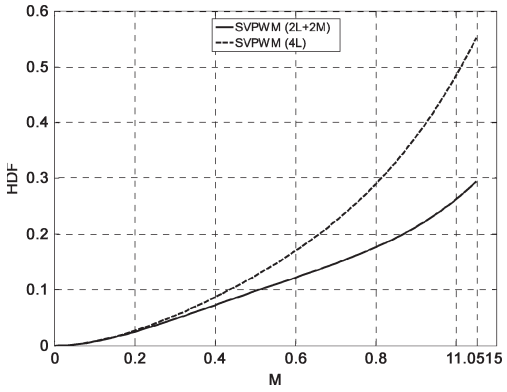

Fig. 9. Total HDFs of two SVPWM schemes.

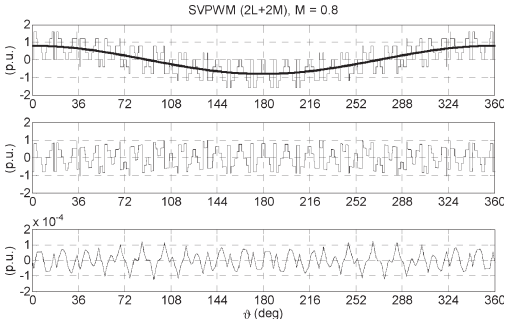

Fig. 10. Simulation results for SVPWM (2L+2M) for $M = 0.8$ at 50 Hz: (Top) Switched phase voltage and reference, (middle) error voltage, and (bottom) current ripple.

small space vectors in the d_2–q_2 plane with SVPWM (4L) will have a smaller impact on the ripple than the application of small and medium vectors with SVPWM (2L+2M). Similar applies to the d_1–q_1 plane, where use of only large space vectors with SVPWM (4L) causes higher HDF values in that plane.

Finally, summation of the HDFs of the two planes in Fig. 8 yields the total flux HDF, which is shown in Fig. 9. Total flux HDF reveals lower values and, thus, a better characteristic for the SVPWM (2L+2M) scheme, when compared to the SVPWM (4L) method, particularly at higher values of the modulation index. It should be noted here that HDFs shown in Figs. 8 and 9 are the total HDFs of the five-phase system for each SVPWM scheme. Per-phase flux HDFs are easily obtainable by dividing the total HDF in Fig. 9 with the number of phases (i.e., five in this case).

VI. Simulation Results

Some simulation results are provided in this section to support theoretical considerations. Simulations are carried out in Matlab for both SVPWM schemes, and only the results for the case of $M = 0.8$ are shown in Figs. 10 and 11. Switching frequency is set to 1 kHz with the fundamental frequency equal

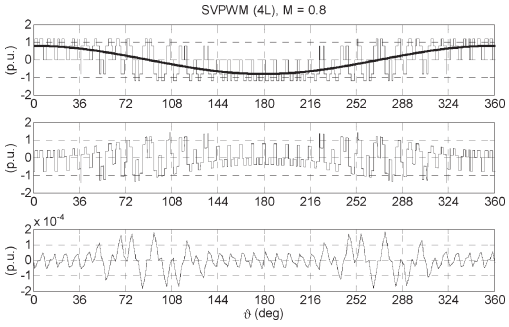

Fig. 11. Simulation results for SVPWM (4L) for $M = 0.8$ at 50 Hz: (Top) Switched phase voltage and reference, (middle) error voltage, and (bottom) current ripple.

TABLE II
COMPARISON OF THE VALUES OF THE CURRENT RIPPLE RMS SQUARED CALCULATED BY NUMERICAL INTEGRATION AND BY USING THE FLUX HDFS

	2L+2M	4L
Total HDF from Fig. 9	0.175	0.2965
Per-phase HDF	0.035	0.0593
I^2_{RMS} using (15)	0.2188e-08	0.3706e-08
I^2_{RMS} (numerical integration using Figs. 10 and 11 traces)	0.2269e-08	0.3798e-08

to 50 Hz. In accordance with Table I and normalization factor of (9), $V_{\mathrm{dc}}/2$ is set to 1 per unit. Figs. 10 and 11 show, in the upper part, switched phase voltage (obtained after subtraction of common mode voltage from the leg voltage) together with the reference (sinusoidal) phase voltage. Based on this, error voltages are determined and applied to a pure integrator, so that the current ripple is obtained (bottom parts of Figs. 10 and 11).

It should be noted that the applied simulation procedure, being based on the phase voltage, assumes that a single inductance value can be used in (5). Thus, the results given here for the current ripple are applicable in five-phase motor drives if and only if the inductance relevant for the switching harmonics in the two planes can be regarded as being the same (for example, a permanent magnet synchronous machine).

Based on the simulation results, several observations can be made. First, it is visible from the time-domain traces in Figs. 10 and 11 that the current ripple of the SVPWM (4L) scheme has higher peak excursions, which can be associated with sectors in which an increased number of commutations occur. Although outside of these intervals the current ripple of the SVPWM (4L) appears to be smaller, it has been already shown that the final HDF is actually worse than that of the SVPWM (2L+2M) scheme. This is further confirmed by using the following calculations, the summary of which is given in Table II.

Using "rms" function in Matlab, the current ripple rms squared is calculated for the current ripple waveforms in Figs. 10 and 11. The values for the two SVPWM techniques are given in the last row of Table II.

The square of the current ripple rms can be calculated directly using the correlation between the current and the flux ripple (5) and the introduced normalization factor for the flux ripple (9). As the inductance of the two planes is the same in the simulations (1 per unit), then the relationship between I^2_{RMS} and the total flux HDF is governed with

$$I^2_{\mathrm{RMS}} = \left(\frac{V_{\mathrm{dc}} T_s}{8}\right)^2 \frac{1}{L^2_\sigma}(HDF_1 + HDF_2) = A \cdot HDF \tag{15}$$

where the HDF values of the two SVPWMs are one-fifth of the values in Figs. 8 and 9 at $M = 0.8$. The scaling constant A in (15) is for 1-kHz switching frequency and $V_{\mathrm{dc}}/2 = 1$ per unit given with $A = 6.25e - 8$. Multiplication of the constant with the per-phase HDFs in the third row of Table II yields the square of the current ripple rms in the fourth row. Comparison of the two sets of current ripple rms squared shows an excellent agreement of the theoretically predicted and numerically calculated values. This verifies correctness of the developed flux HDFs for the two SVPWM methods. The results in Table II also show that, under the condition of the equal inductance in the two planes, SVPWM (4L) will give a significantly higher current ripple rms.

VII. CONCLUSION

Analysis of the switching ripple characteristics of two continuous SVPWM techniques for five-phase VSIs, aimed at sinusoidal output voltage generation, has been reported in this paper. In particular, determination of the flux HDFs has been considered. It is shown that, although SVPWM (4L) is characterized with a smaller flux HDF in the second plane, it simultaneously has a considerably higher flux HDF in the first plane. As a result, the total flux HDF of the SVPWM (4L) is considerably higher than the one of the SVPWM (2L+2M) for all modulation indices above approximately 0.2.

The behavior of the total flux HDF is directly reflected in the behavior of the current ripple only if the inductance relevant for the current ripple is the same in the two planes of the five-phase system, as shown by simulations. This is, however, rarely the case, and the current ripple is therefore considered in much more detail in Part 2 of this paper.

Since the SVPWM (4L) method is more difficult for implementation and is also characterized by the higher average switching frequency, it can be concluded that it should not be used in drive systems where the machine is characterized with the same inductance, relevant for the current ripple, in the two planes.

REFERENCES

[1] E. Levi, R. Bojoi, F. Profumo, H. A. Toliyat, and S. Williamson, "Multiphase induction motor drives—A technology status review," *IET Electr. Power Appl.*, vol. 1, no. 4, pp. 489–516, Jul. 2007.

[2] E. Levi, "Multiphase electric machines for variable-speed applications," *IEEE Trans. Ind. Electron.*, vol. 55, no. 5, pp. 1893–1909, May 2008.

[3] O. Lopez, J. Alvarez, J. Doval-Gandoy, and F. D. Freijedo, "Multilevel multiphase space vector PWM algorithm," *IEEE Trans. Ind. Electron.*, vol. 55, no. 5, pp. 1933–1942, May 2008.

[4] Y. Zhao and T. A. Lipo, "Space vector PWM control of dual three-phase induction machine using vector space decomposition," *IEEE Trans. Ind. Appl.*, vol. 31, no. 5, pp. 1100–1109, Sep./Oct. 1995.

[5] P. S. N. de Silva, J. E. Fletcher, and B. W. Williams, "Development of space vector modulation strategies for five-phase voltage source inverters," in *Proc. IEE PEMD Conf.*, Edinburgh, U.K., 2004, pp. 650–655.

[6] A. Iqbal, E. Levi, M. Jones, and S. N. Vukosavić, "Generalised sinusoidal PWM with harmonic injection for multi-phase VSIs," in *Proc. IEEE Power Electron. Spec. Conf.*, Jeju, Korea, 2006, pp. 2871–2877.

[7] A. Iqbal and E. Levi, "Space vector PWM techniques for sinusoidal output voltage generation with a five-phase voltage source inverter," *Electr. Power Compon. Syst.*, vol. 34, no. 2, pp. 119–140, Feb. 2006.

[8] D. Dujic, E. Levi, M. Jones, G. Grandi, G. Serra, and A. Tani, "Continuous PWM techniques for sinusoidal voltage generation with seven-phase voltage source inverters," in *Proc. IEEE Power Electron. Spec. Conf.*, Orlando, FL, 2007, pp. 47–52.

[9] D. Dujic, M. Jones, and E. Levi, "Space vector PWM for nine-phase VSI with sinusoidal output voltage generation: Analysis and implementation," in *Proc. IEEE IECON*, Taipei, Taiwan, 2007, pp. 1524–1529.

[10] J. W. Kelly, E. G. Strangas, and J. M. Miller, "Multiphase space vector pulse width modulation," *IEEE Trans. Energy Convers.*, vol. 18, no. 2, pp. 259–264, Jun. 2003.

[11] A. Lega, M. Mengoni, G. Serra, A. Tani, and L. Zarri, "Space vector modulation for multiphase inverters based on a space partitioning algorithm," *IEEE Trans. Ind. Electron.*, vol. 56, no. 10, pp. 4119–4131, Oct. 2009.

[12] D. Casadei, D. Dujić, E. Levi, G. Serra, A. Tani, and L. Zarri, "General modulation strategy for seven-phase inverters with independent control of multiple voltage space vectors," *IEEE Trans. Ind. Electron.*, vol. 55, no. 5, pp. 1921–1932, May 2008.

[13] D. Dujic, G. Grandi, M. Jones, and E. Levi, "A space vector PWM scheme for multi-frequency output voltage generation with multiphase voltage source inverters," *IEEE Trans. Ind. Electron.*, vol. 55, no. 5, pp. 1943–1955, May 2008.

[14] D. C White and H. H. Woodson, *Electromechanical Energy Conversion*. New York: Wiley, 1959.

[15] D. G. Holmes and T. A. Lipo, *Pulse Width Modulation for Power Converters—Principles and Practice*. Piscataway, NJ: IEEE Press, 2003, ser. IEEE Press Series on Power Engineering.

[16] S. Xue and X. Wen, "Simulation analysis of two novel multiphase SVPWM strategies," in *Proc. IEEE ICIT*, Hong Kong, 2005, pp. 1401–1406.

[17] S. Xue, X. Wen, and Z. Feng, "A novel multi-dimensional SVPWM strategy of multiphase motor drives," in *Proc. Int. EPE-PEMC*, Portoroz, Slovenia, 2006, pp. 931–935.

[18] H. W. Van der Broeck and H. C. Skudelny, "Analytical analysis of the harmonic effects of a PWM AC drive," *IEEE Trans. Power Electron.*, vol. 3, no. 2, pp. 216–223, Apr. 1988.

[19] J. W. Kolar, H. Ertl, and F. C. Zach, "Influence of the modulation method on the conduction and switching losses of a PWM converter system," *IEEE Trans. Ind. Appl.*, vol. 27, no. 6, pp. 1063–1075, Nov./Dec. 1991.

[20] J. W. Kolar, H. Ertl, and F. C. Zach, "Analytically closed optimization of the modulation method of a PWM rectifier system with a high pulse rate," in *Proc. Int. PCIM Conf.*, Munich, Germany, 1990, pp. 209–223.

[21] S. Fukuda and K. Suzuki, "Harmonic evaluation of carrier-based PWM methods using harmonic distortion determining factor," in *Proc. PCC*, Nagaoka, Japan, 1997, pp. 259–264.

[22] V. Blasko, "Analysis of a hybrid PWM based on modified space-vector and triangle-comparison methods," *IEEE Trans. Ind. Appl.*, vol. 33, no. 3, pp. 756–764, May/Jun. 1997.

[23] A. M. Hava, R. Kerkman, and T. A. Lipo, "Simple analytical and graphical methods for carrier-based PWM-VSI drives," *IEEE Trans. Power Electron.*, vol. 14, no. 1, pp. 49–61, Jan. 1999.

[24] Q. Yin, R. J. Kerkman, T. A. Nondahl, and H. Lu, "Analytical investigation of the switching frequency harmonic characteristic for common mode reduction modulator," in *Conf. Rec. IEEE IAS Annu. Meeting*, Hong Kong, 2005, pp. 1398–1405.

[25] G. Narayanan and V. T. Ranganathan, "Analytical evaluation of harmonic distortion in PWM AC drives using the notion of stator flux ripple," *IEEE Trans. Power Electron.*, vol. 20, no. 2, pp. 466–474, Mar. 2005.

[26] P. A. Dahono, "Analysis and minimization of output current ripple of multiphase PWM inverters," in *Proc. IEEE Power Electron. Spec. Conf.*, Jeju, Korea, 2006, pp. 3024–3029.

[27] P. A. Dahono and Deni, "Analysis and minimization of output current ripple of five-phase PWM inverters," in *Proc. ICEM*, Chania, Greece, 2006.

[28] D. Dujic, M. Jones, and E. Levi, "Analysis of output current ripple rms in multiphase drives using space vector approach," *IEEE Trans. Power Electron.*, vol. 24, no. 8, pp. 1926–1938, Aug. 2009.

[29] D. Dujic, M. Jones, and E. Levi, "Analysis of output current ripple rms in multi-phase drives using polygon approach," *IEEE Trans. Power Electron.*, vol. 25, no. 7, pp. 1838–1849, Jul. 2010.

[30] S. Halasz, "PWM strategies of multi-phase inverters," in *Proc. IEEE IECON*, Orlando, FL, 2008, pp. 916–921.

[31] S. Halasz, "Discontinuous modulation of multiphase inverter-fed AC motor," in *Proc. Eur. Conf. Power Electron. Appl., EPE*, Barcelona, Spain, 2009.

[32] K. Marouani, L. Baghli, D. Hadiouche, A. Kheloui, and A. Rezzoug, "A new PWM strategy based on 24-sector vector space decomposition for a six-phase VSI-fed dual stator induction motor," *IEEE Trans. Ind. Electron.*, vol. 5, no. 5, pp. 1910–1920, May 2008.

Drazen Dujic (S'03–M'09) received the Dipl. Ing. and M.Sc. degrees from the University of Novi Sad, Novi Sad, Serbia, in 2002 and 2005, respectively, and the Ph.D. degree from Liverpool John Moores University, Liverpool, U.K., in 2008.

From 2002 to 2006, he was a Research Assistant with the Department of Electrical Engineering, University of Novi Sad, and from 2006 to 2009, he was a Research Associate with Liverpool John Moores University. He is currently with ABB Corporate Research Centre, Baden-Dättwil, Switzerland. His main research interests are in the areas of design and control of advanced power electronics systems and high-performance drives.

Martin Jones (M'07) received the B.Eng. degree (first class honors) and the Ph.D. degree from Liverpool John Moores University, Liverpool, U.K., in 2001 and 2005, respectively.

From September 2001 to spring 2005, he was a Research Student with Liverpool John Moores University, where he is currently a Senior Lecturer.

Dr. Jones was a recipient of the IEE Robinson Research Scholarship for his Ph.D. studies.

Emil Levi (S'89–M'92–SM'99–F'09) received the M.Sc. and Ph.D. degrees from the University of Belgrade, Belgrade, Serbia, in 1986 and 1990, respectively.

From 1982 to 1992, he was with the Department of Electrical Engineering, University of Novi Sad, Novi Sad, Serbia. In May 1992, he joined Liverpool John Moores University, Liverpool, U.K., where he has been a Professor of electric machines and drives since September 2000.

Dr. Levi serves as Co-Editor-in-Chief of the IEEE TRANSACTIONS ON INDUSTRIAL ELECTRONICS, as an Editor of the IEEE TRANSACTIONS ON ENERGY CONVERSION, and as Editor-in-Chief of the IET Electric Power Applications. He was the recipient of the Cyril Veinott award of the IEEE Power and Energy Society for 2009.

Joel Prieto (S'10) received the B.Eng. degree in electronic engineering from the Universidad Católica Nuestra Señora de la Asunción, Asunción, Paraguay, in 2005 and the M.Sc. degree from the University of Seville, Seville, Spain, in 2009, where he is currently working toward the Ph.D. degree.

Since 2008, he has been with the Electronic Engineering Department, University of Seville.

Mr. Prieto is a recipient of a scholarship from Itaipu Binacional/Parque Tecnológico Itaipu-Py for his Ph.D. studies.

Federico Barrero (M'04–SM'05) was born in Seville, Spain, in 1967. He received the M.Sc. and Ph.D. degrees in electrical and electronic engineering from the University of Seville, Seville, Spain, in 1992 and 1998, respectively.

In 1992, he joined the Electronic Engineering Department, University of Seville, where he is currently an Associate Professor. His recent interests include microprocessor and DSP systems, and control of multiphase ac drives.

3.2. Paper 2

Authors: M. Jones, D. Dujic, E. Levi, J. Prieto y F. Barrero.
Title: Switching Ripple Characteristics of Space Vector PWM Schemes for Five-Phase Two-Level Voltage Source Inverters-Part 2.
Journal: IEEE Transactions on Industrial Electronics.
Volume: 58.
Number: 7.
Pages: 2799-2808.
Date: July 2011.
Abstract: Flux harmonic distortion factors (HDFs) of two space vector pulse width modulation (SVPWM) schemes, aimed at sinusoidal output voltage generation with five-phase voltage source inverters, have been evaluated in Part 1 of this paper. Analytical considerations and numerical integration have been applied in order to determine the switching properties of the considered SVPWM methods. It has been shown that the SVPWM based on four large vectors leads to a considerably higher overall per-phase flux HDF than the method based on two large and two medium space vectors. The purpose of the second part of the paper is to relate flux HDFs to the current ripple and current total harmonic distortion and thus explore further switching characteristics of the two SVPWM techniques. The applied approach is based on simulation and experimentation, in conjunction with the subsequent fast Fourier transform of the waveforms, so that all the results for the ripple are obtained using a methodology completely different from the one in Part 1. Relationships that correlate the current ripple and the flux HDFs are established, and it is further shown that the current ripple can be easily calculated from the flux HDF values of Part 1 if the relevant leakage inductances of the two planes are known. Hence, the complete theory of Part 1 is fully verified by both simulation and experimentation. It is also shown that, in certain cases, the SVPWM based on four large vectors may lead to a smaller current ripple despite a considerably higher flux HDF.

IEEE TRANSACTIONS ON INDUSTRIAL ELECTRONICS, VOL. 58, NO. 7, JULY 2011 2799

Switching Ripple Characteristics of Space Vector PWM Schemes for Five-Phase Two-Level Voltage Source Inverters—Part 2: Current Ripple

Martin Jones, *Member, IEEE*, Drazen Dujic, *Member, IEEE*, Emil Levi, *Fellow, IEEE*, Joel Prieto, *Student Member, IEEE*, and Federico Barrero, *Senior Member, IEEE*

***Abstract*—Flux harmonic distortion factors (HDFs) of two space vector pulse width modulation (SVPWM) schemes, aimed at sinusoidal output voltage generation with five-phase voltage source inverters, have been evaluated in Part 1 of this paper. Analytical considerations and numerical integration have been applied in order to determine the switching properties of the considered SVPWM methods. It has been shown that the SVPWM based on four large vectors leads to a considerably higher overall per-phase flux HDF than the method based on two large and two medium space vectors. The purpose of the second part of the paper is to relate flux HDFs to the current ripple and current total harmonic distortion and thus explore further switching characteristics of the two SVPWM techniques. The applied approach is based on simulation and experimentation, in conjunction with the subsequent fast Fourier transform of the waveforms, so that all the results for the ripple are obtained using a methodology completely different from the one in Part 1. Relationships that correlate the current ripple and the flux HDFs are established, and it is further shown that the current ripple can be easily calculated from the flux HDF values of Part 1 if the relevant leakage inductances of the two planes are known. Hence, the complete theory of Part 1 is fully verified by both simulation and experimentation. It is also shown that, in certain cases, the SVPWM based on four large vectors may lead to a smaller current ripple despite a considerably higher flux HDF.**

***Index Terms*—Current ripple, multiphase drives, space vector pulse width modulation (SVPWM), voltage source inverters (VSIs).**

I. Introduction

STUDIES aimed at obtaining the input/output harmonic contents caused by the pulse width modulation (PWM) operation of three-phase power converters have frequently been conducted by means of computer-aided analysis [1]–[3]. This approach is tedious since it requires a multitude of simulations in order to cover a broad range of operating conditions. Nevertheless, it is regarded in this paper as the most appropriate for the purpose of verifying the correctness of the theoretical considerations and results given in [4] for two space vector PWM (SVPWM) techniques of a five-phase voltage source inverter (VSI) (both aimed at sinusoidal output voltage generation) since it means that the methodology used in this paper is completely different from the one used in [4]. Thus, the analysis in this paper is based on the fast Fourier transform (FFT) of time-domain waveforms, which are obtained by simulation and experimentation.

A number of different continuous PWM techniques for multiphase two-level VSIs have been developed recently [5]–[10]. They can be of the carrier type or space vector type, and the required output voltage may be a single frequency (i.e., pure sinusoidal) or multifrequency. The two PWM techniques for five-phase VSIs, encompassed by this study, are of the space vector type and are aimed at the sinusoidal output voltage generation. They mutually differ with regard to the selection of the active space vectors used to synthesize the reference. The first SVPWM method is based on the application of two large and two medium $(2\mathrm{L} + 2\mathrm{M})$ space vectors per switching period while the second SVPWM technique applies four large (4L) space vectors per switching period. Both active vector selection strategies lead to the same dc bus utilization in the linear modulation region.

As shown in [4], the different selection of active space vectors inherently leads to a different behavior with regard to one of the performance indicators, which is used to assess the quality of the output waveforms, the flux HDF. However, even when the set of applied active space vectors is the same, the flux HDF will differ depending on the type of zero-sequence injection that is used [11], [12]. In [11], a flux HDF was analytically determined for three PWM methods aimed at sinusoidal output voltage generation with a five-phase VSI: sinusoidal PWM, fifth harmonic injection PWM, and SVPWM $(2\mathrm{L} + 2\mathrm{M})$. The approach in [11] is based on vector space decomposition into two planes, thus allowing the determination of, initially, per-plane flux HDFs and, subsequently, per-phase flux HDFs. A vector space decomposition approach is also used in [4] in relation to the two SVPWM techniques considered in this paper. However, the analytical derivations have been replaced by numerical integration in contrast to [11].

An alternative approach is based on the original domain and consideration of polygon connections, which is similar to the use of delta connection in three-phase systems [3]. It has been developed in [12] for a general multiphase (n-phase) system

Manuscript received February 4, 2010; revised May 7, 2010; accepted August 3, 2010. Date of publication August 30, 2010; date of current version June 15, 2011.

M. Jones and E. Levi are with the School of Engineering, Liverpool John Moores University, L3 3AF Liverpool, U.K. (e-mail: m.jones2@ljmu.ac.uk; e.levi@ljmu.ac.uk).

D. Dujic is with the ABB Corporate Research Center, 5400 Baden-Dättwil, Switzerland (e-mail: drazen.dujic@ieee.org).

J. Prieto and F. Barrero are with the Electronic Engineering Department, University of Seville, 41092 Seville, Spain (e-mail: jprieto@esi.us.es; fbarrero@esi.us.es).

Digital Object Identifier 10.1109/TIE.2010.2070778

with an odd number of phases, for the sinusoidal PWM and sinusoidal PWM with the nth harmonic injection. The analyses and findings of [12] have fully verified the results of [11] for the particular (five-phase) case. The most important conclusion of [12] is that the total flux HDF can only be obtained by means of the polygon approach if the HDFs of individual polygons are all at first determined and then accounted for in the total flux HDF evaluation. The results reported in [11] and [12] clearly show that the same value of a per-phase flux HDF results with both the vector space decomposition approach and the polygon approach, provided that all possible polygon connections of a multiphase system are accounted for. This is something that, unfortunately, has not been recognized in [13] and [14], where an attempt to evaluate the output current ripple of a five-phase inverter has been reported, since only a single adjacent polygon connection has been encompassed by the analysis. As a consequence, flux HDF values and squared rms current ripple values in [13] and [14] are only a part of the complete solution rather than the total flux HDF and the total squared rms current ripple.

Another important property of multiphase machines is that the leakage inductances, relevant for the switching harmonics and corresponding current ripple, have, in general, different values in different 2-D planes, which result after the vector space decomposition. As a consequence, the current ripple has to be calculated using the flux HDFs of individual planes, as explained in this paper. This also means that, if the total per-phase flux HDF is obtained for a particular PWM method and a given number of phases using the polygon approach, the calculation of the current ripple requires a conversion from the polygon to plane flux HDFs. The procedure is explained in [12] and is, in essence, a consequence of the fact that an n-phase system ($n =$ odd) is characterized with $(n-1)/2$ sets of different line voltages. The leakage inductances relevant for the current ripple are different on a per-plane basis; however, if polygon connections are used, then it is not possible to define the corresponding per-polygon leakage inductances due to the complicated relationships between the phase- and line-voltage harmonics [12], [15]. Thus, the direct calculation of the current ripple from the polygon flux HDF, as attempted in [13] and [14], is, in essence, not possible for any multiphase machine with different leakage inductances of the planes.

Since the calculation of the current ripple and the total harmonic distortion (THD) has to be always directly related to the individual plane HDFs, the vector space decomposition approach has been followed in [4] and in this paper. The same SVPWM techniques, reviewed in [4], are studied. In what follows, harmonic mapping in the five-phase system is addressed first, with the emphasis placed on the mapping of the even harmonics. The basic definitions are further given, and the functional dependences of the current THD and current ripple on flux HDFs are established. Special emphasis is placed on the need to utilize different leakage inductances in individual planes of the multiphase system in the process of the current ripple calculation. The results of the simulations and experiments are further reported. It is shown that the flux HDFs, obtained in [4], enable an exceptionally accurate prediction of the current ripple, provided that the leakage inductances of all planes are known with a sufficient accuracy.

In terms of the comparison of the two SVPWM techniques, it is shown that the (4L) method, although characterized with a substantially higher flux HDF and voltage THD, can actually lead to a lower current ripple than the (2L + 2M) method. This is the direct consequence of the different leakage inductances in the two planes, presented to the switching harmonics.

II. Properties of a Five-Phase System

A. Harmonic Mapping in a Five-Phase System

A set of five-phase quantities can be decomposed using the Clarke's decoupling transformation ($\varphi = 2\pi/5$)

$$\underline{C}_5 = \frac{2}{5}\begin{bmatrix} 1 & \cos(\varphi) & \cos(2\varphi) & \cos(3\varphi) & \cos(4\varphi) \\ 0 & \sin(\varphi) & \sin(2\varphi) & \sin(3\varphi) & \sin(4\varphi) \\ 1 & \cos(2\varphi) & \cos(4\varphi) & \cos(\varphi) & \cos(3\varphi) \\ 0 & \sin(2\varphi) & \sin(4\varphi) & \sin(\varphi) & \sin(3\varphi) \\ 1/2 & 1/2 & 1/2 & 1/2 & 1/2 \end{bmatrix} \quad (1)$$

into a new set of variables, which belong to two mutually perpendicular planes labeled further on as d_1–q_1 and d_2–q_2. The fifth variable, the zero-sequence component, can be omitted from further consideration due to the star connection of the winding with the isolated neutral point.

An important property of (1) is that it provides clear mapping of the harmonics of different orders into different 2-D planes. Harmonic mapping rules are established by applying the procedure of [16] and are well known for a five-phase system in relation to odd harmonics. In particular, the following applies ($k = 0, 1, 2, 3, \ldots$):

$$\begin{aligned} d_1 - q_1 \qquad & \nu = 10k \pm 1 \\ d_2 - q_2 \qquad & \nu = 10k \pm 3. \end{aligned} \quad (2)$$

Consider next the switching harmonics of a PWM method. These can be given in a general form as

$$\nu_{\text{sw}} = \pm NF \pm l \quad (3)$$

where $F = f_{\text{sw}}/f_1$ is the ratio of the switching frequency to the fundamental frequency, N is a positive integer defining the sideband (SB), and l is a positive integer which determines the position of a particular harmonic in the given SB N [3], [15]. The dominant SB harmonics in the first three SBs are the following [3], [15]:

$$\begin{aligned} &\text{SB1}(N=1) \qquad l = \pm 2 \\ &\text{SB2}(N=2) \qquad l = \pm 1 \text{ and } l = \pm 3 \\ &\text{SB3}(N=3) \qquad l = \pm 2. \end{aligned} \quad (4)$$

If the frequency ratio F is an odd number, then all harmonics of (4) are odd and the harmonic mapping of (2) suffices. However, if the frequency ratio F is an even number, then the odd SBs ($N = 1, 3, \ldots$) contain the even harmonics as the dominant ones. Hence, the even harmonic mapping into the two d–q planes is required in addition to (2).

By applying the harmonic mapping procedure detailed in [16] onto the even harmonics in a five-phase system, it can be shown that the even harmonics map into d–q planes according to the following rules:

$$\begin{aligned} d_1 - q_1 \qquad & \nu = 10k \pm 4 \\ d_2 - q_2 \qquad & \nu = 10k \pm 2. \end{aligned} \tag{5}$$

Harmonics of the order $10k \pm 5$ are the zero-sequence harmonics.

B. Basic Definitions

Modulation index M is again defined as $M = V_1/(V_{\rm dc}/2)$, where V_1 is the peak value of the phase voltage fundamental.

The THD of a phase variable x (voltage or current) is defined as

$$\text{THD}_x = \sqrt{\sum_{\nu=2}^{\infty} X_\nu^2} \Big/ X_1. \tag{6}$$

If the inverter is operated in an open-loop V/f mode, then the inverter dead-time effect leads to the flow of low-order odd current harmonics, which map into the second d–q plane [17]. Since these harmonics are not related to the inverter switching behavior, the THD is calculated in all cases where the dead time exists (experiments and certain simulations) by summing the harmonics in (6) above the tenth.

The THD of the phase voltage or current is related to the corresponding THDs in the two planes of a five-phase system, on the basis of (1), through

$$\text{THD}_x = \sqrt{\text{THD}_{x(d_1-q_1)}^2 + \text{THD}_{x(d_2-q_2)}^2}. \tag{7}$$

The squared harmonic ripple rms value of the phase voltage or current is related to the corresponding THD through

$$X_{\rm rms}^2 = \text{THD}_x^2 X_1^2. \tag{8}$$

III. Correlation Between Current THD and Flux HDF

In a three-phase machine, there is a single inductance relevant for the switching harmonics. This is, however, in general, not the case in multiphase machines. Recall the flux ripple definition in terms of the current ripple and the flux normalization factor introduced in [4] in the process of flux HDF development

$$\Delta\bar{\lambda} = L_\sigma \Delta\bar{i} \tag{9}$$

$$\Delta\lambda_N = L_\sigma \Delta i_N = V_{\rm dc} T_s/8 \tag{10}$$

where L_σ is the equivalent inductance for the switching harmonics. If the equivalent inductance in the two planes is the same, the current ripple and the total flux HDF are related in a simple manner, as already shown in [4]

$$I_{\rm rms}^2 = \left(\frac{V_{\rm dc} T_s}{8}\right)^2 \frac{1}{L_\sigma^2} \text{HDF} = A \cdot \text{HDF} \tag{11}$$

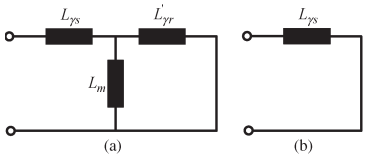

Fig. 1. Equivalent circuit of a five-phase induction machine in (a) d_1–q_1 and (b) d_2–q_2 planes for current THD analysis (L_m = magnetizing inductance and $L_{\gamma s}$ and $L_{\gamma r}$' = stator and rotor leakage inductances, respectively).

where HDF stands for the total per-phase flux HDF of a given PWM method for a certain modulation index value. Hence, the current THD can be given, using (6), (8), and (11), as

$$\text{THD}_i = \left(\frac{V_{\rm dc} T_s}{8}\right) \frac{1}{L_\sigma} \frac{\sqrt{\text{HDF}}}{I_1}. \tag{12}$$

Correlation (12) may suffice for some types of multiphase permanent magnet synchronous machines (for example, the fault tolerant design [5] with surface mounted magnets and no mutual magnetic coupling between stator phases). However, the inductances relevant for the switching harmonics in the two d–q planes will always be different in multiphase induction machines. To obtain realistic values for the squared rms current ripple and for the current THD, per-phase equivalent circuits at the switching frequencies of five-phase machines in the d_1–q_1 and d_2–q_2 planes need to be considered. Since the switching frequency is assumed to be much higher than the fundamental frequency, resistances can be neglected, and the reduced per-phase equivalent schemes, shown in Fig. 1 for an induction machine, are sufficient for the analysis. The equivalent inductances for the d_1–q_1 and the d_2–q_2 planes, respectively, can be given as

$$L_{d_1-q_1} = L_{\gamma s} + \frac{L'_{\gamma r} L_m}{L'_{\gamma r} + L_m} \approx L_{\gamma s} + L'_{\gamma r} \tag{13}$$

$$L_{d_2-q_2} = L_{\gamma s}. \tag{14}$$

The stator leakage inductance in the two planes may or may not be equal, this being dependent on the stator winding design [18]. As shown in [18], if the stator winding is a double layer, the stator leakage inductances of the two planes are, in principle, different. In the five-phase induction machine used for the experiments in this paper, the stator winding is a single layer so that the stator leakage inductance in the two planes may be regarded as the same.

The problem of the frequency-related variation of the rotor leakage inductance of induction machines due to the skin effect is well known [19]. It, in essence, means that the rotor leakage inductance in (13) will have a particular and different value for each switching harmonic, with an ever-decreasing trend as the frequency increases. Considering that the flux HDF, in essence, represents simultaneously all the relevant switching harmonics, it is not possible to account for the frequency-related variation of the rotor leakage inductance, and it is considered a constant further on. While this does not impact the simulation results, the experimental results will obviously be affected.

Let the flux per-phase HDFs of the two d–q planes, obtained in [4] for the two considered SVPWM techniques, be identified with indices 1 and 2, respectively. For a five-phase induction machine, the relationships between the squared rms current ripple and per-plane flux HDFs and the current THD and per-plane flux HDFs, (11) and (12), respectively, then take the following form:

$$I_{\mathrm{rms}}^2 = \left(\frac{V_{\mathrm{dc}}T_s}{8}\right)^2 \left(\frac{\mathrm{HDF}_1}{(L_{d_1-q_1})^2} + \frac{\mathrm{HDF}_2}{(L_{d_2-q_2})^2}\right) \tag{15}$$

$$\mathrm{THD}_i = \left(\frac{V_{dc}T_s}{8}\right) \frac{\sqrt{\mathrm{HDF}_1/L_{d_1-q_1}^2 + \mathrm{HDF}_2/L_{d_2-q_2}^2}}{I_1}. \tag{16}$$

IV. Simulation Study: Voltage THD

A simulation of the generated phase voltages with the two SVPWM methods is performed first. Only the output voltage is generated, and there is no load connected to the inverter. The dead time is taken as zero so that all the harmonics above the fundamental are accounted for in (6) and (7). Since the differences in the flux HDF between different SVPWM techniques are more pronounced at higher modulation index values [4], the modulation index is set to 0.8, and the fundamental frequency is 40 Hz. The dc link voltage is taken as in [4], with $V_{\mathrm{dc}}/2 = 1$ per unit (or 1 V) so that it corresponds to the normalization factor in (10), and the switching frequency is $f_{\mathrm{sw}} = 2$ kHz. As discussed in [4], the average switching frequency of the SVPWM (4L) is therefore 1.4 times higher, i.e., 2.8 kHz.

Upon the creation of the output phase voltages, transformation matrix (1) is applied to get the phase voltage d–q axis components. The FFT is further applied to both the phase voltage and its axis components. The time domain waveforms and associated spectra are shown in Figs. 2 and 3 for the $(2\mathrm{L} + 2\mathrm{M})$ and (4L) SVPWM methods, respectively (phase voltage and its d_1 and d_2 components).

Since the frequency ratio F is an even number $(F = 50)$, then, according to (4), the odd SBs contain dominant even harmonics. According to (5), the 48th and the 52nd harmonics map into the second plane, and it is easy to see from Fig. 3 that this is indeed the case. Similarly, the 46th and the 54th harmonics map into the first plane. This is confirmed in Fig. 3 as well.

The comparison of the phase voltage spectra in Figs. 2 and 3 shows that the SVPWM (4L) is characterized with a much richer spectrum, this being the consequence of the variable switching frequency in inverter legs as one moves from sector to sector. The same conclusion applies to the spectra of the two planes. It can also be observed that the dominant SB2 harmonics of (4) are essentially the same for the two SVPWM methods, but SVPWM (4L) contains additional harmonics in this SB, which do not appear with the $(2\mathrm{L} + 2\mathrm{M})$ method. With regard to the odd SBs, there are clear differences in harmonic amplitudes, and $(2\mathrm{L} + 2\mathrm{M})$ contains far fewer harmonics.

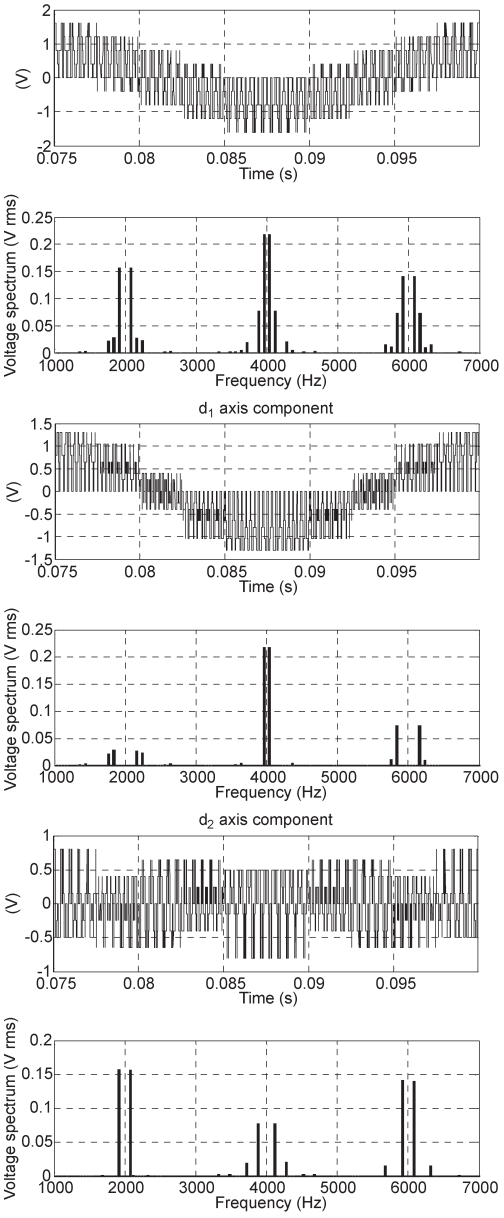

Fig. 2. Phase voltage and its d-axis components at $M = 0.8$ for $(2\mathrm{L} + 2\mathrm{M})$ SVPWM technique (time domain waveforms and spectra).

The values of the individual plane THDs and the total phase voltage THD have been calculated using (6) and are summarized in Table I (all referenced to the fundamental in the first plane). The same study has been repeated for identical

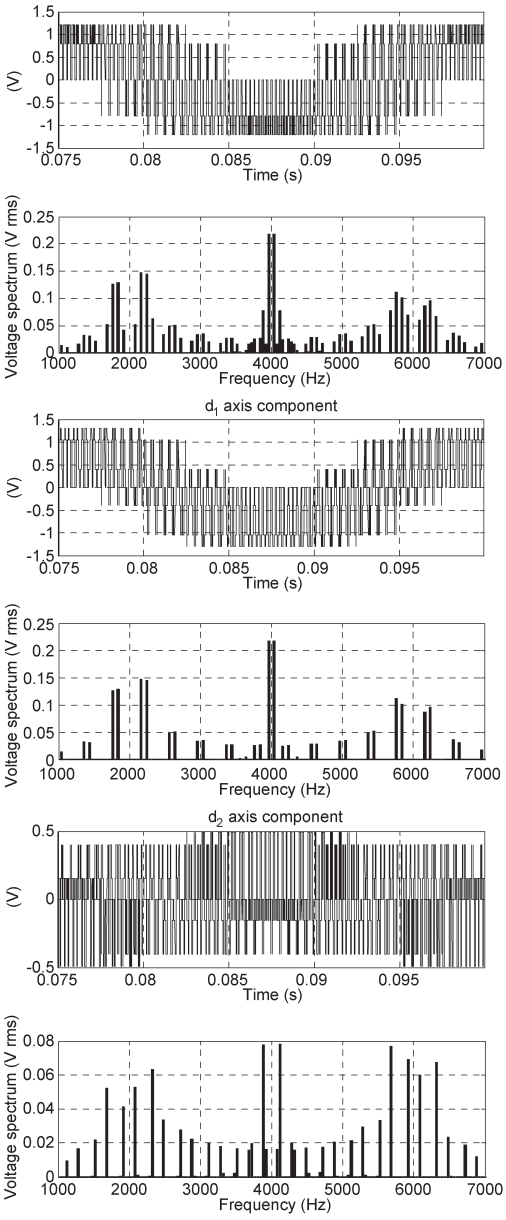

Fig. 3. Phase voltage and its d-axis components at $M = 0.8$ for (4L) SVPWM technique (time domain waveforms and spectra).

conditions, except that the switching frequency was changed and set to 1 kHz. The results are also included in Table I.

The values of the individual plane THDs in Table I show that (4L) has a higher voltage THD in the first plane and a smaller voltage THD in the second plane compared with the $(2L + 2M)$ method. These observations are fully in compliance with the corresponding discussion of harmonic flux trajectories and per-plane HDFs in [4].

TABLE I
TOTAL PHASE VOLTAGE AND PLANE THDS FOR THE CONSIDERED SVPWM METHODS

THD	Total THD	d_1–q_1	d_2–q_2
(2L+2M) @ 2 kHz	0.8108	0.5814	0.5653
(4L) @ 2 kHz	0.9493	0.8577	0.4071
(2L+2M) @ 1 kHz	0.9084	0.6566	0.6277
(4L) @ 1 kHz	1.0349	0.9152	0.4828

It is also obvious from Table I that the reduction in the second plane THD of (4L) is much smaller than the increase in the THD of the first plane. As a consequence, the total phase voltage THD of the SVPWM (4L) is more than 10% higher at both switching frequencies than the corresponding one of the SVPWM $(2L + 2M)$.

V. SIMULATION STUDY: CURRENT RIPPLE AND CURRENT THD

Since the total phase voltage THDs of the two SVPWM techniques show the same trend as the corresponding HDFs, one expects that the same will apply to the stator current THDs, as the case would be in a three-phase machine. However, as shown shortly, this is not necessarily the case when the five-phase machine is of an induction type.

A detailed simulation model has been built, which now includes the five-phase induction machine model as the inverter load. The induction machine model in the stationary reference frame is used, with stator and rotor per-phase leakage inductances of 40 mH each. Thus, in the simulations, leakage inductances relevant for the switching harmonics (13) and (14) are 80 and 40 mH, respectively.

Since the experiments, discussed in the next section, are performed in the open-loop V/f mode of operation with an uncompensated inverter dead time, the inverter simulation model now includes the dead time $(4\ \mu s)$. The dc link voltage is 600 V. Other conditions (output frequency of 40 Hz, modulation index of 0.8. and switching frequencies of 2 and 1 kHz) are the same as in Section IV. To eliminate the impact of the dead time on current ripple and current THD calculations, which leads to pronounced third and seventh stator current harmonics [17], harmonics of the order higher than the tenth are accounted for in (6)–(8).

The stator current waveforms and associated spectra are shown in Figs. 4 and 5 for the switching frequencies of 2 and 1 kHz, respectively, for the two SVPWM methods. The current THDs and squared rms current ripple values, at 1- and 2-kHz switching frequencies, are calculated using (6) and (8) and are summarized in Tables II and III, respectively. As can be seen from Table II, the SVPWM (4L) leads to a smaller value of the current THD (and, hence, squared rms current ripple; see Table III) than the SVPWM $(2L + 2M)$, although the situation with regard to the voltage THDs and flux HDFs is exactly the opposite.

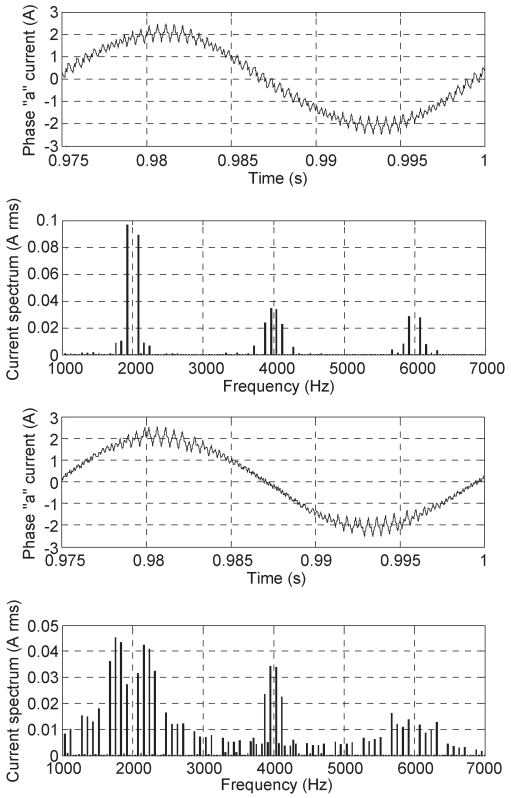

Fig. 4. Stator current and its spectrum for (top) (2L + 2M) and (bottom) (4L) SVPWM methods (2-kHz switching frequency, simulation).

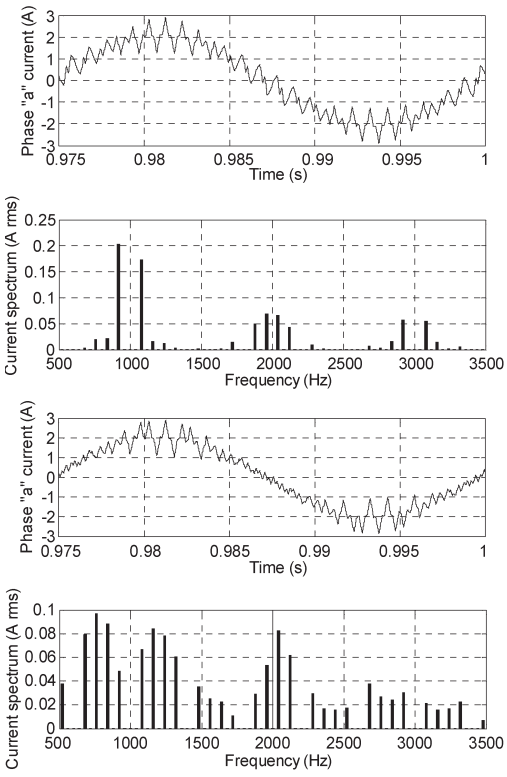

Fig. 5. Stator current and its spectrum for (top) (2L + 2M) and (bottom) (4L) SVPWM methods (1-kHz switching frequency, simulation).

The results reported in Table III are further compared to those obtained by means of (15). The per-phase per-plane HDF values are taken from [4] for the modulation index $M = 0.8$ for both SVPWM methods, and the dc voltage is set to 600 V in (15). For switching frequencies of 1 and 2 kHz, the scaling constants in (15) are equal to 5.625×10^{-3} and 1.40625×10^{-3}, respectively. The inductances of the two planes are 80 and 40 mH, respectively. By using these values, the squared rms current ripple, calculated at two switching frequencies for both SVPWM methods, has the values given in Table IV. A comparison of the results given in Tables III and IV reveals an exceptionally good agreement, considering that the squared rms of the current ripple has been calculated in two completely different manners (using the HDFs in Table IV and using the FFT and (8) in Table III). The match is practically perfect at a 2-kHz switching frequency. Very minor discrepancies appear at 1 kHz since, here, the assumptions used in the flux HDF derivation [4] become less accurate.

Tables II–IV fully verify not only the correctness of the correlation given in (15) between the HDFs and the squared rms current ripple but also the correctness of the plane and total per-phase HDF values for the two SVPWM methods given in [4].

TABLE II
STATOR CURRENT THDs FOR THE CONSIDERED SVPWM METHODS (1- AND 2-kHz SWITCHING FREQUENCIES)

THD/switching frequency	1 kHz	2 kHz
SVPWM (2L+2M)	0.2107	0.1035
SVPWM (4L)	0.1878	0.0953

TABLE III
STATOR CURRENT RIPPLE RMS SQUARED FOR THE CONSIDERED SVPWM METHODS (1- AND 2-kHz SWITCHING FREQUENCIES)

I^2_{RMS}/switching frequency	1 kHz	2 kHz
SVPWM (2L+2M)	0.095	0.023
SVPWM (4L)	0.075	0.019

TABLE IV
STATOR SQUARED RMS CURRENT RIPPLE FOR THE CONSIDERED SVPWM METHODS, CALCULATED USING (15)

	(2L+2M) SVPWM	(4L) SVPWM
HDF_1	0.0115	0.0498
HDF_2	0.0235	0.0095
I^2_{RMS} @ 2 kHz	0.023	0.019
I^2_{RMS} @ 1 kHz	0.093	0.077

A comparison of the squared rms current ripple is finally given in Fig. 6 for the two SVPWM techniques at two considered switching frequencies of 1 and 2 kHz and over the entire

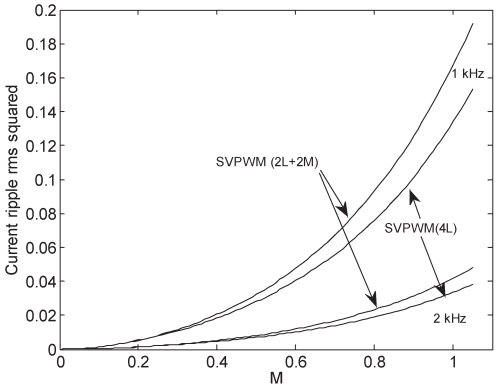

Fig. 6. Squared rms current ripple as function of the modulation index for $(2L + 2M)$ and (4L) SVPWM methods at switching frequencies of 1 and 2 kHz.

range of the modulation index variation in the linear modulation region. These results were produced using (15) and include the points already discussed in conjunction with Table IV.

VI. Experimental Results

An experimental evaluation has been conducted in order to further corroborate the theoretical and simulation results presented so far. All the conditions in the experiment are identical as in the simulation (a dc link voltage of 600 V, switching frequencies, a fundamental frequency of 40 Hz, a modulation index of 0.8, and the inverter dead time), except that the machine parameters are different (these are not known with sufficient accuracy for the evaluation required in (15), and a different machine was therefore used in the simulations). The experimental rig description can be found in [17].

The measured stator current waveforms and their spectra are given in Figs. 7 and 8 for the $(2L + 2M)$ and (4L) SVPWM techniques at switching frequencies of 2 and 1 kHz, respectively. The average switching frequency of the (4L) method is, as noted, 1.4 times higher than the switching frequency of the $(2L + 2M)$ SVPWM. The experimentally determined THDs, obtained using the FFT and (6), are summarized in Table V for $f_{sw} = 1$ and 2 kHz. The results of Table V are further compared to those obtained by the simulation, which are shown in Table II.

The values in Table V confirm experimentally that the stator current THD (and, hence, the squared rms current ripple) is smaller with the (4L) SVPWM method. Hence, this proves qualitatively the simulation results of the preceding section. However, the results of Table V also clearly show the difficulty in using relationship (15) with regard to an actual machine, which stems from the frequency-dependent variation of the rotor leakage inductance.

It is obvious from the definitions used in (15) and (16) that the current THD, expressed in terms of the flux HDF, is inversely proportional to the switching frequency while the

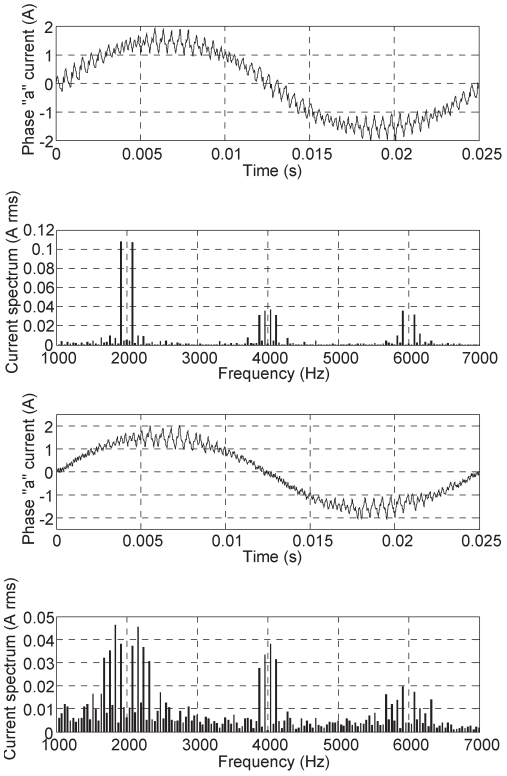

Fig. 7. Experimental results: Stator current and its spectrum for (top) $(2L + 2M)$ and (bottom) (4L) SVPWM methods at 2-kHz switching frequency.

squared rms current ripple is inversely proportional to the square of the switching frequency. Such a relationship clearly exists in the calculation results in Table IV and Fig. 6 (the halving of the switching frequency causes a fourfold increase in the squared rms current ripple). It is also almost satisfied in the simulation results in Tables II and III, where there is a negligible deviation, which can be assigned to the numerical procedure used in the calculations (the doubling of the switching frequency practically halves the current THD and reduces the squared rms current ripple four times). However, the same relationship does not exist in the current THD obtained from the experimental results. The ratios of the current THDs at 1 and 2 kHz are only 1.745 and 1.81 for $(2L + 2M)$ and (4L), respectively, rather than approximately two. The two values can be regarded as mutually very consistent, and the explanation of this behavior is the following: the beneficial increase of the switching frequency is, to some extent, counterbalanced by the reduction of the rotor leakage inductance with the frequency.

The results in Figs. 7 and 8, as well as those in Table V, apply to one specific modulation index value, 0.8, with a 40-Hz output frequency. The same measurements have however been repeated at other values of the modulation index using the $V/f =$ constant control law. As an example, the stator current

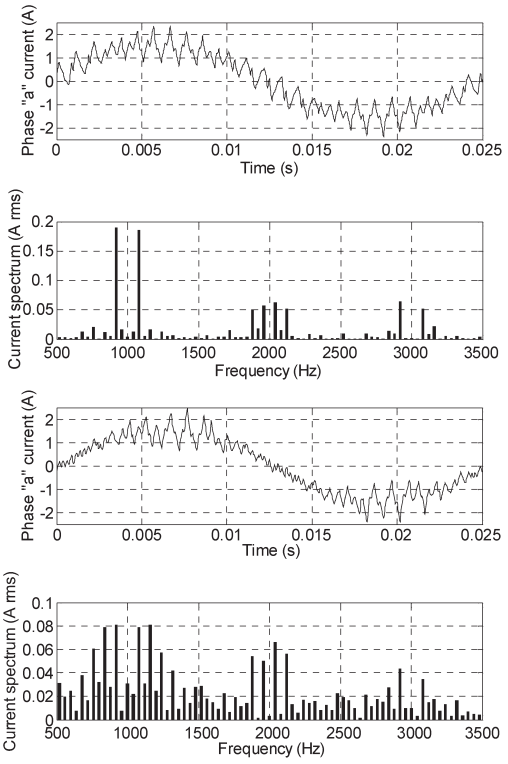

Fig. 8. Experimental results: Stator current and its spectrum for (top) (2L + 2M) and (bottom) (4L) SVPWM methods at 1-kHz switching frequency.

TABLE V
STATOR CURRENT THDs FOR THE CONSIDERED SVPWM METHODS (1- AND 2-kHz SWITCHING FREQUENCIES; EXPERIMENTAL RESULTS)

THD/switching frequency	1 kHz	2 kHz
(2L+2M) SVPWM	0.277	0.1587
(4L) SVPWM	0.244	0.1348

is illustrated in Fig. 9 for a 2-kHz switching frequency at a modulation index of 0.4. The stator current THD has been evaluated in each measurement point and is shown in Fig. 10 as a function of the modulation index for a 2-kHz switching frequency for both the (2L + 2M) and (4L) SVPWM methods. It can be seen from Fig. 10 that the (4L) SVPWM has a lower current THD and that the differences are more pronounced at higher modulation indices, which is similar to the behavior shown in Fig. 6.

The issue of the average switching frequency is finally addressed. All the results presented so far were obtained in both the simulations and the experiments using the same base switching frequency for the two SVPWM methods, meaning that the average switching frequency of the SVPWM (4L) is 1.4 times higher. If one wants to compare the SVPWM techniques under the condition of the same average frequency, the current THD values of the (2L + 2M) in Tables II and V and in Fig. 10

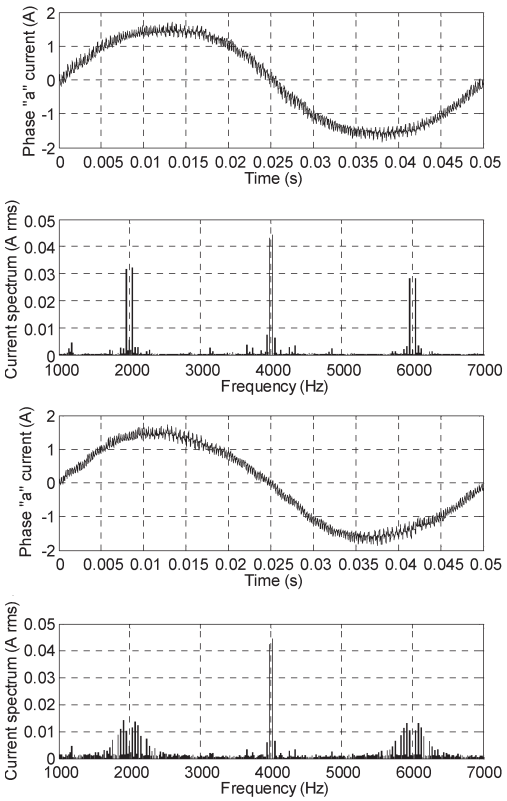

Fig. 9. Experimental results: Stator current and its spectrum for (top) (2L + 2M) and (bottom) (4L) SVPWM methods at 2-kHz switching frequency with modulation index of 0.4 (20-Hz output fundamental frequency).

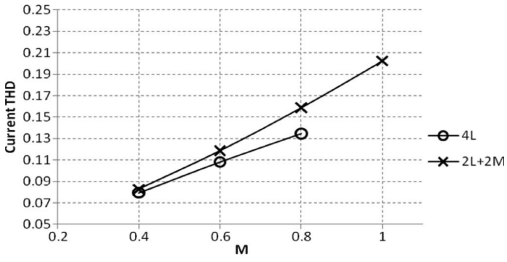

Fig. 10. Experimental results: Current THD at 2-kHz switching frequency for (2L + 2M) and (4L) SVPWM methods (measurement points are at 0.2, 0.4, 0.6, 0.8, and 1.0 modulation index values).

need to be divided by 1.4 for the (2L + 2M) method (and the squared rms current ripple values in Tables III and IV for (2L + 2M) require division with 1.4^2). Quite obviously, under the condition of the equal average switching frequency, the SVPWM (2L + 2M) technique will always offer lower current THD and squared rms current ripple.

VII. Conclusion

This paper has considered the determination of current THDs for two alternative SVPWM methods applicable to five-phase inverters and their relationship with the flux HDFs obtained in [4]. It is shown that, similar to the flux HDF, the voltage THD is considerably better with the SVPWM $(2\mathrm{L} + 2\mathrm{M})$ technique. However, the opposite holds true for the current THDs. Such a situation arises if the basic switching period is kept the same, thus resulting in a 1.4-times-higher average switching frequency with the SVPWM (4L), and if the five-phase machine is of an induction motor type. An explanation for this apparently unexpected behavior has been provided. It has also been observed that, if the current THD is compared under the condition of the same average switching frequency, the SVPWM $(2\mathrm{L} + 2\mathrm{M})$ will always offer a smaller current THD.

The validity of the flux HDF analysis, reported in [4], is fully verified through the established correlations between the flux HDF and the current THD and squared rms current ripple. It is shown that the current THD and the squared rms current ripple, calculated using the flux HDFs and calculated using the FFT of time-domain waveforms, fit practically perfectly.

The problem of the definition of the relevant leakage inductances for switching frequency harmonics, pertinent to multiphase induction machines, has been discussed in detail. The frequency dependent variation of the rotor leakage inductance is of special importance, the impact of which on the stator current THD has been shown by means of the experimental results.

The theoretical considerations are supported by the simulation and experimental results. Having in mind that the (4L) and $(2\mathrm{L} + 2\mathrm{M})$ SVPWM strategies provide the same utilization of the dc bus voltage in the linear modulation region, that the (4L) method is difficult for practical implementation in low-cost DSPs (in contrast to the $(2\mathrm{L} + 2\mathrm{M})$ strategy) due to the uneven switching frequency in individual inverter legs, and that, under the condition of the same average switching frequency, the SVPWM $(2\mathrm{L} + 2\mathrm{M})$ will always yield a smaller current THD and, thus, smaller additional losses in the machine, it has been concluded that, for practical realizations, one should always select the $(2\mathrm{L} + 2\mathrm{M})$ technique.

References

[1] S. R. Bowes and R. R. Clements, "Computer-aided design of PWM inverter systems," *Proc. Inst. Elect. Eng.*, vol. 129, no. 1, pt. B, pp. 1–17, Jan. 1982.

[2] P. D. Ziogas, E. P. Wiechmann, and V. R. Stefanovi, "A computer-aided analysis and design approach for static voltage source inverters," *IEEE Trans. Ind. Appl.*, vol. IA-21, no. 5, pp. 1234–1241, Sep. 1985.

[3] D. G. Holmes and T. A. Lipo, *Pulse Width Modulation for Power Converters—Principles and Practice*. Piscataway, NJ: IEEE Press, 2003, ser. Series on Power Engineering.

[4] D. Dujic, M. Jones, E. Levi, J. Prieto, and F. Barrero, "Switching ripple characteristics of space vector PWM schemes for five-phase two-level voltage source inverters—Part 1: Flux harmonic distortion factors," *IEEE Trans. Ind. Electron*, vol. 58, no. 7, pp. 2405–2414, Jul. 2011.

[5] E. Levi, "Multiphase electric machines for variable-speed applications," *IEEE Trans. Ind. Electron.*, vol. 55, no. 5, pp. 1893–1909, May 2008.

[6] A. Iqbal and E. Levi, "Space vector PWM techniques for sinusoidal output voltage generation with a five-phase voltage source inverter," *Electr. Power Compon. Syst.*, vol. 34, no. 2, pp. 119–140, Feb. 2006.

[7] A. Lega, M. Mengoni, G. Serra, A. Tani, and L. Zarri, "Space vector modulation for multiphase inverters based on a space partitioning algorithm," *IEEE Trans. Ind. Electron.*, vol. 56, no. 10, pp. 4119–4131, Oct. 2009.

[8] D. Casadei, D. Duji, E. Levi, G. Serra, A. Tani, and L. Zarri, "General modulation strategy for seven-phase inverters with independent control of multiple voltage space vectors," *IEEE Trans. Ind. Electron.*, vol. 55, no. 5, pp. 1921–1932, May 2008.

[9] D. Dujic, G. Grandi, M. Jones, and E. Levi, "A space vector PWM scheme for multi-frequency output voltage generation with multi-phase voltage source inverters," *IEEE Trans. Ind. Electron.*, vol. 55, no. 5, pp. 1943–1955, May 2008.

[10] S. Xue and X. Wen, "Simulation analysis of two novel multiphase SVPWM strategies," in *Proc. IEEE ICIT*, Hong Kong, 2005, pp. 1401–1406.

[11] D. Dujic, M. Jones, and E. Levi, "Analysis of output current ripple rms in multiphase drives using space vector approach," *IEEE Trans. Power Electron.*, vol. 24, no. 8, pp. 1926–1938, Aug. 2009.

[12] D. Dujic, M. Jones, and E. Levi, "Analysis of output current ripple rms in multi-phase drives using polygon approach," *IEEE Trans. Power Electron.*, vol. 25, no. 7, pp. 1838–1849, Jul. 2010.

[13] P. A. Dahono, "Analysis and minimization of output current ripple of multiphase PWM inverters," in *Proc. IEEE Power Electron. Spec. Conf.*, Jeju, Korea, 2006, pp. 3024–3029.

[14] P. A. Dahono, Deni, and E.G. Supriatna, "Output current-ripple analysis of five-phase PWM inverters," *IEEE Trans. Ind. Appl.*, vol. 45, no. 6, pp. 2022–2029, Nov./Dec. 2009.

[15] S. Halasz, "PWM strategies of multi-phase inverters," in *Proc. IEEE IECON*, Orlando, FL, 2008, pp. 916–921.

[16] Y. Zhao and T. A. Lipo, "Space vector PWM control of dual three-phase induction machine using vector space decomposition," *IEEE Trans. Ind. Appl.*, vol. 31, no. 5, pp. 1100–1109, Sep./Oct. 1995.

[17] M. Jones, S. Vukosavic, D. Dujic, and E. Levi, "A synchronous current control scheme for multiphase induction motor drives," *IEEE Trans. Energy Convers.*, vol. 24, no. 4, pp. 860–868, Dec. 2009.

[18] D. Hadiouche, H. Razik, and A. Rezzoug, "On the modeling and design of dual-stator windings to minimize circulating harmonic currents for VSI fed ac machines," *IEEE Trans. Ind. Appl.*, vol. 40, no. 2, pp. 506–515, Mar./Apr. 2004.

[19] Y. S. Kwon, J. H. Lee, S. H. Moon, B. K. Kwon, C. H. Choi, and J. K. Seok, "Standstill parameter identification of vector-controlled induction motors using the frequency characteristics of rotor bars," *IEEE Trans. Ind. Appl.*, vol. 45, no. 5, pp. 1610–1618, Sep./Oct. 2009.

Martin Jones (M'07) received the B.Eng. (with first-class honors) and Ph.D. degrees from the Liverpool John Moores University, Liverpool, U.K., in 2001 and 2005, respectively.

He is currently a Senior Lecturer with the Liverpool John Moores University.

Dr. Jones was a recipient of the IEE Robinson Research Scholarship for his Ph.D. studies.

Drazen Dujic (S'03–M'09) received the Dipl. Ing. and M.Sc. degrees from the University of Novi Sad, Novi Sad, Serbia, in 2002 and 2005, respectively, and the Ph.D. degree from the Liverpool John Moores University, Liverpool, U.K., in 2008.

From 2002 to 2006, he was a Research Assistant with the Department of Electrical Engineering, University of Novi Sad. From 2006 to 2009, he was a Research Associate with the Liverpool John Moores University. He is currently with ABB Corporate Research Center, Baden-Dättwil, Switzerland. His main research interests include the design and control of advanced power electronics systems and high-performance drives.

Emil Levi (S'89–M'92–SM'99–F'09) received the M.Sc. and Ph.D. degrees from the University of Belgrade, Belgrade, Serbia, in 1986 and 1990, respectively.

From 1982 to 1992, he was with the Department of Electrical Engineering, University of Novi Sad, Novi Sad, Serbia. Since May 1992, he has been with the Liverpool John Moores University, Liverpool, U.K., where he has been a Professor of electric machines and drives since September 2000.

Dr. Levi is a Co-Editor-in-Chief of the IEEE TRANSACTIONS ON INDUSTRIAL ELECTRONICS, an Editor of the IEEE TRANSACTIONS ON ENERGY CONVERSION, and the Editor-in-Chief of the *IET Electric Power Applications*. He was the recipient of the Cyril Veinott Award of the IEEE Power and Energy Society in 2009.

Joel Prieto (S'10) received the B.Eng. degree in electronic engineering from the Universidad Católica Nuestra Señora de la Asunción, Asunción, Paraguay, in 2005, and the M.Sc. degree from University of Seville, Seville, Spain, in 2009, where he is currently working toward the Ph.D. degree.

Since 2008, he has been with the Electrical Engineering Department, University of Seville.

Mr. Prieto is a recipient of a scholarship from Itaipu Binacional/Parque Tecnológico Itaipu-Py for his Ph.D. studies.

Federico Barrero (M'04–SM'05) was born in Seville, Spain, in 1967. He received the M.Sc. and Ph.D. degrees in electrical and electronic engineering from the University of Seville, Seville, in 1992 and 1998, respectively.

Since 1992, he has been with the Electronic Engineering Department, University of Seville, where he is currently an Associate Professor. His recent interests include microprocessor and DSP systems and control of multiphase ac drives.

3.3. Paper 3

Authors: J. Prieto, M. Jones, F. Barrero, E. Levi, S. Toral.
Title: Comparative Analysis of Discontinuous and Continuous PWM Techniques in VSI-Fed Five-Phase Induction Motor.
Journal: IEEE Transactions on Industrial Electronics.
Volume: 58.
Number: 12.
Pages: 5324-5335.
Date: December 2011.
Abstract: This paper reports on flux harmonic distortion factor and current ripple analysis for various discontinuous pulse-width-modulation (PWM) techniques, which are applicable in conjunction with five-phase two-level inverter-fed induction motors. The analysis is based on the application of the complex space vector approach. The results are compared throughout with the corresponding continuous PWM techniques. Different space vector PWM and carrier-based PWM methods are encompassed by the analysis. This paper is supported by extensive simulation results. Verification of theoretical findings is provided through experimental measurements on a five-phase induction motor.

5324 IEEE TRANSACTIONS ON INDUSTRIAL ELECTRONICS, VOL. 58, NO. 12, DECEMBER 2011

Comparative Analysis of Discontinuous and Continuous PWM Techniques in VSI-Fed Five-Phase Induction Motor

Joel Prieto, *Student Member, IEEE*, Martin Jones, *Member, IEEE*, Federico Barrero, *Senior Member, IEEE*, Emil Levi, *Fellow, IEEE*, and Sergio Toral, *Senior Member, IEEE*

***Abstract*—This paper reports on flux harmonic distortion factor and current ripple analysis for various discontinuous pulse-width-modulation (PWM) techniques, which are applicable in conjunction with five-phase two-level inverter-fed induction motors. The analysis is based on the application of the complex space vector approach. The results are compared throughout with the corresponding continuous PWM techniques. Different space vector PWM and carrier-based PWM methods are encompassed by the analysis. This paper is supported by extensive simulation results. Verification of theoretical findings is provided through experimental measurements on a five-phase induction motor.**

***Index Terms*—Current ripple, discontinuous and continuous pulse width modulation (PWM), flux harmonic distortion factor (HDF), multiphase drives.**

I. Introduction

MULTIPHASE machines are nowadays predominantly supplied from two-level voltage source inverters (VSIs). For the purpose of inverter control, both continuous carrier-based [1], [2] and continuous space vector pulse-width-modulation (SVPWM) techniques [3]–[10] have been developed for various phase numbers, which are capable of generating the required sinusoidal output voltages. The relationship between continuous carrier-based and SVPWM has also been studied, with corresponding analogies and differences established in [11] and [12]. Discontinuous pulse-width-modulation (PWM) techniques for multiphase inverters have received some attention as well, and such PWM schemes are available for five-phase and seven-phase inverters [13]–[16].

Different PWM strategies inherently lead to different behaviors with regard to the performance indicators that can be used to assess the quality of output waveforms not only in three-phase converters [17]–[20] but also for multiphase drives. In very recent times, attention has started to shift from the development of PWM strategies for multiphase VSIs to the evaluation of their switching characteristics, such as flux harmonic distortion factor (HDF) and current ripple. For this purpose, the complex space vector approach has been adapted for use in multiphase systems in [21], where a comprehensive study and a comparison of various continuous PWM techniques for five-phase systems have been reported. This was followed by the extension of the commonly used approach in three-phase systems, based on delta connection, to multiphase systems, based on multiple polygon connections in [22]. It was shown in [22] that in multiphase systems, the total flux HDF and the corresponding current ripple can be correctly calculated, yielding the same results as the complex space vector approach if and only if all polygon connections of a multiphase system are accounted for. As a consequence, it was concluded that the results presented in another attempt at calculating the current ripple in five-phase systems [23] were, in essence, incorrect, since only one polygon connection was used in the analysis. A further study, this time related to two specific continuous SVPWM techniques for five-phase VSIs, has been reported in [24] and [25]. A detailed investigation of both flux HDF and current ripple has been conducted using again the complex space vector approach.

As is obvious from the presented review, discontinuous PWM techniques have been studied to a lesser extent than continuous PWM techniques in relation to multiphase systems. This is particularly true with regard to the flux HDF and the current ripple, where the only considerations available are those of [15]. However, the approach used in [15] is entirely different from that used here, which utilized the complex space vector approach.

This paper presents an evaluation of switching ripple characteristics in terms of flux HDF and current ripple for a number of discontinuous PWM schemes and two different SVPWM schemes. The route followed fully corresponds to that in [21], [24], and [25]. The results obtained for discontinuous methods are at all times compared with those already available for the corresponding continuous methods. Theoretical findings are illustrated with simulation results, which also provide insight into the impact of machine leakage inductances on the current ripple. Experimental verification is carried out on a five-phase induction motor test rig. It is concluded that discontinuous

Manuscript received October 26, 2010; revised January 25, 2011; accepted February 27, 2011. Date of publication March 10, 2011; date of current version September 20, 2011. This work was supported in part by the Spanish Government under Reference DPI2009/07955 and in part by Itaipu Binacional/Parque Tecnológico Itaipu-Py.

J. Prieto, F. Barrero, and S. Toral are with the Electronic Engineering Department, University of Seville, 41092 Seville, Spain (e-mail: jprieto@esi.us.es; fbarrero@esi.us.es; toral@esi.us.es).

M. Jones and E. Levi are with the School of Engineering, Liverpool John Moores University, L3 3AF Liverpool, U.K. (e-mail: E.Levi@ljmu.ac.uk; m.jones2@ljmu.ac.uk).

Color versions of one or more of the figures in this paper are available online at http://ieeexplore.ieee.org.

Digital Object Identifier 10.1109/TIE.2011.2126540

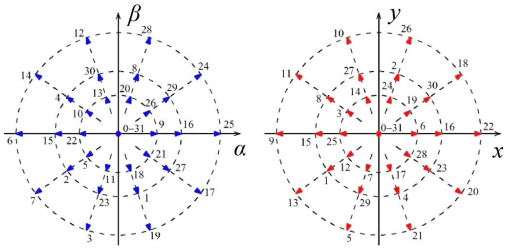

Fig. 1. Voltage vectors in the α–β and x–y planes for a five-phase VSI.

PWM techniques can offer lower current ripple at higher modulation index values, this being similar to three-phase drives.

II. SVPWM Methods for Five-Phase VSIs

In a five-phase VSI, there are $2^5 = 32$ possible vectors (30 active and two zero). Since the load neutral point is isolated, a five-phase VSI can be described in two planes using the decomposition matrix for five-phase systems ($\varphi = 2\pi/5$), i.e.,

$$C_5 = \frac{2}{5}\begin{bmatrix} 1 & \cos\varphi & \cos 2\varphi & \cos 3\varphi & \cos 4\varphi \\ 0 & \sin\varphi & \sin 2\varphi & \sin 3\varphi & \sin 4\varphi \\ 1 & \cos 2\varphi & \cos 4\varphi & \cos 6\varphi & \cos 8\varphi \\ 0 & \sin 2\varphi & \sin 4\varphi & \sin 6\varphi & \sin 8\varphi \\ 1/2 & 1/2 & 1/2 & 1/2 & 1/2 \end{bmatrix}. \quad (1)$$

New variables belong to two mutually perpendicular planes, as shown in Fig. 1, which are labeled α–β and x–y. The fifth variable, i.e., the zero-sequence component, can be omitted from further consideration due to the star connection of the winding with isolated neutral point.

The goal of the modulation scheme is to achieve the desired voltage reference in the α–β plane while zeroing (on average) the voltage in the x–y plane. The modulation index is defined as $M = V_1/(V_{\rm dc}/2)$, where V_1 is the peak value of the sinusoidal reference, whereas the reference voltage space vector in the α–β plane is defined per unit as $\bar{\nu}^* = M\exp(j\vartheta)$. To achieve the desired voltage reference, the SVPWM scheme must select during each switching period four active voltage space vectors and the zero vector [4], [9], [10]. There are two approaches to select the four active vectors. The first and most frequently used approach [10]–[12] is the selection of two large and two medium vectors, which neighbor the reference in the α–β plane (2L+2M). The second approach is the selection of four large vectors (4L) that neighbor the reference [9].

A. SVPWM Based on 2L+2M Vector Selection

The reference voltage in the x–y plane is always zero, whereas in the α–β plane, it is any vector with modulus of up to 1/cos 18° [10] for operation in the linear PWM region. Using a reference voltage vector in the first sector of the α–β plane as an example, the four selected active vectors are as depicted in Fig. 2(a). Their projections in the x–y plane are included

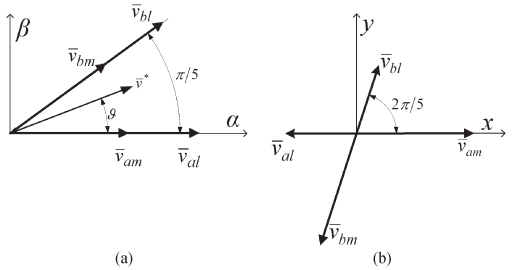

Fig. 2. Selected vectors when the reference is in sector 1 for SVPWM based on (2L+2M) vector selection. (a) α–β plane. (b) x–y plane.

in Fig. 2(b). Let δ_{km} and δ_{kl} be the duty cycles of medium and large vectors, and let $K_1 = \sin\pi/5$, $K_2 = \sin 2\pi/5$, and $J_1 = \cos\pi/5$. The duty cycles in sector s are then governed with

$$\begin{aligned} \delta_{am} &= MK_1\sin\left(s\frac{\pi}{5}-\vartheta\right) \quad \delta_{bm} = MK_1\sin\left(\vartheta-(s-1)\frac{\pi}{5}\right) \\ \delta_{al} &= MK_2\sin\left(s\frac{\pi}{5}-\vartheta\right) \quad \delta_{bl} = MK_2\sin\left(\vartheta-(s-1)\frac{\pi}{5}\right) \\ \delta_z &= 1-MK_2\cos\left((2s-1)\frac{\pi}{10}-\vartheta\right) \end{aligned} \quad (2)$$

where δ_z refers to the zero vector duty cycle, which will be shared between $\bar{\nu}_0$ and $\bar{\nu}_{31}$ vectors. Different choices for the zero vector duty cycle subdivision lead to continuous and discontinuous PWM techniques. Despite the fact that there is an infinite number of possibilities to subdivide δ_z into δ_0 and δ_{31}, the performance and simplicity constraints of practical PWM-VSI drives reduce this to a small number of practically viable choices [26]. The continuous SVPWM and the discontinuous DPWMMAX, DPWMMIN, DPWM0, DPWM1, DPWM2, and DPWM3 will be analyzed in detail. These modulation techniques are an extension of the cases known for three-phase discontinuous modulation techniques [17], [26], and they are obtained by modifying the zero state partitioning of δ_z, depending on the sector within which the reference is, according to Fig. 3.

An important property of the (2L+2M) SVPWM vector selection is the correlation with well-known carrier-based methods (both continuous and discontinuous). Fig. 4 illustrates the modulation and zero-sequence signal waveforms of the continuous carrier-based PWM with offset addition (TIPWM), which is equivalent to continuous SVPWM, as well as for a variety of possible discontinuous PWM techniques.

The expressions in (2) are general for all sectors, but the order of vector application is not the same [10], [12]. The sequence is $\bar{\nu}_0, \bar{\nu}_{am}, \bar{\nu}_{bl}, \bar{\nu}_{al}, \bar{\nu}_{bm}, \bar{\nu}_{31}, \bar{\nu}_{bm}, \bar{\nu}_{al}, \bar{\nu}_{bl}, \bar{\nu}_{am}, \bar{\nu}_0$ in odd and $\bar{\nu}_0, \bar{\nu}_{bm}, \bar{\nu}_{al}, \bar{\nu}_{bl}, \bar{\nu}_{am}, \bar{\nu}_{31}, \bar{\nu}_{am}, \bar{\nu}_{bl}, \bar{\nu}_{al}, \bar{\nu}_{bm}, \bar{\nu}_0$ in even sectors.

B. SVPWM Based on 4L Vector Selection

An alternative selection of the vectors follows the idea introduced in [8] for an asymmetrical six-phase motor drive,

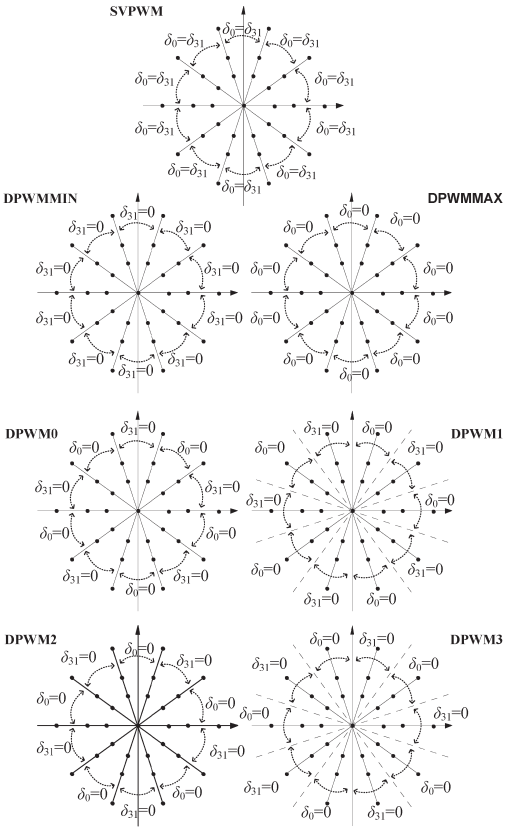

Fig. 3. Zero state partitioning for the analyzed SVPWM techniques. The following applies: for SVPWM $\delta_{31} = \delta_0 = 0.5\delta_z$; for DPWMAX $\delta_0 = 0$; and for DPWMIN $\delta_{31} = 0$, regardless of the sector.

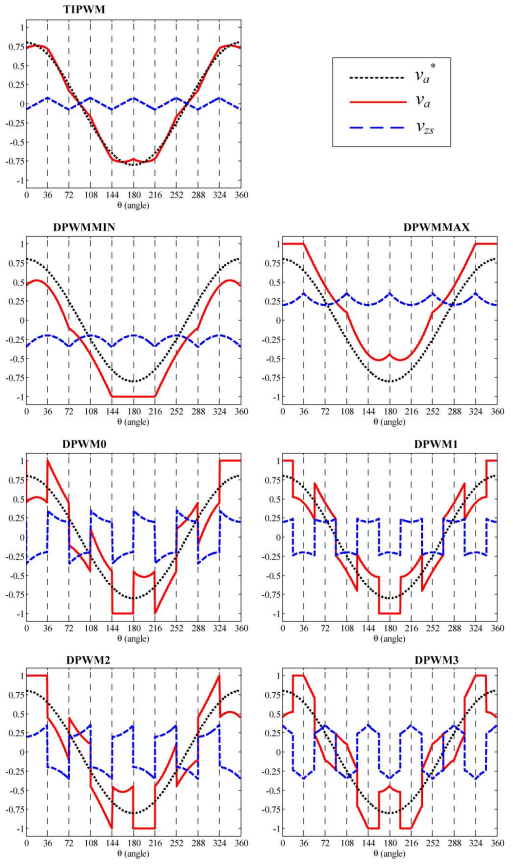

Fig. 4. Modulating and zero-sequence signals for continuous (TIPWM) and discontinuous carrier-based PWM techniques using $M = 0.8$.

which was then adapted to five-phase systems in [9]. Four neighboring large vectors are selected instead of two large and two medium, as illustrated in Fig. 5(a). The mapping of the active vectors into the x–y plane is shown in Fig. 5(b).

The most important consequence of this selection is the different switching pattern obtained when considering the continuous SVPWM. The switching frequency of the (4L) SVPWM method requires a threefold increase in the switching frequency in one inverter leg in each sector [24], so that the average switching frequency is 1.4 times higher than with the (2L+2M) SVPWM method [24].

Regardless of this difference, there are similarities between the (4L) and (2L+2M) SVPWM methods: 1) The maximum modulation index in the linear region is the same [24]. 2) The order of application of the active vectors in the odd sectors is mirrored from the even sectors, e.g., the sequence is $\bar{\nu}_0, \bar{\nu}_{cl}, \bar{\nu}_{al}, \bar{\nu}_{bl}, \bar{\nu}_{dl}, \bar{\nu}_{31}, \bar{\nu}_{dl}, \bar{\nu}_{bl}, \bar{\nu}_{al}, \bar{\nu}_{cl}, \bar{\nu}_0$ for odd sectors, whereas $\bar{\nu}_0, \bar{\nu}_{dl}, \bar{\nu}_{bl}, \bar{\nu}_{al}, \bar{\nu}_{cl}, \bar{\nu}_{31}, \bar{\nu}_{cl}, \bar{\nu}_{al}, \bar{\nu}_{bl}, \bar{\nu}_{dl}, \bar{\nu}_0$ is the sequence for even sectors. 3) The dwell times of medium vectors for the (2L+2M) SVPWM method coincide with the dwell times of the more distant vectors from the reference in the (4L) SVPWM case, and the zero vectors have the same dwell time value. The dwell times for all vectors as a function of the

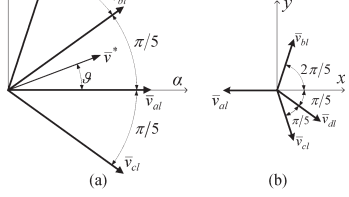

Fig. 5. Selected vectors when the reference is in sector 1 for SVPWM based on (4L) vector selection. (a) α–β plane. (b) x–y plane.

reference vector modulus and position (sector and angle) are given as

$$\begin{aligned}
\delta_{al} &= MK_1\left[\sin\left(\vartheta-(s-1)\frac{\pi}{5}\right)+(2J_1-1)\sin\left(s\frac{\pi}{5}-\vartheta\right)\right]\\
\delta_{bl} &= MK_1\left[\sin\left(s\frac{\pi}{5}-\vartheta\right)+(2J_1-1)\sin\left(\vartheta-(s-1)\frac{\pi}{5}\right)\right]\\
\delta_{cl} &= MK_1\sin\left(s\frac{\pi}{5}-\vartheta\right)\\
\delta_{dl} &= MK_1\sin\left(\vartheta-(s-1)\frac{\pi}{5}\right)\\
\delta_z &= 1-K_2M\cos\left((2s-1)\frac{\pi}{10}-\vartheta\right). \qquad (3)
\end{aligned}$$

The zero state partitioning, as illustrated in Fig. 3 for (2L+2M) SVPWM, applies to (4L) SVPWM as well.

III. Flux HDF Analysis

As noted, the current ripple analysis is based on the flux HDF approach in [21], [22], [24], [25] and utilizes the complex space vector approach, which is already used in the evaluation of the continuous PWM techniques in [21], [24], and [25]. The harmonic flux represents the time integral of the harmonic voltage vector (i.e., the voltage error vector caused during generation of the output voltage reference vector). The complex space vector approach allows for the analysis to be performed in several steps and offers great insight into the mechanism of creation of the output current ripple. In that way, at first, it is possible to graphically illustrate the trajectories of the harmonic flux, in each of the two planes, over a switching period. Then, the squared harmonic flux rms is calculated, which is different for every modulation scheme. Finally, the flux HDF (obtained from the integrated squared harmonic flux over the fundamental period) is determined in each plane. The procedure in [21], [22], and [24] is briefly reviewed in what follows, in conjunction with its application to discontinuous PWM techniques.

A. Harmonic Flux Trajectories

At any arbitrary time instant, there is an error between the applied voltage vector and the reference vector because of the discrete nature of the inverter. This deviation of the output voltage will cause current ripple when applied over the load. The model for the analysis can be simplified into

$$\Delta\bar{i}=\frac{\bar{\nu}-\bar{\nu}^*}{L_\sigma}\Delta t \qquad (4)$$

where $\bar{\nu}$ represents the space vectors activated over the time interval Δt within a switching period, $\bar{\nu}^*$ is the reference voltage vector, and L_σ is the equivalent inductance for the switching harmonics. Since this equivalent inductance is not as simple to define in multiphase systems [21], [22] as in the case of three-phase systems, the notion of harmonic flux $\Delta\overline{\lambda}$ [26] is used, where

$$\Delta\overline{\lambda}=L_\sigma\Delta\bar{i}=(\bar{\nu}-\bar{\nu}^*)\Delta t. \qquad (5)$$

This definition allows the analysis of the harmonic flux to independently be performed in each plane. Based on (5) and assuming zero initial value for the deviation of the harmonic flux, it is possible to generate harmonic flux trajectories (trajectories of error voltage vectors) in both planes over the switching period for all SVPWM schemes (continuous and discontinuous). Due to the existence of the symmetrical switching pattern, it is enough to consider only one-half of the switching period and obtain deviations of the harmonic flux ($\Delta\lambda$) at the end of every subinterval over the first half of the switching period. The normalization factor for the harmonic flux is selected the same as in [21] and [24], i.e.,

$$\Delta\lambda_N=L\Delta i_N=\frac{V_{\rm dc}T_s}{8}. \qquad (6)$$

Expression (5) can now be applied to each plane, respecting the ordering of applied vectors. Since the order is different for (2L+2M) and (4L) methods, and different sequence orders are used in the odd and even sectors, the applied active vectors are denoted as I to IV to be able to consider the general case. The harmonic flux trajectory value at the end of every subinterval is given by [24]

$$\begin{aligned}
\Delta\overline{\lambda}(0) &= 0\\
\Delta\overline{\lambda}(t_1) &= -\delta_0\bar{\nu}^*T_s/2\\
\Delta\overline{\lambda}(t_2) &= \Delta\overline{\lambda}(t_1)+\delta_I(\bar{\nu}_I-\bar{\nu}^*)T_s/2\\
\Delta\overline{\lambda}(t_3) &= \Delta\overline{\lambda}(t_2)+\delta_{II}(\bar{\nu}_{II}-\bar{\nu}^*)T_s/2\\
\Delta\overline{\lambda}(t_4) &= \Delta\overline{\lambda}(t_3)+\delta_{III}(\bar{\nu}_{III}-\bar{\nu}^*)T_s/2\\
\Delta\overline{\lambda}(t_5) &= \Delta\overline{\lambda}(t_4)+\delta_{IV}(\bar{\nu}_{IV}-\bar{\nu}^*)T_s/2\\
\Delta\overline{\lambda}(t_6) &= \Delta\overline{\lambda}(t_5)-\delta_{31}\bar{\nu}^*T_s/2. \qquad (7)
\end{aligned}$$

Figs. 6 and 7 show the harmonic flux trajectories over a subcycle for the applied vectors with $M=0.8$ and $\vartheta=0^\circ$, 12°, 24°, and 36°. Only the trajectories of continuous SVPWM, DPWMMAX ($\delta_0=0$), and DPWMMIN ($\delta_{31}=0$), for both (2L+2M) and (4L) selections, are plotted to emphasize the following important facts:

1) As stated in [21], the harmonic flux trajectories in the x–y plane are not a function of the zero space vector duty cycle [Figs. 6(d) and 7(d)]. Because the differences between continuous and discontinuous methods rely on zero state partitioning, both continuous and discontinuous methods have the same harmonic flux trajectory, which is, however, different for (2L+2M) and (4L) SVPWM techniques.
2) The harmonic flux trajectories of (4L) discontinuous methods are with larger trajectories in the α–β plane, compared with the trajectories of the (2L+2M) SVPWM.
3) The harmonic flux trajectories of (4L) discontinuous and (4L) continuous methods are quite similar in the α–β plane.
4) The harmonic flux trajectories of the (2L+2M) SVPWM are with smaller excursions from the origin in the α–β plane, compared with the trajectories of the (4L) SVPWM scheme.
5) The harmonic flux trajectories of the (4L) SVPWM are with smaller excursions from the origin in the x–y plane, compared with the trajectories of the (2L+2M) SVPWM.

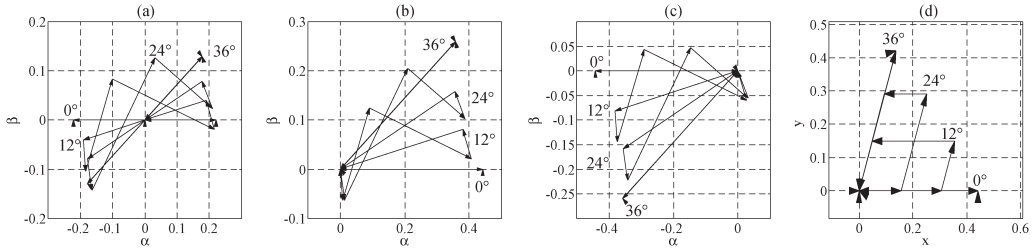

Fig. 6. Harmonic flux trajectories over a subcycle $(T_s/2)$ for $M = 0.8$. Considered methods: (a) continuous (2L+2M) SVPWM, α–β plane; (b) (2L+2M) DPWMMAX, α–β plane; (c) (2L+2M) DPWMMIN, α–β plane; and (d) plane x–y for all considered methods with (2L+2M).

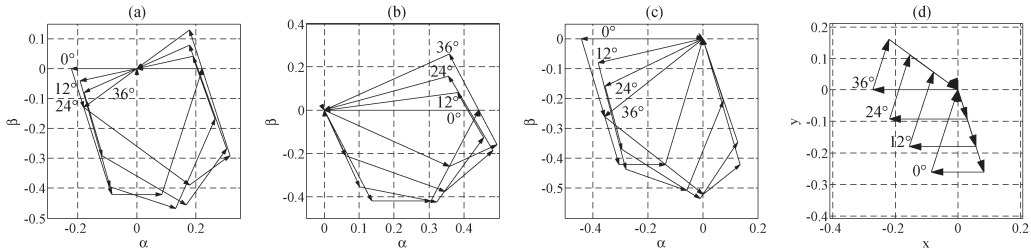

Fig. 7. Harmonic flux trajectories over a subcycle $(T_s/2)$ for $M = 0.8$. Considered methods: (a) continuous (4L) SVPWM, α–β plane; (b) (4L) DPWMMAX, α–β plane; (c) (4L) DPWMMIN, α–β plane; and (d) plane x–y for all considered methods with (4L).

6) Continuous SVPWMs have equal zero state partition while discontinuous SVPWMs do not. This means that $\Delta\overline{\lambda}(t_1)$ and $\Delta\overline{\lambda}(t_5)$ in the α–β plane will be symmetrical to the origin for continuous methods, but this will not be the case for discontinuous techniques.

B. Squared Harmonic Flux

The second step involves an analysis of the harmonic flux over the switching period, so the average squared value of the harmonic flux is taken as a figure of merit. Since the first and second halves of the trajectory have the same rms value due to symmetry, calculating only for $T_s/2$ is sufficient. Therefore, the following integral has to be solved:

$$\Delta\lambda^2_{abcde-RMS} = \frac{2}{T_s}\int_0^{\frac{T_s}{2}} \Delta\lambda^2_{abcde}dt. \tag{8}$$

The left-hand side of (8) represents all five phases, so the total five-phase system solution is obtained. The quantity $\Delta\lambda^2_{abcde}$ can be related to the harmonic flux deviations in each of the two 2-D planes [21], so that (8) takes the form

$$\begin{aligned}\Delta\lambda^2_{abcde-RMS} &= \Delta\lambda^2_{abcde-RMS\alpha\beta} + \Delta\lambda^2_{abcde-RMSxy} \\ &= \frac{5}{2}\frac{2}{T_s}\left[\int_0^{\frac{T_s}{2}} \left[\Delta\lambda^2_\alpha + \Delta\lambda^2_\beta\right] dt + \int_0^{\frac{T_s}{2}} \left[\Delta\lambda^2_x + \Delta\lambda^2_y\right] dt\right]. \end{aligned}\tag{9}$$

Expression (9) can be separated into several integrals in accordance with the existing subintervals, and by manipulating according to the procedure detailed in [21], it is possible to obtain a very general solution in each of the two 2-D planes, which can easily be evaluated numerically. The squared harmonic flux rms characteristics of the (2L+2M) and (4L) modulation techniques analyzed in this paper are plotted in Figs. 8–11.

It can be seen that every modulation method has a unique and different characteristic in the α–β plane, whereas the characteristic in the x–y plane is the same for all (2L+2M) and (4L) methods, respectively. Again, some conclusions can be made on the basis of Figs. 8–11. Those related to continuous (2L+2M) and (4L) SVPWMs are the following [24]:

1) $\alpha-\beta$ plane: (2L+2M) has significantly lower values of the squared harmonic flux than (4L), with peak values appearing around $M = 0.6$, which are followed by a decrease as the modulation index increases toward the maximum value. Conversely, the characteristic of (4L) is always increasing with the modulation index.
2) $x-y$ plane: The squared harmonic flux rms of the (4L) SVPWM is with lower values than that of the (2L+2M) SVPWM. This is so because the selected vectors for (4L) SVPWM in the x–y plane are within the circle with the minimum modulus.

As noted, the plots in the x–y plane are the same for continuous and discontinuous schemes and only depend on the vector selection, so that there is a unique characteristic for all (2L+2M) schemes and another characteristic for all (4L) methods. This is so since the harmonic flux trajectories in this

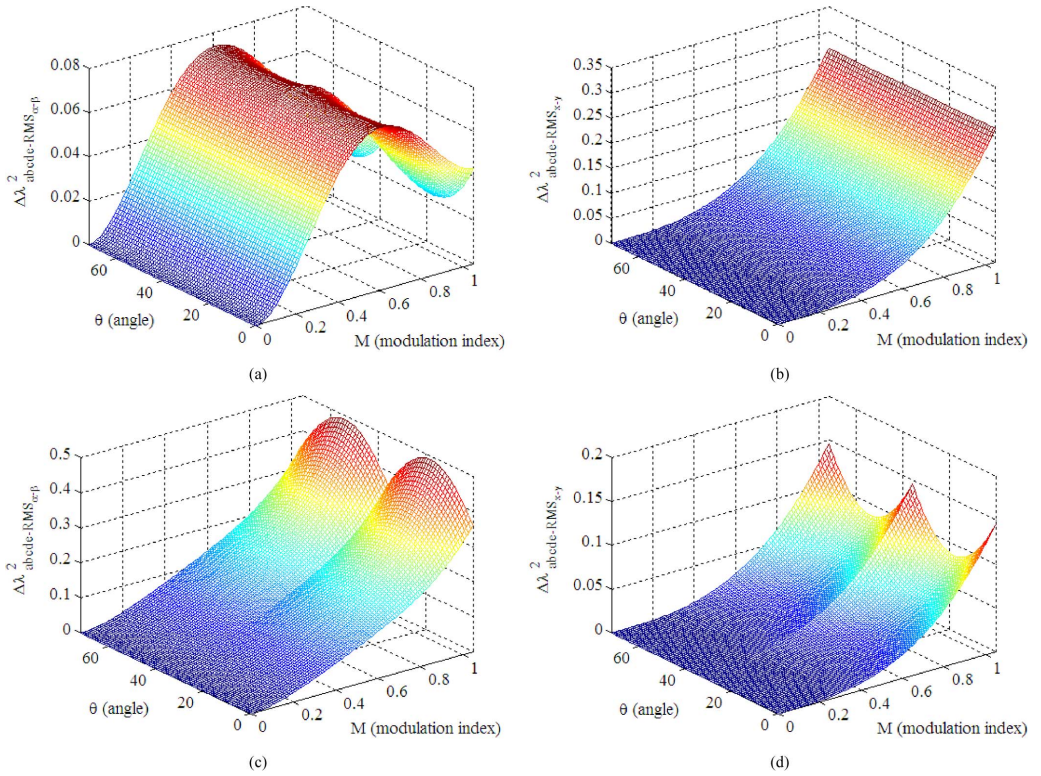

Fig. 8. Squared harmonic flux of continuous SVPWM. (a) (2L+2M) SVPWM, α–β plane. (b) (2L+2M) SVPWM, x–y plane. (c) (4L) SVPWM, α–β plane. (d) (4L) SVPWM, x–y plane.

plane are not a function of the zero state partitioning, so that the squared harmonic flux rms is also independent of this.

When discontinuous schemes are examined for (2L+2M) selection (Fig. 9), the following applies to the α–β plane:

1) As in the case of the continuous method, the peak values appear around $M = 0.6$, and then the value decreases as the modulation index increases. The squared harmonic flux rms values for the maximum modulation index are quite similar in magnitude.
2) If DPWMMAX and DPWMMIN were plotted for all sectors (Fig. 9(a) and (b) is only plotted for the first two sectors), then the shape of the curves would be the same, but shifted 36°.
3) The DPWM0, DPWM1, DPWM2, and DPWM3 characteristics can be derived from DPWMMAX and DPWMMIN depending on the sector (or half sector). For example, DPWM0 is like DPWMMIN in sector 1, but like DPWMMAX in sector 2 [from Figs. 3 and 9(c)], whereas DPWM1 is the same as DPWMMAX in the first half sector 1 and the second half sector 2, and it is like DPWMMIN in between these two half sectors.
4) It can be expected, on the basis of the analysis of Fig. 9, that DPWMMAX, DPWMMIN, DPWM0, and DPWM2 will have the same current harmonic content, whereas DPWM1 and DPWM3 should have better and worse current harmonic contents, respectively.

With regard to discontinuous schemes based on (4L) vector selection, only one plot is shown in Fig. 10. This is so because all have an almost identical shape, so that no differences can be observed in this type of plot. Fig. 11 shows a slice of Figs. 8–10 for $M = 0.9$, revealing the angular position dependencies of the squared harmonic flux in the α–β plane for every technique. The squared harmonic flux in the α–β plane for all (2L+2M) analyzed techniques is qualitatively the same for different modulation indices, and a similar behavior is obtained when only (4L) methods are considered. However, the ratios of squared harmonic flux values for (2L+2M) and (4L) modulation schemes are not necessarily as in Fig. 11 for all modulation index values. Other modulation indices can offer different qualitative behavior, and the curves obtained using (4L) and (2L+2M) methods can have crossovers anywhere.

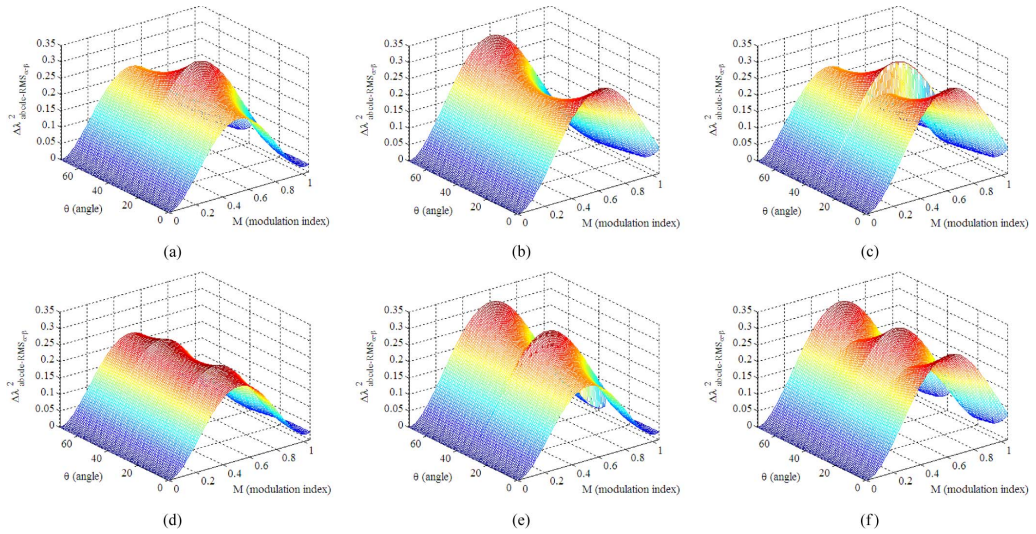

Fig. 9. Squared harmonic flux in α–β plane for discontinuous (2L+2M) SVPWM. (a) DPWMMAX. (b) DPWMMIN. (c) DPWM0. (d) DPWM1. (e) DPWM2. (f) DPWM3.

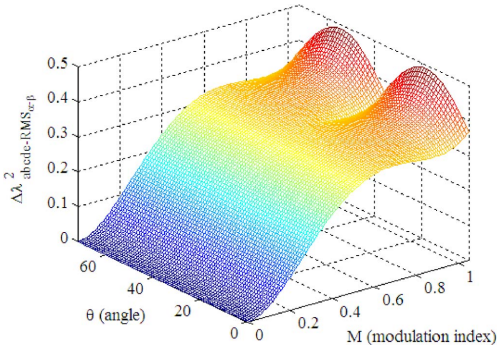

Fig. 10. Squared harmonic flux in α–β plane for discontinuous PWM techniques using (4L) vector selection.

Because the zero state partition is the same for (2L+2M) and (4L) vector selections, the DPWM0, DPWM1, DPWM2, and DPWM3 characteristics can be derived from DPWMMAX and DPWMMIN depending on the sector (or half sector).

Analyzing the same figure, the correspondence between various curves and zones is as follows (underlined letters identify DPWMMAX curves, whereas bold font represents DPWMMIN curves):

(4L) DPWMMAX → A-F-G-D

(4L) DPWMMIN → **E-B-C-H**

(4L) DPWM0 → **E-B**-G-D

(4L) DPWM1 → A-**B-C**-D.

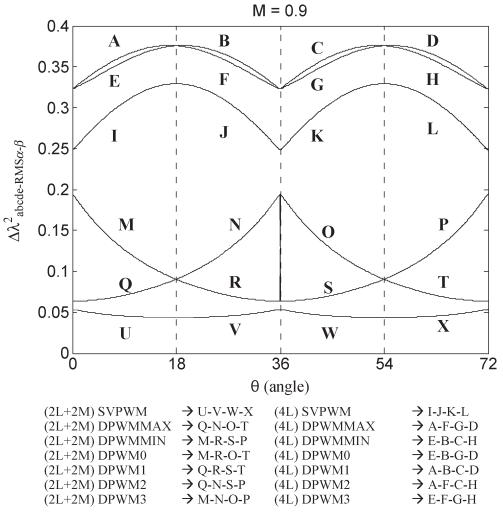

(2L+2M) SVPWM	→ U-V-W-X	(4L) SVPWM	→ I-J-K-L
(2L+2M) DPWMMAX	→ Q-N-O-T	(4L) DPWMMAX	→ A-F-G-D
(2L+2M) DPWMMIN	→ M-R-S-P	(4L) DPWMMIN	→ E-B-C-H
(2L+2M) DPWM0	→ M-R-O-T	(4L) DPWM0	→ E-B-G-D
(2L+2M) DPWM1	→ Q-R-S-T	(4L) DPWM1	→ A-B-C-D
(2L+2M) DPWM2	→ Q-N-S-P	(4L) DPWM2	→ A-F-C-H
(2L+2M) DPWM3	→ M-N-O-P	(4L) DPWM3	→ E-F-G-H

Fig. 11. Squared harmonic flux in α–β plane for all analyzed techniques when $M = 0.9$.

Hence, again, the DPWM0, DPWM1, DPWM2, and DPWM3 characteristics can be derived from DPWMMAX and DPWMMIN. It can be expected that DPWMMAX, DPWMMIN, DPWM0, and DPWM2 will have the same current harmonic content, but in contrast to (2L+2M) schemes, now the DPWM3 will have smaller and DPWM1 higher current harmonics.

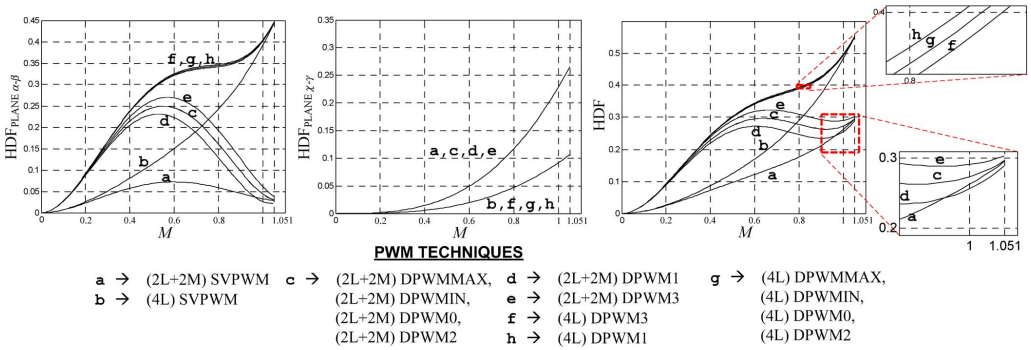

Fig. 12. HDF curves for the range of the achievable modulation indices for the same base switching frequency.

TABLE I
AVERAGE SWITCHING FREQUENCY (ASF) NORMALIZED WITH RESPECT TO SWITCHING FREQUENCY OF CONTINUOUS SVPWM (2L+2M)

PWM method	ASF	PWM method	ASF
(2L+2M) SVPWM	1	(4L) SVPWM	1.4
(2L+2M) DPWMMAX	0.8	(4L) DPWMMAX	1
(2L+2M) DPWMMIN	0.8	(4L) DPWMMIN	1
(2L+2M) DPWM0	0.8	(4L) DPWM0	1
(2L+2M) DPWM1	0.8	(4L) DPWM1	1
(2L+2M) DPWM2	0.8	(4L) DPWM2	1
(2L+2M) DPWM3	0.8	(4L) DPWM3	1

C. Flux HDFs

Finally, to obtain flux HDFs in each of the planes, the squared harmonic flux has to be integrated over the fundamental period. For the same reasons as before, the integration should be performed over the first two sectors, e.g.,

$$\Delta\lambda^2_{abcde-RMSF} = \frac{5}{2\pi}\int_0^{\frac{2\pi}{5}} \Delta\lambda^2_{abcde-RMS}d\vartheta. \qquad (10)$$

The polynomial closed-form solution of (10) is not always easy to express in short and compact form, as demonstrated in [21] and [22]. Therefore, the HDFs of the analyzed modulation schemes are obtained by numerical integration of (10) in Matlab and are shown in Fig. 12 for (2L+2M) and (4L) modulation methods using the same base switching frequency. The base switching frequency of 1 per unit corresponds to the switching frequency of the continuous SVPWM (2L+2M) method. The relationship between the average switching frequency and the base switching frequency for studied methods is listed in Table I. The correlation between the HDF considering the average switching frequency and the base switching frequency is

$$\mathrm{HDF_{av}} = (\mathrm{ASF})^2 \cdot \mathrm{HDF_{base}}. \qquad (11)$$

Since the discontinuous (2L+2M) methods have two fewer switchings per carrier cycle than the continuous SVPWM (2L+2M) method, the sideband harmonics of the discontinuous methods are wider and larger in magnitude. The same should be the case for continuous (4L) SVPWM and all discontinuous methods with (4L) vector selection, because the number of switchings is not the same for all legs. The following applies to the HDF behavior.

1) In the α–β plane, (2L+2M) SVPWM has a significantly lower flux HDF (as the modulation index increases) compared with (4L) SVPWM [24]. The continuous SVPWM in each of the two vector selection cases has a lower HDF than the corresponding discontinuous methods if the same base switching frequency is considered. In the high-modulation index range, the discontinuous methods are superior to continuous SVPWM in the case of (2L+2M) vector selection for the same ASF because of the factor $(0.8)^2$ in (11).
2) In the x–y plane, all modulation schemes with (2L+2M) and (4L) methods, respectively, have the same behavior. In this plane, (4L) selections have lower HDFs. However, the differences are much smaller between the two vector selection schemes. It should be noted that the impact of the x–y plane on the current ripple is more pronounced as the modulation index increases.
3) For (2L+2M) selections, DPWM1 is better than other discontinuous techniques, and for (4L) selections, DPWM3 is better. However, in both cases, the improvement is marginal, and the modulator selection criteria should be based on other characteristics, such as the switching losses.
4) DPWMMIN, DPWMMAX, DPWM0, and DPWM2 have the same HDF for the corresponding cases of (2L+2M) or (4L) vector selection. This agrees with the statements given in the previous section, where the harmonic flux was analyzed.

IV. SIMULATION RESULTS

To verify the analytical results obtained so far for various modulation schemes, a number of simulations have been performed using Matlab/Simulink. The current total harmonic distortion (THD) is used as the figure of merit. Detailed explanations regarding correlations between HDFs, current ripple of the α–β and x–y planes, total THD evaluation, and leakage

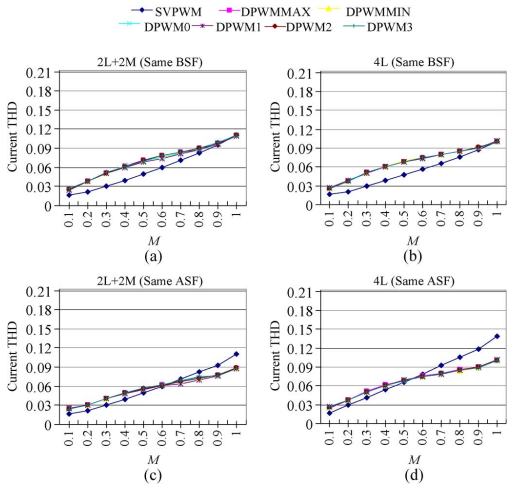

Fig. 13. Simulation results: stator current THD versus achievable modulation index for continuous and discontinuous SVPWM methods using (a) (b) the same base switching frequency (BSF), and (c) (d) the same average switching frequency (ASF) for comparative purpose.

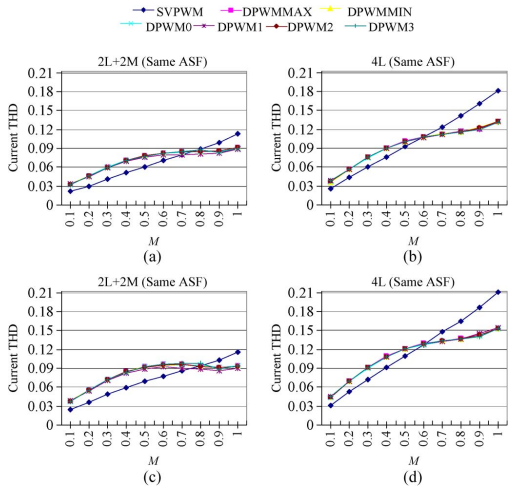

Fig. 14. Simulation results: stator current THD versus modulation index for continuous and discontinuous SVPWM methods and with $R_s = 12.85\ \Omega$, $R_r = 11.15\ \Omega$, $L_{ls} = 85.8$ mH, $L_m = 687.8$ mH and (a) (b) $L_{lr} = 21.4$ mH and (c) (d) $L_{lr} = 2.14$ mH. The same average switching frequency is used for comparative purposes.

inductance impact on the two planes are available in [25]. It suffices here to state the current THD in the following form [25]:

$$\mathrm{THD}_i = \left(\frac{V_{\mathrm{dc}} T_s}{8}\right) \frac{\sqrt{HDF_{\alpha-\beta}/L_{\alpha-\beta}^2 + HDF_{x-y}/L_{x-y}^2}}{I_1} \tag{12}$$

where $L_{\alpha-\beta}$ and L_{x-y} represent the equivalent inductances of the two planes for switching harmonics, $HDF_{\alpha-\beta}$ and HDF_{x-y} are the flux HDFs of the two planes, I_1 is the rms value of the fundamental, and the subscripts refer to the planes α–β or x–y. In (12), $L_{\alpha-\beta} \approx L_{ls} + L_{lr}$, and $L_{x-y} = L_{ls}$.

A five-phase induction machine with parameters $R_s = 12.85\ \Omega$, $R_r = 11.15\ \Omega$, $L_{ls} = 85.8$ mH, $L_{lr} = 85.8$ mH, and $L_m = 687.8$ mH has been used. These are the parameters of the machine that are subsequently tested experimentally. The dc bus voltage is set to 300 V. V/f operation mode is utilized, and the modulation index and the fundamental frequency are changed from $M = 0.1$ at $f = 5$ Hz to $M = 1$ at $f = 50$ Hz. The stator current of one phase has been recorded, and the current THD has been calculated on the basis of the fast Fourier transform (FFT) of the current waveform in steady-state operation for any particular pair of modulation index/frequency values.

Fig. 13 shows simulation results for all the analyzed methods. Fig. 13(a) and (b) depicts the cases when the base switching frequency is set to 2 kHz. It follows from Fig. 13 that the continuous modulation techniques yield a lower current THD than the discontinuous techniques. The current THD increases with the modulation index. The (2L+2M) DPWM1 technique offers the lowest current THD for higher modulation indices among the discontinuous (2L+2M) methods, whereas the current THDs for discontinuous (4L) methods are very similar. These facts agree with the analytical results obtained in the previous section.

It was shown in [25] that the THD is inversely proportional to the switching frequency, whereas the HDF is inversely proportional to the squared switching frequency. Consequently, all the analyzed modulation techniques were simulated using the same average switching frequency for a fair comparison. The average switching frequency was also set to 2 kHz, and the obtained results are presented in Fig. 13(c) and (d). It can be observed that the discontinuous methods offer lower current THD values at higher modulation indices (the curves intersect around $M = 0.6$ for (2L+2M) schemes and around $M = 0.5$ for (4L) techniques). Considering the pairs of plots shown in Fig. 13(a)–(c) and (b)–(d), all the relationships in Table I are verified.

Let us consider the case of $M = 1$ for the sake of example. In this case, continuous (2L+2M) SVPWM and all discontinuous (4L) methods lead to practically the same values in Fig. 13(a)–(d), respectively. However, the current THD for (2L+2M) discontinuous methods is now lower due to the 0.8 factor in Table I (the ratio in Fig. 13(c) is $0.088/0.11 = 0.80$), whereas the THD of the continuous (4L) is now increased by the factor of 1.4, according to Table I (the ratio in Fig. 13(d) is $0.139/0.1 = 1.39$). Finally, the (2L+2M) SVPWM techniques offer a lower current THD than the (4L) SVPWM methods under the assumption of the same average switching frequency.

An important fact is that the lag in the current created by the inductances does not affect the current ripple of any modulation scheme. The current ripple only depends on the ratio of rotor-to-stator leakage inductance [25], according to (12). Fig. 14 presents additional simulation results used to analyze

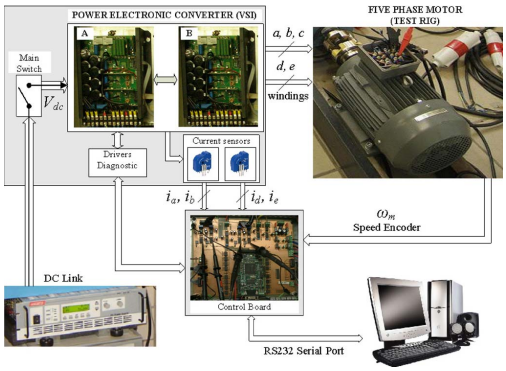

Fig. 15. Experimental system, including the power and control modules at the left side and the five-phase induction machine at the right side.

this dependence. The same average switching frequency has been used, but different rotor leakage inductance parameters were tested: $L_{lr} = 21.4$ mH and $L_{lr} = 2.14$ mH. The obtained results can be summarized as follows:

1) If $L_{lr} \ll L_{ls}$ is considered so that in (12) $L_{\alpha-\beta} \approx L_{x-y}$ [Fig. 14(c) and (d)], then the HDF and current THD plots have the same shape, since the current THD curves are practically proportional to the flux HDF curves. This is expected on the basis of (12).
2) If $L_{lr} < L_{ls}$ [Fig. 14(a) and (b)] or $L_{lr} = L_{ls}$ (Fig. 13), then the current THD waveforms differ from the flux HDF waveforms as follows:
   a) Consider the (2L+2M) methods [Figs. 13(c) and 14(a)]: The discontinuous methods generate smaller differences than before ($L_{lr} \ll L_{ls}$) for medium modulation indices, whereas the obtained values using high modulation indices are the same.
   b) Consider the (4L) modulation schemes [Figs. 13(d) and 14(b)]: All discontinuous methods produce nearly the same results (similar to the analysis of the flux HDF curves). However, the current THD increases when L_{lr}/L_{ls} decreases. Depending on the L_{lr}/L_{ls} ratio, the current THD for the highest modulation indices can be lower or higher than that obtained using the corresponding (2L+2M) technique.
3) An increase in L_m generates a higher current THD due to the reduction of the fundamental current I_1. A decrease in the leakage inductances produces lower equivalent inductances in the α–β and x–y planes and hence higher current THD.

V. Experimental Results

To validate the theoretical and simulation results, an experimental evaluation has been conducted. The test rig is based on a 30-slot 2-pairs-of-pole 4-kW three-phase induction machine, whose stator has been rewound to give a five-phase induction machine with three pairs of poles. The parameters of the machine have been determined using conventional tests (no-load and blocked rotor tests) at 50 Hz with inverter supply, and the obtained values are those used in the simulations (Fig. 13). A schematic of the rig and photos of the complete system is given in Fig. 15. Five phases of two conventional three-phase VSIs from Semikron (SKS21F) were used to drive the machine. The dc link voltage was also set to 300 V using a dc power supply system. The control system is based on the MSK28335 board, and the induction machine was operated in the same manner as in the simulation tests. A stator phase current was measured in steady state (no-load operating conditions) using a dynamic signal analyzer (Agilent 35670A) and a current probe (Hameg HZ56-2). Fig. 16 shows the phase "a" current waveform for (2L+2M) SVPWM, (2L+2M) DPWMAX, and (2L+2M) DPWMMIN techniques for $M = 1$. For each pair of modulation index/frequency values, such a waveform is recorded for each PWM method. The FFT is further executed, and the current THD for that operating point is evaluated.

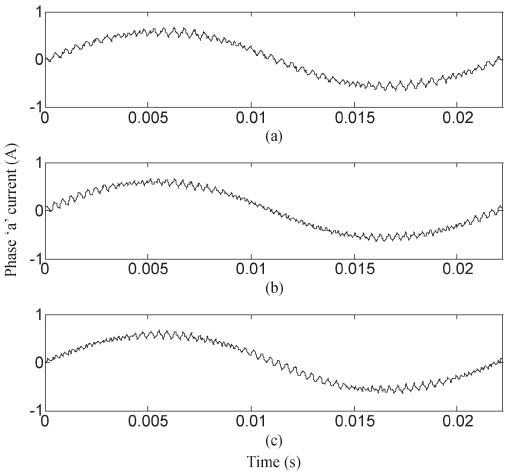

Fig. 16. Experimental results. Current waveforms for (a) (2L+2M) SVPWM, (b) (2L+2M) DPWMMAX, and (c) (2L+2M) DPWMMIN at $M = 1$.

The experimental results are shown in Fig. 17. Comparison with the simulation results in Fig. 13 reveals a satisfactory agreement, both qualitatively and quantitatively, despite unavoidable measurement errors. Another important issue is that the THD calculation in (12) uses fixed values of leakage inductances for all harmonic frequencies, with parameters having been determined at 50 Hz. In reality, however, the leakage inductance of the rotor is likely to be very different (lower) at switching frequency due to the skin effect. Moreover, due to the frequency dependence of the rotor leakage inductance, different values apply to different sidebands of multiples of the switching frequency. Hence, the discrepancies between the simulation and experimental results in Figs. 13 and 17 are unavoidable. It can be observed, by comparing experimental results in Fig. 17(c) and (d) with those shown in Fig. 14(a) and (b), that the experimental results show an excellent agreement with the calculations done with a lower rotor leakage

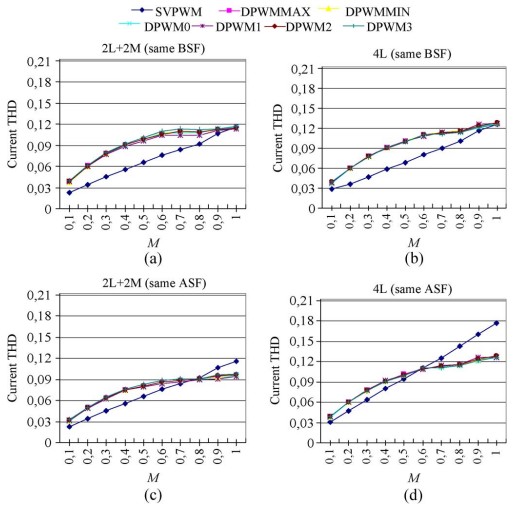

Fig. 17. Experimental results. Stator current THD versus modulation index for continuous and discontinuous SVPWM methods using (a) (b) the same base switching frequency (BSF) and (c) (d) the same average switching frequency (ASF).

inductance value (here 21.4 mH, or 1/4 of the value determined at 50 Hz).

Finally, from the previous analysis, simulation results, and experimental results, it can be concluded that (2L+2M) SVPWM should be used for low modulation indices, whereas any (2L+2M) discontinuous modulation technique can be used at high modulation indices, when considering the same average switching frequency. Another advantage of (2L+2M) techniques is the easiness of implementation in low-cost Digital Signal Processor (DSPs), in contrast to (4L) methods, which have uneven switching frequency in individual inverter legs.

VI. Conclusion

In this paper, the analysis of the switching characteristics in PWM VSI supplied five-phase drives has been extended from the already available analyses for continuous PWM methods to discontinuous PWM techniques. Although a five-phase drive was considered, further extensions to higher phase numbers are relatively straightforward. The correlation between continuous and discontinuous modulation methods is established as an extension of the conventional three-phase systems supplied from two-level VSIs. Although modulation techniques based on (4L) vector selection cannot be developed using the carrier-based approach, they are, in principle, feasible with the space vector approach.

The current ripples generated by continuous and discontinuous SVPWM, DPWMMAX, DPWMMIN, and DPWM0 to DPWM3, using (2L+2M) and (4L) vector selection methods, are studied. A complete analysis, including theoretical development, simulations, and, finally, experimental verification, is reported. The impact of rotor leakage inductance value on current THD is also studied. On the basis of the obtained results, it is possible to conclude that, if the same average switching frequency is considered, continuous (2L+2M) SVPWM has the best harmonic current performance (the lowest current THD) in the range of low modulation index values. A discontinuous (2L+2M) DPWM1 offers the best performance in the high modulation index range.

References

[1] A. Iqbal, E. Levi, M. Jones, and S. N. Vukosavi, "Generalised sinusoidal PWM with harmonic injection for multi-phase VSIs," in *Proc. IEEE Power Electron. Spec. Conf.*, Jeju, Korea, 2006, pp. 2871–2877.

[2] L. Zarri, M. Mengoni, A. Tani, G. Serra, and D. Casadei, "Minimization of the power losses in IGBT multiphase inverters with carrier-based pulse width modulation," *IEEE Trans. Ind. Electron.*, vol. 57, no. 11, pp. 3695–3706, Nov. 2010.

[3] D. Hadiouche, L. Baghli, and A. Rezzoug, "Space-vector PWM techniques for dual three-phase ac machines: Analysis, performance evaluation, and DSP implementation," *IEEE Trans. Ind. Appl.*, vol. 42, no. 4, pp. 1112–1122, Jul./Aug. 2006.

[4] J. W. Kelly, E. G. Strangas, and J. M. Miller, "Multiphase space vector pulse width modulation," *IEEE Trans. Energy Convers.*, vol. 18, no. 2, pp. 259–264, Jun. 2003.

[5] A. Lega, M. Mengoni, G. Serra, A. Tani, and L. Zarri, "Space vector modulation for multiphase inverters based on a space partitioning algorithm," *IEEE Trans. Ind. Electron.*, vol. 56, no. 10, pp. 4119–4131, Oct. 2009.

[6] K. Marouani, L. Baghli, D. Hadiouche, A. Kheloui, and A. Rezzoug, "A new PWM strategy based on a 24-sector vector space decomposition for a six-phase VSI-fed dual stator induction motor," *IEEE Trans. Ind. Electron.*, vol. 55, no. 5, pp. 1910–1920, May 2008.

[7] S. Halasz, "PWM strategies of multi-phase inverters," in *Proc. IEEE IECON*, Orlando, FL, 2008, pp. 916–921.

[8] Y. Zhao and T. A. Lipo, "Space vector PWM control of dual three-phase induction machine using vector space decomposition," *IEEE Trans. Ind. Appl.*, vol. 31, no. 5, pp. 1100–1109, Sep./Oct. 1995.

[9] S. Xue and X. Wen, "Simulation analysis of two novel multi-phase SVPWM strategies," in *Proc. IEEE ICIT*, Hong Kong, 2005, pp. 1401–1406.

[10] A. Iqbal and E. Levi, "Space vector PWM techniques for sinusoidal output voltage generation with a five-phase voltage source inverter," *Elect. Power Compon. Syst.*, vol. 34, no. 2, pp. 119–140, Feb. 2006.

[11] D. Dujic, M. Jones, and E. Levi, "Continuous carrier-based vs. space vector PWM for five-phase VSI," in *Proc. IEEE Region 8 EUROCON: Int. Conf. 'Computer as a Tool'*, Warsaw, Poland, 2007, pp. 1772–1779.

[12] A. Iqbal and S. Moinuddin, "Comprehensive relationship between carrier-based PWM and space vector PWM in a five-phase VSI," *IEEE Trans. Power Electron.*, vol. 24, no. 10, pp. 2379–2390, Oct. 2009.

[13] O. Ojo and G. Dong, "Generalized discontinuous carrier-based PWM modulation scheme for multi-phase converter-machine systems," in *Conf. Rec. IEEE IAS Annu. Meeting*, Hong Kong, 2005, pp. 1374–1381.

[14] X. F. Zhang, F. Yu, H. S. Li, and Q. G. Song, "A novel discontinuous space vector PWM control for multiphase inverter," in *Proc. Int. SPEEDAM*, Taormina, Italy, 2006, pp. 1133–1136.

[15] S. Halasz, "Discontinuous modulation of multiphase inverter-fed AC motor," presented at the European Conf. Power Electronics and Applications (EPE), Barcelona, Spain, 2009, Paper 0569.

[16] M. A. Khan, S. M. Ahmed, A. Iqbal, and H. Abu-Rub, "Discontinuous space vector PWM strategies for a seven-phase voltage source inverter," in *Proc. IEEE Annu. Meeting IECON*, Porto, Portugal, 2009, pp. 397–402.

[17] D. G. Holmes and T. A. Lipo, "IEEE Press series on power engineering," in *Pulse Width Modulation for Power Converters—Principles and Practice*. Piscataway, NJ: IEEE Press, 2003.

[18] M. Malinowski, "Adaptive modulator for three-phase PWM rectifier/inverter," in *Proc. Int. Conf. PEMC*, Kosice, Slovakia, 2000, pp. 1.35–1.40.

[19] A. M. Hava, R. J. Kerkman, and T. A. Lipo, "A high performance generalized discontinuous PWM algorithm," *IEEE Trans. Ind. Appl.*, vol. 34, no. 5, pp. 1059–1071, Sep./Oct. 1998.

[20] L. Asiminoaei, P. Rodriguez, and F. Blaabjerg, "Application of discontinuous PWM modulation in active power filters," *IEEE Trans. Power Electron.*, vol. 23, no. 4, pp. 1692–1706, Jul. 2008.

[21] D. Dujic, M. Jones, and E. Levi, "Analysis of output current ripple RMS in multiphase drives using space vector approach," *IEEE Trans. Power Electron.*, vol. 24, no. 8, pp. 1926–1938, Aug. 2009.
[22] D. Dujic, M. Jones, and E. Levi, "Analysis of output current ripple RMS in multi-phase drives using polygon approach," *IEEE Trans. Power Electron.*, vol. 25, no. 7, pp. 1838–1849, Jul. 2010.
[23] P. A. Dahono, Deni, and E. G. Supriatna, "Output current-ripple analysis of five-phase PWM inverters," *IEEE Trans. Ind. Appl.*, vol. 45, no. 6, pp. 2022–2029, Nov./Dec. 2009.
[24] D. Dujic, M. Jones, E. Levi, J. Prieto, and F. Barrero, "Switching ripple characteristics of space vector PWM schemes for five-phase two-level voltage source inverters—Part 1: Flux harmonic distortion factors," *IEEE Trans. Ind. Electron.*, vol. 58, no. 7, pp. 2789–2798, Jul. 2011, DOI: 10.1109/TIE.2010.2070777.
[25] M. Jones, D. Dujic, E. Levi, J. Prieto, and F. Barrero, "Switching ripple characteristics of space vector PWM schemes for five-phase two-level voltage source inverters—Part 2: Current ripple," *IEEE Trans. Ind. Electron.*, vol. 58, no. 7, pp. 2799–2808, Jul. 2011, DOI: 10.1109/TIE.2010.2070778.
[26] A. M. Hava, R. J. Kerkman, and T. A. Lipo, "Simple analytical and graphical methods for carrier-based PWM-VSI drives," *IEEE Trans. Power Electron.*, vol. 14, no. 1, pp. 49–61, Jan. 1999.

Joel Prieto (S'10) received the B.Eng. degree in electronic engineering in 2005 from the Universidad Católica Nuestra Señora de la Asunción, Asunción, Paraguay, and the M.Sc. degree in 2009 from the University of Seville, Seville, Spain, where he is currently working toward the Ph.D. degree.

He was the recipient of a scholarship from Itaipu Binacional/Parque Tecnológico Itaipu-Py for his Ph.D. studies.

Martin Jones (M'07) received the B.Eng. degree (first class honors) and the Ph.D. degree from the Liverpool John Moores University, Liverpool, U.K., in 2001 and 2005, respectively.

From September 2001 to Spring 2005, he was a Research Student with the Liverpool John Moores University. He is currently a Senior Lecturer with Liverpool John Moores University. He was the recipient of the IEE Robinson Research Scholarship for his Ph.D. studies

Federico Barrero (M'04–SM'05) received the M.Sc. and Ph.D. degrees in electrical and electronic engineering from the University of Seville, Seville, Spain, in 1992 and 1998, respectively.

Since 1992, he has been with the Electronic Engineering Department, University of Seville, where he is currently an Associate Professor.

Dr. Barrero received the Best Paper Award from the IEEE TRANSACTIONS ON INDUSTRIAL ELECTRONICS in 2009.

Emil Levi (S'89–M'92–SM'99–F'09) received the M.Sc. and Ph.D. degrees from the University of Belgrade, Belgrade, Serbia, in 1986 and 1990, respectively.

From 1982 to 1992, he was with the Department of Electrical Engineering, University of Novi Sad, Novi Sad, Serbia. Since May 1992, he has been with the Liverpool John Moores University, Liverpool, U.K., where he has been a Professor of electric machines and drives since September 2000. He serves as Editor-in-Chief of the *IET Electric Power Applications*.

Dr. Levi serves as Co-Editor-in-Chief of the IEEE TRANSACTIONS ON INDUSTRIAL ELECTRONICS and as Editor of the IEEE TRANSACTIONS ON ENERGY CONVERSION. He was the recipient of the Cyril Veinott Award from the IEEE Power and Energy Society in 2009.

Sergio Toral (M'01–SM'06) received the M.Sc. and Ph.D. degrees in electrical and electronic engineering from the University of Seville, Seville, Spain, in 1995 and 1999, respectively.

He is currently an Associate Professor with the Department of Electronic Engineering, University of Seville.

Dr. Toral received the Best Paper Award from the IEEE TRANSACTIONS ON INDUSTRIAL ELECTRONICS in 2009.

3.4. Paper 4

Authors: J. Prieto, F. Barrero, E. Levi, S. Toral, M. Jones y M. J. Durán.
Title: Analytical Evaluation of Switching Characteristics in Five-Phase Drives with Discontinuous Space Vector Pulse Width Modulation Techniques.
Journal: EPE Journal.
Volume: 23.
Number: 2.
Pages: 24-33.
Date: June 2013.
Abstract: This paper deals with flux harmonic distortion factor (HDF) and current ripple analysis for various discontinuous space vector PWM (SVPWM) techniques, applicable in conjunction with five-phase two-level inverter-fed ac motor drives. The analysis is based on the application of the recently developed polygon approach for multiphase systems. The results are compared throughout with the corresponding continuous SVPWM techniques. Two different SVPWM methods, based on different selections of the active vectors, are encompassed by the analysis. The analytical study is supported with simulation and experimental result, obtained using a five-phase induction motor.

Joel Prieto, Federico Barrero, Emil Levi, Sergio Toral, Martin Jones, Mario J. Durán

Analytical Evaluation of Switching Characteristics in Five-Phase Drives with Discontinuous Space Vector Pulse Width Modulation Techniques

Joel Prieto, Federico Barrero, Sergio Toral, Universidad de Sevilla, Sevilla, Spain
Emil Levi, Martin Jones, Liverpool John Moores University, Liverpool, UK
Mario J. Durán, Universidad de Málaga, Málaga, Spain

Keywords: Multiphase drives, Harmonic Analysis, Space Vector Pulse Width Modulation (SVPWM)

Abstract

This paper deals with flux harmonic distortion factor (HDF) and current ripple analysis for various discontinuous space vector PWM (SVPWM) techniques, applicable in conjunction with five-phase two-level inverter-fed ac motor drives. The analysis is based on the application of the recently developed polygon approach for multiphase systems. The results are compared throughout with the corresponding continuous SVPWM techniques. Two different SVPWM methods, based on different selections of the active vectors, are encompassed by the analysis. The analytical study is supported with simulation and experimental result, obtained using a five-phase induction motor.

Introduction

Multiphase machines are nowadays predominantly supplied from two-level voltage source inverters (VSIs). For the purpose of the VSI control, both continuous carrier-based and space vector PWM methods have been developed, for various phase numbers, which generate sinusoidal output voltages. The relationship between continuous carrier-based and space vector PWM has also been studied [1,2]. Discontinuous PWM techniques for multiphase inverters have received some attention as well, and such PWM schemes are available for five-phase and seven-phase inverters [3-7].

Different PWM strategies lead to different behaviour with regard to the performance indicators that can be used to assess the quality of output waveforms. Recently, an effort has been put into evaluation of the switching characteristics (flux HDF and current ripple) of multiphase PWM strategies. For this purpose, the complex space vector approach has been adapted to use in multiphase systems in [8], where a comprehensive study and comparison of various continuous PWM techniques for five-phase systems have been reported. This was followed by the extension of the commonly used approach in three-phase systems, based on delta connection, to multiphase systems, based on multiple polygon connections in [9]. A further study related to two specific continuous SVPWM techniques for five-phase VSIs has been reported in [10,11]. Detailed investigation of both flux HDF and current ripple has been conducted, using again the complex space vector approach.

Discontinuous multiphase PWM techniques have been studied to a lesser extent than the corresponding continuous PWM methods. This is especially true with regard to the flux HDF and current ripple, where the only considerations available are those of [5,12]. However, the approach used in [5] is different from the one used here, which utilises the polygon approach developed in [9] for continuous PWM techniques.

This paper evaluates switching ripple characteristics, in terms of flux HDF and current ripple, for a number of discontinuous PWM schemes, which are obtained from two specific continuous SVPWM algorithms for five-phase VSIs. The polygon connection and its conversion into equivalent star connection are used to compare PWM algorithms, obtaining their HDF characteristics and the generated current ripple. The route followed corresponds to the one in [9], while the corresponding continuous SVPWM schemes have been covered in [10,11]. The results obtained for discontinuous SVPWM methods are compared to those available for corresponding continuous methods. Theoretical findings are illustrated with experimental results collected from a five-phase induction motor drive. It is shown that discontinuous PWM techniques, similar as in three-phase drives, can offer lower current ripple at higher modulation indices.

Considered SVPWM techniques

A five-phase VSI is characterized with 32 space vectors (30 active plus two zero states), which have projections in two orthogonal planes according to the Clarke decomposition theory and assuming that the machine has star connected winding with isolated neutral point. Fig. 1 illustrates space vector projections in these planes. To achieve the desired reference in the first ($\alpha - \beta$) plane while simultaneously zeroing the voltage (on average) in the second ($x - y$) plane, it is necessary to select four active vectors. In the two available SVPWM methods [10], the active vectors are selected either as two medium and two large that border the reference in the first plane, termed further on as (2L + 2M) method, or as four large vectors neighbouring the reference, denoted further on as (4L) method. These two vector selections are illustrated in Figs. 2 and 3. Table 1 summarizes the duty cycles (relative ontimes over the switching period (δ) of active vectors selected, where the modulation index is defined as $M = V_1/(V_{dc}/2)$, s is an integer from 1 to 10 representing the sector where the reference is placed in the ($\alpha - \beta$) plane, V_1 is the peak of the fundamental voltage, and the defined constants are $K_1 = \sin \pi/5$, $K_2 = \sin 2\,\pi/5$, $J_1 = \cos \pi/5$ and $J_2 = \cos 2\,\pi/5$.

Regardless of the vector selection scheme, both (2L + 2M) and (4L) SVPWM techniques achieve the same utilisation of the DC bus voltage [10]. Also, the duty cycles of the zero vectors (δ_z) are the same and equally shared between two zero states. The most important consequence of using either (2L + 2M) or (4L) vector selection schemes is the different switching pattern, which means that the number of commutations within a period is not the same: the average switching frequency of the (4L) SVPWM method is 1.4 times higher than with the (2L + 2M) SVPWM method [10].

Table 1: Duty cycles of active vectors applied in SVPWM techniques

(2L + 2M) SVPWM	(4L) SVPWM
$\delta_{am} = MK_1 \sin\left(s\frac{\pi}{5} - \vartheta\right)$	$\delta_{cl} = MK_1 \sin\left(s\frac{\pi}{5} - \vartheta\right)$
$\delta_{al} = MK_2 \sin\left(s\frac{\pi}{5} - \vartheta\right)$	$\delta_{al} = MK_1\left[\sin\left(\vartheta - (s-1)\frac{\pi}{5}\right) + (2J_1 - 1)\sin\left(s\frac{\pi}{5} - \vartheta\right)\right]$
$\delta_{bm} = MK_1 \sin\left(\vartheta - (s-1)\frac{\pi}{5}\right)$	$\delta_{bl} = MK_1\left[\sin\left(s\frac{\pi}{5} - \vartheta\right) + (2J_1 - 1)\sin\left(\vartheta - (s-1)\frac{\pi}{5}\right)\right]$
$\delta_{bl} = MK_2 \sin\left(\vartheta - (s-1)\frac{\pi}{5}\right)$	$\delta_{dl} = MK_1 \sin\left(\vartheta - (s-1)\frac{\pi}{5}\right)$
$\delta_z = 1 - MK_2 \cos\left((2s-1)\frac{\pi}{10} - \vartheta\right)$	$\delta_z = 1 - MK_2 \cos\left((2s-1)\frac{\pi}{10} - \vartheta\right)$

The (2L+2M) and (4L) continuous SVPWM techniques can be extended to discontinuous methods by using only one zero voltage vector within a switching period. Although an infinite number of discontinuous patterns can be developed, the six relevant cases are DPWMMAX, DPWMMIN, DPWM0, DPWM1, DPWM2 and DPWM3. The main consequence of using a discontinuous method is that the switching state of one VSI leg is kept constant during the switching period.

Table 2 shows different methods of zero state partitioning which yield continuous and all the discontinuous modulation techniques discussed in this paper. These partitions are valid for both (2L + 2M) and (4L) schemes. Note that DPWM0, DPWM1, DPWM2 and DPWM3 can be derived from DPWMMAX and DPWMMIN depending on the sector (or half-sector). For example, DPWM0 is like DPWMMIN in sector 1, but like DPWMMAX in sector 2; DPWM1 is the same as DPWMMAX in the first half-sector 1 and the second half-sector 2, while it is like DPWMMIN in between these two half-sectors.

Polygonal analysis of five-phase SVPWM techniques

The approach in the flux HDF evaluation follows the one developed in [9], where the analysis was however only applied to continuous modulation techniques. A previous work also compares the obtained flux HDF using continuous and discontinuous modulation techniques, but the proposed analysis was based on a completely different analytical approach, the complex space vector technique [12]. Here, the method proposed in [9] is extended to discontinuous modulation techniques, and obtained results are validated against those presented in [12].

The polygonal approach is based on the two possible polygon connections of the five-phase system (Fig. 4) and utilization of the H-bridge inverter and an equivalent load (Fig. 5), as detailed in [9]. The phase load is represented with a resistance (R), an inductance (L) and an internal electromotive force or emf (e) connected in series. It is assumed for the analysis that switching frequency is much higher than the fundamental frequency, so that the resistance can be neglected during a switching period and the current variation can be assumed linear. The load emf can be also considered constant and equal to the reference line voltage during the switching period.

The first step in the proposed analysis is the establishment of the switching patterns that characterise the modulation techniques. Different switching patterns are shown in Fig. 6a for the (2L +

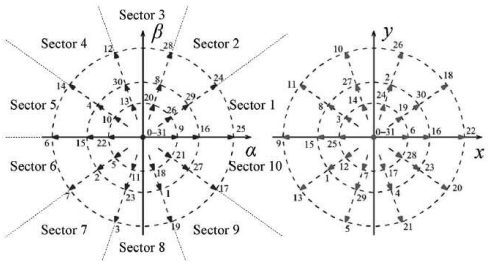

Fig. 1: Voltage vectors in the $\alpha - \beta$ and $x - y$ planes for a five-phase VSI

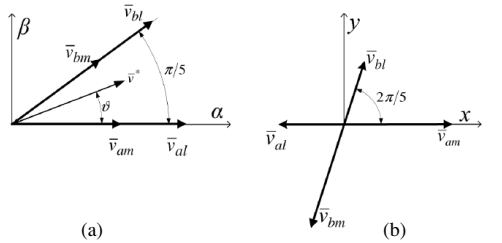

Fig. 2: Selected vectors when reference is in sector 1 for (2L+2M) SVPWM: a) $\alpha - \beta$, plane b) $x - y$ plane

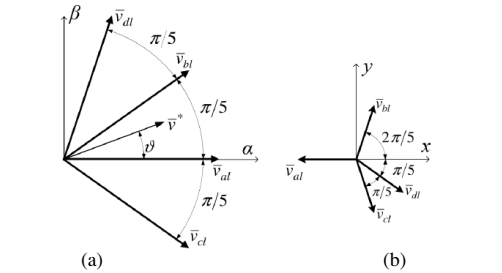

Fig. 3: Selected vectors when reference is in sector 1 for (4L) SVPWM: a) $\alpha - \beta$, plane b) $x - y$ plane

Joel Prieto, Federico Barrero, Emil Levi, Sergio Toral, Martin Jones, Mario J. Durán

Table 2: Zero state duty cycle δ_z partitioning for all considered modulation techniques

	Sector 1	Sector 2	Sector 3	Sector 4	Sector 5	Sector 6	Sector 7	Sector 8	Sector 9	Sector 10
SWPWM	$\delta_0 = \delta_{31} = \delta_z/2$									
DPWMMAX	$\delta_0 = 0$									
DPWMMIN	$\delta_{31} = 0$									
DPWM0	$\delta_{31} = 0$	$\delta_0 = 0$	$\delta_{31} = 0$	$\delta_0 = 0$	$\delta_{31} = 0$	$\delta_0 = 0$	$\delta_{31} = 0$	$\delta_0 = 0$	$\delta_{31} = 0$	$\delta_0 = 0$
DPWM1		$\delta_{31} = 0$	$\delta_0 = 0$	$\delta_{31} = 0$	$\delta_0 = 0$	$\delta_{31} = 0$	$\delta_0 = 0$	$\delta_{31} = 0$	$\delta_0 = 0$	$\delta_{31} = 0$
DPWM2	$\delta_0 = 0$	$\delta_{31} = 0$	$\delta_0 = 0$	$\delta_{31} = 0$	$\delta_0 = 0$	$\delta_{31} = 0$	$\delta_0 = 0$	$\delta_{31} = 0$	$\delta_0 = 0$	$\delta_{31} = 0$
DPWM3		$\delta_0 = 0$	$\delta_{31} = 0$	$\delta_0 = 0$	$\delta_{31} = 0$	$\delta_0 = 0$	$\delta_{31} = 0$	$\delta_0 = 0$	$\delta_{31} = 0$	$\delta_0 = 0$

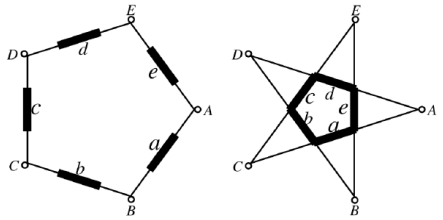

Fig. 4: Five-phase machine windings showing adjacent polygon connection (left), and non-adjacent polygon connection (right).

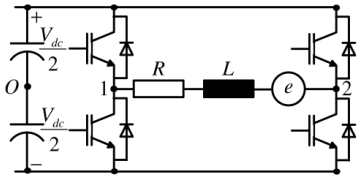

Fig. 5: H-bridge inverter and the equivalent phase load representation for the analysis

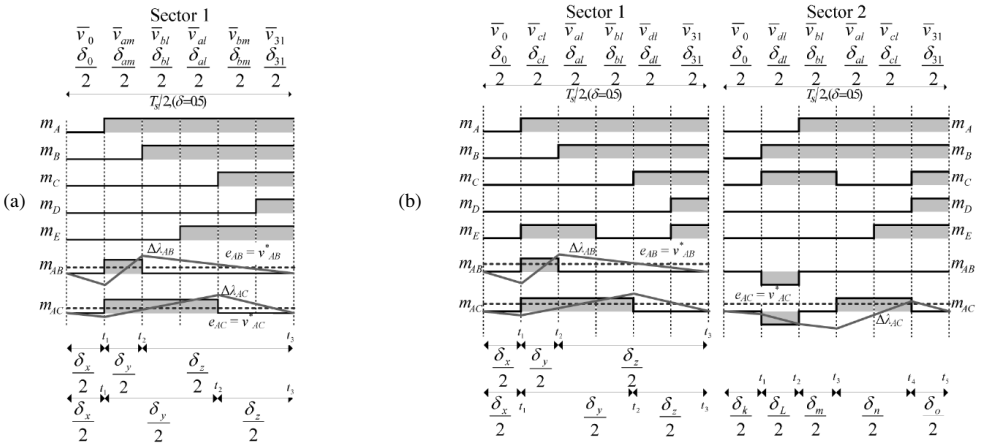

Fig. 6: Switching patterns over the first half of the switching period for: a) (2L + 2M) SVPWM in sector 1, b) (4L) SVPWM in sectors 1 and 2

2M) case and in Fig. 6b for the (4L) case. Figs. 6a and 6b represent the switching pattern of each leg (m_A, m_B, m_C, m_D and m_E), and the adjacent and the non-adjacent line voltages (m_{AB} and m_{AC}, respectively), during the first half of a switching period ($T_s/2$). The continuous PWM case is shown. Ten commutations appear in each switching period and sector in the (2L + 2M) SVPWM, two per leg.

Fig. 6b shows the switching pattern in sectors 1 and 2 for the (4L) SVPWM. It requires fourteen commutations in a switching period: four legs are similar as in the (2L + 2M) case, but one leg has six commutations. As can be seen from Fig. 6b, the leg with an increased number of commutations changes from sector to sector.

Discontinuous (2L + 2M) schemes can be derived from Fig. 6a, using the δ_0 and δ_{31} values given in Table 2. When considering a discontinuous SVPWM method, the number of commutations per switching period decreases. For instance, leg A remains clamped for the (2L + 2M) DPWMMAX method in sector 1 ($\delta_0 = 0$ in sector 1, according to Table 2), while the same happens with leg D for the (2L + 2M) DPWMMIN technique in sector 1 (in this case $\delta_{31} = 0$, Table 2). Total number of commutations for (2L + 2M) SVPWM methods in a switching period reduces to eight. The discontinuous (4L) SVPWM switching patterns can be also deduced considering the δ_0 and δ_{31} values given in Table 2 and using Fig. 6b. For discontinuous (4L) SVPWM techniques the total number of commutations is reduced to ten.

The polygon analysis is carried out using the duty cycles shown in Table 1. The reasons behind this approach are that equivalent carrier-based PWM techniques for all the continuous and discontinuous (4L) SVPWM methods are not available, and that for (4L) SVPWM there is an excessive number of integration intervals (see Table 2). The reference line voltages using either (2L + 2M) or (4L) techniques are the same. These values are expressed as follows:

$$\begin{aligned} v^*_{AB} &= M\left(\cos\left(\vartheta\right)-\cos\left(\vartheta-2\pi/5\right)\right) \\ &= 2K_1M\sin\left(\pi/5-\vartheta\right) \\ v^*_{AC} &= M\left(\cos\left(\vartheta\right)-\cos\left(\vartheta-4\pi/5\right)\right) \\ &= 2K_2M\sin\left(2\pi/5-\vartheta\right) \end{aligned} \tag{1}$$

An error exists between the applied and the reference voltage vectors at any instant of time due to the discrete nature of the inverter. This error produces current ripple in the load, and generates the harmonic flux ($\Delta\lambda$), which can be given as:

$$\Delta\lambda = L_\sigma \Delta i = (v - v^*)\Delta t \tag{2}$$

where v is the instantaneous line voltage of each polygon connection, v^* is the reference line voltage during the switching period, and L_σ is the inductance of the equivalent load which is much more difficult to define in multiphase machines than in the three-phase case [9,11]. Notice that the harmonic flux normalisation factor, introduced in [9] as $\lambda_N = V_{dc}T_s/8$, is also utilised here.

Next, the harmonic flux generated on the load during a switching period must be determined. Table 3 in Appendix characterises the subintervals that appear in a switching period of the analytical analysis. These subintervals depend on the considered polygon and sector, as shown in Fig. 6. Notice that (2L + 2M) schemes have only three different intervals (further on *x*, *y*, *z*). The same applies to (4L) techniques, however five subintervals appear in sectors 2, 3, 7 and 8 (from now on *k*, *l*, *m*, *n*, *p*) when considering the non-adjacent polygon. If v_{12} is the line voltage defined in Fig. 5, then $v_{12} = v_{AB}$ for the adjacent polygon (polygon 1) and $v_{12} = v_{AC}$ for the non-adjacent polygon (polygon 2). The normalized harmonic flux deviations at the end of the *x*, *y*, *z* subintervals (see Table 3, Appendix) are:

$$\begin{aligned} &\Delta\lambda(0) = 0 \\ &\Delta\lambda(t_1) = -2v_{12}\delta_x \\ &\Delta\lambda(t_2) = -2v_{12}\delta_x + 2\left(sign(v_{12})\cdot 2 - v_{12}\right)\delta_y \\ &\Delta\lambda(t_3) = 0 \end{aligned} \tag{3}$$

However, the normalized harmonic flux deviations at the end of the *k*, *l*, *m*, *n*, *p* subintervals are in sectors 2, 3 given with:

$$\begin{aligned} &\Delta\lambda(0) = 0 \\ &\Delta\lambda(t_1) = -2v_{12}\delta_k \\ &\Delta\lambda(t_2) = -2v_{12}\delta_k + 2(-\text{sign}(v_{12})\cdot 2 - v_{12})\delta_l \\ &\Delta\lambda(t_3) = -2v_{12}\delta_k + 2(-\text{sign}(v_{12})\cdot 2 - v_{12})\delta_l - 2v_{12}\delta_m \\ &\Delta\lambda(t_4) = -2v_{12}\delta_k + 2(-\text{sign}(v_{12})\cdot 2 - v_{12})\delta_l - 2v_{12}\delta_m \\ &\qquad +2(\text{sign}(v_{12})\cdot 2 - v_{12})\delta_n \\ &\Delta\lambda(t_5) = 0 \end{aligned} \tag{4}$$

while in sectors 7, 8 the corresponding expressions are:

$$\begin{aligned} &\Delta\lambda(0) = 0 \\ &\Delta\lambda(t_1) = -2v_{12}\delta_k \\ &\Delta\lambda(t_2) = -2v_{12}\delta_k + 2(\text{sign}(v_{12})\cdot 2 - v_{12})\delta_l \\ &\Delta\lambda(t_3) = -2v_{12}\delta_k + 2(\text{sign}(v_{12})\cdot 2 - v_{12})\delta_l - 2v_{12}\delta_m \\ &\Delta\lambda(t_4) = -2v_{12}\delta_k + 2(\text{sign}(v_{12})\cdot 2 - v_{12})\delta_l - 2v_{12}\delta_m \\ &\qquad +2(-\text{sign}(v_{12})\cdot 2 - v_{12})\delta_n \\ &\Delta\lambda(t_5) = 0 \end{aligned} \tag{5}$$

As the next step, the squared value of the harmonic flux over the switching period has to be obtained. This evaluation can be conducted, due to the existing symmetry in two half-periods of the switching period, using one half of the switching period as follows:

$$\Delta\lambda^2{}_{RMS} = \frac{2}{T_s}\int_0^{T_s/2}\Delta\lambda^2(t)\,dt \tag{6}$$

Assuming a linear change of $\Delta\lambda$, the continuous integration defined in (6) can be replaced by a generic solution. This solution depends on the number of subintervals evaluated during the switching period. As a consequence, different expressions are valid depending on the number of subintervals. The generic solution for sectors characterised by three subintervals is given with

$$\Delta\lambda^2{}_{RMS} = \frac{1}{3}\begin{bmatrix} \delta_x\Delta\lambda^2(t_1) \\ +\delta_y[\Delta\lambda^2(t_1)+\Delta\lambda(t_1)\Delta\lambda(t_2)+\Delta\lambda^2(t_2)] \\ +\delta_z\Delta\lambda^2(t_2) \end{bmatrix} \tag{7}$$

while the solution for sectors with five subintervals is

$$\Delta\lambda^2{}_{RMS} = \frac{1}{3}\begin{bmatrix} \delta_k\Delta\lambda^2(t_1) \\ +\delta_l[\Delta\lambda^2(t_1)+\Delta\lambda(t_1)\Delta\lambda(t_2)+\Delta\lambda^2(t_2)] \\ +\delta_m[\Delta\lambda^2(t_2)+\Delta\lambda(t_2)\Delta\lambda(t_3)+\Delta\lambda^2(t_3)] \\ +\delta_n[\Delta\lambda^2(t_3)+\Delta\lambda(t_3)\Delta\lambda(t_4)+\Delta\lambda^2(t_4)] \\ \delta_p\Delta\lambda^2(t_4) \end{bmatrix} \tag{8}$$

Next, the flux *HDF* is determined by integrating the squared harmonic flux over a fundamental period. Assuming positive values of emf and taking into account the symmetric properties of the line voltages, this evaluation can be reduced to the positive half-waveform of the fundamental line voltage for polygons 1 and 2, respectively, so that the following is obtained:

$$HDF_{P1} = \Delta\lambda^2{}_{RMSF} = \frac{1}{\pi}\int_{-4\pi/5}^{\pi/5}\Delta\lambda^2{}_{RMS}\,d\vartheta \tag{9}$$

$$HDF_{P2} = \Delta\lambda^2{}_{RMSF} = \frac{1}{\pi}\int_{-3\pi/5}^{2\pi/5}\Delta\lambda^2{}_{RMS}\,d\vartheta \tag{10}$$

It must be noted that (9) and (10) are divided into a number of integrals, depending on the angular span involved in a particular discontinuous modulation technique. While SVPWM, DPWMMAX, DPWMMIN, DPWM0 and DPWM2 techniques split the original integral into segments of $\pi/5$ radians span, DWPM1 and DPWM3 methods use $\pi/10$ radians span.

Joel Prieto, Federico Barrero, Emil Levi, Sergio Toral, Martin Jones, Mario J. Durán

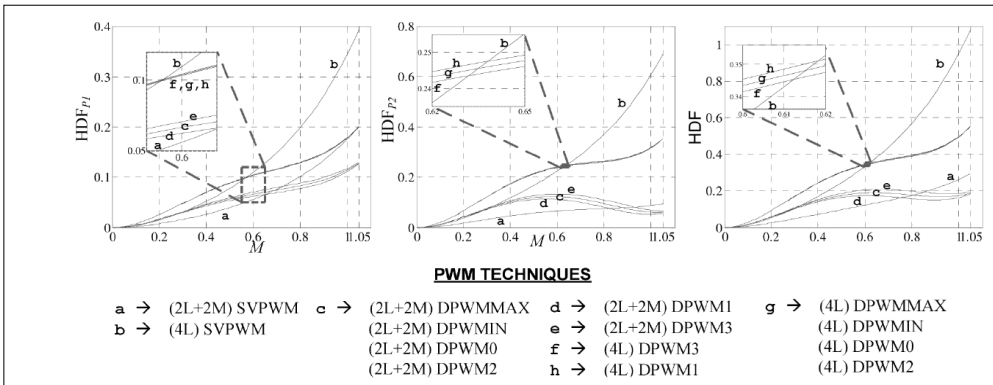

Fig. 7: Flux HDF for all considered PWM techniques for the same average switching frequency

The per-phase flux *HDF* of the equivalent star connection is obtained by summing (9) and (10) and dividing by 5. The analytical expressions of flux *HDF* using individual polygons and complete flux *HDF* solution are evaluated and detailed in Tables 4 and 5 (see Appendix). These analytical expressions, which define *HDF* as a function of the modulation index, are used to examine the behaviour of all the discontinuous SVPWM techniques and to compare them with the corresponding continuous schemes. To make a fair comparison of the flux *HDF*, the same average switching frequency (*ASF*) should be used. For this purpose squared harmonic flux rms (i.e. *HDF*) has to be pre-multiplied by the squared average switching frequency (ASF^2). If the continuous (2L + 2M) SVPWM switching frequency is considered as the base switching frequency (*ASF* = 1), for all discontinuous (4L) PWM techniques *ASF* = 1; for continuous (4L) SVPWM *ASF* = 1.4, and *ASF* = 0.8 for all discontinuous (2L + 2M) techniques. Hence the derived analytical expressions are multiplied by ASF^2, and plots are shown in Fig. 7.

The obtained theoretical results for the same base switching frequency and listed in Tables 4 and 5 are identical to those reported in [12] for continuous and discontinuous SVPWM schemes. It can be seen in Fig. 7 that continuous (2L + 2M) SVPWM (curve a) achieves the best performance for low modulation index *M*, while discontinuous (2L + 2M) techniques (curves c, d, e) are better for the high-range modulation indices. Among them, DPWM1 is better than the other ones. The cross-over between the best curves is around *M* = 0.76, for (2L + 2M) DPWM1 and continuous (2L + 2M) SVPWM. In the case of (4L) SVPWM schemes, the trends for continuous and discontinuous schemes are the same, but the difference between discontinuous techniques is marginal. It can also be noted that the higher average switching frequencies penalise the performance of all (4L) techniques.

Current ripple RMS

Flux *HDF* determination does not depend on the load, and it is very helpful in real applications for the analysis of the generated current ripple and the calculation of the current *THD*. The final goal in the polygonal analysis is to derive the current *THD* from the flux *HDF* for any load in the star topology. To obtain these relationships, a correspondence between flux *HDF* using the polygonal and complex space vector approaches must be established. This is so because different harmonics are multiplied by different factors for each set of line voltages applied to the load. The correspondence between flux *HDFs* obtained using the polygonal and complex space vector approaches can be given as:

$$HDF_{\mathrm{P1}} = \left(2K_1\right)^2 HDF_{\alpha\beta} + \left(2K_2\right)^2 HDF_{\mathrm{xy}} \tag{11}$$

$$HDF_{P2} = \left(2K_2\right)^2 HDF_{\alpha\beta} + \left(2K_1\right)^2 HDF_{\mathrm{xy}} \tag{12}$$

$$HDF_{\mathrm{P1}} + HDF_{\mathrm{P2}} = 4\left(K_1^2 + K_2^2\right)\left(HDF_{\alpha\beta} + HDF_{\mathrm{xy}}\right) \tag{13}$$

$$HDF_{\mathrm{P1}} + HDF_{\mathrm{P2}} = 5\left(HDF_{\alpha\beta} + HDF_{\mathrm{xy}}\right) \tag{14}$$

The first step to obtain the current THD is to derive squared current ripple rms from the flux HDF analysis. This is a complex task because it is not easy to identify a unique inductance for each polygon. However, use of (11) to (14) and the space vector approach simplify this step, allowing the following expressions for the current ripple to be derived:

$$Irms_{\mathrm{P1}}^2 = \left(\frac{V_{\mathrm{dc}}T_{\mathrm{s}}}{8}\right)^2 \left(2K_1\right)^2 \frac{HDF_{\alpha\beta}}{L_{\alpha\beta}^2} + \left(2K_2\right)^2 \frac{HDF_{\mathrm{xy}}}{L_{\mathrm{xy}}^2} \tag{15}$$

$$Irms_{\mathrm{P2}}^2 = \left(\frac{V_{\mathrm{dc}}T_{\mathrm{s}}}{8}\right)^2 \left(2K_2\right)^2 \frac{HDF_{\alpha\beta}}{L_{\alpha\beta}^2} + \left(2K_1\right)^2 \frac{HDF_{\mathrm{xy}}}{L_{\mathrm{xy}}^2} \tag{16}$$

$$Irms_{\mathrm{polygonal}}^2 = 4\left(K_1^2 + K_2^2\right)\left(\frac{V_{\mathrm{dc}}T_{\mathrm{s}}}{8}\right)^2 \left(\frac{HDF_{\alpha\beta}}{L_{\alpha\beta}^2} + \frac{HDF_{\mathrm{xy}}}{L_{\mathrm{xy}}^2}\right) \tag{17}$$

Here $L_{\alpha\beta}$, and L_{xy} are the equivalent inductances of the $\alpha\beta$, and *xy* planes for switching harmonics, and $L_{\alpha\beta} \approx L_{\mathrm{ls}} + L_{\mathrm{lr}}$, $L_{\mathrm{xy}} = L_{\mathrm{ls}}$. It follows from (17) that squared current ripple rms is five times higher using the polygonal connection approach than the per-phase value of the equivalent star-connected load, obtained using the complex space vector technique. The per-phase value of the equivalent star connected load is thus 1/5 of the value obtained using (17). Finally, per-phase stator current *THD* can be obtained from (15) and (16) as

$$THD_{\mathrm{star}} = \sqrt{\frac{\left(Irms_{\mathrm{P1}}^2 + Irms_{\mathrm{P2}}^2\right)/5}{Irms_{\mathrm{fundP1}}^2/\left(2K_1\right)^2}} = \sqrt{\frac{\left(Irms_{\mathrm{P1}}^2 + Irms_{\mathrm{P2}}^2\right)/5}{Irms_{\mathrm{fundP2}}^2/\left(2K_2\right)^2}} \tag{18}$$

Simulation and experimental results

In order to verify analytical and theoretical results, a simulation study has been performed using Matlab/Simulink. Fig. 8 summarizes obtained results for the (2L + 2M) and (4L) modulation methods. Stator current THD is employed as the figure of merit and a five-phase induction machine with the following electrical parameters is used: R_s = 12.85 Ω, R_r = 11.15 Ω, L_{ls} = 85.8 mH, L_{lr} = 21.4 mH, L_m = 687.8 mH. DC bus voltage is set to 600 V, and *V/f* operation mode is utilised, with the modulation index and the fundamental frequency changed from M = 0.1 @ f = 5 Hz to M = 1 @ f = 50 Hz. Stator current of one phase was recorded for both polygon connections, and current THD in steady state operation for the equivalent load in the star topology was calculated according to (18) and plotted in Fig. 8.

An experimental evaluation has been also conducted with the load connected in the star topology. Experimental tests have been performed on a five-phase induction machine with parameters given above, operated in the open loop with *V/f* = const. profile for ten operating points, for each modulation technique. All PWM schemes were implemented in a TMS320LF28335 Texas Instruments DSP, using an average switching frequency of 2 kHz. The DC link voltage was approximately 600 V. Harmonic content of a phase current has been measured and the THD evaluated. Fig. 9 presents the obtained results, showing the stator current THDs as a function of the modulation index.

As expected from theoretical results, the current THD increases with the modulation index for all the analysed techniques, and continuous methods offer lower THD values than discontinuous ones for low modulation indices when the same average switching frequency is considered. A good agreement is obtained between simulation and experimental results, confirming that the stator current THD can be predicted in real applications from the analytical flux HDF. The small differences visible for discontinuous schemes in Fig. 7 cannot be observed in simulation and experimental results. It can be also noted that (2L + 2M) continuous SVPWM can be used for low modulation indices, while any (2L + 2M) discontinuous SVPWM technique offers better performance at high modulation indices, when considering the same average switching frequency. (4L) SVPWM techniques offer worse behaviour (higher THD) at the same average switching frequency. Notice also that (2L + 2M) techniques enable an easier implementation in real-time using DSPs, since (4L) methods require an increased number of commutations in one inverter leg in each sector.

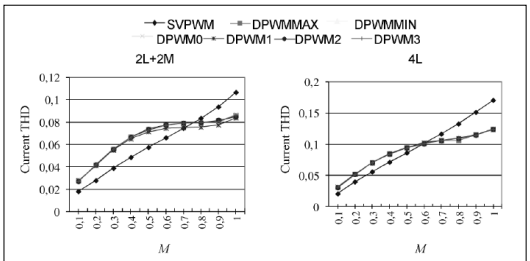

Fig. 8: Simulation results: values for current THD at 2 kHz average switching frequency, for (a) (2L + 2M) SVPWM methods, (b) (4L) SVPWM techniques.

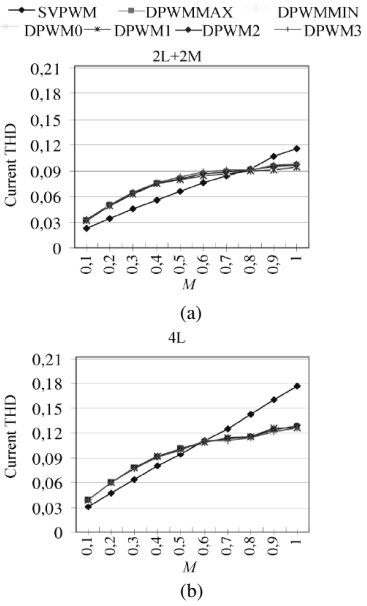

Fig. 9: Experimental results: measured values for current THD at 2 kHz average switching frequency, for (a) (2L + 2M) SVPWM methods, (b) (4L) SVPWM techniques.

Conclusion

The polygon-based analysis of output current ripple of a five-phase inverter, using discontinuous space vector PWM techniques, is presented in this paper and compared to the performance obtained with corresponding continuous SVPWM methods. It is shown analytically and experimentally that (2L+2M) PWM methods are better than (4L) techniques. For high modulation index range, discontinuous (2L+2M) DPWM1 offers the best performance. The full set of analytical expressions which describe HDF of each individual technique is also provided.

References

[1] D. Dujic, M. Jones, E. Levi, "Continuous carrier-based vs. space vector PWM for five-phase VSI," The IEEE Region 8 EUROCON 2007: Int. Conf. on 'Computer as a Tool', Warsaw, Poland, 2007, pp. 1772-1779.

[2] A. Iqbal, S. Moinuddin, "Comprehensive relationship between carrier-based PWM and space vector PWM in a five-phase VSI," IEEE Trans. on Power Electronics, vol. 24, no. 10, 2009, pp. 2379-2390.

[3] O. Ojo, G. Dong, "Generalized discontinuous carrier-based PWM modulation scheme for multi-phase converter-machine systems," Proc. IEEE Industry Applications Society Annual Meeting IAS, Hong Kong, 2005, pp. 1374-1381.

[4] X.F. Zhang, F. Yu, H.S. Li, Q.G. Song, "A novel discontinuous space vector PWM control for multiphase inverter," Proc. Int. Symp. Power Electronics, Electrical Drives, Automation and Motion SPEEDAM, Taormina, Italy, 2006, pp. 1133-1136.

[5] S. Halasz, "Discontinuous modulation of multiphase inverter-fed AC motor," Proc. European Conf. on Power Electronics and Applications EPE, Barcelona, Spain, 2009, CD-ROM paper 0569.

[6] M.A. Khan, S.M. Ahmed, A. Iqbal, H. Abu-Rub, "Discontinuous space vector PWM strategies for a seven-phase voltage source inverter," Proc. IEEE Industrial Electronics Society Annual Meeting IECON, Porto, Portugal, 2009, pp. 397-402.

[7] L. Zarri, M. Mengoni, A. Tani, G. Serra, D. Casadei, "Minimization of the power losses in IGBT multiphase inverters with carrier-based pulsewidth modulation," IEEE Trans. on Industrial Electronics, vol. 57, no. 11, 3695 -3706, 2010.

[8] D. Dujic, M. Jones, E. Levi, "Analysis of output current ripple rms in multiphase drives using space vector approach," IEEE Trans. on Power Electronics, vol. 24, no. 8, 2009, pp. 1926-1938.

[9] D. Dujic, M. Jones, E. Levi, "Analysis of output current ripple rms in multi-phase drives using polygon approach," IEEE Trans. on Power Electronics, vol.25, no.7, 2010, pp.1838-1849.

[10] D. Dujic, M. Jones, E. Levi, J. Prieto, F. Barrero, "Switching ripple characteristics of space vector PWM schemes for five-phase two-level voltage source inverters - Part 1: Flux harmonic distortion factors," IEEE Trans. on Industrial Electronics, vol. 58, no. 7, pp. 2789–2798, 2011.

[11] M. Jones, D. Dujic, E. Levi, J. Prieto, F. Barrero, "Switching ripple characteristics of space vector PWM schemes for five-phase two-level voltage source inverters - Part 2: Current ripple," IEEE Trans. on Industrial Electronics, vol. 58, no. 7, pp. 2799–2808, 2011.

[12] J. Prieto, M. Jones, F. Barrero, E. Levi, S. Toral, "Comparative analysis of discontinuous and continuous PWM techniques in VSI-fed five-phase induction motor," IEEE Trans. on Industrial Electronics, vol. 58, no. 12, pp. 5324-5335, 2011.

The authors

Joel Prieto received the B.Eng. degree in Electronic Engineering from the Universidad Católica Nuestra Señora de la Asunción, Paraguay, in 2005, and MSc degree from University of Seville, Spain, in 2009. In 2008, he joined the Electronic Engineering Department at University of Seville, Spain, where he is working toward his PhD degree. Mr. Prieto is a recipient of Scholarship from Itaipu Binacional/Parque Tecnológico Itaipu–Py for his PhD studies.

Federico Barrero received the MSc and PhD degrees in Electrical and Electronic Engineering from the University of Seville, Spain, in 1992 and 1998, respectively. In 1992, he joined the Electronic Engineering Department at the University of Seville, where he is currently an Associate Professor. He received the Best Paper Award from the IEEE Transactions on Industrial Electronics for 2009 and the IET Electric Power Applications Premium Award 2012.

Emil Levi received his MSc and the PhD degrees in Electrical Engineering from the University of Belgrade, Yugoslavia in 1986 and 1990, respectively. From 1982 till 1992 he was with the Dept. of Elec. Engineering, University of Novi Sad. He joined Liverpool John Moores University, UK in May 1992 and is since September 2000 Professor of Electric Machines and Drives. He serves as an Editor of the IEEE Trans. on Energy Conversion, a Co-Editor-in-Chief of the IEEE Trans. on Industrial Electronics, and as the Editor-in-Chief of the IET Electric Power Applications. He is the recipient of the Cyril Veinott Award of the IEEE Power and Energy Society for 2009 and the Best Paper Award of the IEEE Trans. on Industrial Electronics for 2008.

Sergio Toral Marín is Professor in the Department of Electronic Engineering at the University of Seville. His research interests include multiphase electrical machines, embedded operating systems, wireless sensor networks, and intelligent transportation systems. Dr. Toral received a PhD in electrical and electronic engineering from the University of Seville. He is a senior member of IEEE.

Martin Jones received his B.Eng degree (First Class Honours) in Electrical Engineering from the Liverpool John Moores University, UK in 2001. He was a research student at the Liverpool John Moores University from September 2001 till Spring 2005, when he received his PhD degree. Dr Jones was a recipient of the IEE Robinson Research Scholarship for his PhD studies and is currently with Liverpool John Moores University as a Reader. His research is in the area of high performance ac drives.

Mario J. Duran was born in Málaga, Spain, in 1975. He received the M.Sc. and Ph.D. degrees in Electrical Engineering from the University of Málaga Spain, in 1999 and 2003, respectively. He is currently an Associate Professor with the Electrical Engineering Department at the University of Málaga. His research interests include modeling and control of multiphase drives and renewable energies conversion systems.

Appendix

Table 3: Characterisation of the considered subintervals in the analytical analysis. Each sector and polygon is detailed in a switching period

	(2L + 2M)		(4L)	
Sector (range)	Polygon 1	Polygon 2	Polygon 1	Polygon 2
1 (0, π/5)	$\delta_x = \delta_0$ $\delta_y = \delta_{am}$ $\delta_z = \delta_{bl} + \delta_{al} + \delta_{bm} + \delta_{31}$	$\delta_x = \delta_0$ $\delta_y = \delta_{am} + \delta_{bl} + \delta_{al}$ $\delta_z = \delta_{bm} + \delta_{31}$	$\delta_x = \delta_0$ $\delta_y = \delta_{cl}$ $\delta_z = \delta_{al} + \delta_{bl} + \delta_{dl} + \delta_{31}$	$\delta_x = \delta_0$ $\delta_y = \delta_{cl} + \delta_{al} + \delta_{bl}$ $\delta_z = \delta_{dl} + \delta_{31}$
2 (π/5, 2π/5)	$\delta_x = \delta_0$ $\delta_y = \delta_{bm}$ $\delta_z = \delta_{al} + \delta_{bl} + \delta_{am} + \delta_{31}$	$\delta_x = \delta_0 + \delta_{bm}$ $\delta_y = \delta_{al}$ $\delta_z = \delta_{bl} + \delta_{am} + \delta_{31}$	$\delta_x = \delta_0$ $\delta_y = \delta_{dl}$ $\delta_z = \delta_{bl} + \delta_{al} + \delta_{cl} + \delta_{31}$	$\delta_k = \delta_0$ $\delta_l = \delta_{dl}$ $\delta_m = \delta_{bl}$ $\delta_n = \delta_{al} + \delta_{cl}$ $\delta_p = \delta_{31}$
3 (2π/5, 3π/5)	$\delta_x = \delta_0$ $\delta_y = \delta_{am} + \delta_{bl}$ $\delta_z = \delta_{al} + \delta_{bm} + \delta_{31}$	$\delta_x = \delta_0 + \delta_{am}$ $\delta_y = \delta_{bl}$ $\delta_z = \delta_{al} + \delta_{bm} + \delta_{31}$	$\delta_x = \delta_0 + \delta_{cl} + \delta_{al}$ $\delta_y = \delta_{bl} + \delta_{dl}$ $\delta_z = \delta_{31}$	$\delta_k = \delta_0$ $\delta_l = \delta_{cl}$ $\delta_m = \delta_{al}$ $\delta_n = \delta_{bl} + \delta_{dl}$ $\delta_p = \delta_{31}$
4 (3π/5, 4π/5)	$\delta_x = \delta_0 + \delta_{bm}$ $\delta_y = \delta_{al} + \delta_{bl}$ $\delta_z = \delta_{am} + \delta_{31}$	$\delta_x = \delta_0$ $\delta_y = \delta_{bm} + \delta_{al} + \delta_{bl}$ $\delta_z = \delta_{am} + \delta_{31}$	$\delta_x = \delta_0 + \delta_{dl}$ $\delta_y = \delta_{bl} + \delta_{al}$ $\delta_z = \delta_{cl} + \delta_{31}$	$\delta_x = \delta_0$ $\delta_y = \delta_{dl} + \delta_{bl} + \delta_{al}$ $\delta_z = \delta_{cl} + \delta_{31}$
5 (4π/5, π)	$\delta_x = \delta_0 + \delta_{am} + \delta_{bl}$ $\delta_y = \delta_{al} + \delta_{bm}$ $\delta_z = \delta_{31}$	$\delta_x = \delta_0$ $\delta_y = \delta_{am} + \delta_{bl} + \delta_{al} + \delta_{bm}$ $\delta_z = \delta_{31}$	$\delta_x = \delta_0$ $\delta_y = \delta_{cl} + \delta_{al}$ $\delta_z = \delta_{bl} + \delta_{dl} + \delta_{31}$	$\delta_x = \delta_0$ $\delta_y = \delta_{cl} + \delta_{al} + \delta_{bl} + \delta_{dl}$ $\delta_z = \delta_{31}$
6 (– π, – 4π/5)	$\delta_x = \delta_0 + \delta_{bm} + \delta_{al} + \delta_{bl}$ $\delta_y = \delta_{am}$ $\delta_z = \delta_{31}$	$\delta_x = \delta_0 + \delta_{bm}$ $\delta_y = \delta_{al} + \delta_{bl} + \delta_{am}$ $\delta_z = \delta_{31}$	$\delta_x = \delta_0 + \delta_{dl} + \delta_{bl} + \delta_{al}$ $\delta_y = \delta_{cl}$ $\delta_z = \delta_{31}$	$\delta_x = \delta_0 + \delta_{dl}$ $\delta_y = \delta_{bl} + \delta_{al} + \delta_{cl}$ $\delta_z = \delta_{31}$
7 (– 4π/5, – 3π/5)	$\delta_x = \delta_0 + \delta_{am} + \delta_{bl} + \delta_{al}$ $\delta_y = \delta_{bm}$ $\delta_z = \delta_{31}$	$\delta_x = \delta_0 + \delta_{am} + \delta_{bl}$ $\delta_y = \delta_{al}$ $\delta_z = \delta_{bm} + \delta_{31}$	$\delta_x = \delta_0 + \delta_{cl} + \delta_{al} + \delta_{bl}$ $\delta_y = \delta_{dl}$ $\delta_z = \delta_{31}$	$\delta_k = \delta_0$ $\delta_l = \delta_{cl} + \delta_{al}$ $\delta_m = \delta_{bl}$ $\delta_n = \delta_{dl}$ $\delta_p = \delta_{31}$
8 (– 3π/5, – 2π/5)	$\delta_x = \delta_0 + \delta_{bm} + \delta_{al}$ $\delta_y = \delta_{bl} + \delta_{am}$ $\delta_z = \delta_{31}$	$\delta_x = \delta_0 + \delta_{bm} + \delta_{al}$ $\delta_y = \delta_{bl}$ $\delta_z = \delta_{am} + \delta_{31}$	$\delta_x = \delta_0$ $\delta_y = \delta_{dl} + \delta_{bl}$ $\delta_z = \delta_{al} + \delta_{cl} + \delta_{31}$	$\delta_k = \delta_0$ $\delta_l = \delta_{dl} + \delta_{bl}$ $\delta_m = \delta_{al}$ $\delta_n = \delta_{cl}$ $\delta_p = \delta_{31}$
9 (– 2π/5, – π/5)	$\delta_x = \delta_0 + \delta_{am}$ $\delta_y = \delta_{bl} + \delta_{al}$ $\delta_z = \delta_{bm} + \delta_{31}$	$\delta_x = \delta_0 + \delta_{am}$ $\delta_y = \delta_{bl} + \delta_{al} + \delta_{bm}$ $\delta_z = \delta_{31}$	$\delta_x = \delta_0 + \delta_{cl}$ $\delta_y = \delta_{al} + \delta_{bl}$ $\delta_z = \delta_{dl} + \delta_{31}$	$\delta_x = \delta_0 + \delta_{cl}$ $\delta_y = \delta_{al} + \delta_{bl} + \delta_{dl}$ $\delta_z = \delta_{31}$
10 (– π/5, 0)	$\delta_x = \delta_0$ $\delta_y = \delta_{bm} + \delta_{al}$ $\delta_z = \delta_{bl} + \delta_{am} + \delta_{31}$	$\delta_x = \delta_0$ $\delta_y = \delta_{bm} + \delta_{al} + \delta_{bl} + \delta_{am}$ $\delta_z = \delta_{31}$	$\delta_x = \delta_0 + \delta_{dl} + \delta_{bl}$ $\delta_y = \delta_{al} + \delta_{cl}$ $\delta_z = \delta_{31}$	$\delta_x = \delta_0$ $\delta_y = \delta_{dl} + \delta_{bl} + \delta_{al} + \delta_{cl}$ $\delta_z = \delta_{31}$

Table 4: Flux HDF for (2L + 2M) PWM techniques using the polygon connection and the same base switching frequency

PWM Method	HDF Analytical expression
SVPWM (2L + 2M)	$HDF_{P1} = \frac{1}{16\pi}\left(8\pi - 35K_1 + 20K_2 - 2\pi J_1 - 10\pi J_2\right)M^4 - \frac{8}{9\pi}\left(3K_1 - K_2\right)M^3 + \frac{1}{3}\left(1 - J_2\right)M^2$ $HDF_{P2} = \frac{1}{16\pi}\left(6\pi - 15K_1 + 5K_2 + 4\pi J_1 - 2\pi J_2\right)M^4 - \frac{8}{9\pi}\left(K_1 + 3K_2\right)M^3 + \frac{1}{3}\left(1 + J_1\right)M^2$ $HDF = \frac{1}{16\pi}\left(14\pi - 50K_1 + 25K_2 + 2\pi J_1 - 12\pi J_2\right)M^4 - \frac{16}{9\pi}\left(2K_1 + K_2\right)M^3 + \frac{1}{3}\left(2 + J_1 - J_2\right)M^2$
DPWMMAX, DPWMMIN, DPWM0, DPWM2 (2L+2M)	$HDF_{P1} = \frac{1}{8\pi}\left(6\pi - 5K_1 + 10K_2 - 6\pi J_2\right)M^4 - \frac{1}{9\pi}\left(159K_1 - 53K_2\right)M^3 + \frac{4}{3}\left(1 - J_2\right)M^2$ $HDF_{P2} = \frac{1}{8\pi}\left(6\pi + 5K_1 + 15K_2 + 6\pi J_1\right)M^4 - \frac{1}{9\pi}\left(98K_1 + 69K_2\right)M^3 + \frac{4}{3}\left(1 + J_1\right)M^2$ $HDF = \frac{1}{8\pi}\left(12\pi + 25K_2 + 6\pi J_1 - 6\pi J_2\right)M^4 - \frac{1}{9\pi}\left(257K_1 + 16K_2\right)M^3 + \frac{4}{3}\left(2 + J_1 - J_2\right)M^2$
DPWM1 (2L + 2M)	$HDF_{P1} = \frac{1}{4\pi}\left(3\pi + 15K_1 - 5K_2 - 3\pi J_2\right)M^4 + \frac{2}{9\pi}\left(45 - 12K_1 + 4K_2 - 45J_1 - 90J_2\right)M^3 + \frac{4}{3}\left(1 - J_2\right)M^2$ $HDF_{P2} = \frac{1}{4\pi}\left(3\pi + 10K_1 + 5K_2 + 3\pi J_1\right)M^4 + \frac{2}{9\pi}\left(-4K_1 - 12K_2 - 45J_1 - 45J_2\right)M^3 + \frac{4}{3}\left(1 + J_1\right)M^2$ $HDF = \frac{1}{4\pi}\left(6\pi + 25K_1 + 3\pi J_1 - 3\pi J_2\right)M^4 + \frac{2}{9\pi}\left(45 - 16K_1 - 8K_2 - 90J_1 - 135J_2\right)M^3 + \frac{4}{3}\left(2 + J_1 - J_2\right)M^2$
DPWM3 (2L + 2M)	$HDF_{P1} = \frac{1}{4\pi}\left(3\pi - 20K_1 + 15K_2 - 3\pi J_2\right)M^4 + \frac{2}{9\pi}\left(-45 - 147K_1 + 49K_2 + 45J_1 + 90J_2\right)M^3 + \frac{4}{3}\left(1 - J_2\right)M^2$ $HDF_{P2} = \frac{1}{4\pi}\left(3\pi - 5K_1 + 10K_2 + 3\pi J_1\right)M^4 + \frac{2}{9\pi}\left(-94K_1 - 57K_2 + 45J_1 + 45J_2\right)M^3 + \frac{4}{3}\left(1 + J_1\right)M^2$ $HDF = \frac{1}{4\pi}\left(6\pi - 25K_1 + 25K_2 + 3\pi J_1 - 3\pi J_2\right)M^4 + \frac{2}{9\pi}\left(-45 - 241K_1 - 8K_2 + 90J_1 + 135J_2\right)M^3 + \frac{4}{3}\left(2 + J_1 - J_2\right)M^2$

Table 5: Flux HDF for (2L + 2M) PWM techniques using the polygon connection and the same base switching frequency

PWM Method	HDF Analytical expression
SVPWM (4L)	$HDF_{P1} = \frac{1}{16\pi}\left(8\pi - 35K_1 + 20K_2 - 2\pi J_1 - 10\pi J_2\right)M^4 + \frac{1}{9\pi}\left(-24K_1 + 8K_2\right)M^3 + \frac{1}{3}\left(1 - J_2\right)M^2$ $HDF_{P2} = \frac{1}{16\pi}\left(6\pi - 15K_1 + 5K_2 + 4\pi J_1 - 2\pi J_2\right)M^4 + \frac{1}{9\pi}\left(-96K_1 + 37K_2\right)M^3 + \frac{1}{3}\left(1 + J_1\right)M^2$ $HDF = \frac{1}{16\pi}\left(14\pi - 50K_1 + 25K_2 + 2\pi J_1 - 12\pi J_2\right)M^4 + \frac{1}{3\pi}\left(-40K_1 + 15K_2\right)M^3 + \frac{1}{3}\left(2 + J_1 - J_2\right)M^2$
DPWMMAX, DPWMMIN, DPWM0, DPWM2 (4L)	$HDF_{P1} = \frac{1}{8\pi}\left(6\pi - 5K_1 + 10K_2 - 6\pi J_2\right)M^4 + \frac{1}{9\pi}\left(-159K_1 + 53K_2\right)M^3 + \frac{4}{3}\left(1 - J_2\right)M^2$ $HDF_{P2} = \frac{1}{8\pi}\left(6\pi + 5K_1 + 15K_2 + 6\pi J_1\right)M^4 + \frac{1}{9\pi}\left(-186K_1 - 8K_2\right)M^3 + \frac{4}{3}\left(1 + J_1\right)M^2$ $HDF = \frac{1}{8\pi}\left(12\pi + 25K_2 + 6\pi J_1 - 6\pi J_2\right)M^4 - \frac{5}{3\pi}\left(23K_1 - 3K_2\right)M^3 + \frac{4}{3}\left(2 + J_1 - J_2\right)M^2$
DPWM1 (4L)	$HDF_{P1} = \frac{1}{16\pi}\left(12\pi + 30K_1 - 5K_2 - 12\pi J_2\right)M^4 - \frac{1}{9\pi}\left(18 + 189K_1 - 113K_2 + 24J_1 + 6J_2\right)M^3 + \frac{4}{3}\left(1 - J_2\right)M^2$ $HDF_{P2} = \frac{1}{16\pi}\left(12\pi + 25K_1 + 20K_2 + 12\pi J_1\right)M^4 - \frac{1}{9\pi}\left(42 + 156K_1 - 82K_2 + 66J_1 + 24J_2\right)M^3 + \frac{4}{3}\left(1 + J_1\right)M^2$ $HDF = \frac{1}{16\pi}\left(24\pi + 55K_1 + 15K_2 + 12\pi J_1 - 12\pi J_2\right)M^4 - \frac{5}{9\pi}\left(12 + 69K_1 - 39K_2 + 18J_1 + 6J_2\right)M^3 + \frac{4}{3}\left(2 + J_1 - J_2\right)M^2$
DPWM3 (4L)	$HDF_{P1} = \frac{1}{16\pi}\left(12\pi - 50K_1 + 45K_2 - 12\pi J_2\right)M^4 - \frac{1}{9\pi}\left(-18 + 129K_1 + 7K_2 - 24J_1 - 6J_2\right)M^3 + \frac{4}{3}\left(1 - J_2\right)M^2$ $HDF_{P2} = \frac{1}{16\pi}\left(12\pi - 5K_1 + 40K_2 + 12\pi J_1\right)M^4 - \frac{1}{9\pi}\left(-42 + 216K_1 + 98K_2 - 66J_1 - 24J_2\right)M^3 + \frac{4}{3}\left(1 + J_1\right)M^2$ $HDF = \frac{1}{16\pi}\left(24\pi - 55K_1 + 85K_2 + 12\pi J_1 - 12\pi J_2\right)M^4 - \frac{5}{9\pi}\left(-12 + 69K_1 + 21K_2 - 18J_1 - 6J_2\right)M^3 + \frac{4}{3}\left(2 + J_1 - J_2\right)M^2$

3.5. Paper 5

Authors: J. Prieto, E. Levi, F. Barrero y S. Toral.
Title: Output current ripple analysis for asymmetrical six-phase drives using double zero-sequence injection PWM.
Conferencia: Proceedings of 37th Annual Conference on IEEE Industrial Electronics Society (IECON 2011).
Pages: 3692-3697.
Date: November 2011.
Abstract: Modulation techniques for asymmetrical six-phase drives have been extensively studied during the last decade. This has included analysis of the switching behavior, in terms of harmonic flux distortion factor and current ripple rms value, for a number of available PWM methods. One particular PWM technique, which is frequently applied in practice, is the so-called double zero-sequence injection. Switching characteristics of this method have not been examined so far, and this paper attempts to fill in this gap. A theoretical study is reported at first. Theoretical findings are verified by experimental investigation, which includes comparison with a number of other PWM techniques for asymmetrical six-phase inverter-fed drives.

Output Current Ripple Analysis for Asymmetrical Six-Phase Drives Using Double Zero-Sequence Injection PWM

Joel Prieto[1], Emil Levi[2], Federico Barrero[1], Sergio Toral[1]
[1]Dpto. de Ingeniería Electrónica
Universidad de Sevilla
41092 Sevilla, Spain
{jprieto,fbarrero,toral}@esi.us.es
[2]School of Engineering
Liverpool John Moores University
Liverpool L3 3AF, United Kingdom
e.levi@ljmu.ac.uk

***Abstract*—Modulation techniques for asymmetrical six-phase drives have been extensively studied during the last decade. This has included analysis of the switching behavior, in terms of harmonic flux distortion factor and current ripple rms value, for a number of available PWM methods. One particular PWM technique, which is frequently applied in practice, is the so-called double zero-sequence injection. Switching characteristics of this method have not been examined so far, and this paper attempts to fill in this gap. A theoretical study is reported at first. Theoretical findings are verified by experimental investigation, which includes comparison with a number of other PWM techniques for asymmetrical six-phase inverter-fed drives.**

I. Introduction

A number of PWM techniques have been developed over the years for multiphase voltage source inverters [1-7]. This has included various phase numbers, such as five, six, seven, etc. The investigations are mostly concerned with Space Vector Pulse Width Modulation (SVPWM) because of the easiness of digital implementation and a better insight into the modulation scheme behavior, when compared to the carrier-based PWM methods. One particularly frequently analyzed case is an asymmetrical six-phase drive, with two three-phase stator windings displaced in space by 30 degrees, with isolated neutral points. A variety of different modulation techniques has been developed for such drives [3-7], which in essence can be viewed as being supplied from two three-phase inverters with outputs shifted in phase by 30 degrees.

An important property of all modulation strategies is the switching behavior, since it governs the current ripple rms value. It is usually analyzed using the flux harmonic distortion factor (HDF) approach and detailed studies have been performed recently for both asymmetrical six-phase inverters [4,5] and multiphase inverters with odd numbers of phases [8-11]. The PWM schemes for asymmetrical six-phase inverters, which have been analyzed in detail in [4,5] in terms of the HDF and current ripple are the following: continuous (C6_SVPWM12) and discontinuous (D6_SVPWM12_A, D6_SVPWM12_B1, D6_SVPWM12_B2) SVPWM based on 12 sectors, and continuous (C6_SVPWM24) and discontinuous (D6_SVPWM24_B1, D6_SVPWM24_B2) SVPWM based on 24 sectors. With regard to the HDF, under the conditions of the same average switching frequency and the DC bus voltage, better behavior was exhibited by the schemes based on 24 sectors.

One particular PWM method, that has not been encompassed by the analyses in [4,5], is the double zero-sequence injection, developed in [6,7] in mutually equivalent space vector and carrier-based form. The principle consists in utilization of two three-phase modulators (carrier or space vector based) whose reference inputs are shifted by 30 degrees. The method is very simple for both understanding and practical implementation and is thus widely used.

The purpose of this paper is therefore to investigate the switching characteristics, using vector space decomposition (VSD) approach, of double zero-sequence injection PWM technique. The results, in terms of both HDF and current ripple, are at all times compared with corresponding results for the PWM techniques encompassed by [4,5]. It is shown that the HDF of this PWM method compares favorably with HDF of the C6_SVPWM12 in most of the modulation range. Theoretical analysis is supported by extensive experimental verification.

II. Review of Modulation Techniques Based on Vector Space Decomposition

Figure 1 illustrates an asymmetrical six-phase drive, supplied from a six-phase voltage source inverter (VSI). The 6-phase VSI has a total number of $2^6 = 64$ different switching states defined by six switching functions, which correspond to the six inverter legs [S_a, S_b, S_c, S_d, S_e, S_f], where $S_i \in \{0,1\}$. Different switching states and the voltage of the DC link (V_{DC}) define the phase voltages which can in turn be mapped into the α–β and x–y subspaces according to the VSD approach [3]. Hence, the 64 different on/off combinations

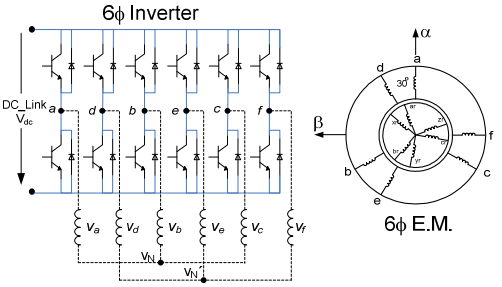

Fig. 1. Scheme of an asymmetrical six-phase (dual three-phase) AC drive.

978-1-61284-972-0/11/$26.00 ©2011 IEEE

of the six VSI legs lead to 64 switching states in the α–β and x–y subspaces. Figure 2 shows the active vectors in the α–β and x–y subspaces, where each switching state is identified by two octal numbers which correspond to the binary numbers $[S_aS_bS_c]$ and $[S_dS_eS_f]$, respectively. It must be noted that the 64 possible switching states imply only 49 different voltage space vectors in the α–β and x–y subspaces. Nevertheless, redundant states have to be considered because they have a different impact on the switching patterns.

The aim of a SVPWM technique is to select a particular switching pattern to control four variables simultaneously during each sampling period (i.e., time period during which the reference voltage space vector is averaged with the selected vectors), thus generating the required α–β reference voltages and zeroing the x–y voltages. The SVPWM techniques discussed in this paper are based on the 12 sector and 24 sector approaches in the α–β plane, as in [3-5].

The modulation index is defined as $M = V_1/(V_{dc}/2)$, where V_1 is the peak value of the sinusoidal reference, while reference voltage space vector in the α–β plane is defined in per-unit as $\bar{v}^* = M \exp(j\vartheta)$. Since there are four controlled variables, four active voltage vectors and zero voltage vectors need to be chosen and applied during each sampling period, according to the reference voltage vector amplitude and the sector location.

In the SVPWM techniques elaborated in [3,4] four active vectors with the maximum magnitude in the α–β subspace are employed to synthesize the reference voltage vector. Figure 3 shows the selected active voltage vectors when the reference is in one of the sectors (sector 1). The selected vectors correspond to the smallest ones in the x–y subspace, and two consecutively applied vectors must be opposite in phase in the x–y subspace. In this way, each change in the applied active vector leads to a sequence of small increases or decreases in the x–y voltages, keeping the average voltage in the x–y subspace equal to zero. For SVPWM schemes introduced in [5], where 24 sectors are considered, four active vectors are selected again to synthetize the reference voltage vector. The selected vectors include three that are the same as in 12-sector scheme and one vector that is different, as illustrated in Fig. 4, which depicts vector selection when the reference voltage vector is in sector one.

In both vector selection schemes the reference vector $\bar{v}^*$ in the α–β subspace is used to locate the required four voltage vectors and to compute the space vector switching instants during the sampling period T_s, using the following equation [3]:

$$\begin{bmatrix} T_1 \\ T_2 \\ T_3 \\ T_4 \\ T_0 \end{bmatrix} = \begin{bmatrix} V_1^\alpha & V_2^\alpha & V_3^\alpha & V_4^\alpha & 0 \\ V_1^\beta & V_2^\beta & V_3^\beta & V_4^\beta & 0 \\ V_1^x & V_2^x & V_3^x & V_4^x & 0 \\ V_1^y & V_2^y & V_3^y & V_4^y & 0 \\ 1 & 1 & 1 & 1 & 1 \end{bmatrix}^{-1} \cdot \begin{bmatrix} \bar{v}_\alpha^* \\ \bar{v}_\beta^* \\ 0 \\ 0 \\ 1 \end{bmatrix} \cdot T_s \qquad (1)$$

Selected active voltage vectors (V_1 to V_4) have to yield a unique and positive solution of equation (1).

The differences between the continuous and discontinuous SVPWM techniques appear in the selected switching sequences and the applied zero voltage vector states. More details, regarding the discontinuous PWM schemes encompassed by this study are available in [4-5].

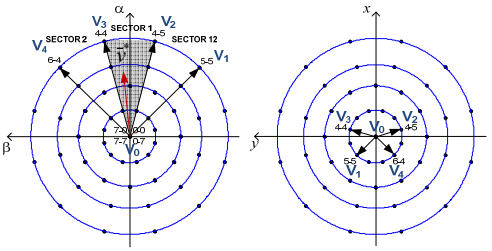

Fig. 3. Voltage vector selection in 12-sector based SVPWM techniques (voltage reference $U_{ref} \neq 0$ in α–β subspace, and zero reference in x–y subspace).

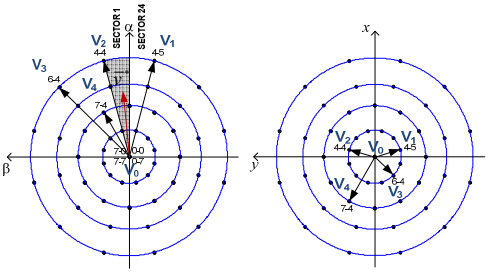

Fig. 4. Voltage vector selection in 24-sector based SVPWM techniques (voltage reference $U_{ref} \neq 0$ in α–β subspace, and zero reference in x–y subspace).

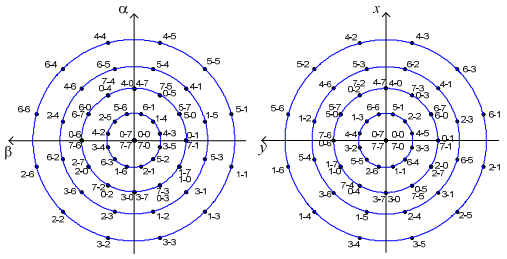

Fig. 2. Voltage space vectors and switching states in the α–β and x–y subspaces for a 6–phase asymmetrical VSI.

III. Double Zero-Sequence Injection PWM

This method has been introduced in [7] in carrier-based form and is simpler than the vector space decomposition technique from the point of view of the implementation complexity, because the inverter is treated as a dual three-phase structure, rather than the six-phase system. The equivalent space vector approach is described in [6]. Selecting the appropriate voltage vectors and computing their on-durations becomes straightforward because the six-phase

inverter is divided into two independently switched three-phase inverters with a common DC bus voltage. Therefore, the six-phase inverter is considered as two three-phase inverters with common DC bus. The principle is illustrated in Fig. 5.

In carrier-based version modulating signals are obtained using two groups of three fundamental signals displaced in time by $\pi/6$ radians, and there is a phase displacement of $2\pi/3$ radians between signals in each group. The fundamental signals are summed with an appropriate zero-sequence signal. Then, these signals are compared with a high-frequency carrier waveform (usually a triangular signal). Any modulating signal can be given as $v_k(t) = v_k^*(t) + v_{zs}(t)$, where $v_k^*(t)$ is the sinusoidal reference for phases $k = a,b,c,d,e,f$ and two $v_{zs}(t)$ represents the zero-sequence signals (one for each three-phase inverter). Modulation index is again defined as $M = V_1/(V_{dc}/2)$, where V_1 is the peak of the sinusoidal reference. Modulating signals $v_k(t)$ are all in the range (–1, 1) and the triangular carrier is within the same range. Carrier-based version is depicted in Fig. 6.

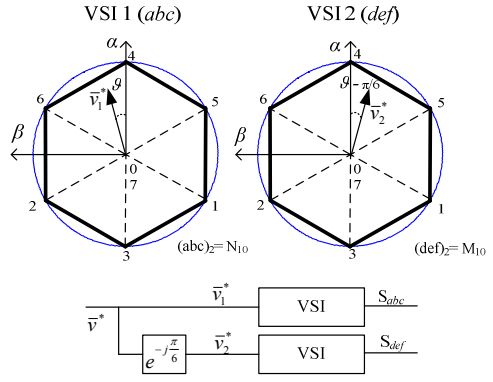

Fig. 5. Principle of double zero-sequence injection using dual three-phase inverter approach in space vector form.

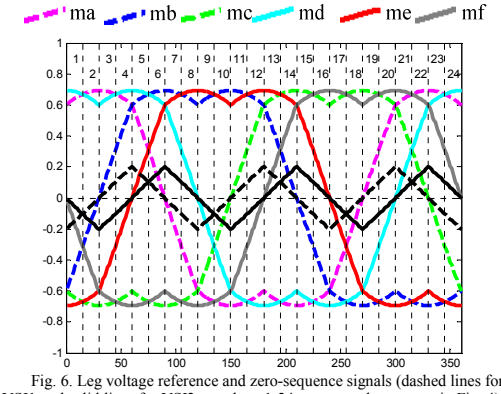

Fig. 6. Leg voltage reference and zero-sequence signals (dashed lines for VSI1 and solid lines for VSI2; numbers 1-24 correspond to sectors in Fig. 4).

IV. Representation of Double Zero-Sequence Injection using VSD Approach

In order to perform HDF and current ripple analysis, the dual three-phase space vector representation of Fig. 5 is translated into corresponding vectors triggered in the asymmetrical six-phase inverter voltage vector space of Fig. 2, in the α–β and x–y planes. For this purpose the carrier-based version of the double zero-sequence injection, shown in Fig. 6, is used. For example, the phase sequence in sector 1 of Fig. 6 is *d,a,f,b,c,e*. The corresponding switching sequence of the two three-phase inverters is 000-000(0-0), 000-100 (0-4), 100-100 (4-4), 100-101 (4-5), 110-101 (6-5), 111-101 (7-5), 111-111 (7-7), 111-101 (7-5), 110-101 (6-5), 100-101 (4-5), 100-100 (4-4), 000-100 (0-4), 000-000(0-0). The notation in brackets in the given switching sequence corresponds to the notation used in Fig. 7 to identify the applied vectors in the α–β and x–y planes of the six-phase system. Figure 7 also includes the resultant applied vectors in the next three sectors (two to four) of Fig. 6. The phase sequence for all 24 sectors of Fig. 6 is given in Table I, and the triggered vectors in the six-phase system can be determined using the same approach as illustrated here for sector 1.

It should be noted that the pattern of applied space vectors of Fig. 7, for the first four sectors (i.e. 60 degrees), repeats itself for the subsequent sectors with four-sector period. It should also be emphasized that, in terms of the number of utilized space vectors, double zero-sequence injection actually applies five active vectors (plus zero vector) in switching period, which makes it very different from all the other PWM techniques. Also, the initial zero vector with which the sequence starts is always 000-000, while in all the other PWM schemes starting vector alternates between four possible zero states.

Finally, it is worth mentioning that the triggered space vectors in any sector ensure zero average value of the voltage in the x–y plane, while simultaneously creating required reference in the α–β plane.

V. HDF and Current Ripple Analysis

The principles of the flux HDF and current ripple analysis for multiphase systems have been established recently in [4,5,8-10]. Two approaches are possible. In the first one, utilized here as well, the determination of the HDF is based on the space vector approach, while the other possibility is the polygon approach. As confirmed in [8], both approaches yield the same result in terms of total HDF for a given PWM technique and the phase number.

Regardless of the way in which the total flux HDF is determined, it is necessary to calculate individual plane flux HDFs in order to be able to evaluate the current ripple rms value. This is so since the inductances, relevant for the current ripple, are in multiphase machines different for the α–β and x–y planes. As shown in [10], the current ripple rms value is related to HDFs of the two planes through:

$$I_{\text{rms}}^2 = \left(\frac{V_{dc}T_s}{8}\right)^2 \left(\frac{HDF_{\alpha-\beta}}{L_{\alpha-\beta}^2} + \frac{HDF_{x-y}}{L_{x-y}^2}\right) \qquad (2)$$

TABLE I: MODULATING SIGNAL ORDERING FOR DOUBLE ZERO-SEQUENCE INJECTION IN 24 SECTORS

Sector	Phase signals					
1	v_d^*	v_a^*	v_f^*	v_b^*	v_c^*	v_e^*
2	v_a^*	v_d^*	v_b^*	v_f^*	v_e^*	v_c^*
3	v_a^*	v_d^*	v_b^*	v_e^*	v_f^*	v_c^*
4	v_d^*	v_a^*	v_b^*	v_e^*	v_c^*	v_f^*
5	v_d^*	v_b^*	v_a^*	v_e^*	v_c^*	v_f^*
6	v_b^*	v_d^*	v_e^*	v_a^*	v_f^*	v_c^*
7	v_b^*	v_e^*	v_d^*	v_a^*	v_f^*	v_c^*
8	v_e^*	v_b^*	v_d^*	v_a^*	v_c^*	v_f^*
9	v_e^*	v_b^*	v_d^*	v_c^*	v_a^*	v_f^*
10	v_b^*	v_e^*	v_c^*	v_d^*	v_f^*	v_a^*
11	v_b^*	v_e^*	v_c^*	v_f^*	v_d^*	v_a^*
12	v_e^*	v_b^*	v_c^*	v_f^*	v_a^*	v_d^*

Sector	Phase signals					
13	v_e^*	v_c^*	v_b^*	v_f^*	v_a^*	v_d^*
14	v_c^*	v_e^*	v_f^*	v_b^*	v_d^*	v_a^*
15	v_c^*	v_f^*	v_e^*	v_b^*	v_d^*	v_a^*
16	v_f^*	v_c^*	v_e^*	v_b^*	v_a^*	v_d^*
17	v_f^*	v_c^*	v_e^*	v_a^*	v_b^*	v_d^*
18	v_c^*	v_f^*	v_a^*	v_e^*	v_d^*	v_b^*
19	v_c^*	v_f^*	v_a^*	v_d^*	v_e^*	v_b^*
20	v_f^*	v_c^*	v_a^*	v_d^*	v_b^*	v_e^*
21	v_f^*	v_a^*	v_c^*	v_d^*	v_b^*	v_e^*
22	v_a^*	v_f^*	v_d^*	v_c^*	v_e^*	v_b^*
23	v_a^*	v_d^*	v_f^*	v_c^*	v_e^*	v_b^*
24	v_d^*	v_a^*	v_f^*	v_c^*	v_b^*	v_e^*

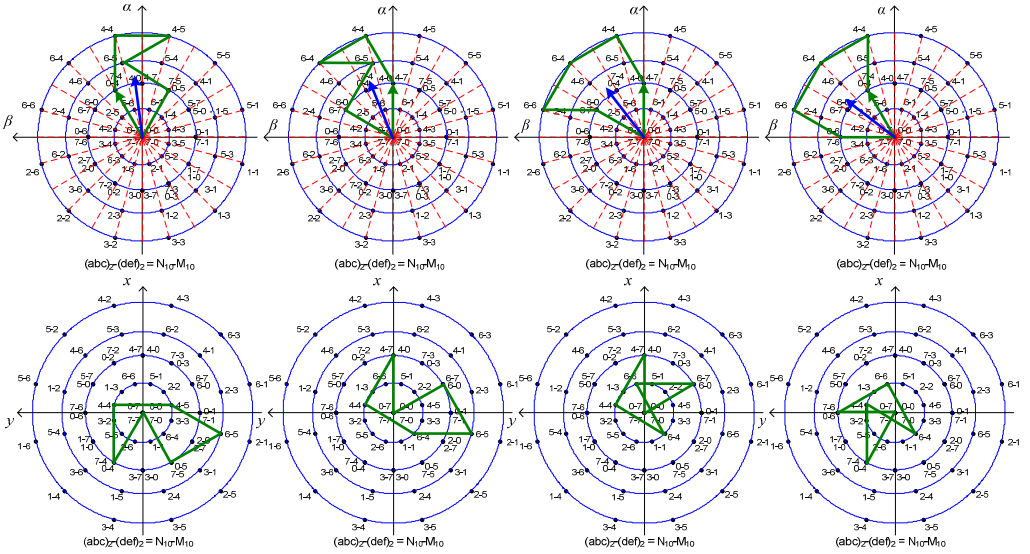

Fig. 7. Voltage vectors selected with double zero-sequence injection PWM, represented in the two planes of the six-phase space for the first four sectors (voltage reference $\vec{v}^* \neq 0$ in α–β subspace, and zero reference in x–y subspace).

Here V_{dc} and T_s stand for the DC bus voltage and switching period, while the inductances of the two planes are for an induction machine governed with $L_{\alpha\text{-}\beta} \approx L_{ls}+L_{lr}$, $L_{x\text{-}y} = L_{ls}$ [10]. Total flux HDF, which represents all six phases, is related to the per-plane HDFs through:

$$HDF = HDF_{\alpha-\beta} + HDF_{x-y} \tag{3}$$

It should be noted that although analytical expressions for individual HDFs of the two planes can be derived (and have been derived) [4,5], they are far too complex and long to include here. The calculated HDFs, illustrated further on in Fig. 8 that includes individual plane and total HDFs as functions of the modulation index, have been obtained using Matlab.

Since both continuous and discontinuous PWM techniques are studied, the HDF is evaluated under the condition of the same average switching frequency, i.e. as:

$$HDF = (\mathrm{ASF})^2\, HDF_{base} \tag{4}$$

where *ASF* represents the ratio of the switching frequency of a PWM method with respect to the C6_SVPWM12 switching frequency.

Figure 8 includes results, in addition to those for the double zero-sequence injection, for a number of other PWM techniques listed in the Section II, for comparative purposes. As can be seen, double zero-sequence injection PWM (ZSIPWM) is characterized with a lower HDF value in the α–β plane than both continuous and discontinuous PWM

techniques based on 12 sectors, across the entire modulation range. However, the values of HDF are higher than the corresponding ones for the 24-sector based PWM methods.

The situation in the x–y plane is however quite different. Here double zero-sequence injection offers the highest HDF values for the upper modulation region than any other considered PWM method. This is so since double zero-sequence injection utilizes space vectors which belong to the second largest group in the x–y plane (Fig. 7). These vectors are not utilized in any other PWM technique.

As a consequence of the described behavior in the two planes and the dominant influence of the α–β plane, the total HDF of the double zero-sequence injection method is offering an average overall HDF value, Fig. 8c. In principle, HDF values are lower than 12-sector methods but higher than with 24-sector methods.

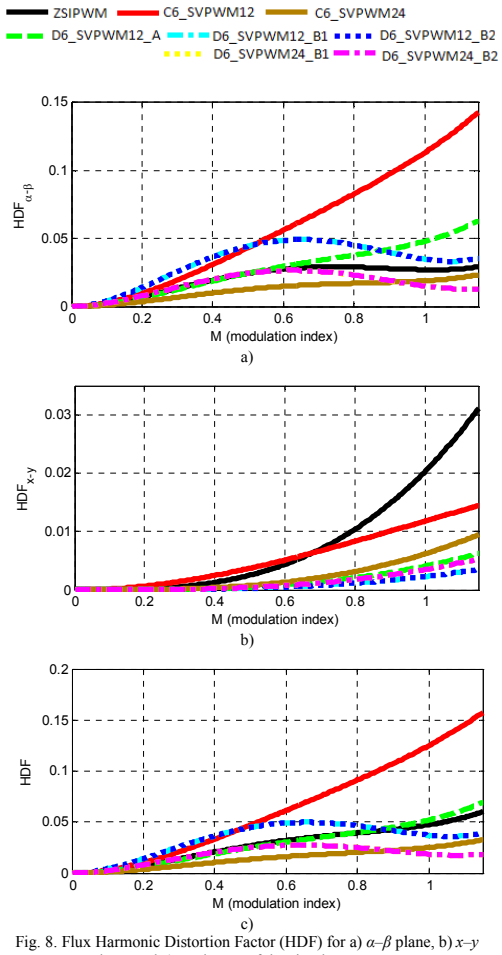

Fig. 8. Flux Harmonic Distortion Factor (HDF) for a) α–β plane, b) x–y plane, and c) total HDF of the six-phase system.

VI. Experimental Results

Experimental tests are performed in order to examine the properties of the double zero-sequence injection technique. The test rig is based on a conventional 36 slot, 2 pairs of poles, 4 kW 3-phase induction machine, whose stator has been rewound to give a 36 slot, 3 pairs of poles, asymmetrical six–phase induction machine. A schematic of the rig of the complete system is given in Fig. 9.

The control system is based on the TMS320LF28335 Texas Instruments DSP and the MSK28335 system. The TMS320LF28335 DSP is chosen because it offers twelve independent PWM output signals that can be synchronized using only one internal timer. DC bus voltage is set to 300V. V/f operation mode is utilised, and modulation index and fundamental frequency are changed from $M = 0.1$ @ $f = 5$ Hz to $M = 1.0$ @ $f = 50$ Hz. For $M = 1.1$ the fundamental frequency is also $f = 50$ Hz. Stator current of one phase has been recorded, and current ripple rms squared has been calculated on the basis of the FFT of the current waveform in steady state operation for any particular pair of modulation index/frequency values. Inverter average switching frequency is equalised for all PWM methods and is set to 2 kHz.

It is well-known that dead time leads to generation of low-order output voltage harmonics which are undesirable and would be absent in the linear PWM region if dead time were not to exist [12]. As a consequence, in multiphase drives, significant low order stator current harmonics may be present (for example, the 3rd and the 7th in a five-phase induction

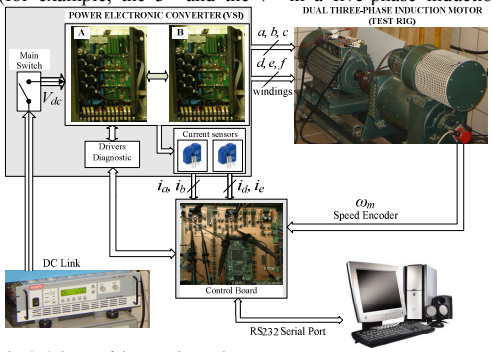

Fig. 9. Scheme of the experimental set-up.

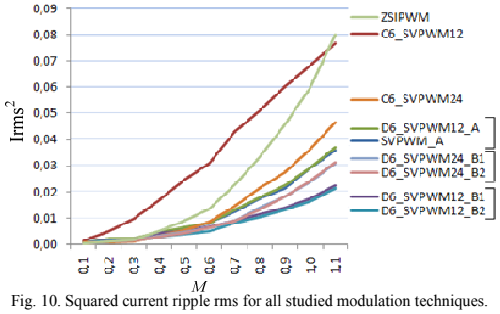

Fig. 10. Squared current ripple rms for all studied modulation techniques.

machine, [13]). To mitigate the impact of these harmonics on current ripple and current THD calculations, only harmonics of the order higher than the 10th are accounted for in the following tests and dead time has also been kept at minimum in the power converter.

The experimental results, showing square of the current ripple rms against the modulation index, are given in Fig. 10. One curve in Fig. 10 applies to the double zero-sequence injection (ZSIPWM) and all the other 12-sector and 24-sector based techniques, described previously.

It should be noted that the SVPWM technique of [3] is additionally included in Fig. 10 (denoted as SVPWM_A). It was not discussed previously since its behavior is identical to D6_SVPWM12_A although it is continuous PWM scheme. This is confirmed by complete overlap of the corresponding traces in Fig. 10.

Results of Fig. 10 show that the behavior of the squared current ripple rms follows the pattern obtained for the flux HDF in the *x-y* plane. This qualitatively similar behavior is due to the relationship between leakage inductances in the α–β plane and *x*–*y* planes, as explained in conjunction with (2). As a consequence, those modulations techniques with a lower flux HDF in the *x*–*y* plane offer lower current ripples for the tested machine. The double zero-sequence modulation method offers similar current ripple to most of the other PWM methods up to the modulation index $M = 0.35$. Above this modulation index value double zero-sequence injection becomes inferior to all but one modulation technique, namely C6_SVPWM12. Interestingly enough, the 12-sector based discontinuous techniques of B-type yield the lowest current ripple, although the HDFs are lower for 24-sector based methods. This is again the consequence of the different inductances in the two planes, relevant for the current ripple.

VII. Conclusions

The paper reports on the switching behavior of the double zero-sequence injection PWM method for asymmetrical six-phase drives. This is a technique that has been frequently analyzed in both carrier-based and space vector form, but its switching characteristics have not been reported before.

Using the equivalence between the time domain sectors in the carrier-based version and the angular sectors of the complex plane in the space vector version, the vectors used by the dual three-phase modulator are translated into the equivalent vectors triggered in the six-phase system. It is shown that, in contrast to all the other available PWM methods, double zero-sequence injection utilizes five active vectors in each switching period. Corresponding representation of the triggered vectors is established in both planes of the six-phase system, using VSD.

Principles of flux HDF and current ripple analysis, established recently for multiphase systems, are further applied to establish theoretical values for the flux HDF. The results obtained for the double zero-sequence injection are compared against those for the other available techniques and it is concluded that, in terms of the HDF, this technique compares favorably with the other methods. However, due to the correlation between plane HDFs and the current ripple rms, double zero-sequence injection is characterized with rather high current ripples and is worse in most of the modulation region than for all but one other PWM technique, at least for the induction machine used here in the experiments.

Double zero-sequence injection is by far the simplest PWM technique for practical implementation. However, the advantages brought in by the easiness of realization represent a trade off, since the current ripple is among the highest ones.

Acknowledgment

The authors gratefully acknowledge PTI-Itaipú Binacional and the Spanish Government (National Research, Development and Innovation Plan, under reference DPI2009-07955, the Junta de Andalucía 2010 research program, under reference TEP-5791, and the Ministry of Education) for the financial support provided.

References

[1] E. Levi, R. Bojoi, F. Profumo, H.A. Toliyat, S. Williamson, "Multiphase induction motor drives – A technology status review," *IET Electric Power Applications*, vol. 1, no. 4, pp. 489–516, 2007.

[2] R. Bojoi, E. Levi, F. Farina, A. Tenconi, F. Profumo, "Dual three–phase induction motor drive with digital current control in the stationary reference frame," *IEE Proc.–Electric Power Applications*, vol. 153, no. 1, pp. 129–139, 2006.

[3] Y. Zhao, T.A. Lipo, "Space vector PWM control of dual three–phase induction machine using vector space decomposition," *IEEE Trans. on Ind. Applications*, vol. 31, no. 5, pp. 1100–1109, 1995.

[4] D. Hadiouche, L. Baghli, A. Rezzoug, "Space–vector PWM techniques for dual three–phase AC machines: Analysis, performance evaluation, and DSP implementation," *IEEE Trans. on Ind. Applications*, vol. 42, no. 4, pp. 1112–1122, 2006.

[5] K. Marouani, L. Baghli, D. Hadiouche, A. Kheloui, A. Rezzoug, "A new PWM strategy based on a 24–sector vector space decomposition for a six–phase VSI–fed dual stator induction motor," *IEEE Trans. on Ind. Electronics*, vol. 55, no. 5, pp. 1910–1920, 2008.

[6] A. Bakhshai, G. Joos, H. Jin, "Space vector PWM control of a split–phase induction machine using the vector classification technique," *13th Annual Conference Proceedings of Applied Power Electronics Conference and Exposition*, *APEC*, 1998, pp. 802–808.

[7] R. Bojoi, A. Tenconi, F. Profumo, G. Griva, D. Martinello, " Complete analysis and comparative study of digital modulation techniques for dual three–phase AC motor drives," *IEEE Power Electronics Specialists Conference*, *PESC*, Cairns, Australia, 2002, pp. 851–857.

[8] D. Dujic, M. Jones, E. Levi, "Analysis of output current ripple RMS in multi–phase drives using polygon approach," *IEEE Trans. on Power Electronics,* vol. 25, no. 7, 2010, pp. 1838–1849.

[9] D. Dujic, M. Jones, E. Levi, J. Prieto, F. Barrero, "Switching ripple characteristics of space vector PWM schemes for five–phase two–level voltage source inverters – Part 1: Flux harmonic distortion factors," *IEEE Trans. on Ind. Electronics,* vol. 58, no. 7, pp. 2789–2798, 2011.

[10] M. Jones, D. Dujic, E. Levi, J. Prieto, F. Barrero, "Switching ripple characteristics of space vector PWM schemes for five–phase two–level voltage source inverters – Part 2: Current ripple," *IEEE Trans. on Ind. Electronics,* vol. 58, no. 7, pp. 2799–2808, 2011.

[11] J. Prieto, M. Jones, F. Barrero, E. Levi, S. Toral, "Comparative Analysis of Discontinuous and Continuous PWM Techniques in VSI-Fed Five-Phase Induction Motor," *IEEE Trans. on Ind. Electronics,* vol. 58, no. 12, 2011 (to appear, DOI: 10.1109/TIE.2011.2126540).

[12] C.M. Wu, W.H. Lau, H. Shu-Hung, "Analytical technique for calculating the output harmonics of an H-bridge inverter with dead time," *IEEE Trans. on Circuits and Systems I: Fundamental Theory and Applications*, vol.46, no.5, pp.617-627, 1999.

[13] M. Jones, D. Dujic, E. Levi, S.N. Vukosavic, "Dead-Time Effects in Voltage Source Inverter Fed Multi-Phase AC Motor Drives and Their Compensation," *Proc. European Conf. on Power Electronics and Applications EPE*, Barcelona, Spain, 2009, CD-ROM paper 0001.

3.6. Paper 6

Authors: M.J. Durán, J. Prieto, F. Barrero, J.A. Riveros y H. Guzmán.
Title: Space-Vector PWM With Reduced Common-Mode Voltage for Five-Phase Induction Motor Drives.
Journal: IEEE Transactions on Industrial Electronics.
Volume: 60.
Number: 10.
Pages: 4159-4168.
Date: October 2013.
Abstract: The growing interest in multiphase electrical drives has required the extension of control schemes and modulation techniques already well known for three-phase drives. Specifically, different and more complex space-vector pulse width modulation (SVPWM) methods have been developed for multiphase machines taking into account the increased number of switching possibilities and the new components resulting from generalized Clarke's transformation. In spite of the intensive work undertaken in the last decade, no SVPWM techniques with common-mode voltage (CMV) reduction have been developed for five-phase drives. This work proposes two SVPWM methods that are capable of reducing the peak-to-peak CMV by 40

IEEE TRANSACTIONS ON INDUSTRIAL ELECTRONICS, VOL. 60, NO. 10, OCTOBER 2013 4159

Space-Vector PWM With Reduced Common-Mode Voltage for Five-Phase Induction Motor Drives

Mario J. Durán, Joel Prieto, *Student Member, IEEE*, Federico Barrero, *Senior Member, IEEE*, José A. Riveros, and Hugo Guzman

***Abstract*—The growing interest in multiphase electrical drives has required the extension of control schemes and modulation techniques already well known for three-phase drives. Specifically, different and more complex space-vector pulse width modulation (SVPWM) methods have been developed for multiphase machines taking into account the increased number of switching possibilities and the new components resulting from generalized Clarke's transformation. In spite of the intensive work undertaken in the last decade, no SVPWM techniques with common-mode voltage (CMV) reduction have been developed for five-phase drives. This work proposes two SVPWM methods that are capable of reducing the peak-to-peak CMV by 40% and 80% compared to standard five-phase modulation strategies. Reduction of the CMV is done at the expense of higher phase voltage and current distortion. Simulation and experimental results confirm the CMV reduction and quantify the performance penalties of the proposed methods.**

***Index Terms*—Common-mode voltage (CMV), five-phase induction machines, multiphase systems, space-vector pulse width modulation (SVPWM).**

I. Introduction

THE WORLDWIDE agreement to develop three-phase AC electrical grids has limited the use of multiphase machines in favor of three-phase machines with capability to be directly connected to the mains. Nevertheless, the advent of modern digital signal processors (DSPs) and power electronics has awaken the interest on multiphase machines since the beginning of the 21st century. Multiphase machines have found a niche of applications in autonomous systems such as traction or ship propulsion where the mandatory use of a power inverter does not restrict the number of phases anymore [1]–[3]. More recently, multiphase machines have also been proposed in full-power wind energy conversion systems where the existence of an intermediate dc link allows the use of multiphase wind generators [4].

The intensive research on multiphase machines has led to the development of drive topologies and modes of operation nonexistent in standard three-phase drives, including the use of multimotor drives with single inverter supply [5], operation with enhanced torque in concentrated-winding motors [6], [7], or fault-tolerant modes of operation [8], [9]. In addition to these novel developments, well-established concepts of three-phase drives have also been reviewed for multiphase drive implementation. Control schemes including vector control [1], direct torque control [10], or predictive control [11]–[15] have been successfully extended for multiphase systems. Similarly, modulation schemes have been modified to consider the new degrees of freedom existing in multiphase converters. The extension of carrier-based pulse width modulation (PWM) techniques for distributed-winding machines in single-motor configuration has been straightforward [4], but the space-vector PWM (SVPWM) techniques [16] or the consideration of non-sinusoidal voltage supply for multimotor, fault-tolerant, and torque-enhanced drives has required an increased complexity [17], [18]. In any case, a wide range of modulation techniques has been developed including continuous and discontinuous multiphase PWM methods for two-level voltage source inverters (VSIs) [19], multilevel multiphase PWM techniques [20], [21], or modulation for open-end drive topologies [22]. In spite of the vast work undertaken to develop multiphase modulations and control schemes, there is a lack of analysis of the common-mode voltage (CMV) reduction in five-phase drives.

Reduction of CMV has been an issue of interest in the design of PWM techniques because CMV is known to cause electromagnetic interference, breakdown of winding insulation, and fault activation of current detector circuits and leakage currents that may damage the motor bearings [23]–[28]. A percentage of the CMV (typically 10% [28]) appears between the motor shaft and the grounded motor frame, allowing parasitic currents to flow via the motor bearings. These leakage currents, associated to the shaft-to-frame voltage, depend on variables like the motor speed, bearing temperature, type of bearings, or power level to name a few [24]. They can severely damage the bearings and reduce the drive robustness. While the displacement bearing currents are generated by the dv/dt of the inverter, the electric discharge machining (EDM) bearing currents are generated when the peak value of the CMV exceeds a certain threshold, causing the dielectric breakdown of the bearing lubricant [23]–[27]. Aiming to avoid bearing currents,

Manuscript received March 12, 2012; revised June 19, 2012; accepted July 28, 2012. Date of publication September 7, 2012; date of current version May 16, 2013. This work was supported in part by the Spanish Government (National Research, Development, and Innovation Plan, under references DPI2011-25396 and DPI2009-07955, and Junta de Andalucía 2010 research program, under reference TEP-5791) and in part by Itaipu Binacional/Parque Tecnológico Itaipu—Paraguay.

M. J. Durán is with the Department of Electrical Engineering, University of Málaga, 29071 Malaga, Spain (e-mail: mjduran@uma.es).

J. Prieto, F. Barrero, J. A. Riveros, and H. Guzman are with the Department of Electronic Engineering, University of Seville, 41092 Seville, Spain (e-mail: jprieto@esi.us.es; fbarrero@esi.us.es; jariveros@esi.us.es; hguzman@esi.us.es).

Color versions of one or more of the figures in this paper are available online at http://ieeexplore.ieee.org.

Digital Object Identifier 10.1109/TIE.2012.2217719

different modulation techniques for three-phase machines have been proposed both for two-level [28]–[30] and three-level [31], [32] VSIs. Sine-triangle PWM with interleaved carriers [30] inherently reduces the appearance of the zero vectors {000} and {111}, thus reducing the rms value of the CMV but still allowing CMV peaks of $\pm V_{\rm dc}/2$. Zero vectors can, however, be fully eliminated by substituting the zero vectors by active vectors in phase opposition with equal duty cycles. This approach is adopted in [29] proving that the peak values of the CMV can be reduced to $\pm V_{\rm dc}/6$. Carrier-based version of this strategy can be found in [28] with some modifications of the basic idea of [29]. All these works are, however, devoted to three-phase drives and have not been extended to five-phase drives so far.

This work extends the fundamental idea of [29] to the case of one of the most interesting multiphase drives from the application point of view, the five-phase induction motor drive. As in three-phase drives [28]–[30], the modulation techniques with reduced CMV can be used in any multiphase application where the bearings can be damaged due to the peak-to-peak CMV. Five-phase VSIs, in comparison to their three-phase counterparts, present an increased complexity because the number of voltage vectors is increased (from $2^3 = 8$ to $2^5 = 32$), the size of the voltage vectors is not unique (zero, small, medium, and large vectors are present), and an additional subspace appears (so-called $x-y$ plane) [1]. Compared to the three-phase case, the dv/dt of the CMV in five-phase drives is inherently reduced because it is, in general, equal to $V_{\rm dc}/n$, being n the number of phases of the system. Nevertheless, the peak-to-peak CMV remains as in the three-phase case equal to $V_{\rm dc}$. Similar to the approach adopted for three-phase drives [28]–[30], the modification of the switching pattern cannot reduce the dv/dt but can effectively reduce the peak-to-peak CMV. In the five-phase system, the CMV presents now six different levels, and elimination of zero vectors does not ensure minimum CMV peak values as it occurs in three-phase VSIs. All these issues are discussed and analyzed, and two SVPWM algorithms for the reduction of CMV in five-phase VSIs are proposed and compared to standard five-phase SVPWM.

This paper is structured as follows. Next section analyzes the CMV in five-phase induction motor drives. Section III describes the modeling of the five-phase VSI and presents the basic outlines to mitigate CMV in a five-phase drive. Two proposed SVPWM techniques with CMV reduction capability are described in Section IV. These techniques are analyzed in Section V, where simulation and experimental results are presented and discussed. The conclusions are summarized in the last section.

II. CMV in Five-Phase Drives

Five-phase induction motor drives have attracted much attention among multiphase induction motor drives as an alternative to standard three-phase drives [1]. This work considers a drive with a distributed-winding five-phase induction motor with 72° of spatial displacement between stator windings and a two-level five-phase inverter (Fig. 1).

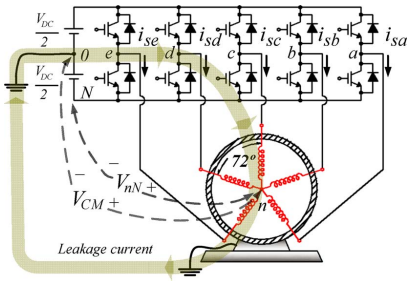

Fig. 1. Two-level five-phase induction motor drive scheme showing the leakage currents flowing via the grounded motor frame.

The CMV, from now on $V_{\rm CM}$, relates the motor neutral voltage to the midpoint of the dc link, and its expression in two-level three-phase drives is [32]

$$V_{\rm CM} = \frac{V_{\rm dc}}{3} \cdot (S_a + S_b + S_c) - \frac{V_{\rm dc}}{2} = V_{\rm nN} - \frac{V_{\rm dc}}{2} \qquad (1)$$

where $V_{\rm dc}$ is the dc link voltage, $V_{\rm nN}$ relates the motor neutral voltage to the negative rail of the VSI (Fig. 1), and $S_i \in \{0, 1\}$ denotes the switching functions of each VSI leg. From (1), it follows that the maximum peak value of the CMV is $|V_{\rm CM}| = V_{\rm dc}/2$, the minimum voltage variation is $\pm V_{\rm dc}/3$, and the number of CMV levels is four.

Most of the techniques for CMV reduction avoid the zero states $\{S_a S_b S_c\} = \{000\}$ or $\{111\}$, maintaining the voltage variation of $\pm V_{\rm dc}/3$ but reducing the peak value of the CMV to $V_{\rm dc}/6$ (66% of reduction). Consequently, the dv/dt (cause of displacement bearing currents) remains constant, but the reduction of the maximum $|V_{\rm CM}|$ helps to mitigate the main source of leakage current, namely, the EDM bearing currents.

The expression of the CMV in five-phase drives can be directly extrapolated from (1) as

$$V_{\rm CM} = \frac{V_{\rm dc}}{5} \cdot (S_a + S_b + S_c + S_d + S_e) - \frac{V_{\rm dc}}{2}. \qquad (2)$$

In this case, the maximum peak value of the CMV is still $|V_{\rm CM}| = V_{\rm dc}/2$, but the number of CMV levels is increased to six and the minimum voltage variation is reduced to $\pm V_{\rm dc}/5$. Therefore, in spite of dealing with a two-level VSI, the CMV presents more levels because additional switching combinations are possible due to the multiphase nature of the converter. The dv/dt is thus reduced in five-phase drives independent of which SVPWM technique is selected.

From (2), it can be deduced that the switching combinations generate six different values of the CMV: $\pm 0.1 \cdot V_{\rm dc}$, $\pm 0.3 \cdot V_{\rm dc}$, and $\pm 0.5 \cdot V_{\rm dc}$. The switching states can be grouped (Table I) into those that generate the following:

1) large CMV ($\pm 0.5 \cdot V_{\rm dc}$): switching states with all switches on or vice versa, referred to as 0–5;
2) medium CMV ($\pm 0.3 \cdot V_{\rm dc}$): switching states with one switch on and four switches off or vice versa, referred to as 1–4;

TABLE I
MAGNITUDE OF CMV ACCORDING TO THE SWITCHING STATES

	Switching state	$\lvert V_{CM} \rvert$
Large CMV (0–5)	{00000}, {11111}	$0.5 \cdot V_{DC}$
Medium CMV (1–4)	{00001} {00010} {00100} {01000} {10000}	$0.3 \cdot V_{DC}$
	{11110} {11101} {11011} {10111} {01111}	
Small CMV (2–3)	{00011} {00101} {01001} {10001} {00110} {01010} {10010} {01100} {10100} {11000}	$0.1 \cdot V_{DC}$
	{11100} {11010} {10110} {01110} {11001} {10101} {01101} {10011} {01011} {00111}	

3) small CMV ($\pm 0.1 \cdot V_{\rm dc}$): switching states with two switches on and three switches off or vice versa, referred to as 2–3.

As in the three-phase case, zero vectors (0–5) generate the higher CMV and must therefore be avoided if the bearing voltage needs to be diminished. However, avoiding the selection of zero vectors only reduces the CMV by 40%, so the use of medium CMV voltage vectors should be also restrained in order to further reduce the bearing voltage.

III. FIVE-PHASE VSIS AND CMV MITIGATION

Two-level five-phase VSIs (Fig. 1) have $2^5 = 32$ different switching states. A switching function $S_k \in \{0, 1\}$ can be defined in a way that S_k is one when phase k is connected to the positive rail of the VSI (top switch on and bottom switch off) and S_k is zero when phase k is connected to the negative rail of the VSI (top switch off and bottom switch on). The state of the converter is then determined by the switching state of its five legs, which can be defined as

$$\underline{S} = [S_a \quad S_b \quad S_c \quad S_d \quad S_e] \tag{3}$$

where vector notation is indicated using underlined variables. Each switching state is numbered from now on according to its binary number

$$S_a \cdot 2^4 + S_b \cdot 2^3 + S_c \cdot 2^2 + S_d \cdot 2^1 + S_e \cdot 2^0. \tag{4}$$

In addition, leg voltages can then be expressed as

$$V_{kN} = S_k \cdot V_{\rm dc} \tag{5}$$

being $V_{\rm dc}$ the voltage of the dc link. Assuming that the five-phase induction machine (Fig. 1) has an isolated neutral, the phase voltages can be calculated as

$$v_{kn} = \frac{4}{5} V_{kN} - \frac{1}{5} \sum_{i=1, i \neq k}^{5} V_i. \tag{6}$$

Phase voltages can then be mapped into the α–β and x–y subspaces using the current invariant transformation provided

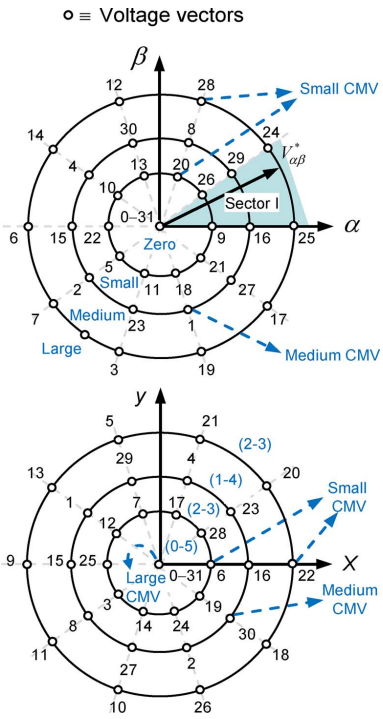

Fig. 2. Zero, small, medium, and large vectors in the α–β and x–y planes using the five-phase power converter and its correspondence with the small (2–3), medium (1–4), and large (0–5) CMV switching states.

by the general Clarke's transformation [1]

$$\begin{bmatrix} v_\alpha \\ v_\beta \\ v_x \\ v_y \\ v_0 \end{bmatrix} = \frac{2}{5} \begin{bmatrix} 1 & \cos(\alpha) & \cos(2\alpha) & \cos(3\alpha) & \cos(4\alpha) \\ 0 & \sin(\alpha) & \sin(2\alpha) & \sin(3\alpha) & \sin(4\alpha) \\ 1 & \cos(2\alpha) & \cos(4\alpha) & \cos(6\alpha) & \cos(8\alpha) \\ 0 & \sin(2\alpha) & \sin(4\alpha) & \sin(6\alpha) & \sin(8\alpha) \\ \frac{1}{2} & \frac{1}{2} & \frac{1}{2} & \frac{1}{2} & \frac{1}{2} \end{bmatrix} \times \begin{bmatrix} v_{an} \\ v_{bn} \\ v_{cn} \\ v_{dn} \\ v_{en} \end{bmatrix} \tag{7}$$

where $\alpha = 2\pi/5$. The last row of the transformation corresponds to the zero sequence component discussed in the previous section. The α–β voltage vectors can be represented in two different planes providing zero, small, medium, and large voltage vectors [1]. Note that the size of the voltage vectors in α–β or x–y subspaces is different from the size of the CMV referred to in the previous section (see Table I and Fig. 2 for clarification). From the relations shown in Table I and Fig. 2, it follows that the elimination of medium voltage vectors seems not critical because the control remains for low and high modulation indices using small and large voltage vectors, respectively.

Elimination of zero (0–5) and medium (1–4) vectors is also acceptable in the overmodulation region because large (2–3) vectors can still be chosen. As a general rule, the following relationships apply.

1) Switching states 0–5 generate zero voltage vectors both in $\alpha-\beta$ and $x-y$ subspaces and provide large CMV ($\pm 0.5 \cdot V_{\rm dc}$).
2) Switching states 1–4 generate medium voltage vectors both in $\alpha-\beta$ and $x-y$ subspaces and provide medium CMV ($\pm 0.3 \cdot V_{\rm dc}$).
3) Switching states 2–3 generate small voltage vectors in $\alpha-\beta$ plane and large voltage vectors in $x-y$ plane or vice versa and provide small CMV ($\pm 0.1 \cdot V_{\rm dc}$).

For the sake of example, switching state 25 corresponds to the switching state [1 1 0 0 1] according to (4) and generates a large voltage vector in the first sector of the $\alpha-\beta$ subspace, a small voltage vector in the fifth sector of the $x-y$ subspace, and a small CMV of $0.1 \cdot V_{\rm dc}$.

IV. SVPWM With Reduced CMV in Five-Phase Drives

Standard SVPWM for three-phase VSIs has been recently extended to multiphase drives [16]–[21]. Although the principle of operation of the SVPWM is similar, the algorithm has additional complexity because the number of voltage vectors is increased from $2^3 = 8$ to $2^5 = 32$, the number of sectors is increased from six to ten, and the number of subspaces is also increased with the appearance of the nonelectromechanically related $x-y$ voltage components [1]. Four different SVPWM techniques are described in this section: SVPWM1 is the standard technique for five-phase VSIs in the linear region, and SVPWM2 and SVPWM4 are different proposals that aim to reduce CMV. Notice that SVPWM3 will be also presented to introduce SVPWM4 technique.

A. SVPWM1: Large, Medium, and Zero Voltage Vectors

In the initial attempts to develop multiphase SVPWM algorithms, only two active vectors per sector (the largest ones in the $\alpha-\beta$ plane in Fig. 2) were selected to generate the reference voltage in the $\alpha-\beta$ subspace $v^*_{\alpha\beta}$. However, this procedure leads to low-order voltage harmonics due to high $x-y$ voltage components. Consequently, this modulation technique has become acceptable only in the overmodulation zone. To overcome this shortcoming, standard SVPWM for five-phase drives in the linear range applies four active vectors per sector (large and medium ones in Fig. 2) to simultaneously achieve the voltage reference in the $\alpha-\beta$ subspace ($v^*_{\alpha\beta}$) and cancel the $x-y$ voltage components ($v_{xy} = 0$) [16]. Zero vectors 0–31 are then applied during the rest of the sampling period.

For the sake of example, let us consider a reference voltage vector $v^*_{\alpha\beta}$ that is located in sector I (upper plot, Fig. 2). Large (24, 25) and medium (16, 29) voltage vectors are selected to be applied during the sampling period T_s [Fig. 3(a)]. Selected vectors are preordered to ensure that only one switching cycle per phase occurs, thus maintaining the switching frequency equal to $1/T_s$. According to the definition of (4), this task

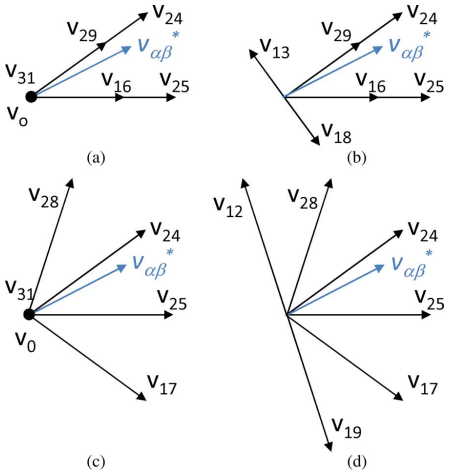

Fig. 3. Voltage vectors selected for the SVPWM in the first sector. (a) Case 1: Large, medium, and zero vectors. (b) Case 2: Large, medium, and phase-opposed vectors. (c) Case 3: Large, adjacent large, and zero vectors. (d) Case 4: Large, adjacent large, and phase-opposed vectors.

implies applying the vectors in ascending order. For example, in sector I, the order becomes 0, 16, 24, 25, 29, and 31. Once the switching states are properly ordered, voltage vectors are applied twice to obtain a symmetrical switching pattern [Fig. 4(a)]. The times of application of the active vectors 16, 24, 25, and 29 can be calculated as

$$\begin{bmatrix} t_1 \\ t_2 \\ t_3 \\ t_4 \end{bmatrix} = \begin{bmatrix} v_{1\alpha} & v_{2\alpha} & v_{3\alpha} & v_{4\alpha} \\ v_{1\beta} & v_{2\beta} & v_{3\beta} & v_{4\beta} \\ v_{1x} & v_{2x} & v_{3x} & v_{4x} \\ v_{1y} & v_{2y} & v_{3y} & v_{4y} \end{bmatrix}^{-1} \begin{bmatrix} v^*_\alpha \\ v^*_\beta \\ 0 \\ 0 \end{bmatrix} T_s \qquad (8)$$

where subscripts 1–4 refer to the four preordered active vectors ($1 \equiv 16, 2 \equiv 24, 3 \equiv 25$, and $4 \equiv 29$), subscripts $\alpha, \beta, x,$ and y refer to the voltage components after Clarke's transformation (7), and superscript $*$ indicates reference values (provided by an outer control loop). Zero vectors 0–31 are then applied during the rest of the sampling period

$$t_0 = T_s - \sum_{k=1}^{4} t_k \qquad (9)$$

being t_0 always positive in the linear region.

The SVPWM using zero, medium, and large voltage vectors in the $\alpha-\beta$ subspace, referred to from now on as Case 1 or SVPWM1, provides six CMV levels ranging from $0.5 \cdot V_{\rm dc}$ to $-0.5 \cdot V_{\rm dc}$, as shown in the lower part of Fig. 4(a). Consequently, in spite of the good performance in terms of phase voltage generation, the peak-to-peak value of the CMV is high (equal to $V_{\rm dc}$). The linear modulation range extends up to $M = 1.0514 = 1/\cos(\pi/10)$, being M the modulation index [19]

$$M = \frac{2 \cdot |V^*|}{V_{\rm dc}} \qquad (10)$$

where $|V^*|$ is the peak value of the ac phase voltage.

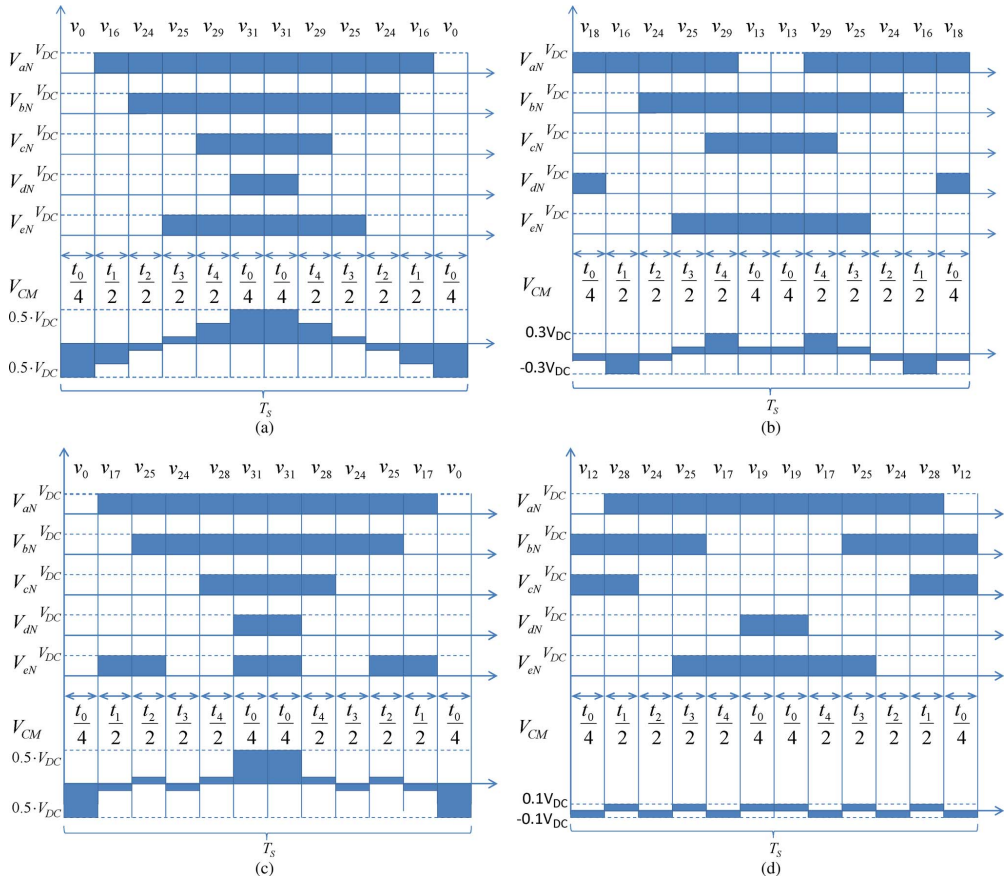

Fig. 4. Switching patterns and CMV for different SVPWM techniques. (a) Large, medium, and zero vectors. (b) Large, medium, and phase-opposed vectors. (c) Large, adjacent large, and zero vectors. (d) Large, adjacent large, and phase-opposed vectors.

B. SVPWM2: Large, Medium, and Phase-Opposed Voltage Vectors

Aiming to reduce the CMV, the zero vectors 0–31 can be replaced by two active vectors in phase opposition both in $\alpha-\beta$ and $x-y$ subspaces. A similar proposal is stated in [29] but for a three-phase power converters. The SVPWM2 proposal extends those ideas to the multiphase case. As far as the time of application of these phase-opposed vectors is the same and equal to $t_0/2$, any two active vectors in phase opposition will generate a zero vector on average and will therefore obtain similar average output voltage as in Case 1 where true zero vectors 0–31 are used. However, some of these vectors generate a switching pattern with more than one switching cycle (on $\rightarrow$ off $\rightarrow$ on or vice versa) per sampling period (T_s), thus increasing the switching frequency. For example, looking at the switching pattern of Fig. 4(a), it follows that vector 0 cannot be replaced by a vector with $S_b = 1$, $S_c = 1$, or $S_e = 1$ if only one switching cycle per sampling period is required. Only three pairs of vectors in phase opposition preserve the constant switching frequency $1/T_s$, ensuring that only one switching cycle per sampling period occurs: 13–18 (small vectors), 15–16 (medium vectors), and 2–29 (medium vectors). Any of these three options generate zero average voltage and preserve constant switching frequency, but vectors 13–18 are selected because of the small generated CMV $(\pm 0.1 \cdot V_{\mathrm{dc}})$. This SVPWM, further on referred to as Case 2 or SVPWM2, is shown in Fig. 3(b) (selected voltage vectors) and Fig. 4(b) (switching pattern and generated CMV). It is noticeable that the elimination of the zero vectors 0–31 reduces the peak CMV by 40%, being the peak CMV equal to $\pm 0.3 \cdot V_{\mathrm{dc}}$ [Fig. 4(b)]. It must be highlighted that the maximum linear modulation range of SVPWM2 is the same as in SVPWM1 (i.e., $M = 1.0514$) because the times of application t_0 of the voltage vectors in phase opposition (13–18) are the same as those of the zero vectors and the active vectors remain the same for both cases.

C. SVPWM3: Large, Adjacent Large, and Zero Voltage Vectors

Cases 1 and 2 make use of the large and medium vectors to generate the $\alpha-\beta$ voltage reference $v^*_{\alpha\beta}$. However, medium vectors generate higher CMV $(\pm 0.3 \cdot V_{\rm dc})$ than small and large vectors $(\pm 0.1 \cdot V_{\rm dc})$. Consequently, it seems convenient to replace medium voltage vectors by small or large vectors in order to further reduce the CMV. A modification of SVPWM1 can be obtained by substituting the medium vectors (16–29 in sector I) by the small vectors (9–26 in sector I). Unfortunately, vectors 25 and 9 do not have y component, while vectors 24 and 26 have negative y component, thus being impossible to satisfy the $v_{xy} = 0$ condition.

Considering that medium voltage vectors generate high CMV and small vectors cannot provide null $x-y$ voltages, large vectors in adjacent sectors are considered next. Focusing on the case of sector I, adjacent large vectors are switching states 28 and 17. It can be observed in Fig. 2 that the location of large (24–25) and adjacent large (28–17) active vectors in the $x-y$ plane is adequate for cancelation.

Let us first consider the case with zero, large, and adjacent large vectors, further on referred to as Case 3 or SVPWM3. This SVPWM3 implies the use of vectors 0, 17, 24, 25, 28, and 31 in sector I [Fig. 3(c)]. Times of application can be calculated according to (8) and (9), and the symmetrical switching pattern of Fig. 4(c) is then obtained. In spite of preordering the selected vectors to obtain minimum average switching frequency, it is noticeable that leg e completes three switching cycles in a sampling period. The average switching frequency is thus increased to $1.4/T_s$ because of these additional switching cycles. Furthermore, application of zero vectors 0–31 maintains the peak-to-peak CMV equal to $V_{\rm dc}$, as shown in the lower part of Fig. 4(c). Both disadvantages make SVPWM3 (also termed 4L SVPWM in [19]) impractical. However, it is possible to replace zero vectors 0–31 in such a way that the switching frequency remains constant and the peak-to-peak CMV is reduced.

TABLE II
COMPARISON OF SVPWM1–SVPWM4

SVPWM	*Switching frequency*	*Maximum linear modulation range*	*Peak CMV*
Case 1	$1/T_s$	1.0514	$\pm 0.5 \cdot V_{DC}$
Case 2	$1/T_s$	1.0514	$\pm 0.3 \cdot V_{DC}$
Case 3	$1.4/T_s$	1.0514	$\pm 0.5 \cdot V_{DC}$
Case 4	$1/T_s$	1.0514	$\pm 0.1 \cdot V_{DC}$

TABLE III
ELECTRICAL PARAMETERS OF THE FIVE-PHASE MACHINE

Parameter	*Value*	*Parameter*	*Value*
R_s [Ω]	12.85	P [kW]	1.4
σL_s [mH]	151.65	p	3
L_s, L_r [mH]	768.80	ω_n [rpm]	990
M [mH]	688.92	J_m [kg·m^2]	0.148
τ_r [ms]	179.49	B_m [N·m·s]	0.036

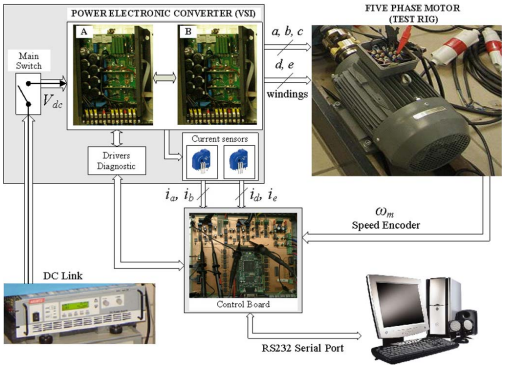

Fig. 5. Experimental system, including the power and control modules at the left side and the five-phase induction machine at the right side.

D. SVPWM4: Large, Adjacent Large, and Phase-Opposed Voltage Vectors

Focusing on the switching pattern of SVPWM3 [Fig. 4(c)], it can be deduced that it is not possible to obtain just one switching cycle in phase e. For this reason, the active vectors are preordered following the sequence 28, 24, 25, and 17. With this new sequence of application, it is now possible to achieve a constant switching frequency if the following are considered.

1) The switching state of phase e for vectors 0 and 31 cannot be changed.
2) The switching state of phases a and d for vectors 0 or 31 can be changed or not.
3) The switching state of phases b and c for both vectors 0 and 31 needs to be mandatorily changed.

The pairs of voltage vectors that comply with the aforementioned conditions are 12–19 (large), 14–17 (large), 28–3 (large), and 30-1 (medium). Any of the first three pairs of switching states can adequately replace vectors 0–31 with constant switching frequency and minimum CMV $(\pm 0.1 \cdot V_{\rm dc})$, reducing the peak-to-peak CMV to 80% compared to SVPWM1. The dv/dt still remains as in the standard SVPWM1 and proposed SVPWM2, being equal to $V_{\rm dc}/5$. Using the pair 12–19 [Fig. 3(d)], referred to from now on as Case 4 or SVPWM4, the switching pattern and generated CMV of Fig. 4(d) are obtained. The set of selected vectors includes the six large vectors adjacent to the reference (three clockwise, three counterclockwise), and the application order is clockwise.

Note that the linear modulation range of Cases 3–4 is the same as in Cases 1–2 (Table II). Using (8) and (9) and imposing the condition $t0 > 0$ for the four different SVPWM techniques, it follows that the linear range lays within the range [0–1.0514]. Similarly, the maximum modulation index in overmodulation zone is $M = 1.2311$ in all four cases because only large vectors are used in the pulse dropping region. A comparison of the features of the four SVPWM techniques is summarized in Table II. As far as the CMV is concerned, Case 4 provides the best performance although a more distorted waveform is expected. Compared to three-phase drives, it must be highlighted that both the dv/dt (due to the multiphase nature of the system)

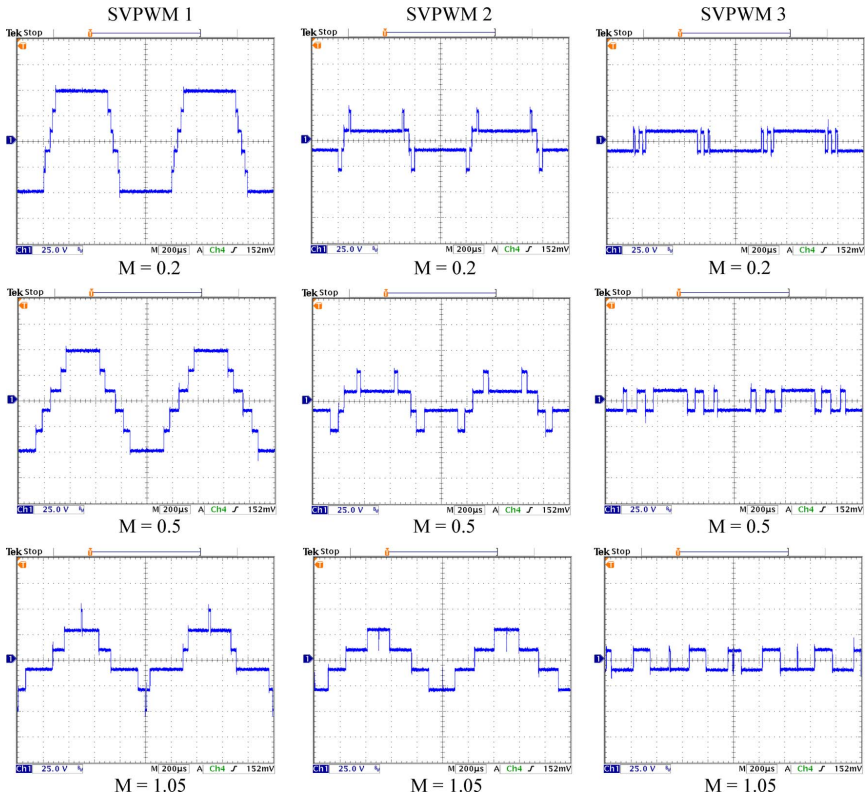

Fig. 6. Experimental CMV in tests supplying a five-phase passive resistive load with different modulation indices ($M = 0.2$, $M = 0.5$, and $M = 1.05$) and different SVPWM techniques. Case 1: Large, medium, and zero vectors; Case 2: Large, medium, and phase-opposed vectors; Case 4: Large, adjacent large, and phase-opposed vectors.

and the peak-to-peak CMV (due to specific switching pattern design) are reduced from $V_{\rm dc}/3$ to $V_{\rm dc}/5$.

V. Simulation and Experimental Results

The reduction of the CMV using modulation strategies SVPWM1, SVPWM2, and SVPWM4 is experimentally verified in a test rig based on a 30-slot two-pairs-of-poles three-phase induction machine, whose stator has been rewound to provide a five-phase induction machine with three pairs of poles. Parameters of the machine have been determined using conventional and standstill tests with inverter supply [33], [34], and the obtained values are those shown in Table III. A schematic of the rig and photographs of the complete system are shown in Fig. 5. Five phases of two conventional three-phase VSIs from Semikron (SKS21F) have been used to drive the machine. The control system is based on the MSK28335 board and the TMS320F28335 DSP, and the induction machine is operated in open-loop mode of operation.

Measurements are obtained using a digital scope, a current probe, and a differential voltage probe (Tektronix TDS3014B, TCP202, and P5205). All simulation and experimental results have been obtained using a switching frequency of 2 kHz. Tests have also been performed using a five-phase passive resistive load. These tests were conducted with a fundamental frequency of 10 Hz and a dc link of 100 V and modulation indices of 0.2, 0.5, and 1.05, while the tests with the five-phase induction machine were obtained with a dc link of 300 V and a fundamental frequency of 25 and 50 Hz, using modulation indices of 0.5 and 1.

Although the time of application of zero vectors is reduced as the modulation index is increased, the qualitative CMV waveforms of Fig. 6 closely resemble those of Fig. 4. Six, four, and two levels of the CMV are obtained implementing SVPWM1, SVPWM2, and SVPWM4, respectively. Peak-to-peak CMV is reduced from 100 V in SVPWM1 test to 60 V in SVPWM2 test and 20 V in SVPWM4 test. These experimental results confirm the 40% and 80% of CMV reduction already predicted in Section IV.

Nevertheless, the elimination of certain switching possibilities is expected to generate more distortion in the phase voltage and currents [30]. This is also confirmed in the phase

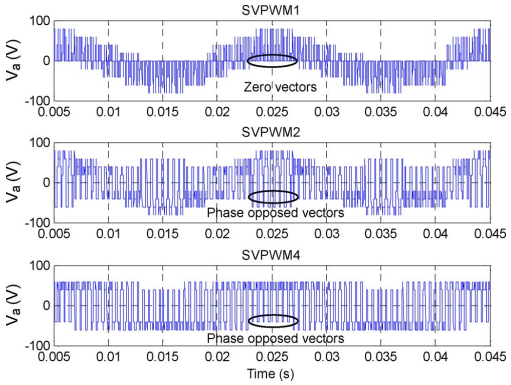

Fig. 7. Simulated phase voltage waveform for modulation index $M = 0.5$ and different SVPWM techniques. Case 1: Large, medium, and zero vectors; Case 2: Large, medium, and phase-opposed vectors; Case 4: Large, adjacent large, and phase-opposed vectors.

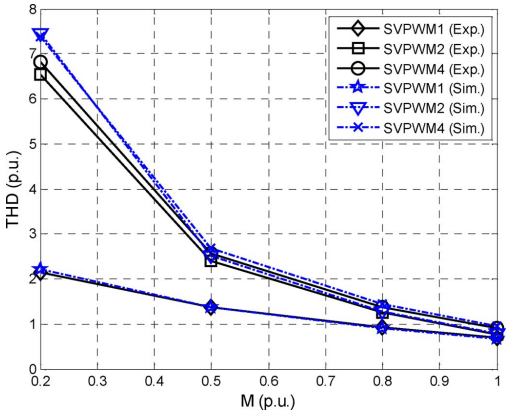

Fig. 8. Simulated and experimental THDs of the phase voltage versus modulation index for different SVPWM techniques. Case 1: Large, medium, and zero vectors; Case 2: Large, medium, and phase-opposed vectors; Case 4: Large, adjacent large, and phase-opposed vectors.

voltage waveform shown in Fig. 7, where it can be noted that the substitution of zero and medium vectors by small/large vectors increases the waveform distortion. In order to quantify the distortion, Fig. 8 shows the simulated and experimental phase voltage total harmonic distortions (THDs) for different modulation indices.

The THD has been calculated considering harmonics up to 15 kHz according to the expression

$$\text{THD} = \frac{\sqrt{V_2^2 + V_3^2 + \cdots + V_n^2}}{V_1} \tag{11}$$

where V_k is the rms value of the kth voltage harmonic.

As expected, the THD is reduced in all cases as the modulation index is increased because the duty cycles of the active vectors become higher. Results from simulations and experiments show good agreement. Fig. 8 also shows the higher distortion for those methods with reduced CMV (SVPWM2 and SVPWM4) compared to standard SVPWM1. The deterioration of the waveforms is more noticeable at low modulation indices where phase-opposed vectors in Cases 2–4 need to be applied during a longer period of time. On the contrary, all methods converge as the limit of the linear modulation region is approached. The narrow difference in terms of THD performance of methods SVPWM2 and SVPWM4 is noticeable. Considering that the peak-to-peak CMV obtained using SVPWM2 is three times higher than using SVPWM4, it can be deduced that SVPWM4 presents better overall performance in terms of phase voltage THD.

Obtained results using the multiphase electrical drive are summarized in Fig. 9. SVPWM1, SVPWM2, and SVPWM4 techniques have been implemented with modulation indices equal to 0.5 and 1. It is shown that phase voltage and current waveforms using SVPWM2 are more distorted than those obtained using SVPWM1, which agrees with results shown in Figs. 7 and 8. This is so because zero vectors have been replaced by active vectors in phase opposition.

Performances of SVPWM1 and SVPWM2 are proved to be similar in terms of phase current distortion and converge at high modulation indices ($M = 1.05$). Notice that phase voltage waveform shows an excellent agreement with simulation results (Fig. 7). CMV for the three methods is also shown in Fig. 9, confirming simulation results shown in Fig. 7: the peak-to-peak CMVs of SVPWM2 and SVPWM4 are 40% and 80% lower, respectively, than that of SVPWM1.

Even though all three methods (SVPWM1, SVPWM2, and SVPWM4) can synthesize both $\alpha-\beta$ and $x-y$ references, the switching harmonics can generate additional torque ripple and losses, respectively. Fig. 10 shows the $\alpha-\beta$ and $x-y$ currents with the three methods for modulation indices $M = 0.4$ and 1.05. It can be noted that the $x-y$ currents are higher using SVPWM2 compared to SVPWM4, while the opposite occurs with the $\alpha-\beta$ currents. It can be concluded that the reduction of the CMV is obtained at the expense of additional losses (SVPWM2) or torque ripple (SVPWM4).

VI. Conclusion

Standard SVPWM techniques for five-phase VSIs generate high peak-to-peak CMV that can be a source of undesired leakage currents. Since each VSI voltage vector is associated to an instantaneous level of the CMV, eliminating certain switching states can reduce the peak-to-peak CMV in five-phase drives. Eliminating zero vectors can reduce the CMV by 40%, and avoiding zero and medium vectors can further reduce the CMV by 80% compared to standard modulations. Both strategies, termed SVPWM2 and SVPWM4 in this work, show similar performance to standard SVPWM1 at high modulation indices, but the performance is diminished at low modulation indices. Even though the peak-to-peak CMV is three times lower using SVPWM4 instead of SVPWM2, higher torque ripples can be obtained due to the absence of medium voltage vectors. Both

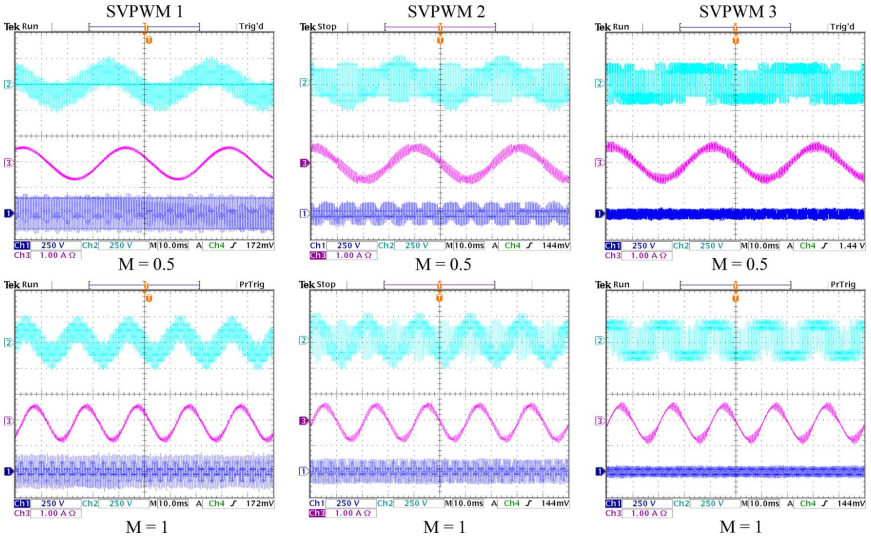

Fig. 9. Experimental phase voltage (upper trace), phase current (middle trace), and CMV (lower trace) in tests supplying the five-phase induction motor with different modulation indices ($M = 0.5$ and $M = 1$) and different modulation techniques (SVPWM1, SVPWM2, and SVPWM4).

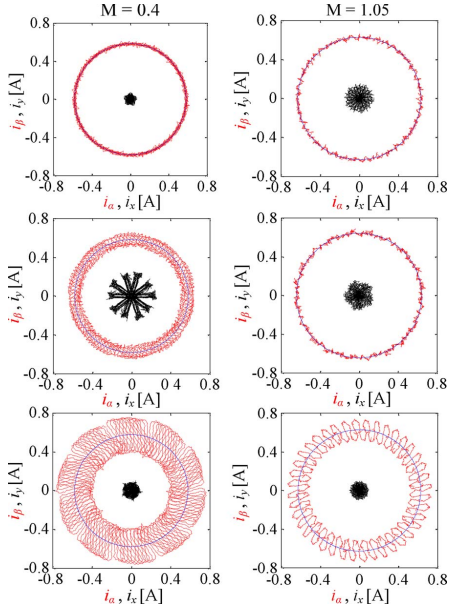

Fig. 10. (Outer circle) Experimental $\alpha-\beta$ currents and (inner trace) $x-y$ currents with modulation indices $M = 0.4-1.05$ and different modulation techniques: (Upper trace) SVPWM1; (middle trace) SVPWM2; and (lower trace) SVPWM4.

SVPWM2 and SVPWM4 show an interesting prospect for industrial applications where the leakage currents produced by high peak-to-peak CMV are a main concern.

REFERENCES

[1] E. Levi, R. Bojoi, F. Profumo, H. Toliyat, and S. Williamson, "Multiphase induction motor drives—A technology status review," *IET Elect. Power Appl.*, vol. 1, no. 4, pp. 489–516, Jul. 2007.

[2] J. A. Riveros, B. Bogado, J. Prieto, F. Barrero, S. Toral, and M. Jones, "Multiphase machines in propulsion drives of electric vehicles," in *Proc. 14th Int. EPE-PEMC*, 2010, pp. 201–206.

[3] L. Parsa and H. A. Toliyat, "Five-phase permanent magnet motor drives for ship propulsion applications," in *Proc. IEEE Elect. Ship Technol. Symp.*, Philadelphia, PA, 2005, pp. 371–378.

[4] M. J. Duran, S. Kouro, B. Wu, E. Levi, F. Barrero, and S. Alepuz, "Six-phase PMSG wind energy conversion system based on medium-voltage multilevel converter," in *Proc. EPE-PEMC*, Birmingham, U.K., 2011, pp. 1–10.

[5] M. Jones, S. N. Vukosavic, and E. Levi, "Parallel-connected multiphase multidrive systems with single inverter supply," *IEEE Trans. Ind. Electron.*, vol. 56, no. 6, pp. 2047–2057, Jun. 2009.

[6] L. Parsa and H. A. Toliyat, "Five-phase permanent-magnet motor drives," *IEEE Trans. Ind. Appl.*, vol. 41, no. 1, pp. 30–37, Jan./Feb. 2005.

[7] M. J. Duran, F. Salas, and M. R. Arahal, "Bifurcation analysis of five-phase induction motor drives with third harmonic injection," *IEEE Trans. Ind. Electron.*, vol. 55, no. 5, pp. 2006–2014, May 2008.

[8] S. Dwari and L. Parsa, "Fault-tolerant control of five-phase permanent-magnet motors with trapezoidal back EMF," *IEEE Trans. Ind. Electron.*, vol. 58, no. 2, pp. 476–485, Feb. 2011.

[9] H. Guzman, M. J. Durán, F. Barrero, and S. Toral, "Fault-tolerant current predictive control of five-phase induction motor drives with an open phase," in *Proc. IEEE IECON*, Melbourne, Australia, pp. 3680–3685.

[10] L. Zheng, J. E. Fletcher, B. W. Williams, and X. He, "A novel direct torque control scheme for a sensorless five-phase induction motor drive," *IEEE Trans. Ind. Electron.*, vol. 58, no. 2, pp. 503–513, Feb. 2011.

[11] H. Miranda, P. Cortés, J. Yus, and J. Rodríguez, "Predictive torque control of induction machine base on state-space model," *IEEE Trans. Ind. Electron.*, vol. 56, no. 6, pp. 1916–1924, Jun. 2009.

[12] J. A. Riveros, J. Prieto, F. Barrero, S. Toral, M. Jones, and E. Levi, "Predictive torque control for five-phase induction motor drives," in *Proc. IECON*, 2010, pp. 2467–2472.

[13] F. Barrero, M. R. Arahal, R. Gregor, S. Toral, and M. J. Durán, "A proof of concept study of predictive current control for VSI driven asymmetrical dual three-phase AC machines," *IEEE Trans. Ind. Electron.*, vol. 56, no. 6, pp. 1937–1954, Jun. 2009.

[14] M. J. Durán, J. Prieto, F. Barrero, and S. Toral, "Predictive current control of dual three-phase drives using restrained search techniques," *IEEE Trans. Ind. Electron.*, vol. 58, no. 8, pp. 3253–3263, Aug. 2011.

[15] F. Barrero, J. Prieto, E. Levi, R. Gregor, S. Toral, M. J. Durán, and M. Jones, "An enhanced predictive current control method for asymmetrical six-phase motor drives," *IEEE Trans. Ind. Electron.*, vol. 58, no. 8, pp. 3242–3252, Aug. 2011.

[16] A. Iqbal and S. Moinuddin, "Comprehensive relationship between carrier-based PWM and space vector PWM in a five-phase VSI," *IEEE Trans. Power Electron.*, vol. 24, no. 10, pp. 2379–2390, Oct. 2009.

[17] O. López, D. Dujic, M. Jones, F. D. Freijedo, J. Doval-Gandoy, and E. Levi, "Multidimensional two-level multiphase space vector PWM algorithm and its comparison with multifrequency space vector PWM method," *IEEE Trans. Ind. Electron.*, vol. 58, no. 2, pp. 465–475, Feb. 2011.

[18] D. Dujic, G. Grandi, M. Jones, and E. Levi, "A space vector PWM scheme for multifrequency output voltage generation with multiphase voltage-source inverters," *IEEE Trans. Ind. Electron.*, vol. 55, no. 5, pp. 1943–1955, May 2008.

[19] D. Dujic, M. Jones, E. Levi, J. Prieto, and F. Barrero, "Switching ripple characteristics of space vector PWM schemes for five-phase two-level voltage source inverters—Part 1: Flux harmonic distortion factors," *IEEE Trans. Ind. Electron.*, vol. 58, no. 7, pp. 2789–2798, Jul. 2011.

[20] L. Gao and J. E. Fletcher, "A space vector switching strategy for three-level five-phase inverter drives," *IEEE Trans. Ind. Electron.*, vol. 57, no. 7, pp. 2332–2343, Jul. 2010.

[21] O. Dordevic, M. Jones, and E. Levi, "A comparison of PWM techniques for three-level five-phase voltage source inverters," in *Proc. EPE-PEMC*, Birmingham, U.K., 2011, pp. 1–10.

[22] E. Levi, M. Jones, and W. Satiawan, "A multiphase dual-inverter supplied drive structure for electric and hybrid electric vehicles," in *Proc. IEEE VPPC*, Lille, France, 2010, pp. 1–7.

[23] J. M. Erdman, R. J. Kerkman, D. W. Schlegel, and G. L. Skibinski, "Effect of PWM inverters on AC motor bearing currents and shaft voltages," *IEEE Trans. Ind. Appl.*, vol. 32, no. 2, pp. 250–259, Mar./Apr. 1996.

[24] A. Muetze and A. Binder, "Don't lose your bearings," *IEEE Ind. Appl. Mag.*, vol. 12, no. 4, pp. 22–31, Jul./Aug. 2006.

[25] M. A. Cash and T. G. Habetler, "Insulation failure prediction in inverter-fed induction machines using line–neutral voltages," in *Proc. IEEE APEC*, 1998, pp. 1035–1039.

[26] E. Zhong and T. A. Lipo, "Improvements in EMC performance of inverter-fed motor drives," *IEEE Trans. Ind. Appl.*, vol. 31, no. 6, pp. 1247–1256, Nov./Dec. 1995.

[27] U. T. Shami and H. Akagi, "Experimental discussions on a shaft end-to-end voltage appearing in an inverter-driven motor," *IEEE Trans. Power Electron.*, vol. 24, no. 6, pp. 1532–1540, Jun. 2009.

[28] R. M. Tallam, R. J. Kerkman, D. Leggate, and R. A. Lukaszewski, "Common-mode voltage reduction PWM algorithm for AC drives," *IEEE Trans. Ind. Appl.*, vol. 46, no. 5, pp. 1959–1969, Sep./Oct. 2010.

[29] Y. S. Lai and F. Shyu, "Optimal common-mode voltage reduction PWM technique for inverter control with considerations of the dead time effects—Part I: Basic development," *IEEE Trans. Ind. Appl.*, vol. 40, no. 6, pp. 1605–1612, Nov./Dec. 2004.

[30] J. W. Kimball and M. Zawodniok, "Reducing common-mode voltage in three-phase sine-triangle PWM with interleaved carriers," *IEEE Trans. Power Electron.*, vol. 26, no. 8, pp. 2229–2236, Aug. 2011.

[31] S. Lakshminarayanan, G. Mondal, P. N. Tekwani, K. K. Mohapatra, and K. Gopakumar, "Twelve-sided polygonal voltage space vector based multilevel inverter for an induction motor drive with common-mode voltage elimination," *IEEE Trans. Ind. Electron.*, vol. 54, no. 5, pp. 2761–2768, Oct. 2007.

[32] H. J. Kim, H. D. Lee, and S. K. Sul, "A new PWM strategy for common-mode voltage reduction in neutral-point-clamped inverter-fed AC motor drives," *IEEE Trans. Ind. Appl.*, vol. 37, no. 6, pp. 1840–1845, Nov./Dec. 2001.

[33] J. A. Riveros, F. Barrero, M. J. Durán, B. Bogado, and S. Toral, "Estimation of the electrical parameters of a five-phase induction machine using standstill techniques. Part I: Theoretical discussions," in *Proc. IEEE IECON*, Melbourne, Australia, pp. 3668–3673.

[34] J. A. Riveros, F. Barrero, M. J. Durán, B. Bogado, and S. Toral, "Estimation of the electrical parameters of a five-phase induction machine using standstill techniques. Part II: Practical implications," in *Proc. IEEE IECON 2011*, Melbourne, Australia, pp. 3674–3679.

Mario J. Durán received the M.Sc. and Ph.D. degrees in electrical engineering from the University of Malaga, Malaga, Spain, in 1999 and 2003, respectively.

He is currently an Associate Professor with the Department of Electrical Engineering, University of Malaga.

Prof. Duran was the recipient of the Best Paper Award from the IEEE TRANSACTIONS ON INDUSTRIAL ELECTRONICS in 2009.

Joel Prieto (S'10) was born in Asuncion, Paraguay. He received the B.Eng. degree in electronic engineering from the Universidad Catolica "Nuestra Señora de la Asuncion," Asuncion, in 2005, and the M.Sc. degree from the University of Seville, Seville, Spain, in 2009, where he is currently working toward the Ph.D. degree.

In 2008, he joined the Department of Electronic Engineering, University of Seville. His research interests include modern modulation and control strategies of multiphase drives.

Mr. Prieto is a recipient of a scholarship from Itaipu Binacional/Parque Tecnologico Itaipu—Paraguay for his Ph.D. studies.

Federico Barrero (M'04–SM'05) was born in Seville, Spain, in 1967. He received the M.Sc. and Ph.D. degrees in electrical and electronic engineering from the University of Seville, Seville, in 1992 and 1998, respectively.

Since 1992, he has been with the Department of Electronic Engineering, University of Seville, where he is currently an Associate Professor. His recent interests include microprocessor and digital signal processor device systems, sensor networks, and control of multiphase ac drives.

José A. Riveros received the B.Eng. degree in electronic engineering from the Universidad Nacional de Asunción, San Lorenzo, Paraguay, in 2007 and the M.Sc. degree from the University of Seville, Seville, Spain, in 2010, where he is working toward the Ph.D. degree.

Since 2009, he has been with the Department of Electronic Engineering, University of Seville.

Mr. Riveros is a recipient of a scholarship from Itaipu Binacional/Parque Tecnológico Itaipu—Paraguay for his Ph.D. studies.

Hugo Guzman received the B.Eng. degree in electronic engineering from the Pontificia Universidad Javeriana, Bogota, Colombia, in 2009 and the M.Sc. degree from the University of Seville, Seville, Spain, in 2011, where he has been working toward the Ph.D. degree in the Department of Electronic Engineering since 2010.

Since 2007, he he has been with the Department of Electronic Engineering, University of Seville, as a Research Assistant.

3.7. Paper 7

Authors: M.J. Duran, J. Prieto y F. Barrero.
Title: Space Vector PWM With Reduced Common-Mode Voltage for Five-Phase Induction Motor Drives Operating in Overmodulation Zone.
Journal: IEEE Transactions on Power Electronics.
Volume: 28.
Number: 8.
Pages: 4030-4040.
Date: August 2013.
Abstract: This study presents a space vector pulsewidth modulation algorithm for five-phase converters operating in the overmodulation region that forbids the use of zero vectors, covering the whole overmodulation range and providing minimum $x-y$ voltages. Avoiding zero vectors reduces the content of low-order current harmonics and, at the same time, reduces the common-mode voltage (CMV) by 40 %. The method is first implemented using medium and large voltage space vectors, showing good performance in terms of current harmonic content. Then, the algorithm is applied to the case when four large vectors are used, further reducing the peak-to-peak CMV by 80 % and still demonstrating a satisfactory performance. Both methods are experimentally compared to existing overmodulation algorithms obtaining better current quality and lower peak-to-peak CMV.

4030 IEEE TRANSACTIONS ON POWER ELECTRONICS, VOL. 28, NO. 8, AUGUST 2013

Space Vector PWM With Reduced Common-Mode Voltage for Five-Phase Induction Motor Drives Operating in Overmodulation Zone

Mario J. Durán, Joel Prieto, *Student Member, IEEE*, and Federico Barrero, *Senior Member, IEEE*

***Abstract*—This study presents a space vector pulsewidth modulation algorithm for five-phase converters operating in the overmodulation region that forbids the use of zero vectors, covering the whole overmodulation range and providing minimum x–y voltages. Avoiding zero vectors reduces the content of low-order current harmonics and, at the same time, reduces the common-mode voltage (CMV) by 40%. The method is first implemented using medium and large voltage space vectors, showing good performance in terms of current harmonic content. Then, the algorithm is applied to the case when four large vectors are used, further reducing the peak-to-peak CMV by 80% and still demonstrating a satisfactory performance. Both methods are experimentally compared to existing overmodulation algorithms obtaining better current quality and lower peak-to-peak CMV.**

***Index Terms*—Common-mode voltage (CMV), multiphase drives, overmodulation, space vector pulsewidth modulation (SVPWM).**

I. Introduction

AMONG the different advantages of multiphase drives, the enhanced robustness provided by the additional phases is one of the most attractive features [1]. Fault tolerance of multiphase induction motor drives makes them suitable for safety-critical or low-maintenance applications like electrical vehicles or offshore wind energy systems, respectively, [2], [3]. The failure of a power switch in the electronic converter or the open circuit of a faulted motor phase can be overcome modifying the control strategy to continue operating without torque ripples or vibrations [4]. Nevertheless, the sources of potential failures in multiphase drives are of different natures and some of them cannot be solved at the control stage. For example, the breakdown of the windings insulation or the damage of the motor bearings is frequently caused by the voltage appearing between the motor shaft and the grounded motor frame [5]–[7]. This shaft-to-frame voltage is a percentage of the common-mode voltage (CMV) defined by the bearing voltage ratio [8] and generates parasitic currents that flow through the motor bearings, spoiling the drive robustness [9]. Neither the redundancy provided by the additional phases nor the modifications in the control scheme can help in the prevention of these types of failures.

There is not a single mechanism to explain the appearance of the common-mode leakage currents. Both electric discharge machining (EDM) and displacement bearing currents (dv/dt) can flow when the peak-to-peak CMV exceeds a certain threshold or due to sharp changes in the CMV [5]–[9]. Even though it is possible to protect the bearings using grounding brushes in the drive-end shaft, this solution is costly and involves additional maintenance that reduces the overall reliability [5]. For this reason, the most simple and nonexpensive solution is to reduce the CMV in the modulation stage by designing suitable pulsewidth modulation (PWM) techniques [10]–[14]. The dv/dt of the CMV is inherently reduced in multiphase PWM techniques, being equal to the dc-link voltage (V_{DC}) over n, where n is the number of phases of the multiphase drive ($n = 5$ in this study). However, the peak-to-peak CMV remains equal to the dc-link voltage as in three-phase drives. For this reason, it is necessary to use specific PWM strategies in order to reduce the main source of EDM bearing currents, namely the peak-to-peak CMV. Carrier-based and space vector versions of PWM techniques with reduced CMV have been proposed for three-phase drives operating in the linear region [11]–[14]. In all cases, the reduction of the peak-to-peak CMV is obtained avoiding zero switching states that generate the highest values of the CMV. When three-phase converters enter the overmodulation zone, the zero vectors no longer need to be used, and consequently, the operation in the pulse dropping region inherently provides low CMV. However, this is not the case in multiphase converters because the overmodulation algorithms become more complex due to the additional voltage space vectors and subspaces [1].

Application of the generalized Clarke's transformation to the switching states of a five-phase converter provides $2^5 = 32$ space vectors (zero, small, medium, and large), two subspaces (α–β and x–y) and ten sectors in the α–β subspace [15]–[17]. Initial attempts to design space vector pulsewidth modulation (SVPWM) algorithms in the overmodulation region used two large vectors per sector to average the α–β reference voltages, typically obtained from an outer loop in a field-oriented control [18]. Unfortunately, the non-null x–y voltage components that result from this solution find a low impedance path, generating

Manuscript received July 4, 2012; revised September 17, 2012; accepted November 4, 2012. Date of current version January 18, 2013. This work was supported by the Spanish Government (National Research, Development and Innovation Plan, under references DPI2011-25396 and DPI2009-07955, and Junta de Andalucía 2010 research program, under reference TEP-5791) and Itaipu Binacional/Parque Tecnológico Itaipu-Paraguay. Recommended for publication by Associate Editor P. Barbosa.

M. J. Durán is with the Department of Electrical Engineering, University of Málaga, 29071 Málaga, Spain (e-mail: mjduran@uma.es).

J. Prieto and F. Barrero are with the Department of Electronic Engineering, University of Seville, 41092 Seville, Spain (e-mail: jprieto@esi.us.es; fbarrero@us.es).

Color versions of one or more of the figures in this paper are available online at http://ieeexplore.ieee.org.

Digital Object Identifier 10.1109/TPEL.2012.2229394

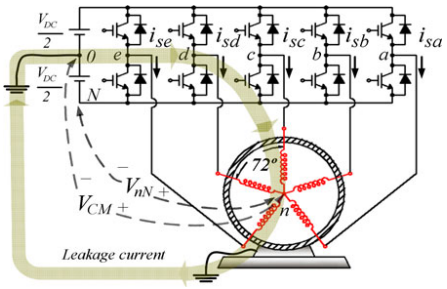

Fig. 1. Two-level five-phase induction motor drive scheme showing the leakage currents flowing via the grounded motor frame.

high stator currents that spoil the drive efficiency. This shortcoming was solved using two medium and two large vectors per sector and canceling x–y voltages by adjusting the times of application of the four selected voltage space vectors [19]. The method in [19], further on referred as SVPWM1, achieves an optimal solution in the linear region, but it did not restrict the use of zero vectors in the overmodulation region. The time of application of the zero vectors in [19] becomes zero only when the reference voltage vector is located in the middle of the sector, but it is not null otherwise. This use in the pulse dropping zone provides a suboptimal solution and generates large peak-to-peak CMV.

This study presents an SVPWM algorithm for five-phase converters operating in the overmodulation region that forbids the use of zero vectors, covering the whole overmodulation range and providing minimum x–y voltages. The algorithm is first applied to the case where two medium and two large vectors per sector are selected (as in [19]). This solution, further on referred as SVPWM2, fully avoids the use of zero vectors reducing the peak-to-peak CMV by 40% compared to SVPWM1. Next, the algorithm is applied considering two large and two adjacent large vectors per sector. This solution, further on referred as SVPWM3, additionally eliminates the use of medium voltage space vectors, reducing the peak-to-peak CMV by 80% compared to SVPWM1. The performance of the three methods (SVPWM1, SVPWM2, and SVPWM3) is compared in the whole overmodulation range up to the ten-step mode of operation. Even though the algorithm is applied to a five-phase system, it remains valid for any multiphase converter with an odd number of phases.

This paper is structured as follows. Section II describes the SVPWM in the linear zone and the CMV in five-phase drives. Section III details the proposed overmodulation SVPWM algorithms. Section IV describes the experimental rig and shows the comparative experimental results. Conclusions are finally drawn in Section V.

II. Space Vector PWM and CMV in Five-Phase Drives

The five-phase drive consists of a two-level five-phase voltage source inverter (VSI) supplying a five-phase motor (see Fig. 1).

The state of leg k in the five-phase VSI, $k \in \{a, b, c, d, e\}$, is defined by a switching function $S_k \in \{0, 1\}$ that provides 1 when phase k is connected to the positive rail of the VSI (top switch ON and bottom switch OFF) and 0 when phase k is connected to the negative rail of the VSI (top switch OFF and bottom switch ON). The state of the VSI is then determined by the switching vector that contains the states of the five legs

$$\underline{S} = [\, S_a \quad S_b \quad S_c \quad S_d \quad S_e \,] \tag{1}$$

where vector notation is indicated using underlined variables. The voltage of leg k with respect to the negative rail of the VSI can then be expressed as a function of the leg switching function S_k and the dc-link voltage V_{DC}

$$V_{kN} = S_k \cdot V_{\mathrm{DC}}. \tag{2}$$

Since the neutral of the five-phase machine in Fig. 1 is isolated, the phase voltages can be calculated as [20]

$$v_{kn} = \frac{4}{5} V_{kN} - \frac{1}{5} \sum_{i=1, i\neq k}^{5} V_i. \tag{3}$$

Phase voltages of (3) can then be mapped into the α–β and x–y subspaces using the current invariant transformation provided by the general Clarke's transformation [1]

$$\begin{bmatrix} v_\alpha \\ v_\beta \\ v_x \\ v_y \\ v_0 \end{bmatrix} = \frac{2}{5} \begin{bmatrix} 1 & \cos(\alpha) & \cos(2\alpha) & \cos(3\alpha) & \cos(4\alpha) \\ 0 & \sin(\alpha) & \sin(2\alpha) & \sin(3\alpha) & \sin(4\alpha) \\ 1 & \cos(2\alpha) & \cos(4\alpha) & \cos(6\alpha) & \cos(8\alpha) \\ 0 & \sin(2\alpha) & \sin(4\alpha) & \sin(6\alpha) & \sin(8\alpha) \\ 1/2 & 1/2 & 1/2 & 1/2 & 1/2 \end{bmatrix} \times \begin{bmatrix} v_{an} \\ v_{bn} \\ v_{cn} \\ v_{dn} \\ v_{en} \end{bmatrix} \tag{4}$$

where $\alpha = 2\pi/5$. Application of (2)–(4) to the $2^5 = 32$ switching vectors provides 32 voltage space vectors both in α–β and x–y subspaces (see Fig. 2). Each voltage space vector is numbered from now on according to the decimal number of its switching vector (1). Depending on the size of the vectors in the α–β subspace (upper plot in Fig. 2), they are classified in two zero, ten small, ten medium, and ten large voltage space vectors [1]. Zero vectors correspond to switching states 0–5 (all legs with $S_k = 0$ or vice versa), medium vectors correspond to switching states 1–4 (one leg with $S_k = 0$ and four legs with $S_k = 1$ or vice versa) and small/large vectors correspond to switching states 2 and 3 (two legs with $S_k = 0$ and three legs with $S_k = 1$ or vice versa).

Switching states 0–5 and 1–4 generate zero and medium voltage space vectors both in α–β and x–y planes. However, switching states 2 and 3 that correspond to large vectors in the α–β plane generate small vectors in the x–y plane and vice versa (see Table I). In addition to the lengths of the voltage space vectors in α–β and x–y planes, each switching state imposes a certain amount of CMV upon the induction machine. The CMV,

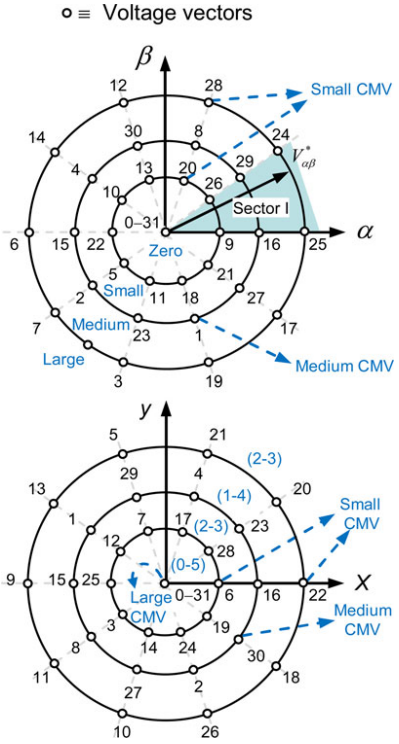

Fig. 2. Zero, small, medium, and large vectors in the α–β and x–y planes using the five-phase power converter and its correspondence with the small (2 and 3), medium (1–4), and large (0–5) CMV switching states.

TABLE I
MAGNITUDE OF CMV ACCORDING TO THE SWITCHING STATES

	Switching states	*α-β Size*	*x-y Size*	$\lvert V_{CM}\rvert$
Large CMV (0-5)	{00000} {11111}	Z	Z	$0.5{\cdot}V_{DC}$
Medium CMV (1-4)	{00001} {00010} {00100} {01000} {10000}	M	M	$0.3{\cdot}V_{DC}$
	{11110} {11101} {11011} {10111} {01111}	M	M	
Small CMV (2-3)	{00011}{11001}{10001} {00110} {01100}{10100} {11000}{00111}{01110}{10011}	L	S	$0.1{\cdot}V_{DC}$
	{00101} {11100} {11010} {10110} {10101} {01101} {01011}{01001}{01010}{10010}	S	L	

from now on V_{CM}, relates the motor neutral voltage to the dc-link midpoint and its expression in two-level five-phase drives is [21]

$$V_{\mathrm{CM}} = \frac{V_{\mathrm{DC}}}{5} \cdot (S_a + S_b + S_c + S_d + S_e) - \frac{V_{\mathrm{DC}}}{2}. \quad (5)$$

From (5), it follows that the maximum peak value of the CMV is $|V_{\mathrm{CM}}| = V_{\mathrm{DC}}/2$, the minimum voltage variation is $\pm V_{\mathrm{DC}}/5$, and the number of CMV levels is six. These six CMV levels can be grouped into three different magnitudes: large CMV ($\pm 0.5{\cdot}V_{\mathrm{DC}}$), medium CMV ($\pm 0.3{\cdot}V_{\mathrm{DC}}$), and small CMV ($\pm 0.1{\cdot}V_{\mathrm{DC}}$). Each switching state is associated with a certain magnitude of the CMV and a certain length of the α–β and x–y voltage space vectors, satisfying that:

1) switching states 0–5 generate zero voltage vectors both in α–β and x–y subspaces, and provide large CMV ($\pm 0.5{\cdot}V_{\mathrm{DC}}$);
2) switching states 1–4 generate medium voltage vectors both in α–β and x–y subspaces, and provide medium CMV ($\pm 0.3{\cdot}V_{\mathrm{DC}}$);
3) switching states 2 and 3 generate small voltage vectors in α–β plane and large voltage vectors in x–y plane or vice versa and provide small CMV ($\pm 0.1{\cdot}V_{\mathrm{DC}}$).

The information of the different switching states is summarized in Table I, where Z, M, and L stand for zero, medium, and large, respectively. The information of the different switching states is summarized in Table I, where Z, M, and L stand for zero, medium, and large, respectively.

It follows from this analysis that the reduction of the peak-to-peak CMV in the design of the SVPWM algorithm can be achieved if switching states 0–5 and/or 1–4 are avoided. The reduction of the peak value of the CMV can in turn help to mitigate EDM bearing currents flowing through the motor bearings [9].

A subgroup of the $2^5 = 32$ switching states previously analyzed needs to be selected by the SVPWM algorithm to fulfill the drive control requirements. The drive control typically has an outer speed/torque loop and two inner current control loops that provide the voltage reference vectors in the α–β subspace, v_α^* and v_β^*. Since x–y voltage components resulting from (4) only generate Joule losses in distributed-winding machines, the references in this plane are kept null from now on, $v_x^* = 0$ and $v_y^* = 0$.

The main task of the SVPWM algorithm is then to synthesize the α–β reference voltage vectors while keeping zero average volt–second in the x–y plane. This aim can only be achieved if a minimum of four active vectors are selected from those depicted in Fig. 2. Regardless of which vectors are selected by the SVPWM algorithm, these four vectors are further on termed as

$$\begin{aligned} \underline{v}_1 &= [\, v_{1\alpha} \quad v_{1\beta} \quad v_{1x} \quad v_{1y} \,] \\ \underline{v}_2 &= [\, v_{2\alpha} \quad v_{2\beta} \quad v_{2x} \quad v_{2y} \,] \\ \underline{v}_3 &= [\, v_{3\alpha} \quad v_{3\beta} \quad v_{3x} \quad v_{3y} \,] \\ \underline{v}_4 &= [\, v_{4\alpha} \quad v_{4\beta} \quad v_{4x} \quad v_{4y} \,]. \end{aligned} \quad (6)$$

The times of application of these four vectors can be calculated as

$$\begin{bmatrix} t_1 \\ t_2 \\ t_3 \\ t_4 \end{bmatrix} = \begin{bmatrix} v_{1\alpha} & v_{2\alpha} & v_{3\alpha} & v_{4\alpha} \\ v_{1\beta} & v_{2\beta} & v_{3\beta} & v_{4\beta} \\ v_{1x} & v_{2x} & v_{3x} & v_{4x} \\ v_{1y} & v_{2y} & v_{3y} & v_{4y} \end{bmatrix}^{-1} \begin{bmatrix} v_\alpha^* \\ v_\beta^* \\ 0 \\ 0 \end{bmatrix} T_s \quad (7)$$

with T_s being the sampling time. Zero vectors are then applied during the rest of the sampling period

$$t_0 = T_s - \sum_{k=1}^{4} t_k. \tag{8}$$

The selection of the four active vectors of (6) is usually done on the basis of the sector where the α–β reference voltage space vector is located. The most popular choice is the application of the two medium and two large vectors delimiting each sector. For the sake of example, in sector I, the four selected active vectors would be 29, 16 (medium) and 24, 25 (large). Preordering these four vectors to obtain minimum switching frequency, the vectors of (6) in sector I are $v_1 \equiv 16$, $v_2 \equiv 24$, $v_3 \equiv 25$, and $v_4 \equiv 29$. Application of two zero, two medium, and two large vectors in a switching period with the times obtained from (7) and (8) provides satisfactory results in the linear region [19] in terms of voltage generation and power quality. Unfortunately, it follows from the analyses shown in Table I that this option generates the maximum peak-to-peak CMV equal to V_{DC}. The use of switching states 0–5 and/or 1–4 can however be avoided in the overmodulation region fulfilling the control requirements with reduced CMV.

III. Overmodulation SVPWM With Reduced CMV in Five-Phase Drives

The linear modulation range extends up to $M = 1.0514 = 1/\cos(\pi/10)$, with M being the modulation index

$$M = \frac{2 \cdot |V^*|}{V_{\mathrm{DC}}} \tag{9}$$

where $|V^*|$ is the peak value of the ac phase voltages. Within the linear range, it is possible to comply with the control requirements (i.e., generation of v_α^* and v_β^* and cancellation of *x*–*y* voltages). On the contrary, for modulation indices above 1.0514, the cancellation of the *x*–*y* voltages is no longer possible and consequently low-order voltage harmonics (of the order $10n\pm3$, $n = 0,1,2,3,\ldots$) appear. Unfortunately, only the stator resistance and leakage inductance exist in the *x*–*y* equations because of the airgap flux cancellation. As a consequence, the low-order *x*–*y* voltage harmonics find a low-impedance path that generates high stator currents that do not contribute to the torque production. For this reason, it becomes fundamental to minimize the *x*–*y* voltage components in the whole operation range, including the overmodulation zone.

Initial attempts to design overmodulation SVPWM algorithms just considered the large neighboring vectors at each sector (24 and 25 in sector I) in the α–β plane, but the resulting *x*–*y* voltages proved to be excessive. Aiming to reduce the *x*–*y* low-order voltage harmonics, the two medium and two large vectors per sector (16, 24, 25, and 29 in sector I) were used in SVPWM1, extending the procedure of the linear region to the overmodulation zone. Nevertheless, the algorithm proposed in [19] (SVPWM1), does not provide minimum *x*–*y* voltages, still applies the zero vectors and does not cover the whole overmodulation range. Aiming to overcome these shortcomings, this study presents an overmodulation algorithm that avoids the use

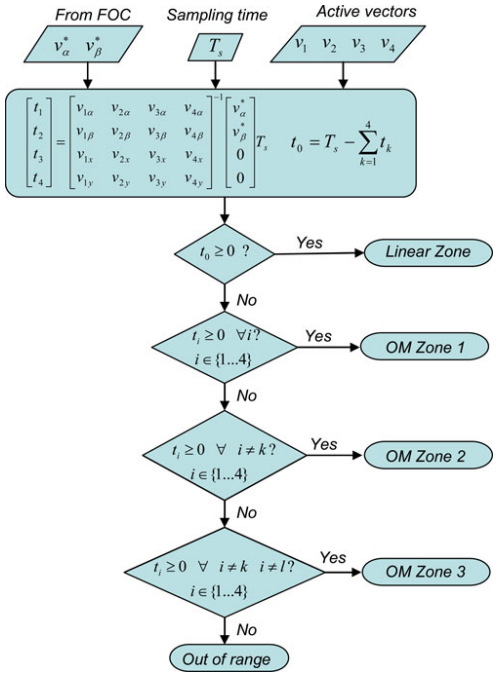

Fig. 3. Flowchart showing the different zones in the linear and overmodulation region.

of zero vectors in the whole overmodulation zone, minimizes the *x*–*y* voltage components and covers the overmodulation region up to the ten-step mode.

The proposed method calculates the times of application of the four active and two zero vectors using (7) and (8) as in a standard SVPWM algorithm in the linear range. The time of application of the zero vectors t_0 is a positive number if the modulation index is below 1.0514. Consequently, if t_0 becomes negative, it means that the VSI needs to operate in the overmodulation region.

Three cases can be distinguished once the pulse dropping region has been entered:

1) if the times of application of the four active vectors are positive, the algorithm is in zone 1.
2) if one of the times of application of the four active vectors is negative (t_k in Fig. 3), the algorithm is in zone 2;
3) if two of the times of application of the four active vectors are negative (t_k and t_l in Fig. 3), the algorithm is in zone 3;
4) if three or more of the times of application of the four active vectors are negative, the algorithm is out of range.

The algorithm uses the signs of the zero and four active vectors (t_0, t_1, t_2, t_3, and t_4) to determine the mode of operation of the modulation technique (see Fig. 3). Since no assumptions are made about the nature of the four active vectors (v_1, v_2, v_3,

and v_4), the method is generally valid. It will be referred as SVPWM2 when it uses the two medium and two large voltage space vectors per sector and SVPWM3 when it uses four large vectors adjacent to the reference (two clockwise, two counterclockwise). The vectors are always preordered in the following form.

1) SVPWM2: vectors are applied in ascending order, so that in sector 1, the order is $v_1 \equiv 16$, $v_2 \equiv 24$, $v_3 \equiv 25$, and $v_4 \equiv 29$.
2) SVPWM3: the order is always clockwise, so that in sector 1, the order is $v_1 \equiv 28$, $v_2 \equiv 24$, $v_3 \equiv 25$, and $v_4 \equiv 17$.

As a general description of the different zones, it can be stated that:

1) in zone 1, the four vectors v_i ($i \in \{1, 2, 3, 4\}$) are applied, the α–β voltage reference is synthesized, and the *x*–*y* voltage is minimized.
2) in zone 2, three active vectors v_i ($i \in \{1, 2, 3, 4\}$, $i \neq k$) are applied, and the α–β voltage reference is synthesized.
3) in zone 3, two active vectors v_i ($i \in \{1, 2, 3, 4\}$, $i \neq k$, $i \neq l$) are applied, and the α–β voltage error is minimized.

Zero vectors, responsible of the highest peak-to-peak CMV, are not applied in any of these zones.

A. Overmodulation in Zone 1: Application of Four Active Vectors

When the overmodulation region is reached, the times of application of the four active vectors can no longer be calculated from (7) because the time of application of the zero vectors becomes negative. This is the moment when the linear modulation region is surpassed and the overmodulation zone 1 is entered. Since the zero vectors are not applied in zone 1, the four active vectors need to be applied during the whole sampling period

$$t_1 + t_2 + t_3 + t_4 = T_s. \tag{10}$$

This restriction implies that v_x^* and v_y^* cannot be simultaneously satisfied because one degree of freedom has been lost. However, it is still possible to synthesize v_α^* and v_β^* and minimize one condition in the *x*–*y* plane like $v_x^2 + v_y^2$.

Fulfilling restriction (10) and synthesizing v_α^* and v_β^* from (7) yields

$$\begin{bmatrix} t_1 \\ t_2 \\ t_3 \end{bmatrix} = \begin{bmatrix} v_{1\alpha} & v_{2\alpha} & v_{3\alpha} \\ v_{1\beta} & v_{2\beta} & v_{3\beta} \\ 1 & 1 & 1 \end{bmatrix}^{-1} \begin{bmatrix} v_\alpha^* T_s - t_4 v_{4\alpha} \\ v_\beta^* T_s - t_4 v_{4\beta} \\ T_s - t_4 \end{bmatrix}. \tag{11}$$

From the linear equations of (11), it is possible to obtain linear relationships between t_1, t_2, and t_3 as functions of t_4

$$\begin{aligned} t_1 &= C_1 + C_2 t_4 \\ t_2 &= C_3 + C_4 t_4 \\ t_3 &= C_5 + C_6 t_4 \end{aligned} \tag{12}$$

where coefficients C_1–C_6 are detailed in the Appendix.

Substituting the linear equation of (12) into the third and fourth rows of (7) allows expressing v_x and v_y as a linear function of t_4

$$\begin{aligned} v_x &= C_7 + C_8 t_4 \\ v_y &= C_9 + C_{10} t_4 \end{aligned} \tag{13}$$

where coefficients C_7–C_{10} are also detailed in the Appendix.

Imposing the condition of minimum value in the magnitude of the *x*–*y* voltage

$$\frac{\partial \left(v_x^2 + v_y^2\right)}{\partial t_4} = 0 = (2C_7C_8 + 2C_9C_{10}) + 2t_4 \left(C_8^2 + C_{10}^2\right) \tag{14}$$

provides a t_4 value as follows:

$$t_4 = -\frac{(C_7C_8 + C_9C_{10})}{(C_8^2 + C_{10}^2)}. \tag{15}$$

Substituting (15) into (11), it is possible to obtain the remaining times of application t_1, t_2, and t_3. From (15) and (11), the times of application of the four active vectors are obtained. This solution is valid, while the active vectors calculated in (11)–(15) are positive, as indicated in the flowchart of Fig. 3. If any of the four active vectors becomes negative, then overmodulation zone 2 is entered.

TABLE II
DWELL TIMES IN THE THREE OVERMODULATION ZONES

Overmodulation zone 1: M=1.1, φ = 10°					
SVPWM2	$v_1 \equiv 16$	$v_2 \equiv 24$	$v_3 \equiv 25$	$v_4 \equiv 29$	$v_0 \equiv 0$
Eq. (7)	t_1=0.29	t_2=0.18	t_3=0.46	t_4=0.11	**t_0=-0.04**
(11)-(15)	t_1=0.24	t_2=0.21	t_3=0.49	t_4=0.06	t_0=0
SVPWM3	$v_1 \equiv 28$	$v_2 \equiv 24$	$v_3 \equiv 25$	$v_4 \equiv 17$	$v_0 \equiv 0$
Eq. (7)	t_1=0.11	t_2=0.35	t_3=0.29	t_4=0.29	**t_0=-0.04**
(11)-(15)	t_1=0.06	t_2=0.38	t_3=0.32	t_4=0.24	t_0=0
Overmodulation zone 2: M=1.2, φ = 10°					
SVPWM2	$v_1 \equiv 16$	$v_2 \equiv 24$	$v_3 \equiv 25$	$v_4 \equiv 29$	$v_0 \equiv 0$
(11)-(15)	t_1=0.14	t_2=0.30	t_3=0.61	**t_4=-0.05**	t_0=0
Eq. (18)	t_1=0.09	t_2=0.27	t_3=0.64	t_4=0	t_0=0
SVPWM3	$v_1 \equiv 28$	$v_2 \equiv 24$	$v_3 \equiv 25$	$v_4 \equiv 17$	$v_0 \equiv 0$
(11)-(15)	**t_1=-0.05**	t_2=0.49	t_3=0.42	t_4=0.14	t_0=0
Eq. (18)	t_1=0	t_2=0.37	t_3=0.54	t_4=0.09	t_0=0
Overmodulation zone 3: M=1.29, φ = 10°					
SVPWM2	$v_1 \equiv 16$	$v_2 \equiv 24$	$v_3 \equiv 25$	$v_4 \equiv 29$	$v_0 \equiv 0$
Eq. (17)	**t_1=-0.1**	t_2=0.30	t_3=0.80	t_4=0	t_0=0
(18)-(22)	t_1=0	t_2=0.28	t_3=0.72	t_4=0	t_0=0
SVPWM3	$v_1 \equiv 28$	$v_2 \equiv 24$	$v_3 \equiv 25$	$v_4 \equiv 17$	$v_0 \equiv 0$
Eq. (17)	t_1=0	t_2=0.20	t_3=0.90	**t_4=-0.1**	t_0=0
(18)-(22)	t_1=0	t_2=0.28	t_3=0.72	t_4=0	t_0=0

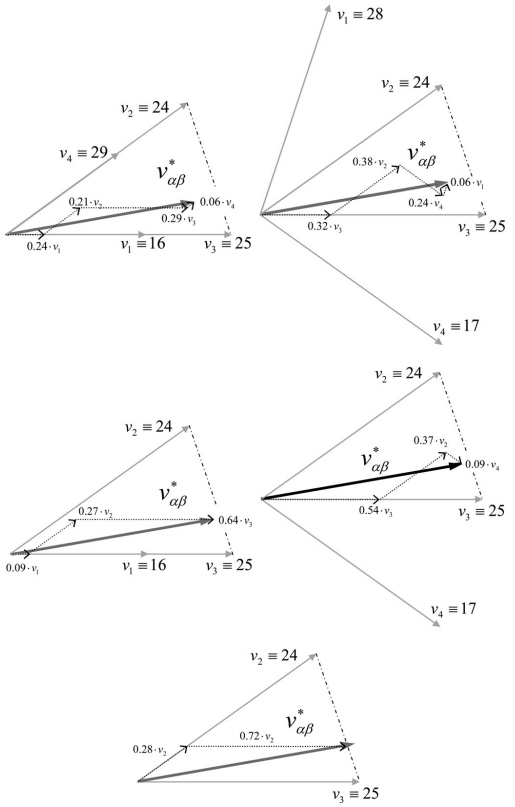

Fig. 4. Generation of the α–β voltage space vector in sector I for SVPWM2 (left) and SVPWM3 (right) in the overmodulation zone 1 ($M = 1.1$, upper plot), zone 2 ($M = 1.2$, middle plot), and zone 3 ($M = 1.29$, lower plot).

TABLE III
ELECTRICAL PARAMETERS OF THE FIVE-PHASE MACHINE

Parameter	*Value*	*Parameter*	*Value*
R_s [Ω]	12.85	P [kW]	1.4
σL_s [mH]	151.65	p	3
L_s, L_r [mH]	768.80	ω_n [rpm]	990
M [mH]	688.92	J_m [kg·m^2]	0.148
τ_r [ms]	179.49	B_m [N·m·s]	0.036

B. Overmodulation in Zone 2: Application of Three Active Vectors

If one of the times of application t_k ($k \in \{1, 2, 3, 4\}$) obtained from (11)–(15) becomes negative, it means that the vector v_k cannot be applied any more. At this instant, the overmodulation in zone 2 uses the three remaining active vectors v_i ($i \in \{1, 2, 3, 4\}$, $i \neq k$) to generate the α–β voltage reference. Without loss of generality, let us assume that the time $t_4 < 0$. Vector v_4 is discarded in overmodulation zone 2 and vectors v_1, v_2, and v_3

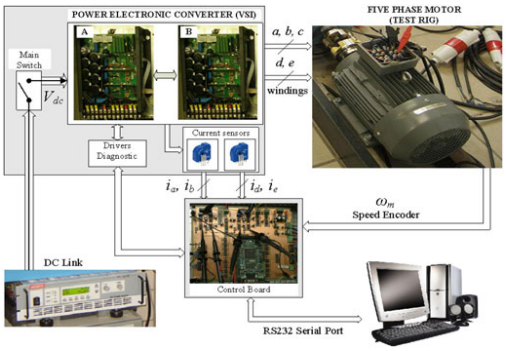

Fig. 5. Experimental system, including the power and control modules at the left side, and the five-phase induction machine at the right side.

are applied during the whole sampling period, satisfying

$$t_1 + t_2 + t_3 = T_s. \tag{16}$$

Restriction (16) together with the generation of the α–β voltage references yields

$$\begin{bmatrix} t_1 \\ t_2 \\ t_3 \end{bmatrix} = \begin{bmatrix} v_{1\alpha} & v_{2\alpha} & v_{3\alpha} \\ v_{1\beta} & v_{2\beta} & v_{3\beta} \\ 1 & 1 & 1 \end{bmatrix}^{-1} \begin{bmatrix} v^*_\alpha \\ v^*_\beta \\ 1 \end{bmatrix} \cdot T_s \tag{17}$$

which corresponds to (11) if the time of application t_4 is zeroed. This solution is again valid while the calculated times are positive. If any of the times calculated in (17) results negative, then overmodulation in zone 3 is entered.

C. Overmodulation in Zone 3: Application of Two Active Vectors

If any of the times calculated in (17) is negative, only the two vectors with positive times of application are used. Without loss of generality, let us consider that $t_1 < 0$. Voltage vector v_1 is then discarded and only vectors v_2 and v_3 are applied during the whole sampling period, fulfilling the following restriction:

$$t_2 + t_3 = T_s. \tag{18}$$

From the first and second rows in (7), it is possible to obtain that

$$T_s \cdot \begin{bmatrix} v_\alpha \\ v_\beta \end{bmatrix} = \begin{bmatrix} v_{2\alpha} & v_{3\alpha} \\ v_{2\beta} & v_{3\beta} \end{bmatrix} \begin{bmatrix} t_2 \\ t_3 \end{bmatrix}. \tag{19}$$

Combining (18) and (19), the errors of the α–β voltages are linearly dependent on the time of application t_2

$$\begin{aligned} v_\alpha - v^*_\alpha &= C_{11} + C_{12} t_2 \\ v_\beta - v^*_\beta &= C_{13} + C_{14} t_2 \end{aligned} \tag{20}$$

where coefficients C_{11}–C_{14} are detailed in the Appendix.

Since only two voltage space vectors are applied and condition (18) is imposed, only one degree of freedom remains, and

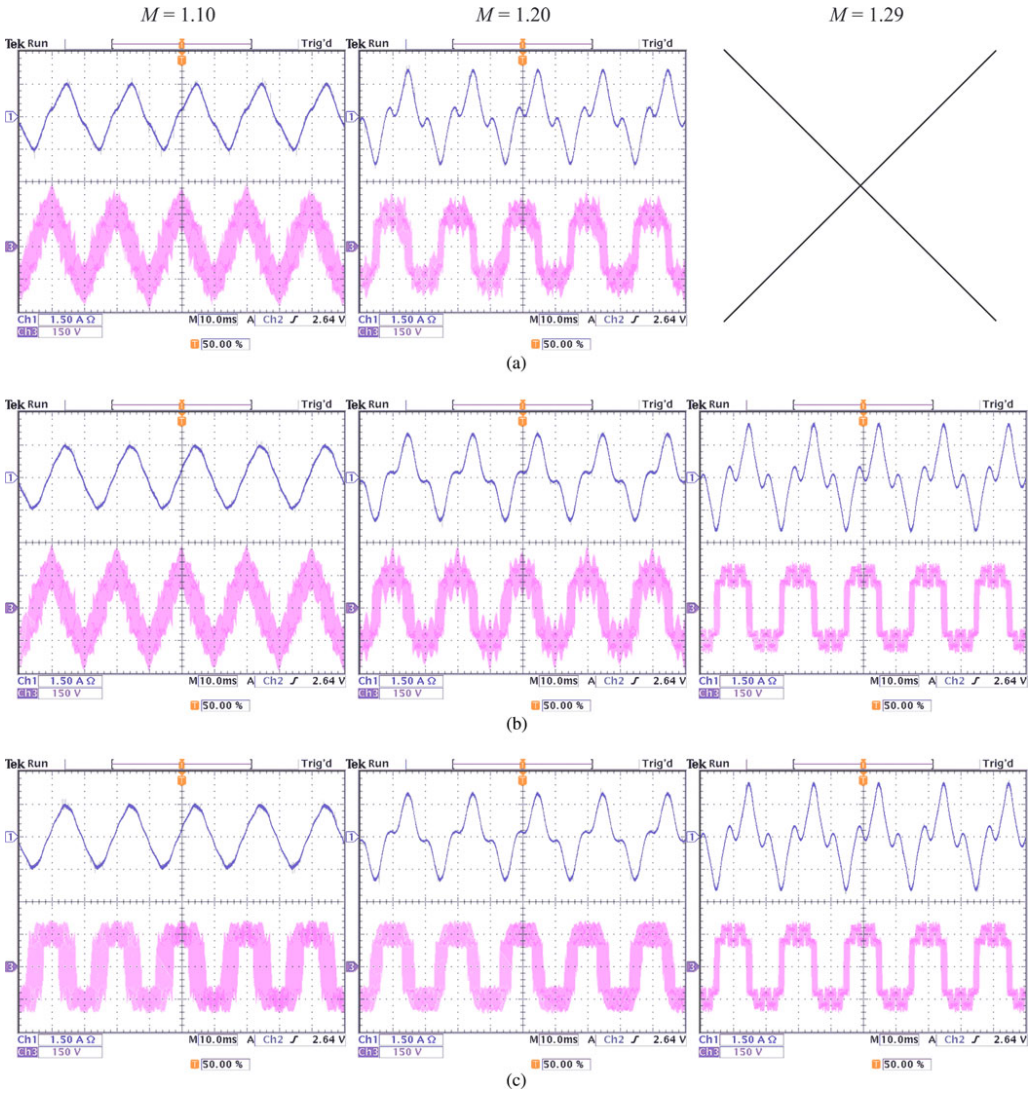

Fig. 6. Phase voltages (lower plots) and currents (upper plots) in overmodulation zones 1 (left), 2 (middle), and 3(right) for modulation indices $M = 1.1$, $M = 1.2$, and $M = 1.29$, respectively. (a) SVPWM1. (b) SVPWM2. (c) SVPWM3.

consequently, it is not possible to simultaneously average v_α^* and v_β^*. However, it is still possible to minimize the α–β voltage error as follows:

$$\frac{\partial(v_\alpha - v_\alpha^*)^2 + (v_\beta - v_\beta^*)^2}{\partial t_2} = (2C_{11}C_{12} + 2C_{13}C_{14}) + 2t_2(C_{12}^2 + C_{14}^2) = 0. \quad (21)$$

From (21), the time of application t_2 providing minimum α–β voltage error is obtained

$$t_2 = \frac{-(C_{12}C_{13} + C_{14}C_{15})}{(C_{13}^2 + C_{15}^2)}. \quad (22)$$

With (18) and (22), the times of application of the two active vectors v_2 and v_3 can be calculated.

Finally, if any of the times t_2 or t_3 is negative, then the ten-step mode of operation has been surpassed and the modulation

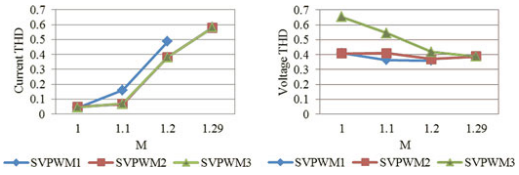

Fig. 7. THD of (left) phase currents and (right) voltages versus modulation index for SVPWM1, SVPWM2, and SVPWM3. Cutoff frequency is 20 kHz.

is out of range (see Fig. 3). To sum up, some of the features of the proposed overmodulation algorithm are the following:

1) the solution is analytical and unique;
2) it can be extended for any multiphase VSI with an odd number of phases;
3) it can be used with any four active vectors per sector;
4) it synthesizes the α–β reference voltage in zones 1 and 2 and provides minimum α–β voltage error in zone 3;
5) it minimizes x–y voltage content in zone 1;
6) compared to SVPWM1, the switching frequency of SVPWM2 and SVPWM3 decreases by 40%, 60%, and 80% as the voltage reference enters overmodulation zones 1, 2, and 3, respectively;
7) both SVPWM2 and SVPWM3 are valid until the ten-step mode of operation achieving a maximum modulation index equal to 1.2944, while SVPWM1 is only valid until the modulation index is equal to 1.236.

D. Application of the Algorithm

The general overmodulation algorithm previously described can be applied to the cases when the four active vectors are the two medium and two large per sector (SVPWM2) and the two large and two adjacent large per sector (SVPWM3). For the sake of example, let us consider $V_{\mathrm{DC}} = 1$ p.u., $T_s = 1$ p.u., an angle of the α–β voltage space vector $\varphi = \mathrm{tg}^{-1}(v^*_\beta / v^*_\alpha) = 10^\circ$, and modulation indices $M = 1.1$, $M = 1.2$, and $M = 1.29$. Table II details the four selected vectors, their times of application, and the equations used in the three overmodulation zones. Fig. 4 takes the times of application of Table II and shows how the overmodulation algorithm synthesizes the α–β voltage space vector in each zone using SVPWM2 (left) and SVPWM3 (right).

When the modulation index is $M = 1.1$, application of (7) shows that the times of application of the four active vectors are positive but the time of application of the zero vector is negative both in SVPWM2 and SVPWM3 (see Table II). The algorithm enters overmodulation zone 1 and uses (11)–(15) to avoid the use of the zero vectors and provide minimum x–y voltages. Voltage space vectors $v_1 \equiv 16$, $v_2 \equiv 24$, $v_3 \equiv 25$, and $v_4 \equiv 29$ in SVPWM2 and $v_1 \equiv 28$, $v_2 \equiv 24$, $v_3 \equiv 25$, and $v_4 \equiv 17$ in SVPWM3 are applied during the times of application shown in Table II [see Fig. 4(a)], which comply with restriction (10). If the modulation index is further increased up to $M = 1.2$, then the application of (11)–(15) reveals that t_4 becomes negative in SVPWM2 and t_1 becomes negative in SVPWM3 (see Table II).

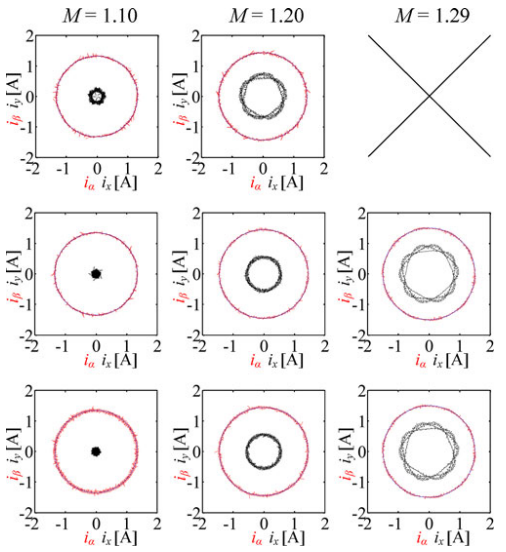

Fig. 8. Phase currents in the α–β and x–y planes for modulation indices $M = 1.1$, $M = 1.2$, and $M = 1.29$ and modulation techniques SVPWM1 (upper plots), SVPWM2 (middle plots), and SVPWM3 (lower plots).

Overmodulation zone 2 has been entered and it is necessary to discard vectors v_4 in SVPWM2 ($v_4 \equiv 29$) and v_1 in SVPWM3 ($v_1 \equiv 28$). The remaining active vectors are applied using the times of application calculated from (18), as shown in Fig. 4(b). These times of application guarantee that α–β voltages are synthesized and restriction (16) is satisfied. When the modulation index approaches the ten-step mode of operation ($M = 1.29$), application of (18) provides negative values of the times t_1 in SVPWM2 and t_4 in SVPWM3. Since vectors v_2 and v_3 are the same in SVPWM2 and SVPWM3, it follows that both methods converge in overmodulation zone 3 which extends the range of operation up to the ten-step mode ($M = 1.294$). The times of application of the large vectors v_2 and v_3 are calculated from (18)–(22), ensuring minimum α–β voltage error. However, the reference α–β voltage space vector ($v^*_{\alpha,\beta}$) cannot be fully generated on average [see Fig. 4(c)].

IV. Experimental Results

The performance in the overmodulation region of strategies SVPWM1, SVPWM2, and SVPWM3 is experimentally verified in a test rig based on a 30 slots, two pairs of poles three-phase induction machine, whose stator has been rewound to provide a five-phase induction machine with three pairs of poles. Parameters of the machine have been determined using conventional and stand-still tests with inverter supply [22], [23], obtaining the values shown in Table III. A schematic of the rig and photos of the complete system are included in Fig. 5.

Five phases of two conventional three-phase VSIs from Semikron (SKS21F) have been used to drive the machine.

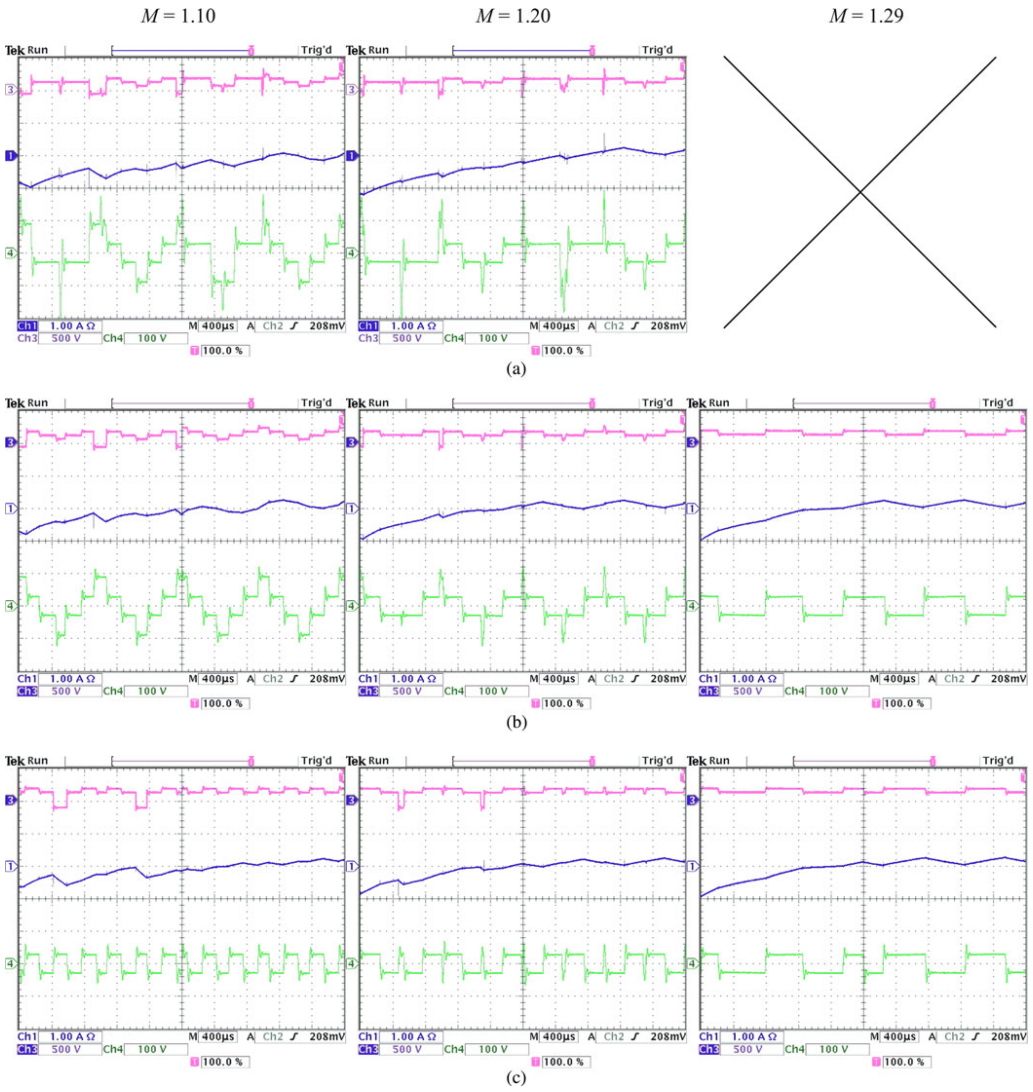

Fig. 9. Zoom (4 ms) of the phase current (upper plots) and CMV (lower plots) in overmodulation zones 1 (left), 2 (middle), and 3 (right) for modulation indices $M = 1.1$, $M = 1.2$, and $M = 1.29$, respectively. (a) SVPWM1. (b) SVPWM2. (c) SVPWM3.

The control system is based on the MSK28335 board and the TMS320F28335 DSP, and the induction machine is operated in open-loop mode. Measurements are obtained using a digital scope, a current probe, and a differential voltage probe (Tektronix TDS3014B, TCP202, and P5205). All experimental results have been obtained with the experimental rig shown in Fig. 5 using a switching frequency of 10 kHz, a dc-link voltage of 300 V, and modulation indices of $M = 1.1$, $M = 1.2$, and $M = 1.29$.

Fig. 6 shows the phase voltages and currents for SVPWM1 [19] and proposed SVPWM2 and SVPWM3. Results using SVPWM1 have only been shown for modulation indices $M = 1.1$ and $M = 1.2$ because the method in [19] does not cover the whole overmodulation region up to the ten-step mode. Current waveforms of SVPWM2 and SVPWM3 prove to be similar for $M = 1.1$ and $M = 1.2$ and fully identical for $M = 1.29$, where both methods converge (zone 3). However, comparison of the phase currents for the three aforementioned methods

shows that the waveforms of SVPWM1 are more distorted. The phase voltage total harmonic distortion (THD) of SVPWM3 is higher than SPVWM1 and SVPWM2 (see Fig. 7) because it contains a higher amount of switching harmonics. Nevertheless, the fundamental and low-order voltage harmonics are similar for SVPWM2 and SVPWM3 and for this reason the current THD is practically equal for both methods (SVPWM2 and SVPWM3), while SVPWM1 presents a higher THD due to the presence of higher low-order harmonics. These low-order harmonics flow in the machine due to the unavoidable *x*–*y* voltages existing in the pulse dropping region (see Fig. 8). The minimization of the *x*–*y* voltages in zone 1 (14) and the elimination of zero vectors in zone 2 (17) result in a lower content of *x*–*y* voltages for SVPWM2 and SVPWM3 compared to SVPWM1. Voltage harmonics, mapped into the *x*–*y* plane, are responsible for the higher distortion of the current (see Fig. 6), higher current THD (see Fig. 7), and higher *x*–*y* current content (see Fig. 8) for SVPWM1 compared to SVPWM2 and SVPWM3. Then, it can be concluded that, from the point of view of the power/current quality, the proposed methods present a better performance in overmodulation zones than the method proposed in [19], normally applied in the modulation of multiphase drives.

In order to evaluate the performance from the point of view of the generated CMV, Fig. 9 shows the zoomed current waveforms and the peak-to-peak values of the CMV using the three methods under consideration. When the modulation index $M = 1.1$, SVPWM1 still applies zero, medium, and large voltage vectors, thus resulting in six CMV levels [see Fig. 9(a)]. Only four levels of the CMV are however obtained using SVPWM2 [see Fig. 9(b)] due to the constraint that eliminates zero vectors (10). Medium vectors are additionally eliminated in SVPWM3 resulting in just two CMV levels [see Fig. 9(c)]. The same analysis holds for $M = 1.2$. It can be concluded that the peak-to-peak CMV, the main cause of EDM bearing currents, is reduced by 40% in SVPWM2 and by 80% in SVPWM3 in the overmodulation region. When the modulation index $M = 1.29$, the proposed algorithm (see Fig. 3) enters overmodulation zone 3, where SVPWM2 and SVPWM3 converge because only the two large vectors of each sector are applied. From the analysis of the currents (see Figs. 6–8) and CMV (see Fig. 9), it can be stated that both SVPWM2 and SVPWM3 strategies outperform SVPWM1, providing lower current THD and peak-to-peak CMV. Even though the performance of SVPWM2 and SVPWM3 is very similar in terms of voltage and current generation (see Figs. 6–8), the CMV in SVPWM3 is three times lower than SVPWM2 in overmodulation zones 1 and 2.

V. Conclusion

This study shows that it is possible to calculate the dwell times in the overmodulation region avoiding the use of zero vectors (zones 1–3), minimizing the *x*–*y* voltage generation (zone 1), synthesizing the α–β reference voltages (zone 2), and minimizing the α–β voltage error (zone 3). This approach allows the VSI to operate in the whole overmodulation region up to the ten-step mode with good performance and a 40% reduction of the CMV. The suggested method for the calculation of the dwell times is generally valid for any four active vectors, but the use of two medium and two large vectors (SVPWM2) and the use of four large vectors (SVPWM3) is explored in this study. Both options provide similar performance in terms of voltage generation and current quality, but the use of four large vectors further reduces the CMV by 80%.

Appendix

Overmodulation zone 1:

$$C_1 = -T_s \frac{(v_\alpha^* - v_{3\alpha}) \cdot (v_{2\beta} - v_{3\beta}) - (v_\beta^* - v_{3\beta}) \cdot (v_{2\alpha} - v_{3\alpha})}{(v_{1\beta} - v_{3\beta}) \cdot (v_{2\alpha} - v_{3\alpha}) - (v_{1\alpha} - v_{3\alpha}) \cdot (v_{2\beta} - v_{3\beta})}$$

$$C_2 = -\frac{(v_{4\beta} - v_{3\beta}) \cdot (v_{2\alpha} - v_{3\alpha}) - (v_{4\alpha} - v_{3\alpha}) \cdot (v_{2\beta} - v_{3\beta})}{(v_{1\beta} - v_{3\beta}) \cdot (v_{2\alpha} - v_{3\alpha}) - (v_{1\alpha} - v_{3\alpha}) \cdot (v_{2\beta} - v_{3\beta})}$$

$$C_3 = -\frac{C_1 \cdot (v_{1\alpha} - v_{3\alpha}) - T_s \cdot (v_\alpha^* - v_{3\alpha})}{v_{2\alpha} - v_{3\alpha}}$$

$$C_4 = -\frac{C_2 \cdot (v_{1\alpha} - v_{3\alpha}) + (v_{4\alpha} - v_{3\alpha})}{v_{2\alpha} - v_{3\alpha}}$$

$$C_5 = T_s - C_1 - C_3$$

$$C_6 = -C_2 - C_4 - 1$$

$$C_7 = \frac{v_{1x} C_1 + v_{2x} C_3 + v_{3x} C_5}{T_s}$$

$$C_8 = \frac{v_{1x} C_2 + v_{2x} C_4 + v_{3x} C_6 + v_{4x}}{T_s}$$

$$C_9 = \frac{v_{1y} C_1 + v_{2y} C_3 + v_{3y} C_5}{T_s}$$

$$C_{10} = \frac{v_{1y} C_2 + v_{2y} C_4 + v_{3y} C_6 + v_{4y}}{T_s}.$$

Overmodulation zone 3:

$$C_{11} = v_{3\alpha} - v_\alpha^* \qquad C_{13} = v_{3\beta} - v_\beta^*$$

$$C_{12} = \frac{v_{2\alpha} - v_{3\alpha}}{T_s} \qquad C_{14} = \frac{v_{2\beta} - v_{3\beta}}{T_s}.$$

References

[1] E. Levi, R. Bojoi, F. Profumo, H. Toliyat, and S. Williamson, "Multiphase induction motor drives—a technology status review," *IET Electr. Power Appl.*, vol. 1, no. 4, pp. 489–516, Jul. 2007.

[2] M. D. Hennen, M. Niessen, C. Heyers, H. J. Brauer, and R. W. De Doncker, "Development and control of an integrated and distributed inverter for a fault tolerant five-phase switched reluctance traction drive," *IEEE Trans. Power Electron.*, vol. 27, no. 2, pp. 547–554, Feb. 2012.

[3] M. J. Duran, S. Kouro, B. Wu, E. Levi, F. Barrero, and S. Alepuz, "Six-phase PMSG wind energy conversion system based on medium-voltage multilevel converter," in *Proc. Eur. Conf. Power Electron. Appl.*, Birmingham, U.K., 2011, pp. 1–10.

[4] A. Tani, M. Mengoni, L. Zarri, G. Serra, and D. Casadei, "Control of multiphase induction motors with an odd number of phases under open-circuit phase faults," *IEEE Trans. Power Electron.*, vol. 27, no. 2, pp. 565–577, Feb. 2012.

[5] J. M. Erdman, R. J. Kerkman, D. W. Schlegel, and G. L. Skibinski, "Effect of PWM inverters on AC motor bearing currents and shaft voltages," *IEEE Trans. Ind. Appl.*, vol. 32, no. 2, pp. 250–259, Mar./Apr. 1996.

[6] A. Muetze and A. Binder, "Don't lose your bearings," *IEEE Ind. Appl. Mag.*, vol. 12, no. 4, pp. 22–31, Jul./Aug. 2006.

[7] M. A. Cash and T. G. Habetler, "Insulation failure prediction in inverter-fed induction machines using line-neutral voltages," in *Proc. IEEE Appl. Power Electron. Conf.*, 1998, pp. 1035–1039.

[8] H. Hussain and H. Toliyat, "Modified SVPWM switching scheme to reduce shaft voltage in five-phase induction motors," presented at the 38th Annu. Conf. IEEE Ind. Electron. Soc., Montreal, Canada, 2012.
[9] R. M. Tallam, R. J. Kerkman, D. Leggate, and R. A. Lukaszewski, "Common-mode voltage reduction PWM algorithm for AC drives," *IEEE Trans. Ind. Appl.*, vol. 46, no. 5, pp. 1959–1969, Sep./Oct. 2010.
[10] U. T. Shami and H. Akagi, "Experimental discussions on a shaft end-to-end voltage appearing in an inverter-driven motor," *IEEE Trans. Power Electron.*, vol. 24, no. 6, pp. 1532–1540, Jun. 2009.
[11] Y. S. Lai and F. Shyu, "Optimal common-mode voltage reduction PWM technique for inverter control with considerations of the dead time effects—I: Basic development," *IEEE Trans. Ind. Appl.*, vol. 40, no. 6, pp. 1605–1612, Nov./Dec. 2004.
[12] J. W. Kimball and M. Zawodniok, "Reducing common-mode voltage in three-phase sine-triangle PWM with interleaved carriers," *IEEE Trans. Power Electron.*, vol. 26, no. 8, pp. 2229–2236, Aug. 2011.
[13] S. Lakshminarayanan, G. Mondal, P. N. Tekwani, K. K. Mohapatra, and K. Gopakumar, "Twelve-sided polygonal voltage space vector based multilevel inverter for an induction motor drive with common-mode voltage elimination," *IEEE Trans. Ind. Electron.*, vol. 54, no. 5, pp. 2761–2768, Oct. 2007.
[14] H. J. Kim, H. D. Lee, and S. K. Sul, "A new PWM strategy for common-mode voltage reduction in neutral-point-clamped inverter-fed AC motor drives," *IEEE Trans. Ind. Appl.*, vol. 37, no. 6, pp. 1840–1845, Nov./Dec. 2001.
[15] J. Prieto, M. Jones, F. Barrero, E. Levi, and S. Toral, "Comparative analysis of discontinuous and continuous PWM techniques in VSI-fed five-phase induction motor," *IEEE Trans. Ind. Electron.*, vol. 58, no. 12, pp. 5324–5335, Dec. 2011.
[16] M. J. Duran, S. Toral, F. Barrero, and E. Levi, "Real-time implementation of multidimensional five-phase space vector pulse width modulation," *IET Electron. Lett.*, vol. 43, no. 17, pp. 949–950, 2007.
[17] D. Dujic, M. Jones, and E. Levi, "Continuous carrier-based vs. space vector PWM for five-phase VSI," in *Proc. IEEE EUROCON*, Warsaw, Poland, 2007, pp. 1772–1779.
[18] M. J. Duran, F. Salas, and M. R. Arahal, "Bifurcation analysis of five-phase induction motor drives with third harmonic injection," *IEEE Trans. Ind. Electron.*, vol. 55, no. 5, pp. 2006–2014, May 2008.
[19] A. Iqbal and E. Levi, "Space vector modulation schemes for a five-phase voltage source inverter," in *Proc. Eur. Conf. Power Electron. Appl.*, Dresden, Germany, Sep. 2005, pp. 1–12.
[20] M. Duran and E. Levi, "Multi-dimensional approach to multiphase space vector pulse width modulation," in *Proc. 32nd Annu. Conf. IEEE Ind. Electron. Soc.*, Paris, France, 2006, pp. 2103–2108.
[21] M. J. Duran, J. A. Riveros, F. Barrero, H. Guzman, and J. Prieto, "Reduction of common-mode voltage in five-phase induction motor drives using predictive control techniques," *IEEE Trans. Ind. Appl.*, Nov./Dec. 2012, to be published.
[22] J. A. Riveros, F. Barrero, M. J. Durán, B. Bogado, and S. Toral, "Estimation of the electrical parameters of a five-phase induction machine using standstill techniques—I: Theoretical discussions," in *Proc. 37th Annu. Conf. IEEE Ind. Electron. Soc.*, Melbourne, Australia, 2011, pp. 3668–3673.
[23] J. A. Riveros, F. Barrero, M. J. Durán, B. Bogado, and S. Toral, "Estimation of the electrical parameters of a five-phase induction machine using standstill techniques—II: Practical implications," in *Proc. IEEE Annu. Conf. IEEE Ind. Electron. Soc.*, Melbourne, Australia, 2011, pp. 3674–3679.

Mario J. Durán was born in Málaga, Spain, in 1975. He received the M.Sc. and Ph.D. degrees in electrical engineering from the University of Málaga, Málaga, in 1999 and 2003, respectively.

He is currently an Associate Professor with the Department of Electrical Engineering, University of Málaga. His research interests include modeling and control of multiphase drives and renewable energies conversion systems.

Joel Prieto (S'10) received the B.Eng. degree in electronic engineering from the Universidad Católica Nuestra Señora de la Asunción, Asunción, Paraguay, in 2005, and the M.Sc. degree from the University of Seville, Seville, Spain, in 2009, where he is currently working toward the Ph.D. degree.

In 2008, he joined the Department of Electronic Engineering, University of Seville. He received scholarship from Itaipu Binacional/Parque Tecnológico Itaipu-Paraguay for his Ph.D. studies.

Federico Barrero (M'04–SM'05) received the M.Sc. and Ph.D. degrees in electrical and electronic engineering from the University of Seville, Seville, Spain, in 1992 and 1998, respectively.

In 1992, he joined the Department of Electronic Engineering, University of Seville, where he is currently an Associate Professor.

Dr. Barrero received the Best Paper Award for the IEEE TRANSACTIONS ON INDUSTRIAL ELECTRONICS in 2009.

3.8. Paper 8

Authors: J. Prieto, F. Barrero, M. J. Durán, S. Toral y M.A. Perales.
Title: SVM Procedure for n-phase VSI With Low Harmonic Distortion in the Overmodulation Region.
Journal: IEEE Transactions on Industrial Electronics.
Volume: 61.
Number: 1.
Pages: 92-97.
Date: January 2014.
Abstract: Space vector modulation (SVM) technique has become a standard method for the impression of voltage references in conventional three-phase voltage source inverters. The method is nowadays used in multiphase (more than three) drives, where linear and overmodulation regions are covered only for the five-phase case. This work proposes a general SVM procedure for linear and overmodulation regions in n-phase drives (being n any odd number, $n > 3$) and simplifies the extension of SVM to the multiphase case. The proposed method achieves the reference voltage at the fundamental frequency while reducing introduced harmonic components in the overmodulation region compared to previous proposals.

92 IEEE TRANSACTIONS ON INDUSTRIAL ELECTRONICS, VOL. 61, NO. 1, JANUARY 2014

SVM Procedure for n-Phase VSI With Low Harmonic Distortion in the Overmodulation Region

Joel Prieto, *Student Member, IEEE*, Federico Barrero, *Senior Member, IEEE*, Mario J. Durán, Sergio Toral Marín, *Senior Member, IEEE*, and Manuel A. Perales

***Abstract*—Space vector modulation (SVM) technique has become a standard method for the impression of voltage references in conventional three-phase voltage source inverters. The method is nowadays used in multiphase (more than three) drives, where linear and overmodulation regions are covered only for the five-phase case. This work proposes a general SVM procedure for linear and overmodulation regions in n-phase drives (being n any odd number, $n > 3$) and simplifies the extension of SVM to the multiphase case. The proposed method achieves the reference voltage at the fundamental frequency while reducing introduced harmonic components in the overmodulation region compared to previous proposals.**

***Index Terms*—Multiphase, overmodulation, space vector pulse width modulation.**

I. Introduction

SPACE vector modulation (SVM) has been recently stated as an excellent algorithm for the control of three-phase voltage source power converters due to its ability to generate the voltage reference after the Clarke's transformation. The reference voltage vector is synthesized in the three-phase case using a combination of the two adjacent active switching vectors in each sector and one or both of the zero vectors. The voltage source converter is usually operated in the linear modulation region, but overmodulation can also be used to improve the dynamic response of the drive increasing the output voltage of the power converter. The main consequence of using overmodulation is the generation of low-order voltage harmonics. Multiphase drives are gaining interest against their three-phase counterpart due to their utility in safe critical propulsion applications. Then, SVM is being nowadays extended to obtain its benefits in the multiphase case. Linear modulation region is reached using different SVM schemes that apply adjacent active voltage vectors to the voltage reference [1]. However, the overmodulation region requires much more attention than in the three-phase case because effective impedances differ between fundamental and some specific harmonics components not involved within the mechanical energy conversion. These low-order harmonic voltage components face very low effective impedances in the multiphase drive, increasing the Joule losses in the machine. Some trials have been made to deal with this problem in [2] developing two different SVM methods in the overmodulation region. Another modulation technique based on a carrier-based approach was studied in [3], where the switching current harmonic content was detailed. Finally, two complex and optimal mathematical solutions for the five phase case have been recently proposed in [4], [5]. The objective proposed in [4] is to minimize the voltage generated in xy planes, while [5] is additionally focused on common mode voltage.

This letter provides a general SVM scheme for duty cycles' computation which covers overmodulation and linear operation regions, extending the range of operation of the power converter into the overmodulation region with a smooth and linear transition characteristic, while minimizing voltage amplitude of unwanted low-order voltage harmonic components. The main contribution of the proposed algorithm comparing to [4], [5] is its simplicity and its ability to be applied to any multiphase system with an odd number of phases, when spatial harmonics are not considered and null xy voltage references are required.

Manuscript received July 30, 2012; revised November 25, 2012; accepted January 7, 2013. Date of publication January 16, 2013; date of current version July 18, 2013. This work was supported by the Spanish Government (National Research, Development and Innovation Plan, under references DPI2011-25396 and Junta de Andalucía 2010 research program, under reference TEP-5791) and Itaipu Binacional/Parque Tecnológico Itaipu-Paraguay.

J. Prieto, F. Barrero, S. Toral Marín, and M. A. Perales are with the Department of Electronic Engineering, University of Seville, 41092 Seville, Spain (e-mail: jprieto@esi.us.es; fbarrero@esi.us.es; toral@esi.us.es; mperales@us.es).

M. J. Durán is with the Department of Electrical Engineering, University of Málaga, 29071 Málaga, Spain (e-mail: mjduran@uma.es).

Color versions of one or more of the figures in this paper are available online at http://ieeexplore.ieee.org.

Digital Object Identifier 10.1109/TIE.2013.2240638

II. SVM in Multiphase Drives

The n-phase drive has a total number of 2^n switching states which correspond to the ON/OFF states of the n converter legs. These states are defined by the switching functions $[S_1, S_2, \ldots, S_n]$ where $S_i \in \{0, 1\}$. Then, each switching state generates a voltage vector that is mapped into $(n-1)/2$ different orthogonal planes according to the general Clarke's transformation given by (1), see equation at the bottom of the next page where $\alpha = 2\pi/n$. This transformation maps harmonic components into different planes according to the following rules: $2nk \pm 1$ harmonics including the fundamental frequency into the $\alpha\beta$ plane, $2nk \pm (2m-1)$ harmonics into xy planes and nk harmonics into the zero-sequence plane, with $1 \leq m \leq (n-1)/2$ and $k = 0, 1, 2, 3 \ldots$ (see (1) at the bottom of the next page). Extrapolation of SVM algorithms to the n-phase case are focused on the $\alpha\beta$ plane because torque is usually related to the current components of this plane. A voltage reference v_{ref} in the $\alpha\beta$ plane is impressed (Fig. 1). This is done like in the three-phase case, and the $\alpha\beta$ plane is divided into $2n$ sectors to find the one that contains v_{ref}. Then, it is applied a linear combination of $(n-1)$ active vectors from those adjacent to the reference $(v_{a1}, v_{a2} \ldots v_{a(n-1)/2}, v_{b1}, v_{b2} \ldots v_{b(n-1)/2}$ in Fig. 1, or v_{ax}

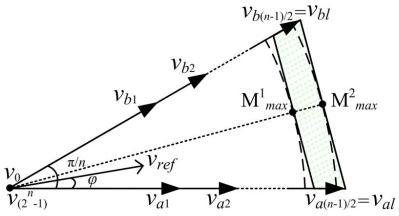

Fig. 1. Selection of active voltage vectors in the $\alpha\beta$ plane extending SVM algorithms for the n-phase drive case.

and v_{bx} in what follows, being $x = 1, 2, \ldots, (n-1)/2$) and the two zero voltage vectors. The voltage reference in other planes are meanwhile zeroed when it is possible (linear modulation area), which it is not the case in the overmodulation region. A SVM algorithm for five-phase drives is proposed in [1]. Two large and two medium vectors are used to reach the reference in the $\alpha\beta$ plane, and the voltage references in other planes are zeroed in the linear modulation region. The SVM that uses a similar approach for n-phase systems will be referred to hereinafter as SVM$_{n-1}$, being n any odd number higher than 3. The technique proposed in [1] is then called SVM$_4$ in what follows. Voltage vectors are usually normalized with respect to half of the dc-link voltage, being their amplitudes defined in (2) in the n-phase system, where $K_x = \sin(x \cdot \pi/n)$

$$|v_{ax}| = |v_{bx}| = \left(\frac{4}{n}\right)\frac{K_x}{K_1}. \tag{2}$$

Therefore, the duty cycles δ_{ax} and δ_{bx} (or time that the voltage vectors v_{ax} and v_{bx} are, respectively, applied during the modulation period to reach v_{ref}) can be obtained for the linear region using (3) and (4), being φ the phase of the reference voltage vector, s the number of the sector where the reference is located, and $(s-1)\pi/n$ and $s\pi/n$ the electrical phases of the lines that delimitate the sector. Notice that zero vectors are also applied to complete the modulation period: $\delta_0 = 1 - \Sigma(\delta_{ax} + \delta_{bx})$

$$\delta_{ax} = M \cdot K_x \cdot \sin(s \cdot \pi/n - \varphi) \tag{3}$$
$$\delta_{bx} = M \cdot Kx \cdot \sin(\varphi - (s-1) \cdot \pi/n). \tag{4}$$

The modulation index M is used in the evaluation of δ_{ax} and δ_{bx}. It is defined as the ratio between the fundamental phase voltage amplitude and half of the dc-link voltage. According to this definition, linear region is limited by $M^1_{\max} = 1/\cos(\pi/(2n))$, while the maximum modulation index is $M^2_{\max} = (4/n) \cdot (K_{(n-1)/2}/K_1) \cdot \cos(\pi/(2n))$ in the overmodulation region. However, the application of SVM$_4$ in the overmodulation region, between $M^1_{\max}$ and $M^2_{\max}$, produces undesirable low-order voltage harmonics in xy planes that must be mitigated.

Another SVM scheme has been used in [2]. It applies only the two largest adjacent voltage vectors in the $\alpha\beta$ plane, and it will be called SVM$_2$ in what follows. Voltage reference is then generated guaranteeing the greatest modulation indices, up to $M^2_{\max}$, at the expense of producing undesirable voltages in xy planes. This means that although the reference at the input of the modulator is purely sinusoidal, the output phase voltages are not. SVM$_2$ uses the two largest vectors of the SVM$_{n-1}$ case, $v_{a(n-1)/2}$ and $v_{b(n-1)/2}$, or v_{al} and v_{al} from now on, respectively, for simplifying their nomenclatures. The duty cycles are then obtained in this case as follows:

$$\delta_{al} = M \cdot n/\left(4K_{\frac{(n-1)}{2}}\right) \cdot \sin(s \cdot \pi/n - \varphi) \tag{5}$$
$$\delta_{bl} = M \cdot n/\left(4K_{\frac{(n-1)}{2}}\right) \cdot \sin(\varphi - (s-1) \cdot \pi/n). \tag{6}$$

It is interesting to mention that in order to generate the fundamental reference voltage vector, (7) and (8) are fulfilled. Notice that the obtained duty cycles must be lower in SVM$_2$ than the sum of the corresponding duty cycles using SVM$_{n-1}$ because introduced voltage vectors have shorter amplitudes. Furthermore, in the linear region, the relationship between duty cycles using SVM$_2$ and SVM$_{n-1}$ remains constant as it is stated in (9), deduced after some algebraic operations replacing (3)–(6) into (7) and (8)

$$|v_{al}| \cdot \delta_{al} = \left(\sum_{x=1}^{\frac{(n-1)}{2}} |v_{ax}| \cdot \delta_{ax}\right) \tag{7}$$
$$|v_{bl}| \cdot \delta_{bl} = \left(\sum_{x=1}^{\frac{(n-1)}{2}} |v_{bx}| \cdot \delta_{bx}\right) \tag{8}$$
$$\left(\sum_{x=1}^{\frac{(n-1)}{2}} \delta_{ax}\right) \Big/ \delta_{al} = \left(\sum_{x=1}^{\frac{(n-1)}{2}} \delta_{bx}\right) \Big/ \delta_{bl} = K_{\frac{(n-1)}{2}} \cdot \sum_{x=1}^{\frac{(n-1)}{2}} K_x \Big/ \sum_{x=1}^{\frac{(n-1)}{2}} K_x^2 = C. \tag{9}$$

$$C_n = \frac{2}{n}\begin{bmatrix} 1 & \cos(\alpha) & \cos(2\alpha) & \cos(3\alpha) & \ldots & \cos(n-1)\alpha \\ 0 & \sin(\alpha) & \sin(2\alpha) & \sin(3\alpha) & \ldots & \sin(n-1)\alpha \\ 1 & \cos(2\alpha) & \cos(4\alpha) & \cos(6\alpha) & \ldots & \cos 2(n-1)\alpha \\ 0 & \sin(2\alpha) & \sin(4\alpha) & \sin(6\alpha) & \ldots & \sin 2(n-1)\alpha \\ \vdots & \vdots & \vdots & \vdots & \vdots & \vdots \\ 1 & \cos\left(\left(\frac{n-1}{2}\right)\alpha\right) & \cos\left(\left(2\frac{n-1}{2}\right)\alpha\right) & \cos\left(\left(3\frac{n-1}{2}\right)\alpha\right) & \ldots & \cos\left(\left(\frac{(n-1)^2}{2}\right)\alpha\right) \\ 0 & \sin\left(\left(\frac{n-1}{2}\right)\alpha\right) & \sin\left(\left(2\frac{n-1}{2}\right)\alpha\right) & \sin\left(\left(3\frac{n-1}{2}\right)\alpha\right) & \ldots & \sin\left(\left(\frac{(n-1)^2}{2}\right)\alpha\right) \\ \frac{1}{2} & \frac{1}{2} & \frac{1}{2} & \frac{1}{2} & \ldots & \frac{1}{2} \end{bmatrix} \tag{1}$$

Some attempts have also been made to extend the SVM into the overmodulation region [2].The most common approach is using SVM_2, which generates low-order voltage harmonics in linear and overmodulation regions as it was stated before. The second approach, also analyzed in [2], extends the method proposed in [1](SVM_4) to operate in the overmodulation region, being only valid for the five-phase case. Large and medium space vectors are used, but any sinusoidal reference above $M^1_{\max}$ limit is considered as being the maximum achievable. Then, δ_0 is forced to zero in the middle of each sector to obtain the maximum possible output. Notice that δ_0 is not zero in the rest of the sector, which indicates that the solution is not optimal as this period is not used to minimize xy components.

III. Proposed Algorithm

The proposed algorithm goes beyond previous developed methods in the overmodulation region. It forces $\delta_0 = 0$ in any position of each sector when the reference voltage vector is within the overmodulation region, reducing xy voltage components. Notice that relationships (7)–(9) are valid for linear region ($M \leq M^1_{\max}$), but can be extended to the overmodulation zone ($M^1_{\max} < M \leq M^2_{\max}$). This extension requires the injection of voltage in the xy planes. The proposed algorithm manages this injection reducing the amplitude of the generated low-order voltage harmonics comparing with previous SVM methods. This goal is reached modifying the relationship established by (9), forcing smaller constant values for the overmodulation region. Then, $\Sigma(\delta_{ax} + \delta_{bx}) > 1$ means that overmodulation region is reached, and duty cycles of the largest vectors should be increased while shorter vectors' duty cycles should be reduced, in order to maintain $\Sigma(\delta_{ax}+\delta_{bx})=1$ and $\delta_0 = 0$. Comparing with [2], that forces $\delta_0 = 0$ in the middle of each sector (SVM_4), the proposed technique forces $\delta_0 = 0$ for the entire sector in the overmodulation region. It is interesting to note that applying largest vectors in the $\alpha\beta$ plane during higher duty cycles allows achieving the fundamental frequency phase voltage. Meanwhile, voltage vectors applied in the xy planes are reduced. This is a direct consequence of the correspondence between largest voltage vectors in the $\alpha\beta$ plane and lower voltage vectors in the xy planes. If largest voltage vectors in the $\alpha\beta$ plane are applied for longer duty cycles, shorter voltage vectors in xy planes are also applied for longer time, reducing average voltage vectors in xy planes and voltage harmonic content. Then, an appropriate constant factor, from now on R, must be established. This is done taking into account that (9) implies

$$\left(\sum_{x=1}^{\frac{(n-1)}{2}} (\delta_{ax} + \delta_{bx})\right) \Big/ (\delta_{al} + \delta_{bl}) = R, \quad R \geq 1. \tag{10}$$

It must be mentioned that $R = C(9)$ in the linear region. If $M^1_{\max} < M \leq M^2_{\max}$ and overmodulation region is reached, $\Sigma(\delta_{ax} + \delta_{bx}) = 1$ while $\delta_0 = 0$, and (10) becomes

$$R = \frac{1}{(\delta_{al} + \delta_{bl})}. \tag{11}$$

```
Evaluate δax and δbx from (3) and (4)
If ( Σ_{x=1}^{(n-1)/2} (δax + δbx) ) ≤ 1 then      'REM linear region
    use δax and δbx values
Else                                              'REM overmodulation zone
    Evaluate δal and δbl from (5) and (6)
    If δal+δbl ≤ 1 then
        R = 1/(δal+δbl)
        Evaluate (12)
    Else
        Reference vector cannot be achieved
    End if
End if
```

Fig. 2. Proposed algorithm.

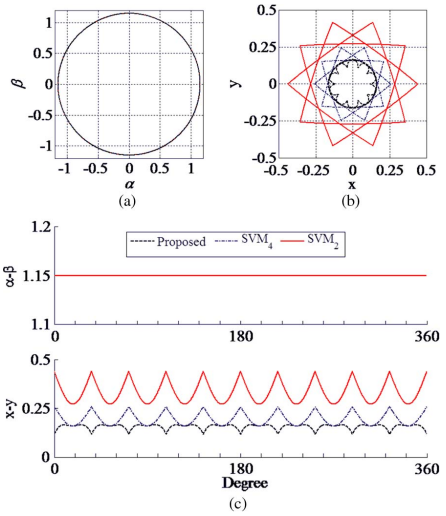

Fig. 3. Proposed SVM technique. Comparison results with the SVM_2 and SVM_4 techniques for a five-phase drive. A modulation index $M = 1.15$ is used, without loss of generality. (a) Voltage circle diagram in $\alpha\beta$ plane, (b) voltage circle diagram in xy plane, and (c) voltage magnitude in $\alpha\beta$ and xy planes.

Finally, the limit case occurs when the reference vector's amplitude is $M^2_{\max}$ and the angle is $k\pi/2n$ (k odd), where $R = 1$. Then, the duty cycle of the active vectors v_{ax} in the n-phase drive can be obtained evaluating (12), shown at the bottom of the next page, while the duty cycles of v_{bx} are generated changing a to b in (12).

The first row in (12) corresponds to (7) and syntheses on average the reference voltage vector in the $\alpha\beta$ plane. The second row corresponds to (10) and guarantees $\delta_0 = 0$ (zero voltage vectors are not applied). The rest of rows are obtained from (3) and (4) after some algebraic manipulation and establish the required proportion between voltage vectors (except the largest ones) to reduce the xy voltage components. In the linear region, $R = C(9)$ and the reference voltage is generated without undesired xy voltage components. In the overmodulation region, R becomes variable, according to (11), to ensure $\delta_0 = 0$ condition and minimize xy voltage components. Compared to [2], where

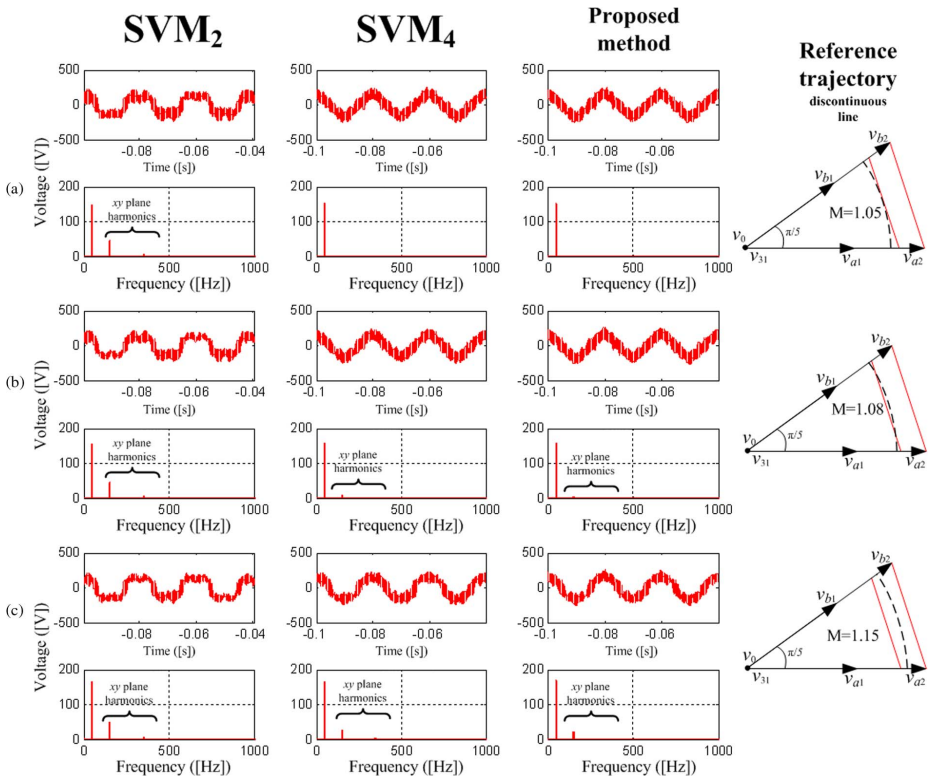

Fig. 4. Experimental comparison for a five-phase drive between SVM_2, SVM_4 and the proposed method. Upper plots show phase voltages, while lower ones correspond to voltage spectra in low-order harmonics. (a) Linear region ($M = 1.05$), (b) $M = 1.08$, and (c) overmodulation region ($M = 1.15$).

R is calculated for a single operation point, condition (11) fully eliminates the need to apply zero vectors in the overmodulation region and reduces the xy voltage components as it is shown next. Notice that (12) is valid for any n-phase system both in the linear and overmodulation ranges. It is also interesting to note that its inverse can be evaluated offline, simplifying the real-time implementation of the method. Fig. 2 shows the high-level description of the proposed technique.

$$\begin{bmatrix} \delta_{a1} \\ \delta_{a2} \\ \delta_{a3} \\ \delta_{a4} \\ \vdots \\ \delta_{a(n-1)/2-1)} \\ \delta_{a(n-1)/2} \end{bmatrix} = \begin{bmatrix} |v_{a1}| & |v_{a2}| & |v_{a3}| & \cdots & |v_{a((n-1)/2-2)}| & |v_{a((n-1)/2-1)}| & |v_{a(n-1)/2} \\ 1 & 1 & 1 & \cdots & 1 & 1 & 1 \\ -K_2/K_1 & 1 & 0 & \cdots & 0 & 0 & 0 \\ 0 & -K_3/K_2 & 1 & \cdots & 0 & 0 & 0 \\ \vdots & \vdots & \vdots & \ddots & \vdots & \vdots & \vdots \\ 0 & 0 & 0 & \cdots & 1 & 0 & 0 \\ 0 & 0 & 0 & \cdots & -K_{(n-1)/2-1}/K_{(n-2)/2} & 1 & 0 \end{bmatrix}^{-1} \cdot \begin{bmatrix} |v_{al}| \cdot \delta_{al} \\ R \cdot \delta_{al} \\ 0 \\ \vdots \\ 0 \\ 0 \\ 0 \end{bmatrix} \quad (12)$$

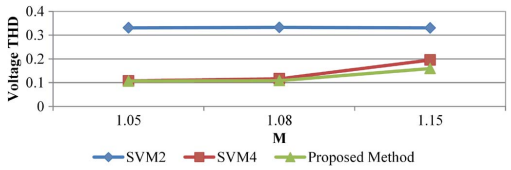

Fig. 5. Phase voltage THD using SVM2, SVM4, and the proposed method.

IV. Results

The proposed method is compared with the SVM_2 and SVM_4 methods [2]. A five-phase case is considered in the linear and overmodulation regions, and simulation and experimental results are presented. Figs. 3 and 4 show obtained results. A modulation index $M = 1.15$ is used in the overmodulation region. Generated voltages in the $\alpha\beta$ plane, the same for all cases, are shown in Fig. 3(a). Fig. 3(b) and (c) depict voltages in the xy plane (only one plane in the five-phase case). Red ink corresponds to SVM_2, blue trace represents SVM_4 method, and black color details the proposed method. The proposed method clearly shows lower voltage components in the xy plane. The reduction of voltage harmonics is also experimentally verified using a 1.4 kW five-phase induction machine with three pair of poles. Obtained results are shown in Fig. 4. Two conventional three-phase voltage source inverter (VSI) from Semikron (SKS21F) were used to drive the motor. The dc-link was set to 300 V using a DC power supply system. The control system is based on the MSK28335 board and stator voltage was measured in steady-state condition using a digital scope and differential voltage probes (Tektronix TDS3014B, P5205). Notice that obtained results are not printed directly from the scope; the data are downloaded from the scope using a personal computer, to improve their final format. The modulation period is 100 μs, corresponding to a switching frequency $f_{sw} = 10$ kHz. The machine is operated in open-loop mode with a fundamental frequency of 50 Hz and using linear [Fig. 4(a)] and overmodulation regions [Fig. 4(b) and (c)]. Modulation indices have been defined $M = 1.05$, $M = 1.08$ and $M = 1.15$, respectively.

Notice that the $M = 1.08$ case [Fig. 4(b)] reaches both linear and overmodulation regions, providing a particular case study to analyze transition between regions. It is clearly shown that SVM_4 and the proposed method similarly reduce the harmonic content (third and seventh harmonic components) in the linear region. However, the proposed method not only reduces xy components in the overmodulation area, but also eliminates the seventh harmonic components (@350 Hz). Fig. 5 compares obtained voltage THD using all the modulation methods in a five-phase VSI. It can be deduced that the proposed method shows the best performance in the overmodulation region. The THD factor has been calculated considering harmonics up to 25 kHz according to the expression:

$$THD = \frac{\sqrt{V_2^2 + V_3^2 + \ldots + V_n^2}}{V_1} \qquad (13)$$

where V_k is the rms value of the kth voltage harmonic.

The viability of the proposed technique has been finally stated for different multiphase cases. Fig. 6 provides simulation

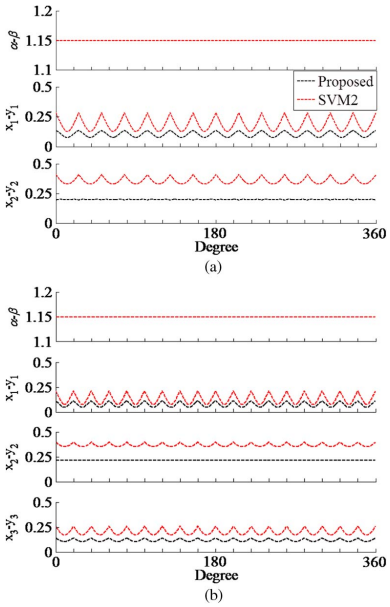

Fig. 6. Comparison results for seven and nine-phase cases using the proposed and SVM_2 techniques. Overmodulation region is considered ($M = 1.15$).

results for the seven and nine-phase cases, where it is compared with an extension of the SVM_2 technique using $M = 1.15$. Proposed technique shows better performance and lower xy voltages which in turn increase the drive efficiency.

V. Conclusion

An SVM algorithm was proposed for the evaluation of the duty cycles in multiphase drives. Voltage references at the fundamental frequency are obtained in the linear region maintaining zero-voltage harmonic contents, as in previous SVM multiphase algorithms. However, it improves the efficiency in the overmodulation region because it reduces the harmonic content and the impressed voltage in the xy planes. Then, the method improves previous n-phase SVM techniques in the overmodulation area, being n any odd number higher than 3.

References

[1] D. Dujic, M. Jones, and E. Levi, "Generalized space vector PWM for sinusoidal output voltage generation with multi-phase voltage source inverters," *Int. J. Ind. Electron. Drives*, vol. 1, no. 1, pp. 1–13, May 2009.

[2] A. Iqbal and E. Levi, "Space vector modulation schemes for a five-phase voltage source inverter," in *Proc. Eur. Conf. Power Electron. Appl.*, Dresden, Germany, Sep. 2005, p. 12.

[3] S. Halasz, "Overmodulation region of multi-phase inverters," in *Proc. 13th EPE-PEMC*, Poznan, Poland, Sep. 2008, pp. 682–689.

[4] G. Carrasco and C. Silva, "Space vector PWM method for five-phase two-level VSI with minimum harmonic injection in the overmodulation region," *IEEE Trans. Ind. Electron.*, vol. 60, no. 5, pp. 2042–2053, May 2013.

[5] M. Duran, J. Prieto, and F. Barrero, "Space vector PWM with reduced common-mode voltage for five-phase induction motor drives operating in overmodulation zone," *IEEE Trans. Power Electron.*, vol. 28, no. 8, pp. 4030–4040, Aug. 2013.

Joel Prieto (S'10) received the B.Eng. degree in electronic engineering from the Universidad Católica Nuestra Señora de la Asunción, Paraguay, in 2005, and the M.Sc. degree from the University of Seville, Seville, Spain, in 2009, where he is currently working toward the Ph.D. degree in the Department of Electronic Engineering.

Mr. Prieto is a recipient of Scholarship from Itaipu Binacional/Parque TecnológicoItaipu-Py for his Ph.D. studies.

Federico Barrero (M'04–SM'05) received the M.Sc. and Ph.D. degrees in electrical and electronic engineering from the University of Seville, Seville, Spain, in 1992 and 1998, respectively.

In 1992, he joined the Department of Electronic Engineering at the University of Seville, where he is currently an Associate Professor.

Dr. Barrero received the Best Paper Award from the IEEE TRANSACTIONS ON INDUSTRIAL ELECTRONICS for 2009 and the *IET Electric Power Applications* Premium Award 2012.

Mario J. Durán was born in Málaga, Spain, in 1975. He received the M.Sc. and Ph.D. degrees in electrical engineering from the University of Málaga, Málaga, Spain, in 1999 and 2003, respectively.

Currently, he is an Associate Professor with the Department of Electrical Engineering at the University of Málaga. His research interests include modeling and control of multiphase drives and renewable energy conversion systems.

Sergio Toral Marín (M'01–SM'06) received the Ph.D. degree in electrical and electronic engineering from the University of Seville, Seville, Spain.

He is a Professor in the Department of Electronic Engineering at the University of Seville. His research interests include multiphase electrical machines, embedded operating systems, wireless sensor networks, and intelligent transportation systems.

Manuel A. Perales received the Ing. Industrial and Doctor Ing. Industrial degrees from the University of Seville, Seville, Spain, in 1995 and 2002, respectively.

He joined the Department of Electronic Engineering at the University of Seville in 1996 as a Researcher, and since 1998, he has been an Assistant Professor in this department. His current research areas are active power filters, modulation techniques, power systems, and digital controllers for power systems.

Capítulo 4

Conclusiones y Futuros Trabajos

4.1. Conclusions

The main conclusions obtained with the development of this thesis are the following:

1. Analytical and space vector pulse width modulation methods applied in three-phase motor drives have been extended to the multiphase case, studied on the basis of the flux Harmonic Distortion Factor and implemented considering different multiphase cases, in particular symmetrical five phase and asymmetrical six phase induction machines. The extension of these modulation methods was not a simple task due to the increment of the switching possibilities (from 2^3 in a conventional three-phase power converter to 2^n in a conventional n-phase power converter, becoming some of these switching possibilities redundant in the generated stator voltage). The dynamic model of the multiphase power converter was obtained using the Space Vector and the Polygon approaches, and the obtained output current-ripple in the multiphase induction machine was parametrized using the harmonic distortion factor. On the basis of the obtained results, different continuous and discontinuous modulation methods were compared, to determine their utility in the control of multiphase drives.

2. Extensions of the analysed multiphase modulation techniques have been proposed to include overmodulation regions and to consider the reduction in the generated common model voltage. These new methods take into account

smooth and easy transitions from the linear to the overmodulation regions in the application of the multiphase modulation techniques and the common mode voltage reduction, in order to increase the robustness of the system and to develop multiphase high performance drives. The extension has been achieved in a straightforward manner and experimental results illustrate the viability and good performance of the proposed techniques.

4.2. Future work

The final objective of this research work is the development of a multiphase propulsion drive with application in EVs. In this sense, some features of the multiphase propulsion system have been reached, but others remain to be addressed in future research. Among these, the following can be highlighted:

1. The development of a standard speed and torque control method is required, with the ability to be extended and generalized to other numbers of phases. Field Oriented Control methods and Direct Torque Control techniques are mainly considered as the most important control techniques in conventional three-phase drives. The multiphase case offers difficulties in the extension and generalization of aforementioned control methods, being one of the most interesting research fields for the development in the near future of multiphase propulsion modules.
2. Fault-tolerance capability of multiphase drives admits the post-fault operation if three or more healthy phases remain, allowing the generation of a symmetrical rotating airgap field and the operation. The development of a flexible, high performance and robust control system for the EV motor drive in normal and post-fault conditions is an interesting goal that remains after this research. This work will also include the analysis and performance of modulation methods in the multiphase drive when some faulty phases appear.
3. The work focuses on the analysis of two particular multiphase machines, a symmetrical five-phase induction rotor cage machine and an asymmetrical six-phase induction rotor cage machine. Different numbers of phases, as well as different technologies in the development of the multiphase machine (wound rotor, permanent magnet and switching reluctance) should be considered to select the one that better fits the final application (EV).

4. Other interesting research areas can be the identification of the electrical parameters of multiphase machines or the introduction of sensorless techniques in the development of speed and torque control methods. While the off-line and on-line identification methods will improve the performance of the applied controllers, sensorless techniques might reduce the final cost and increase the robustness of the multiphase propulsion system. In any case, their applicability in multiphase drives is out of the scope of this work, and will introduce more complexity and computational cost in the development of the multiphase propulsion drive.

Bibliografía

[1] S. Xue and X. Wen, "Simulation analysis of two novel multiphase svpwm strategies," in *IEEE International Conference on Industrial Technology. ICIT '05*, Dec. 2005, pp. 1337–1342.

[2] S. Xue, X. Wen, and Z. Feng, "A novel multi-dimensional svpwm strategy of multiphase motor drives," in *Power Electronics and Motion Control Conference, 2006. EPE-PEMC 2006. 12th International*, Sept 2006, pp. 931 –935.

[3] K. Marouani, L. Baghli, D. Hadiouche, A. Kheloui, and A. Rezzoug, "A new pwm strategy based on a 24-sector vector space decomposition for a six-phase vsi-fed dual stator induction motor," *IEEE Trans. Ind. Electron.*, vol. 55, no. 5, pp. 1910–1920, May 2008.

[4] D. Hadiouche, L. Baghli, and A. Rezzoug, "Space vector pwm techniques for dual three-phase ac machine: analysis, performance evaluation and dsp implementation," in *Conference Record of the IEEE Industry Applications Conference. 38th IAS Annual Meeting.*, vol. 1, Oct. 2003, pp. 648–655 vol.1.

[5] D. Holmes and T. Lipo, *Pulse Width Modulation for Power Converters: Principles and Practice*. IEEE Press - Series on Power Engineering, Piscataway, NJ, 2003.

[6] H. van der Broeck and H.-C. Skudelny, "Analytical analysis of the harmonic effects of a pwm ac drive," *IEEE Trans. Power Electron.*, vol. 3, no. 2, pp. 216 –223, Apr. 1988.

[7] J. Kolar, H. Ertl, and F. Zach, "Influence of the modulation method on the conduction and switching losses of a pwm converter system," in *Industry Applications Society Annual Meeting, 1990., Conference Record of the 1990 IEEE*, Oct 1990, pp. 502–512 vol.1.

[8] V. Blasko, "Analysis of a hybrid pwm based on modified space-vector and triangle-comparison methods," *IEEE Trans. Ind. Appl.*, vol. 33, no. 3, pp. 756–764, May/Jun 1997.

[9] A. Hava, R. Kerkman, and T. Lipo, "Simple analytical and graphical methods for carrier-based pwm-vsi drives," *IEEE Trans. Power Electron.*, vol. 14, no. 1, pp. 49–61, Jan 1999.

[10] G. Narayanan and V. Ranganathan, "Analytical evaluation of harmonic distortion in pwm ac drives using the notion of stator flux ripple," *IEEE Trans. Power Electron.*, vol. 20, no. 2, pp. 466–474, March 2005.

[11] P. Dahono, "Analysis and minimization of output current ripple of multiphase pwm inverters," in *IEEE Power Electronics Specialists Conference. PESC '06.*, June 2006, pp. 1–6.

[12] P. Dahono, Deni, and E. Supriatna, "Output current-ripple analysis of five-phase pwm inverters," *IEEE Trans. Ind. Appl.*, vol. 45, no. 6, pp. 2022 –2029, Nov. 2009.

[13] J. Kolar, H. Ertl, and F. Zach, "Influence of the modulation method on the conduction and switching losses of a pwm converter system," *IEEE Trans. Ind. Appl.*, vol. 27, no. 6, pp. 1063–1075, Nov/Dec 1991.

[14] A. Hava, R. Kerkman, and T. Lipo, "A high-performance generalized discontinuous pwm algorithm," *IEEE Trans. Ind. Appl.*, vol. 34, no. 5, pp. 1059–1071, Sep/Oct 1998.

[15] P. Dahono, Y. Sato, and T. Kataoka, "Analysis and minimization of ripple components of input current and voltage of pwm inverters," *IEEE Trans. Ind. Appl.*, vol. 32, no. 4, pp. 945 –950, Jul/Aug 1996.

[16] D. Dujic, M. Jones, and E. Levi, "Continuous carrier-based vs. space vector pwm for five-phase vsi," in *The International Conference on "Computer as a Tool". EUROCON'07.*, Sept. 2007, pp. 1772–1779.

[17] A. Iqbal and S. Moinuddin, "Comprehensive relationship between carrier-based pwm and space vector pwm in a five-phase vsi," *IEEE Trans. Power Electron.*, vol. 24, no. 10, pp. 2379–2390, Oct. 2009.

[18] O. Ojo and G. Dong, "Generalized discontinuous carrier-based pwm modulation scheme for multi-phase converter-machine systems," in *Conference Record of the IEEE Industry Applications Conference. 40th IAS Annual Meeting.*, vol. 2, Oct. 2005, pp. 1374 – 1381 Vol. 2.

[19] X. Zhang, F. Yu, H. Li, and Q. Song, "A novel discontinuous space vector pwm control for multiphase inverter," in *International Symposium on Power Electronics, Electrical Drives, Automation and Motion. SPEEDAM '06*, May 2006, pp. 1133–1136.

[20] S. Halasz, "Discontinuous modulation of multiphase inverter-fed ac motors," in *13th European Conference on Power Electronics and Applications. EPE '09.*, Sept. 2009, pp. 1–9.

[21] M. Khan, S. Ahmed, A. Iqbal, H. Rub, and S. Moinoddin, "Discontinuous space vector pwm strategies for a seven-phase voltage source inverter," in *Proceedings of the 35th Annual Conference of the IEEE Industrial Electronics Society. IECON '09*, Nov. 2009, pp. 397 –402.

[22] L. Zarri, M. Mengoni, A. Tani, G. Serra, and D. Casadei, "Minimization of the power losses in igbt multiphase inverters with carrier-based pulsewidth modulation," *IEEE Trans. Ind. Electron.*, vol. 57, no. 11, pp. 3695 –3706, Nov. 2010.

[23] D. Dujic, M. Jones, and E. Levi, "Analysis of output current ripple rms in multiphase drives using space vector approach," *IEEE Trans. Power Electron.*, vol. 24, no. 8, pp. 1926–1938, Aug. 2009.

[24] D. Dujic, M. Jones, and E. Levi, "Analysis of output current-ripple rms in multiphase drives using polygon approach," *IEEE Trans. Power Electron.*, vol. 25, no. 7, pp. 1838 –1849, Jul. 2010.

[25] D. Dujic, M. Jones, E. Levi, J. Prieto, and F. Barrero, "Switching ripple characteristics of space vector pwm schemes for five-phase two-level voltage

source inverters - part 1: Flux harmonic distortion factors," *IEEE Trans. Ind. Electron.*, vol. 58, no. 7, pp. 2789–2798, 2011.

[26] M. Jones, D. Dujic, E. Levi, J. Prieto, and F. Barrero, "Switching ripple characteristics of space vector pwm schemes for five-phase two-level voltage source inverters - part 2: Current ripple," *IEEE Trans. Ind. Electron.*, vol. PP, no. 99, pp. 1 –1, 2011.

[27] J. Prieto, M. Jones, F. Barrero, E. Levi, and S. Toral, "Comparative analysis of discontinuous and continuous pwm techniques in vsi-fed five-phase induction motor," *IEEE Trans. Ind. Electron.*, vol. 58, no. 12, pp. 5324–5335, Dec 2011.

[28] M. Jones, S. Vukosavic, D. Dujic, and E. Levi, "A synchronous current control scheme for multiphase induction motor drives," *IEEE Trans. Energy Convers.*, vol. 24, no. 4, pp. 860–868, Dec. 2009.

[29] E. Levi, "Multiphase electric machines for variable-speed applications," *IEEE Trans. Ind. Electron.*, vol. 55, no. 5, pp. 1893–1909, May 2008.

[30] D. Hadiouche, H. Razik, and A. Rezzoug, "On the modeling and design of dual-stator windings to minimize circulating harmonic currents for vsi fed ac machines," *IEEE Trans. Ind. Appl.*, vol. 40, no. 2, pp. 506–515, March-April 2004.

[31] Y.-S. Kwon, J.-H. Lee, S.-H. Moon, B.-K. Kwon, C.-H. Choi, and J.-K. Seok, "Standstill parameter identification of vector-controlled induction motors using the frequency characteristics of rotor bars," *Industry Applications, IEEE Transactions on*, vol. 45, no. 5, pp. 1610–1618, Sept 2009.

[32] J. Erdman, R. Kerkman, D. Schlegel, and G. Skibinski, "Effect of pwm inverters on ac motor bearing currents and shaft voltages," *IEEE Trans. Ind. Appl.*, vol. 32, no. 2, pp. 250–259, Mar 1996.

[33] A. Muetze and A. Binder, "Don't lose your bearings," *IEEE Ind. Appl. Mag.*, vol. 12, no. 4, pp. 22–31, July 2006.

[34] M. Cash and T. Habetler, "Insulation failure prediction in inverter-fed induction machines using line-neutral voltages," in *Applied Power Electronics Conference and Exposition, 1998. APEC '98. Conference Proceedings 1998., Thirteenth Annual*, vol. 2, Feb 1998, pp. 1035–1039 vol.2.

[35] E. Zhong and T. Lipo, "Improvements in emc performance of inverter-fed motor drives," *IEEE Trans. Ind. Appl.*, vol. 31, no. 6, pp. 1247–1256, Nov 1995.

[36] U. Shami and H. Akagi, "Experimental discussions on a shaft end-to-end voltage appearing in an inverter-driven motor," *IEEE Trans. Power Electron.*, vol. 24, no. 6, pp. 1532–1540, June 2009.

[37] R. Tallam, R. Kerkman, D. Leggate, and R. Lukaszewski, "Common-mode voltage reduction pwm algorithm for ac drives," *IEEE Trans. Ind. Appl.*, vol. 46, no. 5, pp. 1959–1969, Sept 2010.

[38] Y.-S. Lai and F.-S. Shyu, "Optimal common-mode voltage reduction pwm technique for inverter control with consideration of the dead-time effects-part i: basic development," *IEEE Trans. Ind. Appl.*, vol. 40, no. 6, pp. 1605–1612, Nov 2004.

[39] J. Kimball and M. Zawodniok, "Reducing common-mode voltage in three-phase sine-triangle pwm with interleaved carriers," *IEEE Trans. Power Electron.*, vol. 26, no. 8, pp. 2229–2236, Aug 2011.

[40] S. Lakshminarayanan, G. Mondal, P. Tekwani, K. Mohapatra, and K. Gopakumar, "Twelve-sided polygonal voltage space vector based multilevel inverter for an induction motor drive with common-mode voltage elimination," *IEEE Trans. Ind. Electron.*, vol. 54, no. 5, pp. 2761–2768, Oct 2007.

[41] H.-J. Kim, H.-D. Lee, and S.-K. Sul, "A new pwm strategy for common-mode voltage reduction in neutral-point-clamped inverter-fed ac motor drives," *IEEE Trans. Ind. Appl.*, vol. 37, no. 6, pp. 1840–1845, Nov 2001.

[42] E. Levi, R. Bojoi, F. Profumo, H. Toliyat, and S. Williamson, "Multiphase induction motor drives - a technology status review," *IET Electric Power Applications*, vol. 1, no. 4, pp. 489–516, July 2007.

[43] D. Dujic, M. Jones, and E. Levi, "Generalised space vector pwm for sinusoidal output voltage generation with multiphase voltage source inverters," *International Journal of Industrial Electronics and Drives*, vol. 1, pp. 1–13(13), 2009. [Online]. Available: http://www.ingentaconnect.com/content/ind/ijied/2009/00000001/00000001/art00001

[44] A. Iqbal and E. Levi, "Space vector modulation schemes for a five-phase voltage source inverter," in *9th European Conference on Power Electronics and Applications. EPE '05.*, 2005, pp. 12 pp.–P.12.

[45] S. Halasz, "Overmodulation region of multi-phase inverters," in *Power Electronics and Motion Control Conference, 2008. EPE-PEMC 2008. 13th*, Sept 2008, pp. 682–689.

[46] G. Carrasco and C. Silva, "Space vector pwm method for five-phase two-level vsi with minimum harmonic injection in the overmodulation region," *IEEE Trans. Ind. Electron.*, vol. 60, no. 5, pp. 2042–2053, May 2013.

[47] M. Duran, J. Prieto, and F. Barrero, "Space vector pwm with reduced common-mode voltage for five-phase induction motor drives operating in overmodulation zone," *IEEE Trans. Power Electron.*, vol. 28, no. 8, pp. 4030–4040, Aug 2013.